

2008

The Effect of Variable Gravity on the Cooling Performance of a 16-Nozzle Spray Array

Levi J. Elston
Wright State University

Follow this and additional works at: https://corescholar.libraries.wright.edu/etd_all



Part of the [Mechanical Engineering Commons](#)

Repository Citation

Elston, Levi J., "The Effect of Variable Gravity on the Cooling Performance of a 16-Nozzle Spray Array" (2008). *Browse all Theses and Dissertations*. 253.
https://corescholar.libraries.wright.edu/etd_all/253

This Thesis is brought to you for free and open access by the Theses and Dissertations at CORE Scholar. It has been accepted for inclusion in Browse all Theses and Dissertations by an authorized administrator of CORE Scholar. For more information, please contact library-corescholar@wright.edu.

THE EFFECT OF VARIABLE GRAVITY ON THE COOLING
PERFORMANCE OF A 16-NOZZLE SPRAY ARRAY

A thesis submitted in partial fulfillment
of the requirements for the degree of
Master of Science in Engineering

By

Levi Jerome Elston

B.S., Wright State University, 2005

2008
Wright State University

WRIGHT STATE UNIVERSITY
SCHOOL OF GRADUATE STUDIES

September 05, 2008

I HEREBY RECOMMEND THAT THE THESIS PREPARED UNDER MY SUPERVISION BY Levi Jerome Elston ENTITLED The Effect of Variable Gravity on the Cooling Performance of a 16-Nozzle Spray Array BE ACCEPTED IN PARTIAL FULFILLMENT OF THE REQUIREMENTS FOR THE DEGREE OF Masters of Science in Engineering.

Scott K. Thomas, Ph.D., Thesis Director

George P. G. Huang, Ph.D., Department Chair

Committee on
Final Examination

Scott K. Thomas, Ph.D.

James A. Menart, Ph.D.

J. Mitch Wolff, Ph.D.

Kirk L. Yerkes, Ph.D.

Joseph F. Thomas, Jr., Ph.D.
Dean, School of Graduate Studies

Abstract

Elston, Levi J., M.S.Egr., Department of Mechanical and Materials Engineering, Wright State University, 2008. *The Effect of Variable Gravity on the Cooling Performance of a 16-Nozzle Spray Array.*

The objective of this thesis was to investigate the cooling performance of a 16-nozzle spray array, using FC-72 as the working fluid, in variable gravity conditions with additional emphasis on fluid management and flow stability. A flight test experiment was modified to accommodate a 16-nozzle spray array, which was then tested in the parabolic flight trajectory environment of NASA's C-9 reduced gravity aircraft. The 16-nozzle array was designed to cool a 25.4×25.4 [mm] area on a thick film resistive heater used to simulate electronic components. Data was taken and reduced as a result of flight tests conducted over the course of two flight weeks (each week consisting of four flights, each flight consisting of 40 to 60 parabolas). The flight tests were conducted in order to examine gravity effects on spray cooling performance and to evaluate a novel liquid-vapor separator design. The mass flow rate through the 16-nozzle spray array ranged from $13.1 \leq \dot{m} \leq 21.3$ [g/s] for the spray cooling analysis and $14 \leq \dot{m} \leq 35$ [g/s] for the separator evaluation. The heat flux at the thick film resistor ranged from $2.9 \leq q'' \leq 25$ [W/cm²], the sub-cooling of the working fluid ranged from $1.6 \leq \Delta T_{sc} \leq 18.4$ [°C], the saturation temperature ranged from $37.4 \leq T_{sat} \leq 47.2$ [°C] and the absorbed air content in the working fluid was $C = 10.1\%$, 14.3% , and 16.8% by volume. The spray chamber pressure ranged from $42 \leq P \leq 78$ [kPa] while the acceleration ranged from $-0.02 \leq a \leq -2.02$ [g]. Two-phase cooling was emphasized, but some single-phase data was also collected. A one-

dimensional model was used to predict the heater surface temperature from the heat input and mean heater base temperature.

It was found that the cooling performance was enhanced in micro-gravity over terrestrial and elevated gravity. In addition, a sudden degradation in performance was found at high mass flow rates in micro-gravity, possibly due to liquid buildup on the surface between the nozzle impact zones. A high degree of subcooling was found to be beneficial, but the dissolved air content had little effect on the heat transfer performance either in micro-gravity or elevated gravity. Also, an improved liquid-vapor separator concept was implemented to enable flow stability during the micro-gravity portions of the flight. Multiple liquid-vapor separator concepts were tested during micro-gravity flights until a final design was settled on. The final separator design went through more rigorous evaluation to compare performance at multiple fill levels, each with a higher percentage of vapor space within the reservoir. It was found that, using the final reservoir design, stable flow operation was achieved in micro-gravity for mass flow rates $\dot{m} = 14, 17.5$ and 21 [g/s].

Contents

1	The Effect of Variable Gravity on the Cooling Performance of a 16-Nozzle Spray Array	1
1.1	Introduction	1
1.2	Experimental Setup	7
1.3	Results and Discussion	19
1.4	Conclusions	34
2	Qualitative Evaluation of a Liquid-Vapor Separator Concept in Micro-Gravity Conditions	36
2.1	Introduction	36
2.2	Experimental Setup	39
2.3	Results and Discussion	49
2.4	Conclusions	57
2.5	Future Work	58
	Bibliography	59
A	Experimental Setup: Additional Figures	63
B	Calibration and Uncertainty Analysis	71
B.1	Flow Meter	71
B.1.1	Calibration Setup	71
B.1.2	Calibration Procedure	71
B.1.3	Uncertainty Analysis	73
B.2	Thermocouples	77
B.2.1	Calibration Setup	77
B.2.2	Calibration Procedure	77
B.2.3	Uncertainty Analysis	78
B.3	Heat Flux to Spray	81

B.3.1	Uncertainty Analysis	84
C	Heater Losses: One-Dimensional Heat Conduction Model	86
C.1	Description/Motivation	86
C.2	One-Dimensional Analytical Model	87
C.3	Determination of the Heat Loss Fraction	92
D	Nondimensionalization	95
D.1	Nondimensional Heat Input	95
D.2	Nondimensional Ratio of Inertia and Acceleration to Viscous Forces	96
D.3	Other Nondimensional Terms	96
E	Procedures for Experimentation	98
E.1	FC-72 Fill Procedure	98
E.2	Test Cards and Test Plan Matrix	100
E.3	Experimental Test Procedure	102
E.3.1	Standard Operating Procedure	104
E.3.2	Emergency Procedure	106
E.3.3	Data Sheets	107
E.4	Fluid Sample Extraction Procedure	107
E.5	FC-72 Membrane Filter Procedure	109
E.6	Heater Replacement Procedure	111
F	Additional Experimental Plots	114
G	Test Equipment Data Package	151

List of Figures

1.1	Heat Transfer Coefficients: Coolants and Capabilities [1].	2
1.2	Array Spray Chamber: (a) Disassembled; (b) Three-Dimensional Array Spray Chamber Design; and (c) Upper Portion of Spray Chamber.	11
1.3	Single Nozzle Characterization: (a) Average Droplet Diameter vs. Volu- metric Flow Rate; (b) Droplet Velocity vs. Volumetric Flow Rate.	12
1.4	Liquid-Vapor Separator.	15
1.5	FC-72 Flow Loop Schematic.	16
1.6	Transient Data Traces of Surface Temperature, Acceleration, Heat Flux, and Nozzle Mass Flow Rate ($\dot{m} = 13.81 \pm 0.32$ [g/s], $\Delta T_{sc} = 11.78 \pm 1.93$ [°C], $C = 10.1\% \pm 1.3\%$): (a) Stable Operation; (b) CHF Events ($((1 - f)q'' =$ 21.17 ± 0.04 [W/cm ²]).	23
1.7	Steady State Heat Flux vs. Surface Superheat: (a) Dimensional Values; (b) Dimensionless Values.	25
1.8	Surface Superheat vs. Acceleration.	26
1.9	The Effect of Flow Rate on the Surface Superheat ($\Delta T_{sc} = 13.73 \pm 2.33$ [°C], $C = 10.1\% \pm 1.3\%$): (a) $a = -0.02 \pm 0.01$ [g]; (b) $a = -1.72 \pm 0.34$ [g].	28
1.10	The Effect of Flow Rate on the Surface Superheat in Elevated and Micro- Gravity ($\Delta T_{sc} = 13.73 \pm 2.33$ [°C], $C = 10.1\% \pm 1.3\%$): (a) $\dot{m} = 14$ and 17.5 [g/s]; (b) $\dot{m} = 14$ and 21 [g/s].	30
1.11	The Effect of Subcooling on the Surface Superheat ($\dot{m} = 14.01 \pm 0.93$ [g/s], $C = 14.3\% \pm 2.2\%$): (a) $a = -0.01 \pm 0.01$ [g]; (b) $a = -1.75 \pm 0.03$ [g].	31
1.12	The Effect of Subcooling on the Surface Superheat in Elevated and Micro- Gravity ($\dot{m} = 14.01 \pm 0.93$ [g/s], $C = 14.3\% \pm 2.2\%$).	32
1.13	The Effect of Air Content, by Volume, on the Surface Superheat ($\Delta T_{sc} =$ 16.66 ± 1.11 [°C], $\dot{m} = 17.43 \pm 0.95$ [g/s]): (a) $a = -0.01 \pm 0.01$ [g], $18.41 \leq$ $\Delta T_{sc} \leq 14.03$, $18.22 \leq \dot{m} \leq 15.91$; (b) $a = -1.69 \pm 0.31$ [g], $18.41 \leq \Delta T_{sc} \leq$ 14.03 , $18.22 \leq \dot{m} \leq 15.91$	33

2.1	Initial Flight Test Reservoir: (a) Cross-Sectional View; (b) Raw Test Data.	41
2.2	Second Generation Reservoir: (a) Cross-Sectional View; (b) Raw Test Data.	42
2.3	Stainless Steel Vane Structure: (a) Design and Cross-Section; (b) Micro-Gravity Operation.	43
2.4	Third Generation Reservoir: (a) Cross-Sectional View; (b) Raw Test Data.	45
2.5	Final Stainless Steel Liquid-Vapor Separator Iteration.	46
2.6	Liquid-Vapor Separator Internal Vane Structure (Isometric and Top Views).	47
2.7	Final Liquid-Vapor Separator Mounted.	47
2.8	Final Reservoir: (a) Cross-Sectional View; (b) Raw Test Data.	48
2.9	Reservoir Fill, Flight 3 (left) and Flight 4 (right).	49
2.10	Micro-Gravity Vapor Space in Reservoir, Flight 3.	51
2.11	Micro-Gravity Vapor Space in Reservoir, Flight 4.	52
2.12	Flow Stability in a Transient Gravitational Environment ($\dot{m} \approx 14$ [g/s]): (a) Flight 3; (b) Flight 4.	53
2.13	Flow Stability in a Transient Gravitational Environment, ($\dot{m} \approx 17.5$ [g/s]): (a) Flight 3; (b) Flight 4.	54
2.14	Flow Stability in a Transient Gravitational Environment, ($\dot{m} \approx 21$ [g/s]): (a) Flight 3; (b) Flight 4.	55
2.15	Flow Stability in a Transient Gravitational Environment, ($\dot{m} \approx 30$ [g/s]): (a) Flight 3; (b) Flight 4.	56
2.16	Flow Stability as a Function of Flow Rate and Fill Level	57
A.1	Experimental Test Setup	64
A.2	Array Spray Chamber Mounted to Experiment	64
A.3	Thick Film Resistive Heater Mounted	65
A.4	Thermocouple Placement Underneath Heater	65
A.5	Chamber Instrumentation Diagram	66
A.6	NASA's C-9 Reduced Gravity Aircraft and In-flight Trajectory	66
A.7	Section View Design of Array Spray Chamber	67
A.8	Single Nozzle Design	67
A.9	16-Nozzle Array Layout	68
A.10	Swirler Insert Design	68
A.11	Sapphire Orifice Design	69
A.12	Single Nozzle Characterization - Sauter Mean Diameter vs. Flow Rate	69
A.13	Single Nozzle Characterization - Droplet Diameter vs. Pressure Drop	69
A.14	Single Nozzle Characterization - Velocity vs. Pressure Drop	70

A.15	Single Nozzle Characterization - Sauter Mean Diameter vs. Pressure Drop	70
A.16	Interface Thermocouple Variation Near CHF ($(1 - f)q'' = 21.4 \pm 0.04$ [W/cm ²], $\dot{m} = 8.00 \pm 0.19$ [g/s])	70
B.1	Flowmeter Calibration Setup	72
B.2	Mass Flow Rate Calibration Uncertainty	75
B.3	Volumetric Flow Rate Calibration Uncertainty	76
B.4	Uncertainty of Heat Transferred to Spray	84
C.1	Possible Heat Losses Not Due to Spray	87
C.2	1-D Model Governing Equations and Boundary Conditions	88
C.3	Heat Loss Indicator (dT vs. time)	93
C.4	Linear Correlation Between Total Heat and Downward Heat Loss	94
E.1	Fill Procedure Setup/Schematic A	100
E.2	Fill Procedure Setup/Schematic B	101
E.3	Example Test Card	101
E.4	Example Test Plan Matrix	102
E.5	Hand Recorded Data Sheet	107
E.6	Camera Hand Recorded Data Sheet	108
E.7	Sample Extraction Schematic-A	110
E.8	Aire-ometer used for measuring air content percentage.	110
E.9	Membrane Filter Diagram	112
F.1	Meta-Stable CHF Regions, Heat Flux Input vs. Surface Temperature Dif- ference: (a) Cases 45-47; (b) Cases 69-72.	115
F.2	Meta-Stable CHF Regions, Dimensionless Heat Flux Input vs. Dimension- less Surface Temperature Difference: (a) Cases 45-47; (b) Cases 69-72.	116
F.3	Dimensional and Non-dimensional Steady State Heat Flux Transferred to Spray for Micro, Terrestrial and Elevated Gravity for Cases 01-04	117
F.4	Dimensional and Non-dimensional Steady State Heat Flux Transferred to Spray for Micro, Terrestrial and Elevated Gravity for Cases 05-08	118
F.5	Dimensional and Non-dimensional Steady State Heat Flux Transferred to Spray for Micro, Terrestrial and Elevated Gravity for Cases 09-12	119
F.6	Dimensional and Non-dimensional Steady State Heat Flux Transferred to Spray for Micro, Terrestrial and Elevated Gravity for Cases 13-16	120
F.7	Effect of Acceleration and Flow Rate on the Surface Temperature Differ- ence ($\Delta T_{sc} = 8.94 \pm 1.37$ [°C]).	121

F.10	Variation of Surface Temperature Difference with Subcooling ($\dot{m} = 13.88 \pm 0.69$ [g/s]): (a) $a = 0.01 \pm 0.01$ [g]; (b) $a = 1.80 \pm 0.08$ [g].	121
F.8	Effect of Subcooling on Cooling Performance: (a) $\dot{m} = 13.66 \pm 0.57$ [g/s]; (b) $\dot{m} = 13.60 \pm 0.58$ [g/s].	122
F.9	Effect of Subcooling on Cooling Performance: (a) $\dot{m} = 16.94 \pm 1.21$ [g/s]; (b) $\dot{m} = 17.31 \pm 1.16$ [g/s].	123
F.11	Variation of Surface Temperature Difference with Subcooling ($\dot{m} = 17.29 \pm 1.22$ [g/s]): (a) $a = 0.01 \pm 0.01$ [g]; (b) $a = 1.79 \pm 0.08$ [g].	124
F.12	Effect of Acceleration and Flow Rate on the Surface Temperature Difference: (a) $\Delta T_{sc} = 12.19 \pm 1.70$ [°C]; (b) $\Delta T_{sc} = 13.35 \pm 1.58$ [°C].	125
F.13	Effect of Acceleration and Flow Rate on the Surface Temperature Difference: (a) $\Delta T_{sc} = 16.75 \pm 1.27$ [°C]; (b) $\Delta T_{sc} = 16.73 \pm 1.09$ [°C].	126
F.14	Surface Temperature Difference vs. Acceleration.	127
F.21	Dimensional and Non-dimensional Steady State Surface Temperature for Micro, Terrestrial and Elevated Gravity	127
F.15	Dimensional and Non-dimensional Steady State Heat Flux Transferred to Spray for Micro, Terrestrial and Elevated Gravity for Cases 45-47	128
F.16	Dimensional and Non-dimensional Steady State Heat Flux Transferred to Spray for Micro, Terrestrial and Elevated Gravity for Cases 49-52	129
F.17	Dimensional and Non-dimensional Steady State Heat Flux Transferred to Spray for Micro, Terrestrial and Elevated Gravity for Cases 53-56	130
F.18	Dimensional and Non-dimensional Steady State Heat Flux Transferred to Spray for Micro, Terrestrial and Elevated Gravity for Cases 57-59	131
F.19	Dimensional and Non-dimensional Steady State Heat Flux Transferred to Spray for Micro, Terrestrial and Elevated Gravity for Cases 61-64	132
F.20	Dimensional and Non-dimensional Steady State Heat Flux Transferred to Spray for Micro, Terrestrial and Elevated Gravity for Cases 65-68	133
F.22	Dimensional and Non-dimensional Steady State Surface Temperature for Micro, Terrestrial and Elevated Gravity	134
F.23	Dimensional and Non-dimensional Steady State Surface Temperature for Micro, Terrestrial and Elevated Gravity	135
F.24	Dimensional and Non-dimensional Steady State Surface Temperature for Micro, Terrestrial and Elevated Gravity	136
F.25	Dimensional and Non-dimensional Steady State Surface Temperature for Micro, Terrestrial and Elevated Gravity	137

F.26	Dimensional and Non-dimensional Steady State Surface Temperature for Micro, Terrestrial and Elevated Gravity	138
F.27	Dimensional and Non-dimensional Steady State Surface Temperature for Micro, Terrestrial and Elevated Gravity	139
F.28	Dimensional and Non-dimensional Steady State Surface Temperature for Micro, Terrestrial and Elevated Gravity	140
F.29	Dimensional and Non-dimensional Steady State Surface Temperature for Micro, Terrestrial and Elevated Gravity	141
F.30	Dimensional and Non-dimensional Steady State Surface Temperature for Micro, Terrestrial and Elevated Gravity	142
F.31	Dimensional and Non-dimensional Steady State Surface Temperature for Micro, Terrestrial and Elevated Gravity	143
F.32	Dimensional and Non-dimensional Steady State Surface Temperature for Micro, Terrestrial and Elevated Gravity	144
F.33	Dimensional and Non-dimensional Steady State Surface Temperature for Micro, Terrestrial and Elevated Gravity	145
F.34	Dimensional and Non-dimensional Steady State Surface Temperature for Micro, Terrestrial and Elevated Gravity	146
F.35	Dimensional and Non-dimensional Steady State Surface Temperature for Micro, Terrestrial and Elevated Gravity	147
F.36	Dimensional and Non-dimensional Steady State Surface Temperature for Micro, Terrestrial and Elevated Gravity	148
F.37	Effect of Dimensionless Subcooling on Cooling Performance: (a) $We =$ 38.23 ± 1.88 ; (b) $We = 38.43 \pm 1.99$	149
F.38	Effect of Dimensionless Subcooling on Cooling Performance: (a) $We =$ 95.85 ± 44.60 ; (b) $We = 105.39 \pm 38.09$	150

List of Tables

1.1	Reduced Gravity Office User’s Guide Loading Requirements.	9
1.2	Thick Film Resistor Layer Information [19].	10
1.3	Summary of the Uncertainty Analysis.	18
1.4	Nominal Parameter Values.	20
A.1	Chamber Thermocouple Locations	66
B.1	Mass Flow Rate Calibration Example	74
B.2	Mass Flow Rate Calibration Example	76
B.3	Sample Thermocouple Calibration Data Set	80
B.4	Heat Transferred to Spray Calculation and Uncertainty	83
C.1	Resistive Heater Properties	87
C.2	Downward Heat Loss	93

Nomenclature

a	Acceleration, m/s^2
A	Area, m^2
b	Heater half width, m
C	Percent dissolved air content by volume, $[V_{\text{air}} / (V_{\text{FC-72}} + V_{\text{air}})] \times 100$
D	Mean droplet diameter, m
f	Fraction of heat lost down the pedestal
Fr	Froude number, v^2/aD
g	Internal heat generation, W/m^3
Ga	Galileo number, $aD^3\rho^2/\mu^2$
$G\Delta$	Nondimensional heat input, $\frac{1}{2}Q/k_rW(T_{\text{sat}} - T_{\infty})$
h	Heat transfer coefficient, $\text{W}/(\text{m}^2\text{-K})$
I	Current, A
k	Thermal conductivity, $\text{W}/(\text{m-K})$
L	Heater layer thickness or heater length, m
m	Mass, kg
\dot{m}	Mass flow rate, kg/s
P	Chamber pressure, kPa
q''	Heat flux, W/m^2
Q	Heat rate, W
R	Electrical resistance, Ω
t	Time, s
T	Temperature, K
\bar{T}	Average Temperature, K
v	Droplet velocity, m/s
V	Volume, m^3 , or voltage, V

\dot{V}	Volumetric flow rate, m ³ /s
W	Heater width, m
We	Weber number, $\rho v^2 D / \sigma$
z	Coordinate

GREEK SYMBOLS

ΔT	Temperature difference, K
μ	Viscosity, Pa-s
ρ	Density, kg/m ³
σ	Surface tension, N/m, or standard deviation
θ	Nondimensional temperature, $(T - T_{\infty, \text{surf}}) / (T_{\text{sat}} - T_{\infty, \text{surf}})$

SUBSCRIPTS

c	Heater ceramic layer (substrate)
d	Downward
∞	Free stream condition
g	Heater glass layer (cover plate)
in	Nozzle inlet
int	Interface between phenolic base and bottom of heater
phen	Phenolic base
r	Heater resistive layer
s	Side
sat	Saturated condition
sc	Subcooling
surf	Heater surface exposed to spray
u	Upward

ACRONYMS

ABS	Acrylonitrile-butadiene-styrene (plastic)
AFRL	Air Force Research Lab
CHF	Critical heat flux
GPIB	General purpose interface bus
JSC	Johnson Space Center, Houston, TX
ITO	Indium tin oxide
MSI	Mini Systems, Inc.

NASA	National Aeronautics and Space Administration
PID	Proportional-integral-differential
RTD	Resistance temperature detector
RTV	Room temperature vulcanization
SOP	Standard operating procedure
TC	Thermocouple
TEDP	Test equipment data package
TFR	Thick film resistor
UDRI	University of Dayton Research Institute
UES	Universal Energy Systems, Inc.
USB	Universal serial bus
VAC	Voltage (A/C)
WSU	Wright State University
WVU	West Virginia University

Acknowledgments

This research effort was done as part of a legacy of in-house work in the thermal lab in AFRL/RZPS, Wright-Patterson Air Force Base, Dayton, OH. I would like to thank Dr. Kirk Yerkes (AFRL) and Dr. Scott Thomas (WSU) into convincing me to experience the many pleasures of flight testing. Thank you to Dr. Lanchao Lin (UDRI) who designed the nozzle array that was flight tested and Mr. Richard Harris (UDRI) for completing the phase Doppler anemometry and nozzle characterization. Also, I would like to offer a special thanks to the rest of my very supportive cast that really made this project successful (and complete): Mrs. Kerri Baysinger, Lt. Ryan Claycamp, Mr. Dave Courson (UDRI), Lt. Christopher de la Pena, Mr. Andrew Fleming, Mr. Paul Kreitzer (WVU), Mr. Travis Michalak (my resident genius that gave me very helpful guidance all along the way), Ms. Cindy Obringer, Ms. Rebekah Puterbaugh, Dr. Thomas Reitz, Lt. Leah Swanson, Mr. Nick Tankersley, Mr. John Tennant (UES), Ms. Sarah Trent, and Lt. Nathan Welty. Lastly, thank you to Mr. John Yaniec, Dr. John McQuillen, and everyone at the NASA Reduced Gravity Office for Coordinating Airplane Space for the experiment and convincing me to get on that damn plane over and over again.

Dedication

Amy,

Your strength and continued support throughout this painful ordeal did not go unnoticed. You helped push me to finish up and I love you even more because of it. I would not be where I am now without you.

Thank you.

Chapter 1

The Effect of Variable Gravity on the Cooling Performance of a 16-Nozzle Spray Array

1.1 Introduction

The increasing need for high power electronic devices drives an increase in thermal management demands due to the inefficiency of electronic components and high density device packaging. Large amounts of excess heat, at high fluxes, must be removed, transported, and rejected to an ambient environment using advanced thermal management approaches. High power technologies often need active cooling methods to remove heat effectively and keep component reliability, usable life, and operability high. Passive methods, such as heat pipes, thermal radiation, and natural convection utilizing enhanced surfaces can be used if the heat flux is small, < 10 [W/cm²]. When higher heat fluxes are generated, active cooling techniques must be utilized to prevent component failure. Figure 1.1 shows the cooling capability bands for various cooling techniques [1]. Many of these techniques, such as single-phase forced convection, pool boiling, flow boiling, jet impingement, and

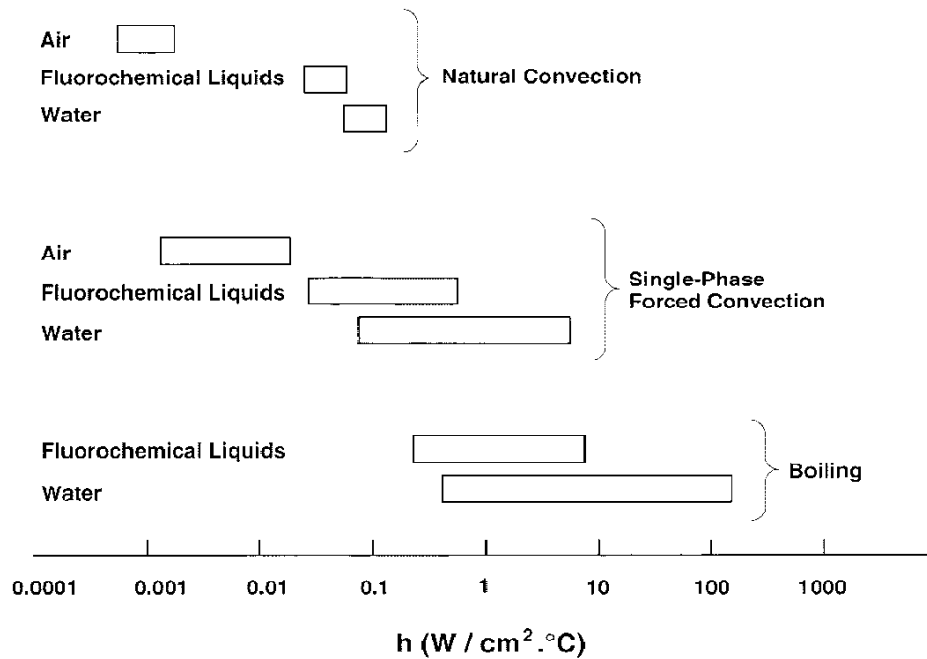


Figure 1.1: Heat Transfer Coefficients: Coolants and Capabilities [1].

spray cooling, have been studied in depth and are currently being used on various types of systems. Mudawar [1] presented many of the higher heat flux cooling schemes and ranked their heat transfer attainability, showing that, under terrestrial gravity, two-phase convection can provide two to three orders-of-magnitude higher heat transfer coefficients over single-phase convection in addition to maintaining closer temperature tolerances due to the latent heat of vaporization.

Many of these technologies have also been investigated in a micro-gravity environment. For instance, Lee et al. [2] investigated the critical heat flux and pool boiling curves for R-113 onboard the space shuttle, demonstrating a reduction in critical heat flux in micro-gravity. On the other hand, pulsating heat pipes, examined by Gu et al. [3], showed an improvement in heat transfer performance in micro-gravity. Kim [4] reviewed the state-of-the-art of the reduced gravity boiling research, concluding that many parameters (electric fields, acoustic fields, flow boiling, and non-condensable gases) can have an effect on the performance, but the mechanisms of the studied parameters are still relatively unclear. The

focus of the current research concentrates on spray cooling.

Spray cooling is a very promising technology with exceptional versatility in which many parameters can be adjusted to fit the needs of the application. Spray cooling is considered one of the most effective methods of high flux heat removal, because the latent heat of vaporization absorbs large amounts of heat with a minimal change in temperature. There are two types of spray cooling: Pressure atomized and vapor atomized. In a pressure atomized spray cooling system, liquid is pumped through a spray nozzle that is designed, using a swirler, to not only generate a spray cone but also to atomize the droplets into an even distribution onto the sprayed surface. In a vapor atomized spray cooling system, pressurized vapor is introduced into the pressurized liquid flow just before the liquid reaches the nozzle. The vapor atomizes the liquid into droplets without the use of a swirler.

Many factors contribute to the effectiveness of a spray cooling system, such as mass flow rate, array nozzle spacing, and subcooling. The phenomena and processes that are involved in spray cooling are not completely understood, but the thin liquid film formed on the heated surface plays an important role. The thickness of this film varies both spatially and temporally. As nucleation occurs on the surface, bubbles grow and eventually burst, perhaps from excessive size or droplet impact, creating a very short period of time where the local film is made up entirely of vapor until new spray droplets can re-wet the surface. In an array of spray nozzles, interactions occur generating uneven film thickness zones. Glassman et al. [5] investigated ways to reduce the liquid buildup between spray cones by placing suction tubes in these areas, thereby increasing the overall heat transfer by reducing the thickness of the liquid film. The effects of bubble growth, coalescence, and popping were all seen to play a significant role.

Many aspects of spray cooling have been investigated experimentally and numerically, including mass flow rate, subcooling, different working fluids, binary fluid mixtures, single nozzle or nozzle arrays, surface roughness (enhancement), flow rate, and nozzle orientation [6]. Ortiz and Gonzalez [7] investigated the effects of mass flow rate, surface rough-

ness, degree of subcooling, and impact angle for steady state and transient conditions. Johnson et al. [8] numerically examined the effect of subcooling and how it enhances the critical heat flux. Selvam et al. [9–13] numerically modeled the vapor bubble dynamics as a function of surface tension, gravity, phase change and viscosity as a follow on to previous numerical spray cooling work including thin film effects, nucleate boiling, droplet impact, droplet velocity, droplet interaction, and droplet density. The effect of dissolved air content on spray cooling performance was investigated by Puterbaugh et al. [14, 15]. Specifically, the sensitivity of CHF with air content was examined for a single nozzle in a terrestrial environment. The results of Puterbaugh et al. [14, 15] suggested that the amount of dissolved air in FC-72 has an insignificant effect on CHF. Kreitzer et al. [16–18] investigated body force effects on spray cooling by applying a high voltage coulombic, electrostatic, force to the spray cone, demonstrating small changes in heat transfer performance under specific conditions. Additionally, Glaspell [19] applied a Kelvin force, a magnetic field, to the spray, achieving results that provided a maximum heat transfer improvement of 5.2% at a 6 [kV] electrode voltage.

The critical heat flux, a phenomenon in which the amount of heat exceeds the heat removal ability of the spray, is a very important design criteria in a spray cooling system. Chow et al. [20] discussed the experimental background and macrolayer dry-out model associated with critical heat flux, suggesting an empirical correlation in which the critical heat flux can be determined using only the Sauter mean diameter of the spray droplets. Lin and Ponnappan [21] investigated the critical heat flux of various fluids including FC-72, FC-87, methanol, and water. Lin et al. [22,23] examined orientation effects (heated surface both vertical and horizontal with the spray facing upward) of a 48-nozzle array using FC-72 in which a 5% increase in critical heat flux, in the horizontal surface case, over the vertical heated surface was demonstrated. Lin et al. [24] explored the spray cooling performance of a binary fluid (50% methanol and 50% water) to reduce the freezing point of water to -40°C while maintaining convective performance near that of water.

Sone et al. [25] investigated the effects of reduced and elevated gravity on spray cooling using water and FC-72 on a MU-300 aircraft. Two separate experiments were conducted, each using the same non-recirculating flow loop that pumped fluid using a pressurized syringe of liquid. Experimental difficulties arose during flight testing that restricted the amount of droplet velocity data obtained, although the data did suggest up to a 20% increase in droplet velocity in reduced gravity.

The first experimental apparatus used by Sone et al. [25] consisted of a copper block heater with a polished and Cr-plated cooling face, with the gravity vector normal to this face. These experiments operated in a transient cooling mode where the block was heated to a certain temperature, the heat was turned off and the spray cooled the block during each parabola. At low flow rates, water showed no distinguishable difference in performance, but at higher flow rates ($We > 80$), the reduced gravity test showed a significant reduction in cooling performance. FC-72, on the other hand, resulted in a substantial increase in CHF and reduction in wall superheat in the reduced gravity test.

The second experimental apparatus used by Sone et al. [25] was an optically transparent indium tin oxide (ITO) heater that allowed for surface video recording during the flight test. The experiments were conducted in a steady state operation mode where the heat flux was held constant during the parabola. Using water as a coolant, a slight degradation in cooling performance was observed in the reduced gravity environment as opposed to the elevated gravity. No parabolic tests of FC-72 were completed using the transparent heater.

Yoshida et al. [26] further investigated effects of gravity on spray cooling performance using a heated copper block and ITO heaters in a non-recirculating flow loop. The work of Yoshida et al. was an extension of the work done by Sone et al. and therefore used the same experimental setups. The flight test experiments showed an increase in CHF for testing with water in micro-gravity, which contradicted the results of Sone et al. [25], whereas with FC-72 in micro-gravity, Yoshida et al. [26] showed an increase in CHF, which agreed with Sone et al. [25].

Baysinger et al. [27] began investigations of micro-gravity spray cooling in the United States utilizing the NASA KC-135 reduced gravity aircraft. An experiment was assembled to investigate gravity effects on a single nozzle spraying FC-72 onto a circular indium tin oxide (ITO) heater mounted atop a cylindrical glass rod. Thermocouples were placed beneath the heater and a one-dimensional heat conduction analysis was conducted to estimate the surface temperature. Significant surface tension flow was observed in and around the nozzle, containment cap, and chamber walls. In micro-gravity the surface tension forces became very dominant not only in the spray chamber, but also in the fluid reservoir that caused significant flow rate dropouts, which led to heater temperature spikes. These flow variations were also noticed in elevated gravity conditions, but not necessarily for the same reasons: Perhaps additional pumping head existed due to flow loop elevation differences. As an extension to this experimental work, Baysinger [28] numerically modeled the ITO heater and glass post under terrestrial gravity conditions.

The experimental setup by Yerkes et al. [29] is very similar to that described by Baysinger et al. [27]. A significant change in the experimental setup was related to improving fluid management and control: A screen was added to the chamber annulus for fluid condensation and containment. Their results demonstrated a decreasing Nusselt number as the nondimensional grouping $(Fr^{1/2}Ga)^{1/2}$ increased, suggesting that in micro-gravity the heat transfer coefficient was higher than at terrestrial or elevated gravity.

Most recently, Michalak et al. [30] further investigated the effect of variable gravity on spray cooling performance, making more modifications to the experimental setup described by both Baysinger et al. [27, 28] and Yerkes et al. [29]. This included changing to a thick film resistive heater that provided the capability to reach higher superheat temperatures without failing. The flight test results showed similar trends as those presented by Yerkes et al. [29]: At a constant heat flux the heater surface temperature was reduced as the gravitational body force decreased, for all flow rates and subcooling amounts examined. The data from Michalak et al. [30] also contained partial gravity tests: Lunar (one-sixth

[g]) and Martian (one-third [g]). Although the cooling performance enhancement for the partial-gravity tests was not as great as the micro-gravity case, an improvement was still apparent. The amount of subcooling in the spray also showed an effect demonstrating an enhancement in the reduced acceleration effect with increasing subcooling. Neither Baysinger et al. [27,28], Yerkes et al. [29], or Michalak et al. [30] investigated acceleration effects on critical heat flux. In addition, they did not track the amount of dissolved air in the test apparatus.

It has been assumed that the high momentum flux of droplets impinging upon a heated surface drives the heat transfer and associated critical heat flux, such that body forces were assumed not to play a significant role in heat transfer [6]. Previous research has shown that many factors contribute to the cooling performance of a spray cooling system and it is difficult to isolate a single parameter. Additionally, single nozzle spray cooling under variable-gravity research has shown that, depending on the working fluid, geometry, and various operating conditions, the cooling performance in micro-gravity can be noticeably higher than in accelerations greater than one [g]. Finally, research involving spray arrays in a variable gravity environment does not exist. This work investigated various parameters that affect the cooling performance of a 16-nozzle spray array in variable-gravity conditions. The objective of the flight test experiment was to show the effects of gravity, flow rate, liquid subcooling, and dissolved air content on array spray cooling performance under the following parameter ranges: $13.1 \leq \dot{m} \leq 21.3$ [g/s], $2.9 \leq q'' \leq 25$ [W/cm²], $1.6 \leq \Delta T_{sc} \leq 18.4$ [°C], $37.4 \leq T_{sat} \leq 47.2$ [°C], $C = 10.1\%$, 14.3% , and 16.8% , $42 \leq P \leq 78$ [kPa], and $-0.02 \leq a \leq -2.02$ [g].

1.2 Experimental Setup

The 16-nozzle spray array experiment consisted of five major components: The support structure, array spray chamber, liquid-vapor separator, heat rejection loop, and data ac-

quisition system. The experiment was designed to fit in a package that would contain all necessary components while maintaining safety requirements and functionality in a variable gravity environment. A test equipment data package (TEDP), shown in Appendix G, was generated according to the guidelines set by NASA [31], which defined the standards to design, construct, and qualify a reduced-gravity flight test experiment. The support structure was designed to meet NASA structural requirements while allowing accessibility to modify components throughout the system. The array spray chamber contained sixteen individual spray nozzles, a resistive heater, and a wick-sump system. The liquid-vapor separator ensured that only liquid was introduced to the nozzle inlet. The heat rejection system recirculated the working fluid, FC-72, that acquired, transported, and rejected heat. Lastly, the data acquisition system not only recorded data from all of the devices in the system, but also included fault monitoring, safety assurance, and control indication.

Each of these components were a part of an existing experimental setup [27–30] that was designed to fly on board the NASA C-9 Reduced Gravity Platform. Modifications were made to accommodate the spray array. First, the single nozzle spray chamber was replaced with a much smaller, lightweight, 16-nozzle array chamber. Also, a one [kW] power supply was mounted for the extra power needed for the larger area heater, and additional temperature cutoffs were installed to monitor for spikes in the heater temperature distribution. Lastly, due to the above modifications, the structure was re-evaluated for strength and flight-worthiness.

The design of the experiment was such that the overall cargo footprint was minimized while keeping the total height well below a standard “standing” operating level. The experiment size was restricted by the cargo door size on the aircraft. The experiment also had to be able to plug directly into the aircraft’s power outlets (110 [VAC]). The total experimental weight, nearly 320 [kg], is in part due to the stringent structural requirements which required the experimental package, including each individual component, to be able to withstand the directional loading detailed in Table 1.1. A factor of safety of two was

Direction	forward	aft	lateral	upward	downward
Loading	9g	3g	2g	2g	6g

Table 1.1: Reduced Gravity Office User’s Guide Loading Requirements.

applied to increase the margin of error. Pull tests using a load cell (Imada DPS-110) were completed on all components at a loading of up to 18 [g].

The experimental package framework was designed starting with a $12.7 \times 1219.2 \times 1830$ [mm] aluminum baseplate. The rigidity of the frame came from the network of T-slotted aluminum extrusions (80/20, Inc.). Extrusion-bracket tests were performed to determine their strength when the frame integrity analysis was conducted. In addition to the component strength pull tests, a step-by-step analysis was completed to determine how best to attach the rig to the airplane by determining the number of bolts and their placement, in accordance with the bolting grid defined by NASA. A detailed analysis of the support structure was created as a requirement for flight onboard the aircraft, as shown in Appendix G.

The 16-nozzle array and chamber are shown in Figure 1.2. The spray chamber housed the 16-nozzle array, thick film resistive (TFR) heater, aluminum foam surround, a pressure transducer port, and seven thermocouples. Liquid FC-72 entered the 16-nozzle assembly through a plenum via a 6.35 [mm] port atop the acrylic case. Liquid droplets were sprayed onto a TFR heater mounted to a phenolic base and any deflected or condensed liquid was then wicked into the aluminum foam surround. The foam provided an inlet to the scavenge ports while reducing the amount of liquid pooling on the heater surface. The enclosure was sealed to an acrylic case with a compressed o-ring. The outer dimensions of the chamber were $87.9 \times 109.2 \times 76.2$ [mm], with a wall thickness of 15.24 [mm]. The nozzle array head consisted of 16 individual nozzles, covering a 25.4×25.4 [mm] area. The individual nozzles were assembled in a four-by-four array with 6 [mm] even spacing. No attempt was made to optimize the 16-nozzle array with respect to spacing. The design of the array of nozzles was based on the single nozzle design in which each individual nozzle operated by

Layer	Position	Thickness (mm)	Thermal Conductivity (W/m-K)
Ceramic Substrate	top (sprayed surface)	$L_c = 0.643$	$k_c = 27$
Resistive Layer (heater)	middle	$L_r = 0.008$	$k_r = 1.04$
Glass Cover	bottom	$L_g = 0.040$	$k_g = 1.04$

Table 1.2: Thick Film Resistor Layer Information [19].

passing liquid through a swirler that rotated the fluid centrifugally so that when the fluid entered the sapphire orifice (Bird Precision), it generated a spray cone. The exit of the nozzle plate was located 21.2 [mm] from the heated surface being sprayed. Additional figures further describing the array design are contained in Appendix A.

A single nozzle was characterized using a phase Doppler anemometer. Droplet diameter, Sauter mean diameter, and droplet velocity were recorded for the desired range of flow rates and pressure drops. Functional relationships for both droplet diameter and droplet velocity as a function of flow rate were determined using a fourth-order polynomial fit, as shown in Figure 1.3. Additional nozzle characterization plots are presented in Appendix A.

Heat was generated using a thick film resistor (Mini Systems, Inc.) with an area of 25.4×25.4 [mm]. The heater was made of a deposited polymer film (resistive layer) sandwiched between a glass cover plate (sprayed surface) and an insulating substrate (ceramic layer). Thicknesses and thermal conductivities of each layer are shown in Table 1.2. Electrical connections to the heater were made by soldering a 0.127 [mm] nickel strap to the heater connection pads. The nickel strap allowed for flexibility from thermal expansion while minimizing stresses.

Separating the heater from the phenolic base was a thin bed of silicon high-temperature RTV that served three purposes: It adhered the heater to the base so that the heater did not move or shift during spray cooling, transport, or reduced gravity, it allowed the heater to expand or contract during heating and cooling without a fixed mount that could induce a crack or other failure, and it minimized thermal expansion stresses, such as a bending

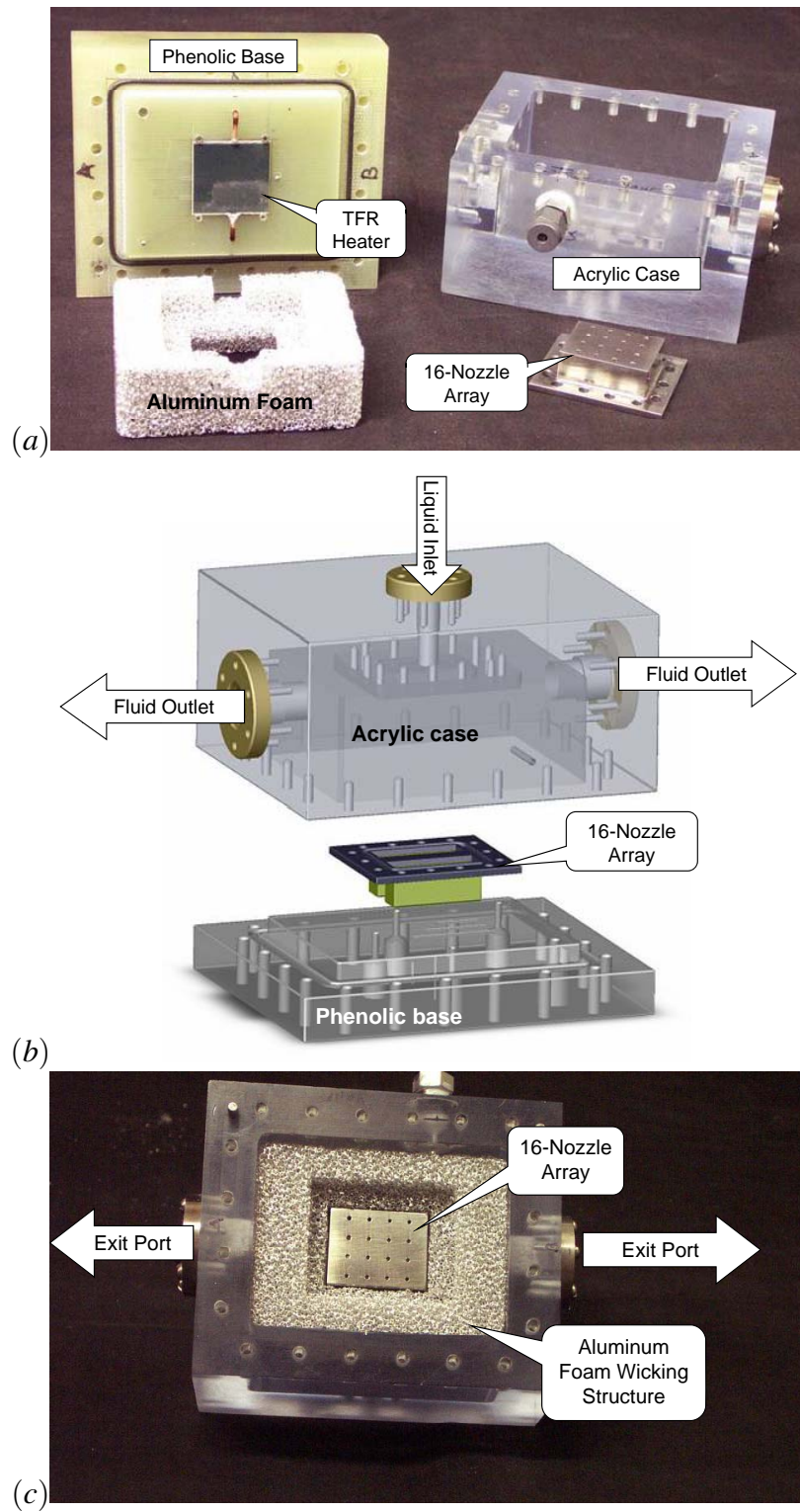
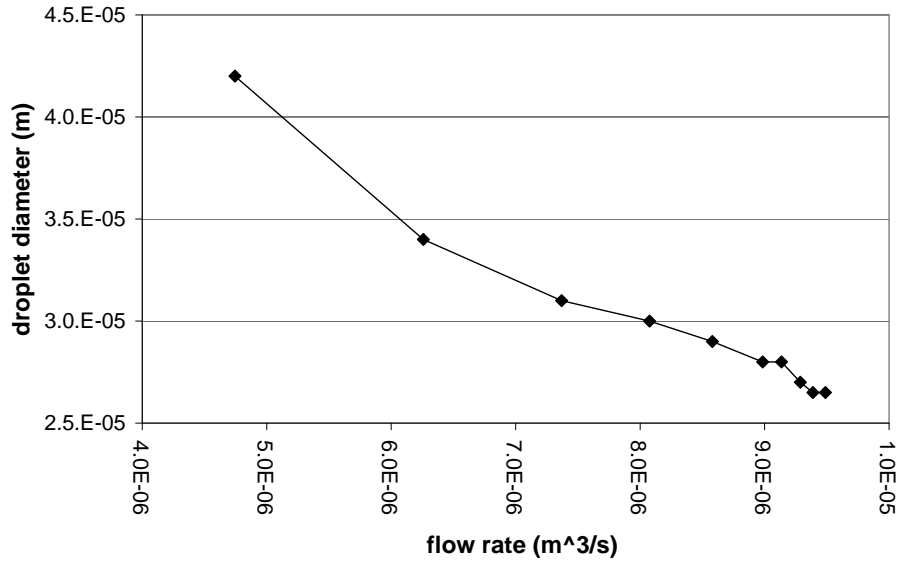
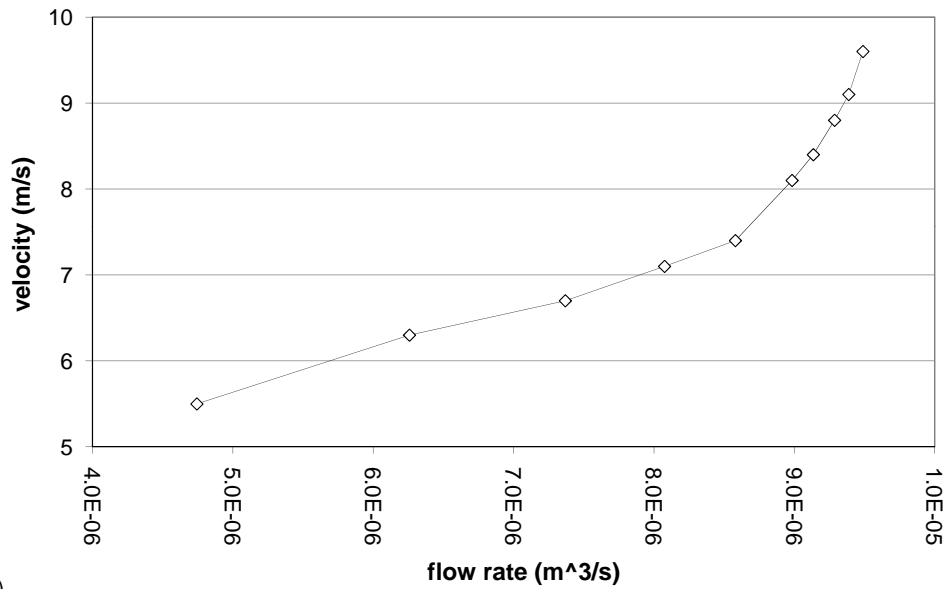


Figure 1.2: Array Spray Chamber: (a) Disassembled; (b) Three-Dimensional Array Spray Chamber Design; and (c) Upper Portion of Spray Chamber.



(a)



(b)

Figure 1.3: Single Nozzle Characterization: (a) Average Droplet Diameter vs. Volumetric Flow Rate; (b) Droplet Velocity vs. Volumetric Flow Rate.

moment due to heating, that would be created if the heater was bolted in place.

The chamber was instrumented with ten type E thermocouples as well as a pressure transducer. Thermocouples were placed in the inlet and both outlet lines of the chamber as well as inside the aluminum containment foam that read an average chamber temperature, which was used to determine saturation conditions within the chamber. Two additional thermocouples were drilled at specific depths beneath the heater surface to calculate the heat loss through the phenolic base which was not associated with spray cooling. The last three thermocouples, directly touching the bottom surface of the thick film resistance heater, gave a rough temperature distribution across the backside of the heater, supplying temperature uniformity data associated with array spray interactions. Three type E miniature thermocouples, 0.508 [mm] diameter, were fitted into individual machined channels to allow the heater to sit flat on the phenolic. The end of each interface thermocouple was bent to allow direct contact to the bottom of the heater substrate. In addition, an epoxy was used to fix the thermocouple tip to the heater bottom to prevent thermocouple re-positioning during thermal expansion. Two additional type E thermocouples protruded into the chamber to measure average surrounding fluid temperatures.

An accurate surface temperature measurement was required to evaluate spray cooling performance. To avoid disturbing the flow across the surface of the heater, three type E thermocouples were positioned on the bottom of the heater to calculate an average temperature on the bottom of the heater. Using a one-dimensional heat conduction analysis, detailed in Appendix C, as well as the heater materials and thicknesses from Table 1.2, a functional relationship was generated to determine the heater surface temperature, T_{surf} , as shown in eqn. (1.1). The heat loss fraction f , the percentage of the heat lost through the bottom of the heater and not removed via the spray, was determined by analysis of steady state heat transfer data obtained during baseline (terrestrial) testing, as shown in Appendix C.3. This fraction was approximated by a linear relationship with heater input power, shown in eqn.

(1.2), with a maximum heat loss of approximately 5.2%.

$$T_{\text{surf}} = \frac{Q}{A} \left(-\frac{(1-f)L_g}{k_g} - \frac{L_r}{2k_r} + \frac{fL_r}{k_r} + \frac{fL_c}{k_c} \right) + \bar{T}_{\text{int}} \quad (1.1)$$

$$f = -0.00016101Q + 0.05239716 \quad (1.2)$$

To assist in containing the spent liquid that drained from the surface during micro-gravity, low density aluminum foam, shown in Figure 1.2(c), was machined to fill the volume that was not directly between the nozzle head and the heated surface. Liquid exited the chamber via two ports on either side by the reduced pressure created by a downstream sump pump. During reduced gravity, surface tension resulted in the liquid collecting within the foam structure, allowing for the liquid to flow out the exit ports.

The purpose of the reservoir, Figure 1.4, was to contain excess fluid, reduce the pressure surges associated with pumping, and isolate the vapor from the transport lines feeding the nozzle pump. It consisted of a transparent container with an inlet at the top and an exit at the bottom. The most important component of the reservoir was the internal liquid-vapor separator, which was a structure consisting of very high surface area vanes which contained the liquid flow while the vapor was forced radially outward. The vapor resided along the outer walls of the chamber while the liquid was pulled out of the central axis exit port and pumped to the array nozzles. The liquid-vapor separator is explained in greater detail in Chapter 2.

Figure 1.5 shows the flow loop schematic for the experiment. The liquid exited the reservoir and entered a magnetically-coupled positive-displacement gear pump (Tuthill Corp.). The gear pump was specifically chosen to pump the working fluid at the required flow rates with sufficient pressure, determined from the phase Doppler anemometer characterization. Next, liquid was pumped through a 15 [μm] in-line filter before it reached a turbine flow meter. After the flowmeter, the liquid passed by a pressure transducer, which measured the high pressure side of the pump, or inlet to the 16-nozzle array. An inline

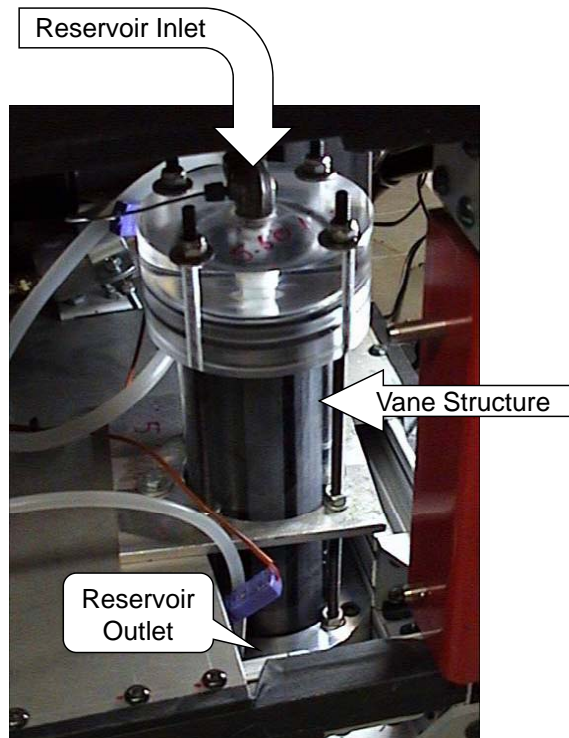


Figure 1.4: Liquid-Vapor Separator.

pressure switch was a safety device to cut off power to the entire system upon an over-pressure spike of 690 [kPa]. The bypass valve was an electrically actuated three-way valve that allowed liquid to either flow through or bypass the preheater and the 16-nozzle array. Under normal operation the bypass valve was set to allow flow through a 12.7 [mm] diameter, 305 [mm] long tubular preheater. The preheater was fabricated using copper pipe wrapped with a nichrome heater wire and covered in fiberfrax insulation. The preheater contained a twisted metal ribbon that more efficiently heated the liquid prior to the nozzle inlet. The preheater could also be used to heat the liquid to vary the subcooling before it entered the nozzle array. Next, liquid entered the spray chamber through a 6.35 [mm] stainless steel tube and exited via two 12.7 [mm] stainless steel tubes that were at a reduced pressure. Immediately after exiting the chamber, the liquid was directed through a series of three liquid-air heat exchangers (Lytron Corp.). Just downstream of the heat exchangers resided a scavenge pump, with a pressure transducer on either side, which fed two-phase

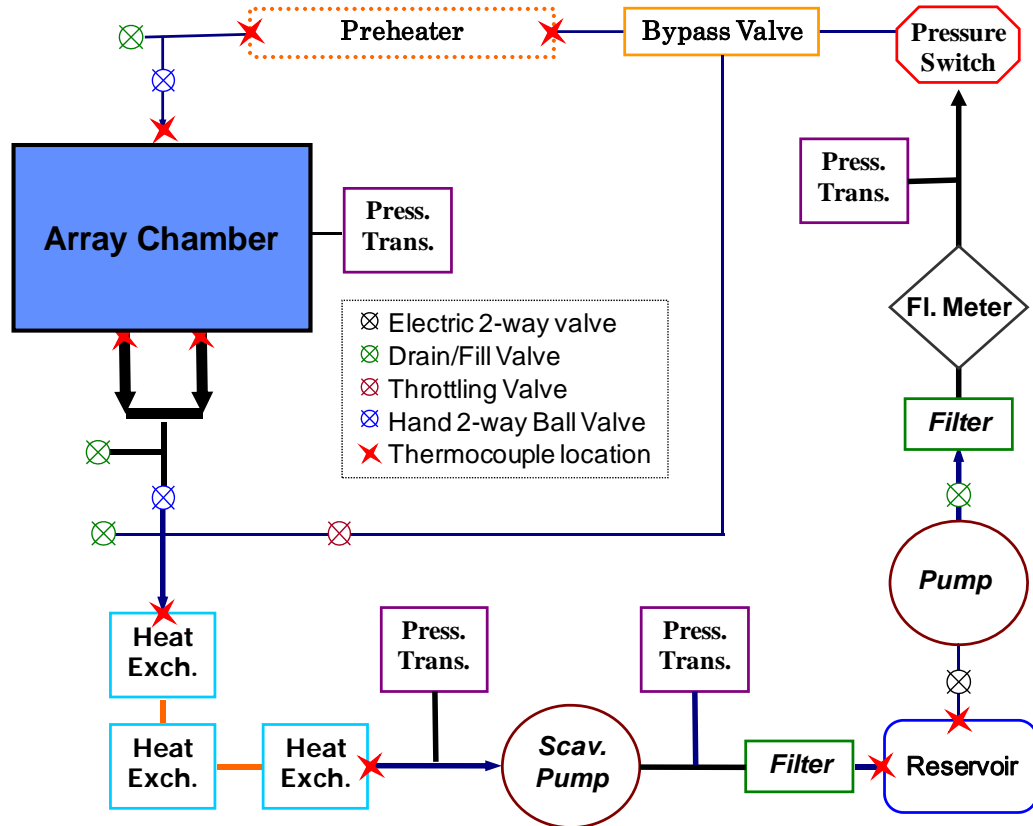


Figure 1.5: FC-72 Flow Loop Schematic.

fluid into a 140 [μm] filter and finally back to the reservoir. The scavenge pump worked with the nozzle pump mentioned earlier to generate a push-pull system that created some redundancy as well as reliability and controllability.

3M Fluorinert FC-72 was chosen as the working fluid because of its low toxicity level, dielectric property, and its low boiling point ($56\text{ }^{\circ}\text{C}$ at 1 [atm]), which allowed most components to be at “touch temperature”. Although the amount of dissolved air in FC-72 can reach nearly 50% by volume, the amount of air was varied between $10.1 \leq C \leq 16.8\%$. The amount of air in the system was determined using aire-ometer measurements gathered via FC-72 sample extraction, as detailed in Appendix E.4. The amount of dissolved air was reduced using a vacuum-based membrane filter attached to the system. If the amount of dissolved air was too low, ambient air was bled into the system, allowed to reach equilibrium throughout the system, and the air content was measured again. The components used

in the removal of air from the system are described in Appendix E.5.

The data acquisition system consisted of a laptop computer connected via a GPIB-to-USB adapter to a data acquisition unit (Agilent Model 34970A). The various instrumentation devices used for this experiment were thermocouples, pressure transducers, flow meters, voltmeters, precision resistors (to accurately measure current via voltage drop), and an accelerometer. In addition to the data acquisition unit, a calibrated reference point (Hart Ice Point Calibrator Model 9101) for the thermocouples was used rather than the data acquisition system's built-in reference. This allowed for a steady state thermocouple reference with a ± 0.005 [°C] stability. The data acquisition software used the manufacturer's calibration information for the accelerometer, voltmeters, precision resistor, flow meters, and pressure transducers.

An uncertainty analysis was performed to be able to accurately report the data and determine the error ranges. The uncertainty was made up of precision error and bias error. The bias error, summarized in Appendix B, was the uncertainty associated with the instruments used to record the data including the associated calibration error. The precision error was due to the scatter of the data.

The bias error associated with the flow meter, thermocouples, heat flux, accelerometer, pressure transducers, and air content are summarized in Table 1.3. The thermocouple bias error was taken from the thermocouple calibration using a RTD and readout (Hart Scientific Models 5628 and 1502A), temperature bath (Hart Scientific Model 6330), and the data acquisition system. The uncertainty associated with each device as well as the maximum deviation from the linear curve-fit were combined to generate the temperature bias error. The heat flux was estimated via two voltage measurements. The first voltage was measured across the resistive heating element in which the uncertainty in this reading was only that associated with the data acquisition system. The second measured voltage was across a precision resistor in series with the heater. This was used to calculate the electrical current through the heater with errors associated with the data acquisition voltage measurement and

		Precision Error		Bias Error σ:	
		Type	Error	Total	
					(Example: Case 01)
T	RTD		± 0.006 [°C]	± 0.078 [°C]	± 0.63 [°C]
	RTD readout		± 0.009 [°C]		
	curvefit		± 0.063 [°C]		
q''	voltage1 (DAQ)		± 0.062 [V]	± 0.258 [W/cm ²]	± 0.00015 [W/cm ²]
	voltage2 (DAQ)		± 0.0055 [V]		
	resistor		± 0.00002 [Ω]		
	heater length		± 0.0000254 [m]		
	heater width		± 0.0000254 [m]		
\dot{m}	manufacturer		± 0.039 [g/s]	± 0.694 [g/s]	± 0.31 [g/s]
	curve-fit		± 0.655 [g/s]		
a	manufacturer		± 0.025 [g]	± 0.025 [g]	± 0.02 [g]
P	manufacturer		± 1.72 [kPa]	± 1.72 [kPa]	± 1.11 [kPa]
C	manufacturer		± 2.0 %	± 2.0 %	± 1.3 %

Table 1.3: Summary of the Uncertainty Analysis.

the precision resistor uncertainty. The heater area was calculated by measuring the length and width using calipers; therefore, the uncertainty was that associated with the calipers. Lastly, the accelerometer, pressure transducers, flow meter, and air content precision error was assumed to be as stated by the manufacturer.

The precision error was the deviation in the data sets. The micro-gravity (or 1.8 [g]) portion of each parabola consisted of only eight to fourteen data points that included some data scattering. To report this scatter the small groups of data were taken as an average data point plus/minus one standard deviation of the data.

Flight tests with the 16-nozzle array were completed using NASA's C-9 Reduced Gravity Aircraft. The C-9 performed parabolic flight trajectories to control the acceleration field seen onboard. Two full flight weeks of testing were completed at NASA JSC Ellington Field. Each flight week consisted of four flights, usually one per day. Each flight consisted of a short amount of time after takeoff to travel to the approved flight zone, which allowed

time for some experimental setup before the forty-sixty parabolas would take place. Each parabola consisted of approximately 25 [s] of micro-gravity and 30 [s] of elevated gravity. In addition to the standard parabolas, 2.0 [g] turns were requested after each set of ten parabolas so that the experiment would have enough time at an elevated gravity to reach steady state at several heater power settings.

Five parameters that were varied throughout the course of the flight weeks were acceleration (a), heater power (Q), mass flow rate (\dot{m}), subcooling ($\Delta T_{sc} = T_{sat} - T_{in}$), and air content (C). During each parabolic maneuver a heater power was set. Typically, this setting was maintained for two to three parabolas to achieve some repeatability in the data. During a group of parabolas, usually ten or twenty, the flow rate and subcooling were maintained constant, while only the heater power was varied. The flow rate and subcooling settings would only be adjusted once or twice over the course of an entire flight so that the effects of acceleration on heat transfer could be investigated.

1.3 Results and Discussion

The objective of the 16-nozzle array flight test experiment was to show the effects of elevated or reduced gravity, mass flow rate, liquid subcooling, and dissolved air content on array spray cooling performance. To simplify the analysis, each flight was broken up into a series of cases, as shown in Table 1.4. Each case, defined as a portion of the flight in which the only parameter adjusted was the heater power, provided a means to look at the data in such a way that minimized the effects of the other parameters.

To investigate the effect of gravity on spray cooling performance the experimental conditions were held constant as the plane went through a variable-gravity maneuver (parabola). During each parabola the heater power, mass flow rate, subcooling, and air content were held constant while the acceleration changed from micro-gravity to elevated gravity. After approximately two or three parabolas, the heater power was increased approximately five

Case #	\dot{m} [g/s]	ΔT_{sc} [°C]	T_{sat} [°C]	a [g]	C [%]
1	14.0	14.2	42.1	-0.02	10.1%
2	14.1	11.3	41.6	-0.98	10.1%
3	13.8	12.6	40.7	-1.87	10.1%
4	14.0	14.2	41.2	-1.92	10.1%
5	18.0	15.1	42.3	-0.02	10.1%
6	18.2	13.6	41.4	-1.00	10.1%
7	17.7	12.9	40.5	-1.86	10.1%
8	18.0	14.6	40.9	-2.02	10.1%
9	21.3	15.3	43.4	-0.02	10.1%
10	21.2	13.9	40.9	-1.05	10.1%
11	21.1	12.7	41.3	-1.88	10.1%
12	20.9	14.8	40.6	-1.89	10.1%
13	14.5	18.4	39.7	-0.02	10.1%
14	14.5	18.0	39.9	-1.00	10.1%
15	14.0	16.1	37.4	-1.88	10.1%
16	14.1	18.1	39.9	-1.90	10.1%
45	13.1	6.39	43.0	-0.01	14.3%
46	13.7	3.01	42.4	-0.99	14.3%
47	13.5	4.86	41.7	-1.77	14.3%
49	16.4	9.86	42.8	-0.01	14.3%
50	18.3	9.58	42.6	-1.01	14.3%
51	17.6	8.93	41.8	-1.78	14.3%
52	18.0	8.88	41.8	-2.00	14.3%
53	14.1	12.4	43.4	-0.01	14.3%
54	14.7	11.0	42.6	-0.98	14.3%
55	14.7	11.2	42.3	-1.75	14.3%
56	15.3	11.5	41.8	-1.85	14.3%
57	15.5	15.5	45.0	-0.01	14.3%
58	18.5	16.9	46.5	-1.02	14.3%
59	18.5	15.9	45.3	-1.74	14.3%
61	13.5	17.8	46.1	-0.01	16.8%
62	13.7	14.5	44.8	-1.01	16.8%
63	14.0	16.0	44.7	-1.86	16.8%
64	14.5	15.7	43.8	-1.92	16.8%
65	16.5	17.9	46.0	-0.01	16.8%
66	17.0	16.8	45.3	-0.98	16.8%
67	17.6	16.9	45.3	-1.84	16.8%
68	18.2	17.0	45.4	-1.88	16.8%
69	13.7	8.96	47.2	-0.01	16.8%
70	13.8	8.29	45.3	-0.98	16.8%
71	13.7	7.71	45.5	-1.72	16.8%
73	17.4	9.86	46.6	-0.01	16.8%
74	17.9	7.65	45.1	-1.04	16.8%
75	18.3	7.86	45.4	-1.70	16.8%

Table 1.4: Nominal Parameter Values.

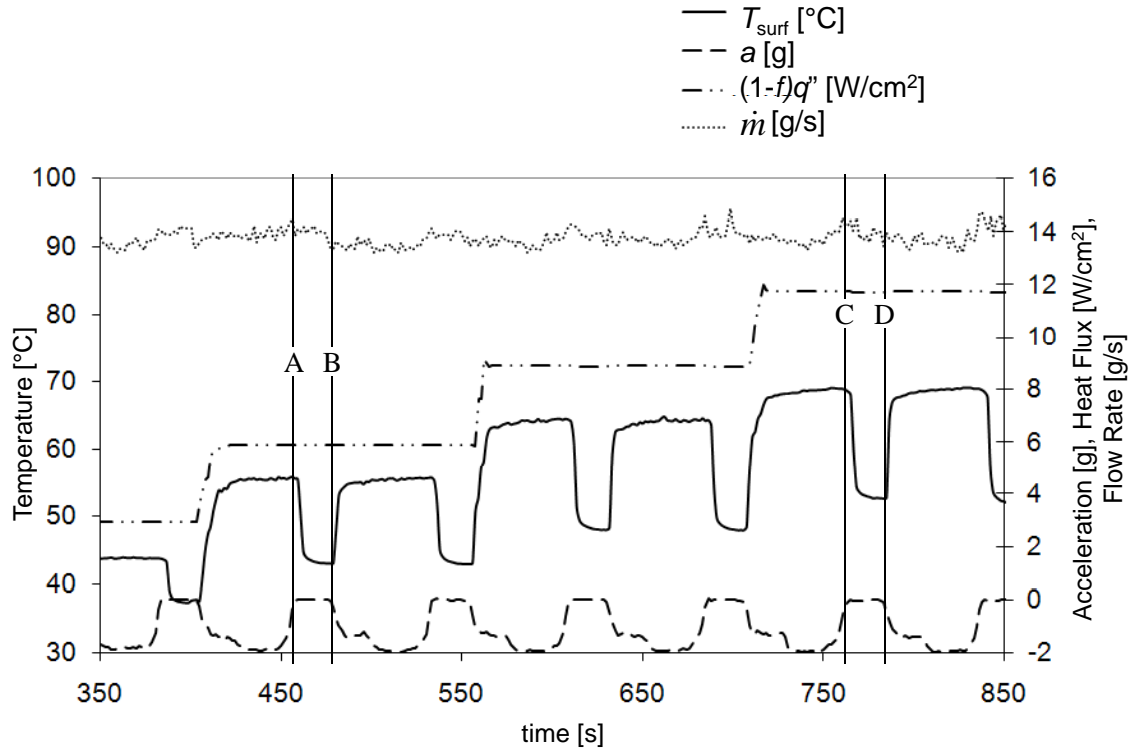
to ten watts. This pattern was repeated until the spray cooling system was near CHF, at which point the heater power was reduced and then increased in small steps to examine the behavior of the system near CHF while undergoing gravitational transients.

Figures 1.6-1.7 explains how the experiment was operated and examines how the cooling performance was impacted by changes in acceleration. Figures 1.8-1.13 show the surface superheat dependence on acceleration, mass flow rate, degree of subcooling, and dissolved air content in both an elevated and micro-gravity environment.

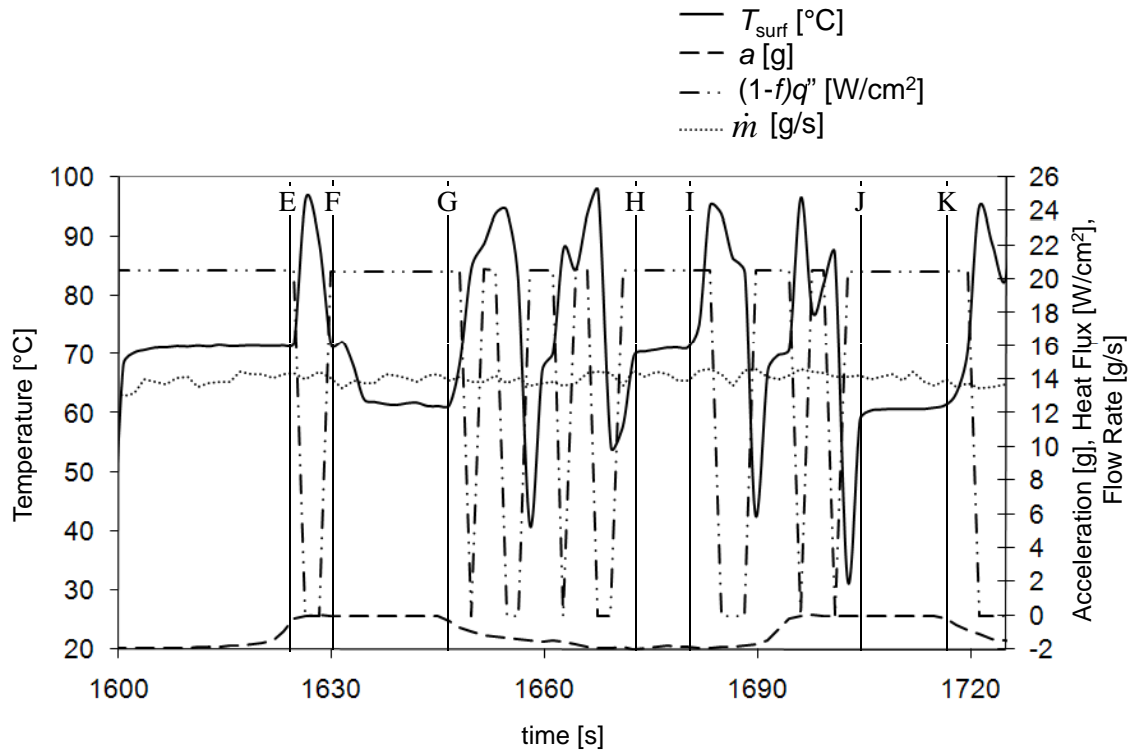
An example data set, shown in Figure 1.6(a), depicts the data collected during seven parabolas. The acceleration, a , is shown towards the bottom of the plot with the axis on the right-hand side, where micro-gravity is shown to be near $a = 0.0$ [g] and elevated gravity is shown near -2.0 [g] (note that the acceleration shown is strictly the magnitude of the vector pointing in the same direction as the spray, normal to the heated surface). The mass flow rate, \dot{m} , is shown toward the top of the graph with the axis on the right-hand side. The heat flux transferred to the spray was incremented as follows: $(1 - f)q'' = 2.90, 5.89, 8.88, \text{ and } 11.76$ [W/cm²]. In this case, two parabolas at each heater setting were recorded before the next increment in heat flux. The subcooling and air content were both held constant during this block of data. As expected, the heater surface temperature, T_{surf} , increased with heat flux. However, T_{surf} showed a significant dependence on acceleration. Looking in more detail at the section between times A and B in Figure 1.6(a), with minimal flow rate fluctuations, a constant heat flux, and a transition from elevated gravity to micro-gravity, the cooling performance was enhanced resulting in a surface temperature reduction of approximately 13 [°C] which was similar to the degree of subcooling ($\Delta T_{\text{sc}} = 11.8 \pm 1.9$ [°C]). Also, between times C and D, a similar enhancement, with a surface temperature reduction of approximately 15 [°C], was noted at a higher heat flux. In fact, the surface temperature decreased during each transition to micro-gravity, and then increased under elevated gravity. This performance dependence on acceleration was witnessed by others: Yerkes et al. [29] and Michalak et al. [30] both showed a decrease in surface temperature

in micro-gravity over terrestrial and elevated gravity.

Figure 1.6(b) displays the data traces of two parabolas with the heater input set to a higher value of $(1 - f)q'' = 20.48 \text{ [W/cm}^2\text{]}$. Initially, the acceleration was $a = -1.91 \text{ [g]}$, and the surface temperature was constant at approximately $T_{\text{surf}} = 71 \text{ [}^\circ\text{C]}$. At point E, the aircraft experienced a transition to micro-gravity, at which time the surface temperature increased dramatically. When the interface temperature reached $T_{\text{int}} = 120 \text{ [}^\circ\text{C]}$, a temperature-activated relay opened the heater circuit, thereby disconnecting power to the heater, preventing damage to the heater. This type of event is indicative of CHF, where a run-away surface temperature is experienced. The spray continued to cool the heater surface until the temperature fell below the limit on the relay, at which time the heater was re-energized at the same heat input prior to the event. The data acquisition cycle time was approximately 2.2 [s] and therefore the temperature could surpass the relay trip-point and fall before the data acquisition unit could record an interface temperature exceeding 120 [°C]. After point F, where the acceleration field was steady at $a = -0.01 \text{ [g]}$, the system returned to equilibrium where the surface temperature decreased to a significantly lower level ($T_{\text{surf}} = 62 \text{ [}^\circ\text{C]}$). It is interesting to note that prior to point E, when $a = -1.91 \text{ [g]}$, CHF was not actually reached. It was only during the transition from elevated gravity to micro-gravity that a CHF event was tripped. When the aircraft transitioned from micro-gravity back to elevated gravity (point G), a CHF event once again tripped until the point at which the acceleration became steady at $a = -1.91 \text{ [g]}$ (point H). At this time, the system again reached equilibrium and the surface temperature reached the previous level ($T_{\text{surf}} = 71 \text{ [}^\circ\text{C]}$). However, after a short time, the surface temperature again suddenly increased (point I). This shows that the heat input of $(1 - f)q'' = 20.48 \text{ [W/cm}^2\text{]}$ is indeed very close to CHF for $a = -1.91 \text{ [g]}$ and possibly tripped CHF as a result of a small perturbation in acceleration. This behavior was deemed to be in a meta-stable region, where small changes in the acceleration field can result in either stable operation or trip a CHF event. At point J, the aircraft again experienced steady micro-gravity, and after the heater was re-energized, the system



(a)



(b)

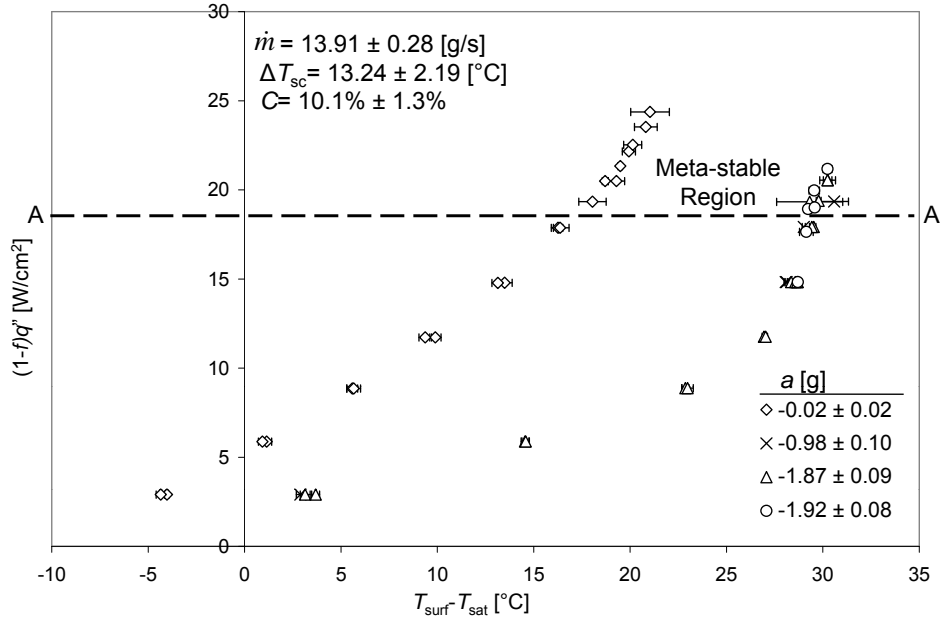
Figure 1.6: Transient Data Traces of Surface Temperature, Acceleration, Heat Flux, and Nozzle Mass Flow Rate ($\dot{m} = 13.81 \pm 0.32$ [g/s], $\Delta T_{sc} = 11.78 \pm 1.93$ [°C], $C = 10.1\% \pm 1.3\%$): (a) Stable Operation; (b) CHF Events ($(1-f)q'' = 21.17 \pm 0.04$ [W/cm²]).

returned to equilibrium where the surface temperature settled back to the previous temperature of $T_{\text{surf}} = 62$ [°C]. Again upon transition from micro-gravity to elevated gravity (point K), a CHF event was tripped, repeating the behavior seen at point G.

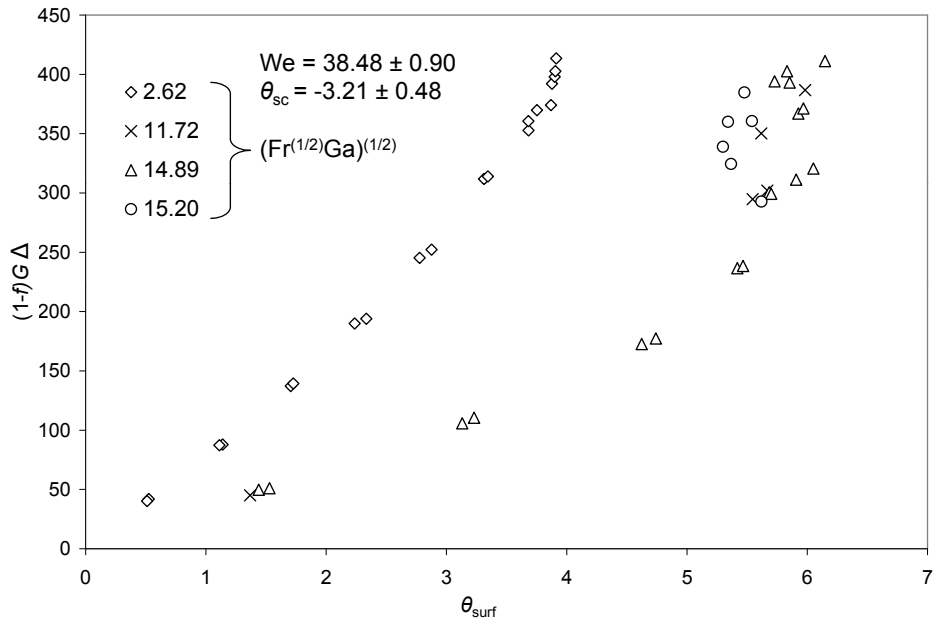
Figure 1.7(a) presents the heat flux convected away from the surface versus the difference between the heater surface temperature and the saturation temperature of the working fluid, FC-72. Positive values of $T_{\text{surf}} - T_{\text{sat}}$ indicate two-phase heat transfer, while negative values indicate single-phase heat transfer. In general, the temperature difference increased with heat flux until CHF was approached. Near this point, the temperature difference did not change appreciably. This behavior was typical of the two-phase process for spray cooling [7, 20–22, 25, 26]. Of particular interest in this figure is the behavior of the data with respect to gravity: For terrestrial and elevated gravity ($a = -0.98, -1.87$ and -1.92 [g]), the results were nearly identical. For micro-gravity, however, the surface superheat was much less at a given heat flux, indicating a significant enhancement in heat transfer in micro-gravity. CHF was also higher (by approximately 3 [W/cm²]) for micro-gravity than for terrestrial and elevated gravity.

The performance enhancement in micro-gravity could be explained by the fluid management system in which the fluid was more easily wicked away from the surface in the absence of gravity, allowing for deeper spray penetration. Yerkes et al. saw a similar trend, but at a much smaller magnitude using a single nozzle. Figure 1.7(b) examines the data in Figure 1.7(a) by casting it in nondimensional terms suggested by Yerkes et al. [29]. For a constant $(1 - f)G\Delta$ the dimensionless temperature difference, θ_{surf} , is vastly different when $(\text{Fr}^{\frac{1}{2}}\text{Ga})^{\frac{1}{2}}$ is varied. Also, for the higher values of $(\text{Fr}^{\frac{1}{2}}\text{Ga})^{\frac{1}{2}}$ the dimensionless surface temperature is less dependent on $(\text{Fr}^{\frac{1}{2}}\text{Ga})^{\frac{1}{2}}$.

Figure 1.7(a) also illustrates the previously mentioned meta-stable region, which occurs above a certain heat flux threshold. Transients from gravitational forces drive the system to an onset of critical heat flux resulting in a sudden temperature increase for a constant heat flux. The horizontal line, A-A, designates the maximum heat flux that does not show the



(a)



(b)

Figure 1.7: Steady State Heat Flux vs. Surface Superheat: (a) Dimensional Values; (b) Dimensionless Values.

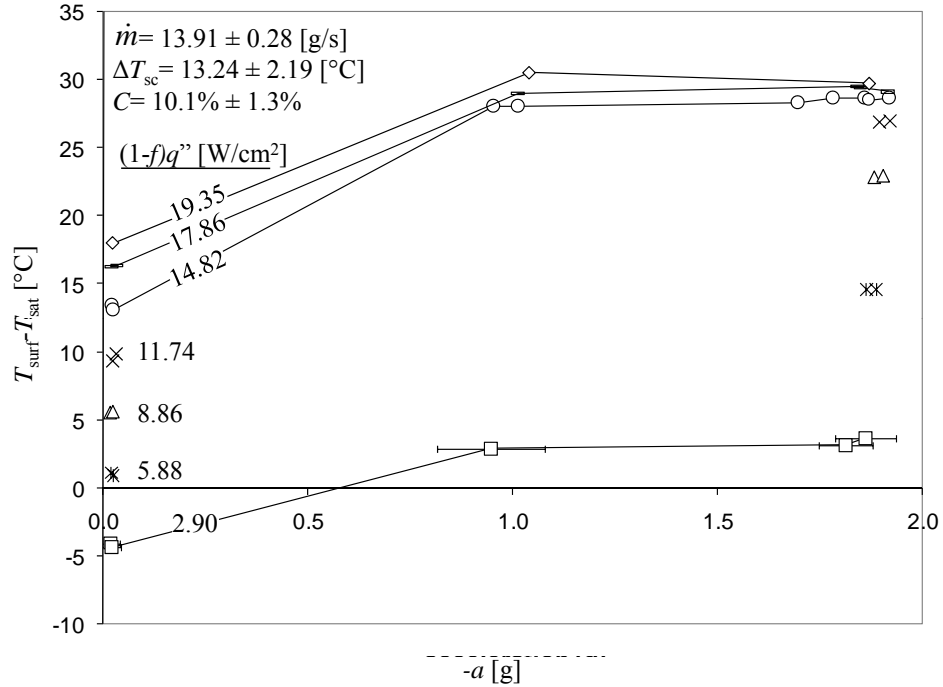


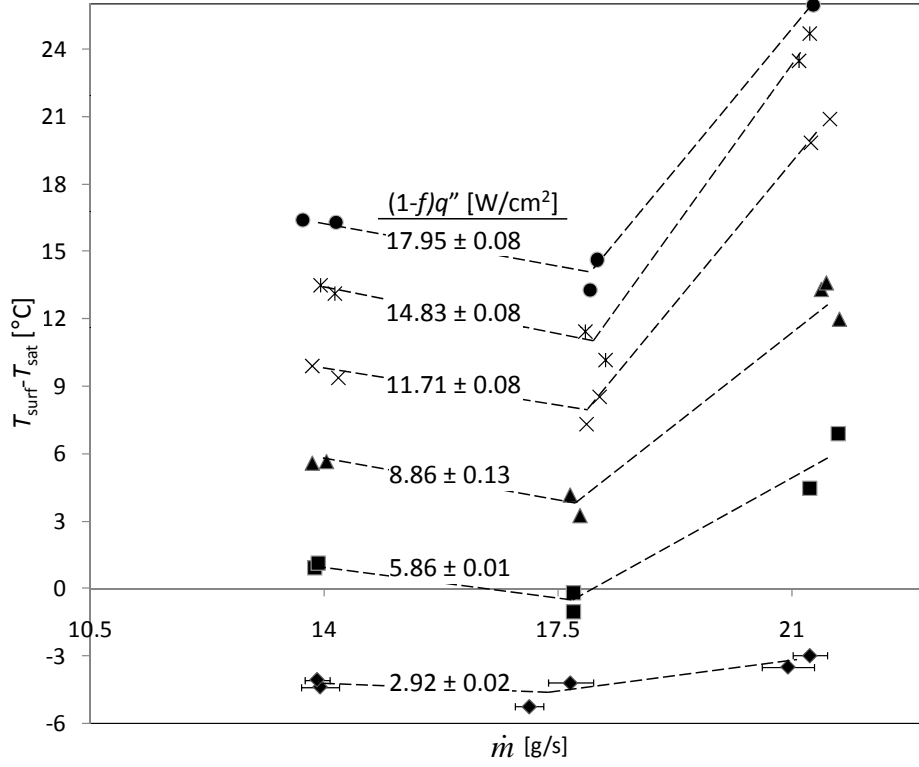
Figure 1.8: Surface Superheat vs. Acceleration.

behavior induced by gravitational transients. Any heat flux above this line could potentially reach CHF in a transient acceleration environment. If the acceleration is stable, the critical heat flux when $a = -0.98, -1.87, \text{ and } -1.92$ [g] is near $q'' = 22$ [W/cm²], while CHF when $a = -0.02$ [g] is near $q'' = 25$ [W/cm²]. Meta-stability poses a significant problem if an aircraft system is designed to be in that meta-stable region: Premature CHF can occur and lead to catastrophic failure.

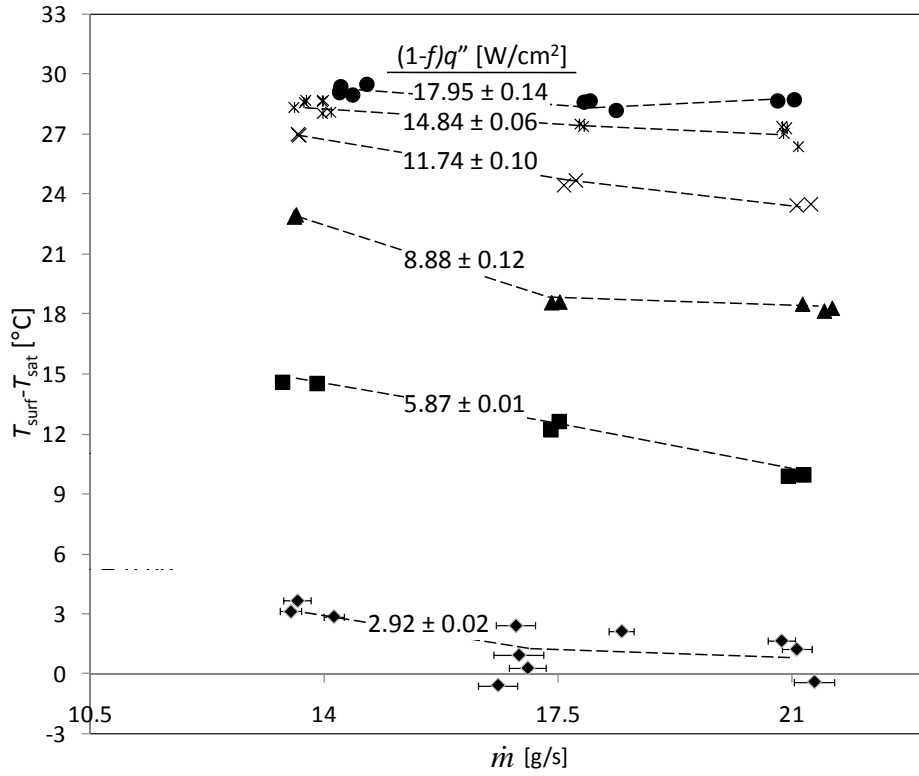
The effect of acceleration on the temperature difference between the surface and saturation is shown in Figure 1.8, where each line represents a different heat flux. Figure 1.8 shows that the surface superheat at terrestrial and elevated gravity are very similar, exhibiting no significant variation due to gravitational body forces. In micro-gravity, however, a dramatic surface temperature drop occurred, displaying a significant performance enhancement. The micro-gravity cooling performance enhancement obtained agrees with the trends found by Sone et al. [25], Yoshida et al. [26], Baysinger et al. [27, 28], Yerkes et al. [29], and Michalak et al. [30].

Figure 1.9 presents the surface superheat for three nominal mass flow rates ($\dot{m} = 14, 17.5, \text{ and } 21 \text{ [g/s]}$). In Figure 1.9(a), where $a = -0.02[\text{g}]$, the surface superheat decreased slightly and then increased significantly with mass flow rate. This increase in the superheat was more pronounced as the heat input increased. In general, a decrease in the surface superheat with increasing mass flow rate is expected, due to the increased impact velocity of the droplets. The dramatic increase in the surface superheat at the highest flow rate may be due to liquid buildup in the array nozzle interaction zones, as described by Glassman et al. [5]. Figure 1.9(b) shows the surface superheat under elevated gravity ($a = -1.72[\text{g}]$). The decrease in the superheat with increasing mass flow rate is again noted, but the sudden increase in the superheat is not present in this case. This may be due to an improvement in the ability of the liquid to exit the heater surface, which is provided by the body force on the liquid. This somewhat reinforces the assumption that the sudden increase seen in Figure 1.9(a) is due to liquid buildup on the heater surface. It is possible that a similar increase in the superheat would also be seen for the elevated gravity case at higher mass flow rates.

Figure 1.10 also illustrates the above mentioned cooling performance due to variation in mass flow rate. Figure 1.10(a) shows that when the mass flow rate was increased from $\dot{m} = 14 \text{ [g/s]}$ to $\dot{m} = 17.5 \text{ [g/s]}$ a similar surface superheat reduction occurred for both elevated and micro-gravity. Figure 1.10(b) shows that when the mass flow rate was increased from $\dot{m} = 14 \text{ [g/s]}$ to $\dot{m} = 21 \text{ [g/s]}$ the surface temperature decreased in elevated gravity but increased in micro-gravity, as shown in Figure 1.9. It is important to note that even though a cooling performance degradation was seen in micro-gravity, the surface superheat was still lower than the elevated gravity case at the same flow rate. The reduction in cooling performance in micro-gravity due to a high mass flow rate was most likely due to excessive liquid buildup on the heater surface, preventing the deep penetration of droplets that occurred in the lower flow rate cases. The micro-gravity cooling performance enhancement seen at lower flow rates diminishes at higher flow rates, suggesting that as the mass flow



(a)



(b)

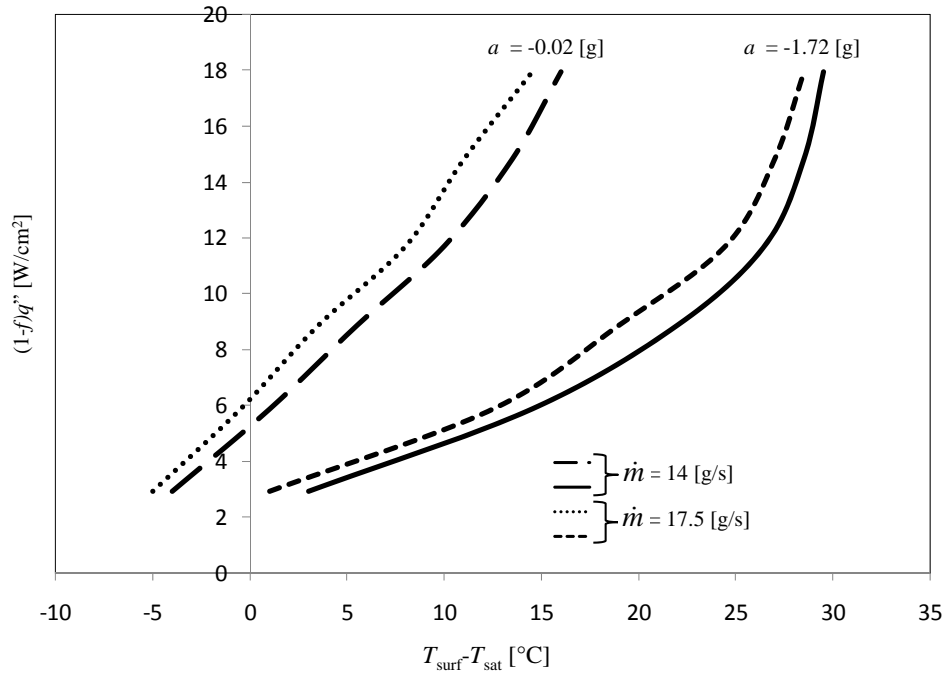
Figure 1.9: The Effect of Flow Rate on the Surface Superheat ($\Delta T_{\text{sc}} = 13.73 \pm 2.33$ [°C], $C = 10.1\% \pm 1.3\%$): (a) $a = -0.02 \pm 0.01$ [g]; (b) $a = -1.72 \pm 0.34$ [g].

continues to increase the cooling performance in micro-gravity would not be appreciably different than in elevated gravity.

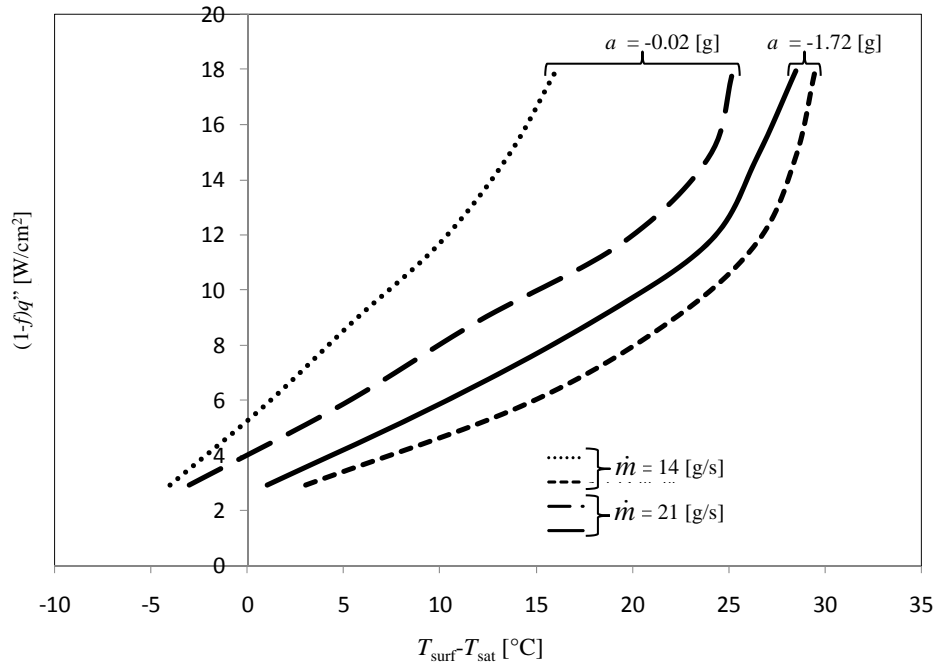
Figure 1.11 shows the effect of liquid subcooling on the surface superheat. This case is for a mass flow rate of $\dot{m} = 14.0$ [g/s], which, as shown in Figure 1.9, is not affected by liquid buildup on the heater surface. For the micro-gravity case (Figure 1.11(a)), the surface superheat decreased with increasing subcooling for all values of heat input. In fact, it appears that the slope of the heat flux lines are nearly constant throughout for the micro-gravity case. In the elevated gravity case shown in Figure 1.11(b), however, the slope of the surface superheat with respect to subcooling varies with heat input: At low heat flux values, the surface temperature drops as subcooling increases, but at high flux values, the surface superheat is nearly constant over the range tested. While bubble dynamics may have played a role in the cooling performance variation due to acceleration, the physical mechanisms related to the heat transfer improvement are not well understood.

Figure 1.12 presents the effect of subcooling on the cooling performance in both elevated and micro-gravity. The four curves on the left-hand side of the plot were taken from micro-gravity test data while the three curves on the right-hand side were taken from elevated gravity test data. In elevated gravity, there was little change in the cooling performance due to variation in the degree of subcooling as seen in Figure 1.11(b). The micro-gravity curves show that an increase in subcooling translated to a steady decrease in the surface superheat as shown in Figure 1.11(a). Also note that as the amount of subcooling decreases in micro-gravity the cooling performance curve nears that of the elevated gravity case, suggesting that when the degree of subcooling approaches zero, the cooling performance enhancement seen in micro-gravity diminishes.

FC-72 has the capability of absorbing up to 48% air by volume. It was suspected that the effect of dissolved air may have also impacted the cooling performance in micro-gravity [29]. However, since air molecules are small enough to fit interstitially, the density change less is than 0.1% between air saturated and degassed FC-72. It was not clear what effect

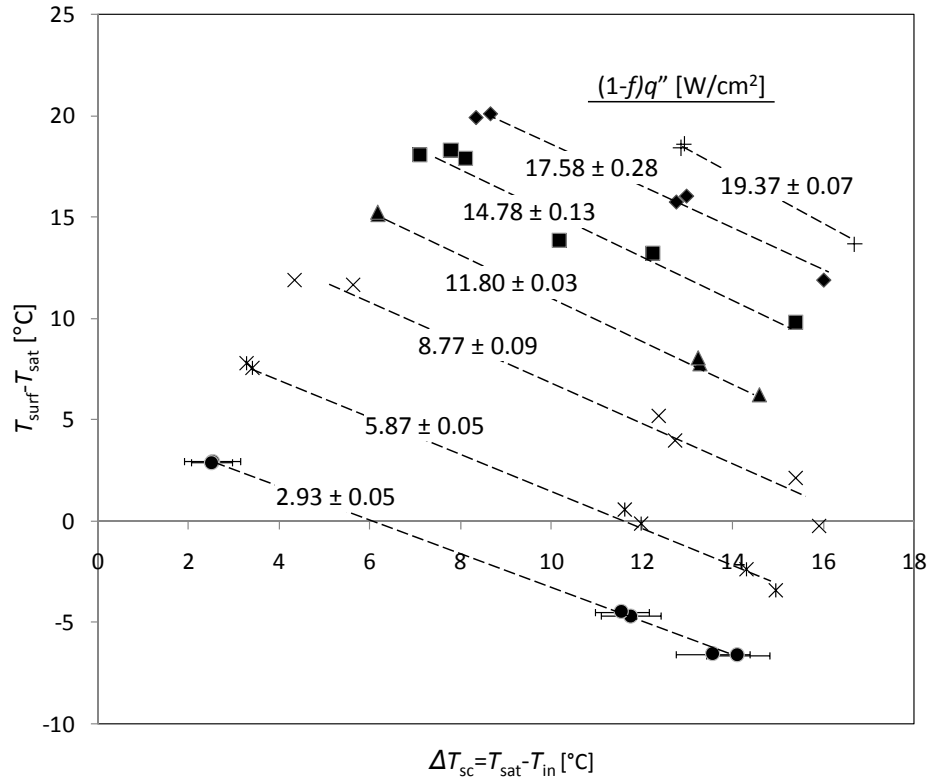


(a)

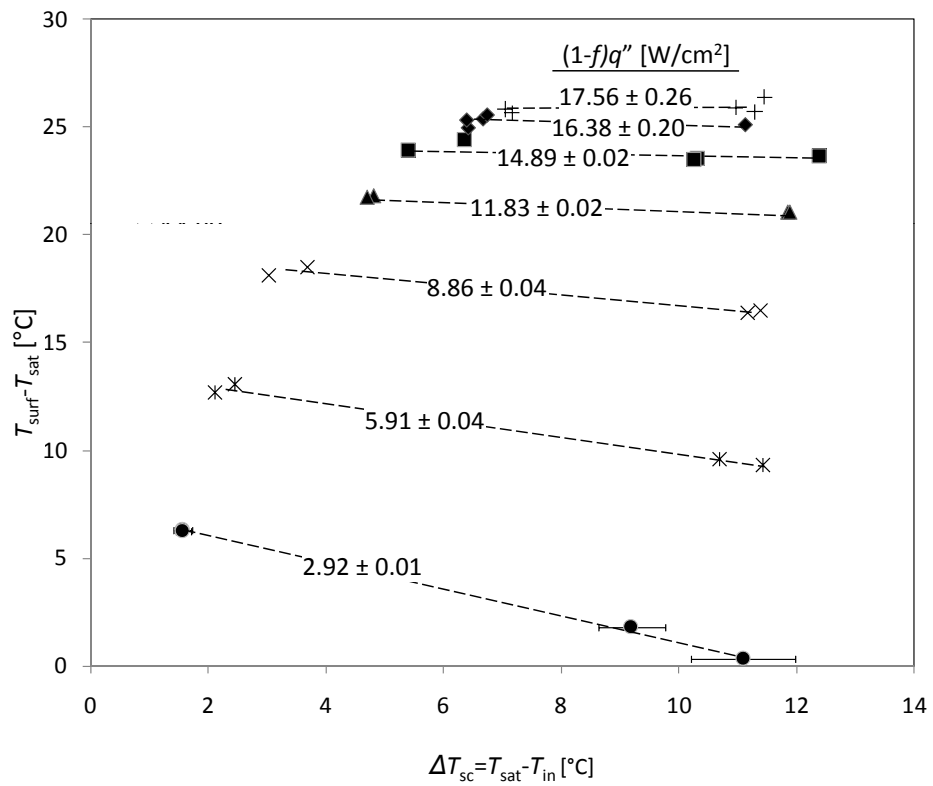


(b)

Figure 1.10: The Effect of Flow Rate on the Surface Superheat in Elevated and Micro-Gravity ($\Delta T_{sc} = 13.73 \pm 2.33$ [°C], $C = 10.1\% \pm 1.3\%$): (a) $\dot{m} = 14$ and 17.5 [g/s]; (b) $\dot{m} = 14$ and 21 [g/s].



(a)



(b)

Figure 1.11: The Effect of Subcooling on the Surface Superheat ($\dot{m} = 14.01 \pm 0.93$ [g/s], $C = 14.3\% \pm 2.2\%$): (a) $a = -0.01 \pm 0.01$ [g]; (b) $a = -1.75 \pm 0.03$ [g].

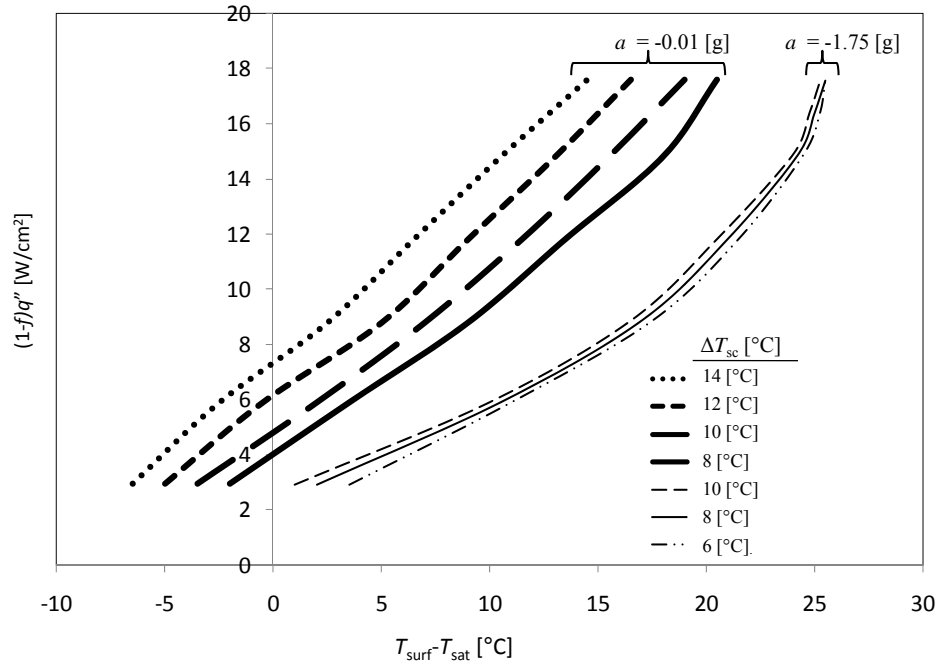
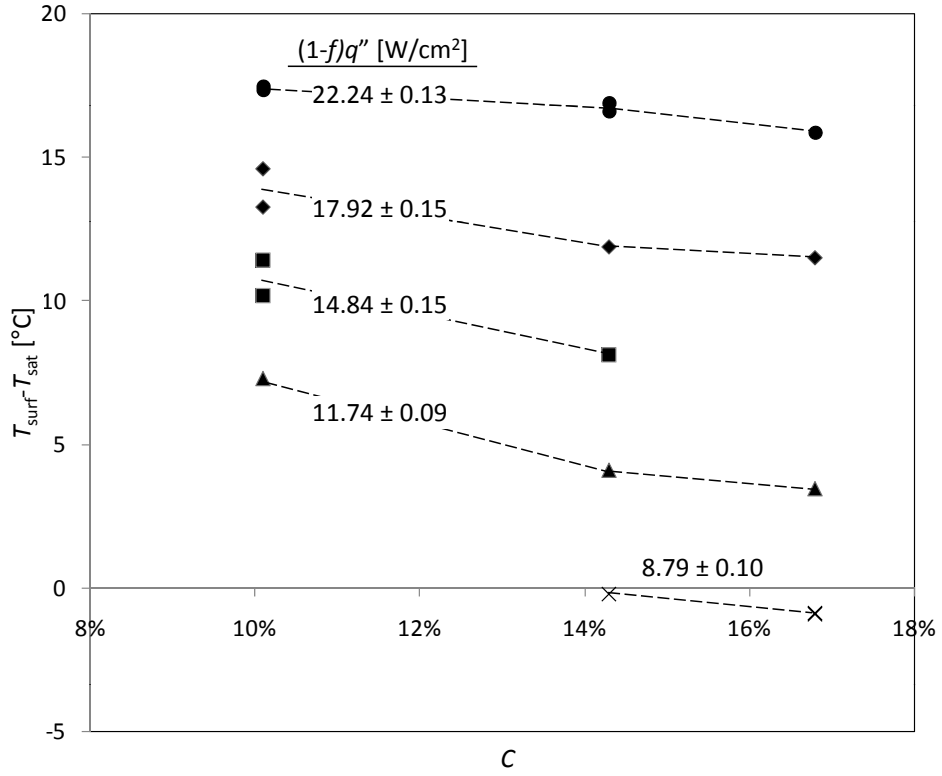


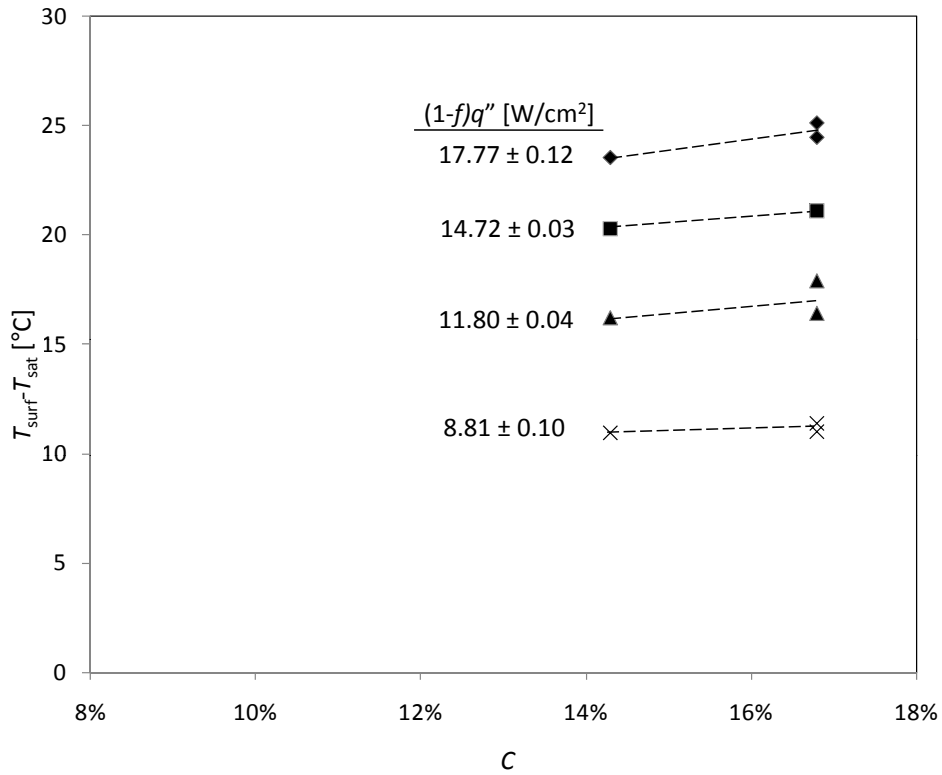
Figure 1.12: The Effect of Subcooling on the Surface Superheat in Elevated and Micro-Gravity ($\dot{m} = 14.01 \pm 0.93$ [g/s], $C = 14.3\% \pm 2.2\%$).

absorbed air had on heat transfer in elevated or micro-gravity. Puterbaugh [15] determined that there was no significant variation in CHF due to dissolved air in FC-72 when saturation pressure was held constant. This suggested that the effect seen by previous researchers could have been a result of varying saturation pressure.

Figure 1.13 shows the effect of air content on the surface superheat. Air content amounts of $C=10.1\%$, 14.3% , and 16.8% were examined in micro-gravity and elevated gravity. Figure 1.13(a) shows a slight decrease in the surface superheat with increasing air content, especially at lower heat flux values. Figure 1.13(b), however, shows that the surface superheat increased slightly with air content in elevated gravity. This variation is considered to be within experimental uncertainty and quite small in comparison to the effects of acceleration, mass flow rate and liquid subcooling.



(a)



(b)

Figure 1.13: The Effect of Air Content, by Volume, on the Surface Superheat ($\Delta T_{\text{sc}} = 16.66 \pm 1.11$ [°C], $\dot{m} = 17.43 \pm 0.95$ [g/s]): (a) $a = -0.01 \pm 0.01$ [g], $18.41 \leq \Delta T_{\text{sc}} \leq 14.03$, $18.22 \leq \dot{m} \leq 15.91$; (b) $a = -1.69 \pm 0.31$ [g], $18.41 \leq \Delta T_{\text{sc}} \leq 14.03$, $18.22 \leq \dot{m} \leq 15.91$.

1.4 Conclusions

The effects of variable gravity on the spray cooling performance of a 16-nozzle array, using FC-72, were investigated. An experiment capable of flying on NASA's reduced gravity aircraft was modified to accommodate the 16-nozzle array chamber with a 25.4×25.4 [mm] heater. The reduced gravity portions of the flight test showed a very repeatable surface temperature reduction from the terrestrial and elevated gravity portions. The effect of acceleration, mass flow rate, degree of subcooling, and air content on the cooling performance of the array were studied:

1. In stable acceleration fields, micro-gravity exhibited a significant decrease in surface superheat over terrestrial gravity. Elevated gravity had no appreciable effect in surface superheat when compared with terrestrial gravity. Although the cooling performance appears to be enhanced due to the reduction of body forces, the data suggests that for an aircraft that undergoes a transient variation of acceleration, a meta-stability condition can occur and will influence the onset of critical heat flux. This can result in a runaway temperature condition leading to electronic component damage or failure.
2. Although cooling performance was enhanced when the mass flow rate increased from $\dot{m} = 14$ [g/s] to $\dot{m} = 17.5$ [g/s] in both elevated and micro-gravity, the cooling performance was degraded when the mass flow rate increased from $\dot{m} = 17.5$ [g/s] to $\dot{m} = 21$ [g/s] in micro-gravity only. This was possibly due to liquid buildup in the nozzle interaction zones, where the liquid thickness is much greater than that directly under the spray.
3. An increase in subcooling dramatically decreased the surface superheat in micro-gravity for all heat fluxes evaluated. In elevated gravity, the subcooling reduced the surface superheat for low heat fluxes and had little effect at high heat fluxes. This may have been due to bubble dynamics on the heater surface.

4. An increase in the amount of dissolved air in the working fluid decreased the surface superheat slightly in micro-gravity, but no significant effect was seen in elevated gravity. A larger variation in air content dissolved in the working fluid, FC-72, may have shown more of an effect.

Chapter 2

Qualitative Evaluation of a Liquid-Vapor Separator Concept in Micro-Gravity Conditions

2.1 Introduction

In a terrestrial closed-loop spray cooling system, the reservoir is used for several purposes. It separates the liquid from the vapor by gravity so that only liquid is delivered to the spray nozzle(s). This ensures a steady flow of liquid to the item being cooled. The reservoir also provides for a certain amount of liquid that is readily available during transient conditions, such as start-up or shutdown. Finally, the reservoir simplifies the working fluid filling procedure by making the amount of working fluid less critical to optimizing performance.

Due to the nature of variable gravity testing, control of the liquid-vapor separation process is required in order to maintain heat transfer performance. Phase separators can be generalized into two basic types: Active and passive. An active separator uses some external power to generate separation whereas a passive separator does not. For many applications, a passive separator is preferred because no additional system power is consumed and

fewer support components are required, reducing complexity and total system weight. The most simplistic phase separator is a container with liquid and vapor in a gravitational field. The more dense liquid phase will separate from the less dense vapor phase due to buoyancy forces where a liquid pickup can be put at the gravitational “bottom” and a vapor pickup, if needed, at the gravitational “top”. Issues arise when gravity is no longer available or in the case of variable gravity in which the direction of the gravitational vector changes. Surface tension and centrifugal forces often overcome variable acceleration forces in aircraft and in spacecraft. A popular active separator type is a cone or cylinder that is rotated and uses centrifugal acceleration to separate the fluid. The primary drawbacks associated with this type of separator are the power requirement, rotary sealing, and reliability.

Shoemaker and Schrage developed a passive free vortex separator (FVS) that uses centrifugal forces to separate phases [32]. This cylindrical type of separator works by injecting a two-phase mixture with a tangential component creating a centrifugal flow field in which the more dense liquid flows along the outer edge, allowing the vapor to collect in the center. To simplify the separation testing, removing condensation/evaporation possibilities, water and air were used as the two phases. The success of the separator was a function of many variables that could be tailored to a specific setup. The injector caused different two-phase flow patterns in the separator, which determined the ability to successfully separate the liquid and gas phases. Furthermore, Schrage et al. dynamically modeled the use of a passive cyclonic separation device (CSD) for phase separation, concluding that the separation process can be seen as a collection of individual bubbles with predictable behavior [33]. The CSD worked very similarly to the FVS previously mentioned, utilizing the centrifugal force generated by a fluid rotating around a cylinder or cone. Barbu et al. investigated acoustic gauge monitoring, a method to check the amount of liquid and gas inside a non-transparent separator, to properly analyze a passive fluid momentum driven vortex separator, utilizing the same fundamental separator theory as Shoemaker and Schrage [32] and Schrage et al. [33], used on NASA’s Immobilized Microbe Microgravity Waste Water Processing Sys-

tem (IMMWPS 2003) and Packed Bed Reactor Experiment (PBRE) space flight systems (PBRE 2005) [34].

Kuravi et al. designed a passive centrifugal tube separator that was tested using water and air as the liquid and gas phases [35]. Helical tubes, with holes on the outer surface, were the basis for the separator. As the fluid traveled through these tubes, centrifugal forces would force the liquid to the outer edge, and therefore, out of the tubes. The wettability of the tube material, tube diameter, and hole size all contributed to its operability. Issues with this separator type involved liquid collection and if the amount of liquid in the line was too low, gas would then exit the holes.

Weislogel and Lichter [36] developed analytical models to design passive vane liquid-vapor separators utilizing capillary flow in interior corners. This style of separator utilized capillary forces to drive the vapor out of a “V” shaped corner. Also, Weislogel et al. [37–39] completed fundamental micro-gravity research on simple vanes utilizing multiple experiments onboard the International Space Station to correlate with numerical simulations. This work has provided a framework to understand the capillary flow processes involved in micro-gravity. Some of the benefits to vane separators is having an integrated reservoir with the separator, less pump work required (no momentum driven separation), and having no moving parts or seals (life cycle failure). Disadvantages of vane separators stem from unresolved problems described by Weislogel such as optimizing the critical corner flow velocity, partial wetting, contact angle hysteresis, and other effects [40].

The issue with many of these passive separator types is the additional pumping power required to push the fluid through a cyclonic or centrifugal separator due to the wall friction associated with separation. The preferred separator would be one that would not require any additional components and power to operate, minimize the amount of additional mass/volume added to the system, and minimize the amount of additional pumping power needed. The research provided in this paper discusses the evolution of a separator subjected to variable gravity that was needed to enable the efficient performance of an array

spray cooling system under the following parameter ranges: $14 \leq \dot{m} \leq 35$ [g/s], $3.0 \leq \Delta T_{sc} \leq 18.4$ [°C], $37.4 \leq T_{sat} \leq 47.2$ [°C], $42 \leq P \leq 78$ [kPa], and $-0.02 \leq a \leq -2.02$ [g].

2.2 Experimental Setup

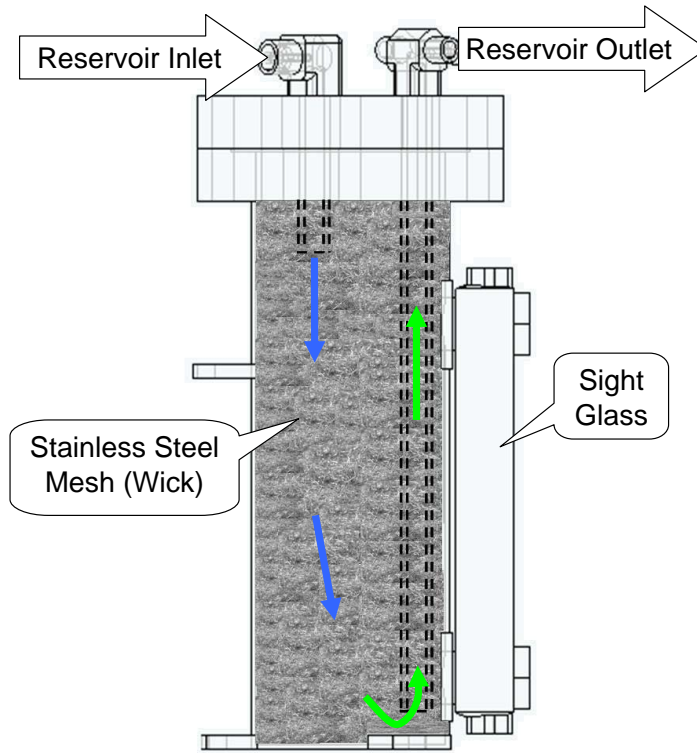
The liquid-vapor separator is perhaps the most easily overlooked yet critical component to making the variable gravity two-phase recirculating experiment function. The purpose of the liquid-vapor separator is to contain excess fluid, reduce the pressure surges associated with pumping, and isolate the vapor from the transport lines. For a terrestrial system, keeping the liquid and vapor separated is quite simple. When a two-phase system is introduced into a reduced gravity environment, surface tension forces can overcome gravitational forces, resulting in surface tension flow which can result in the forcing of fluid away from the “bottom” of the reservoir, making a fixed liquid drain port no longer useful. Spray cooling systems will no longer perform properly if the drain port does not supply a continuous liquid feed.

The reservoir in the spray cooling experiment is where the liquid-vapor separator was installed for testing. The fluid entering the reservoir in this experiment was typically a saturated mixture of liquid and vapor. The configuration of the liquid-vapor separator has evolved as flight test experiments were performed. Initially, the reservoir was made of a stainless steel container that was filled with stainless steel wool to act as a wick to contain the liquid, as shown in Figure 2.1. Fluid entered via a port on the top of the cylindrical reservoir and exited via a long 6.35 [mm] stainless steel tube approximately 6.35 [mm] from the bottom of the reservoir. In addition, a sight glass indicated the fill level of the reservoir under terrestrial gravity conditions. Figure 2.1(b) displays the flow rate dependence on acceleration for four parabolas in series while the system tried to maintain a steady flow rate of approximately $\dot{m} = 8$ [g/s]. During flight testing, reduced gravity flow instabilities issues arose, shown in Figure 2.1(b), in part due to inefficient fluid management in the reservoir as

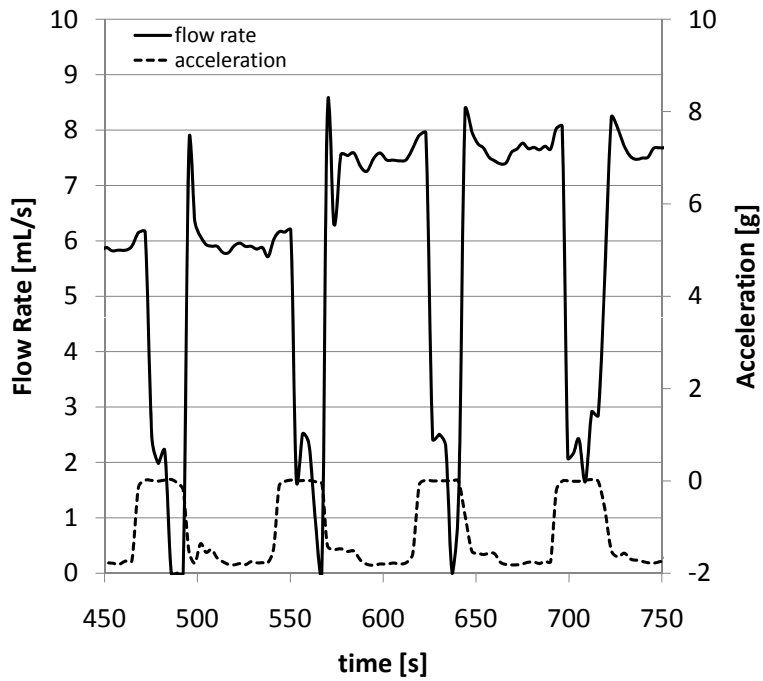
described by Yerkes et al. [29]. When the system entered micro-gravity, the liquid feed was interrupted and the flow rate quickly dropped dramatically until gravity became available again to regain a steady flow rate. This cycle of steady flow during elevated gravity and inconsistent flow during micro-gravity was present in each parabola.

A second generation of reservoir was designed, shown in Figure 2.2(a), which used the same stainless steel cylindrical housing but with a modified internal configuration. The inlet port was not changed, but the stainless steel wool was replaced with a vane structure, shown in Figure 2.3(a), which was made of stainless steel shim stock. The vane structure was designed to utilize capillary forces in interior corners, as Weislogel et al. [36–40] suggested, to contain the liquid to the central core of the liquid-vapor separator, as shown in Figure 2.3(b), while allowing for liquid flow along the length of the vane structure. The capillary action created a force that kept the liquid inward, forcing vapor outward. At the bottom of the vane structure a tube that was the outlet of the reservoir was bent and positioned directly beneath the vane structure, catching the liquid as a funnel. Although quite an improvement over the stainless steel wool reservoir, the second generation reservoir had too much sloshing, which allowed vapor to enter the outlet tube. Figure 2.2(b) shows the flow rate performance as the system experienced variable-gravity for five parabolas in series while the system tried to maintain a steady flow rate of approximately $\dot{m} = 8$ [g/s]. When the experiment entered the micro-gravity portion of the first parabola, the flow rate would drop out after a few seconds and would regain steady flow until the next micro-gravity portion. During each elevated gravity portion, the reservoir would begin to refill, but could not reach the fill level seen during the prior micro-gravity portion before another micro-gravity portion started. The successive reduction in fill level created quicker and more extended flow dropouts until the system could not supply the reservoir with sufficient liquid to continue operation.

Figure 2.4(a) shows the third generation reservoir which included a stainless steel mesh wick placed at the bottom of the metallic vane structure. This wick contained the liquid

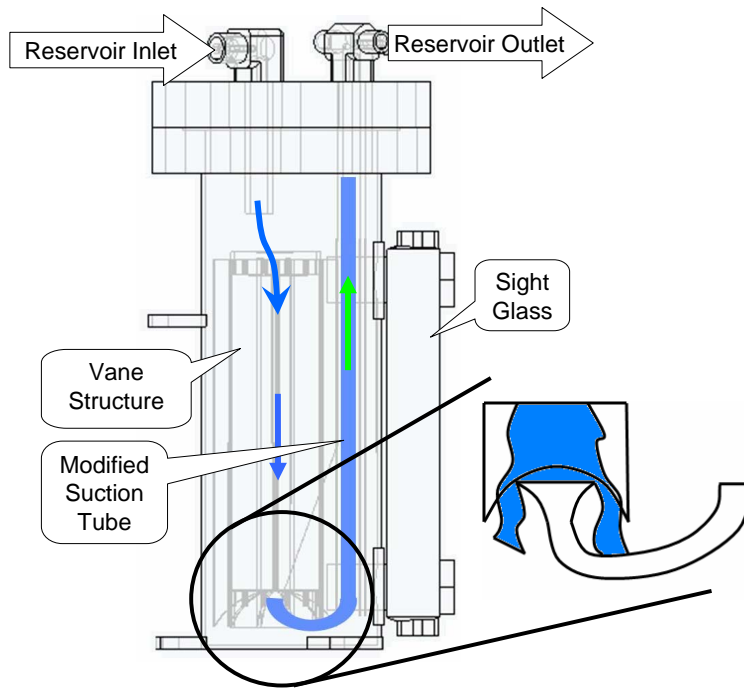


(a)

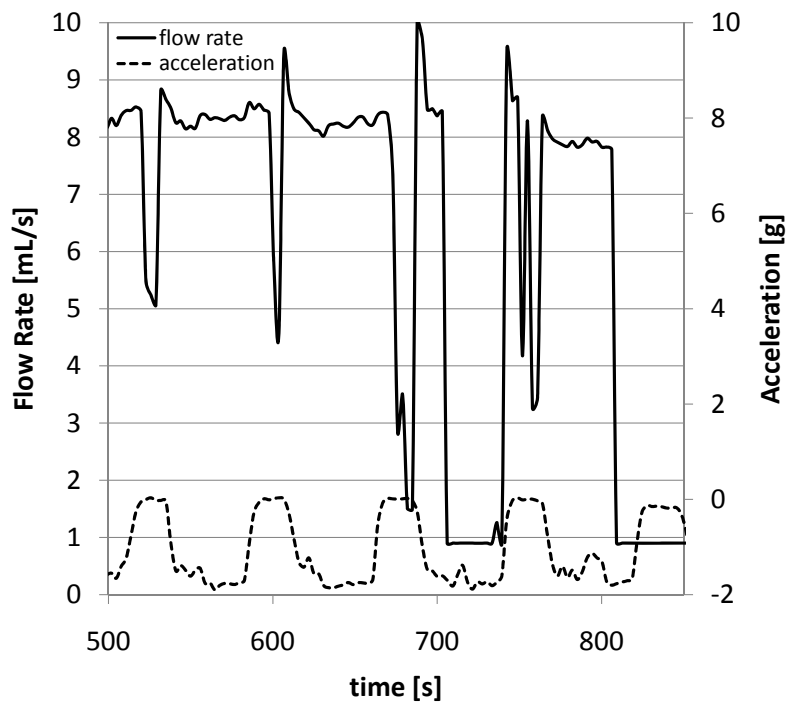


(b)

Figure 2.1: Initial Flight Test Reservoir: (a) Cross-Sectional View; (b) Raw Test Data.



(a)



(b)

Figure 2.2: Second Generation Reservoir: (a) Cross-Sectional View; (b) Raw Test Data.

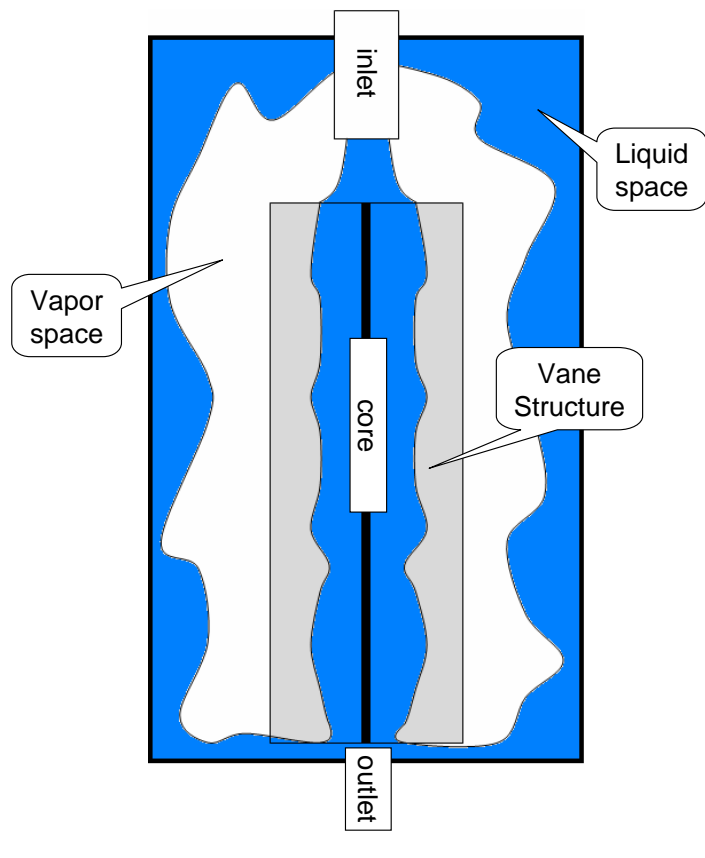
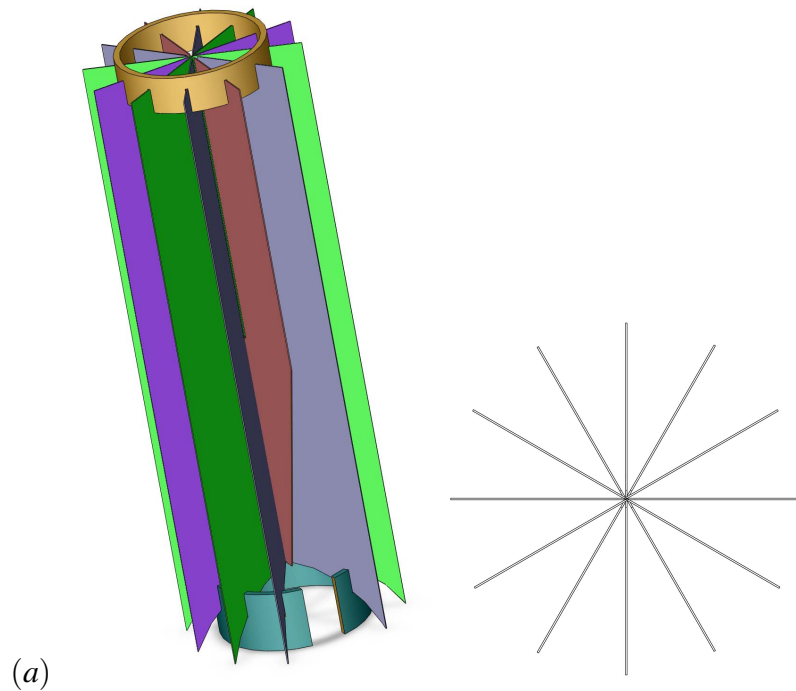
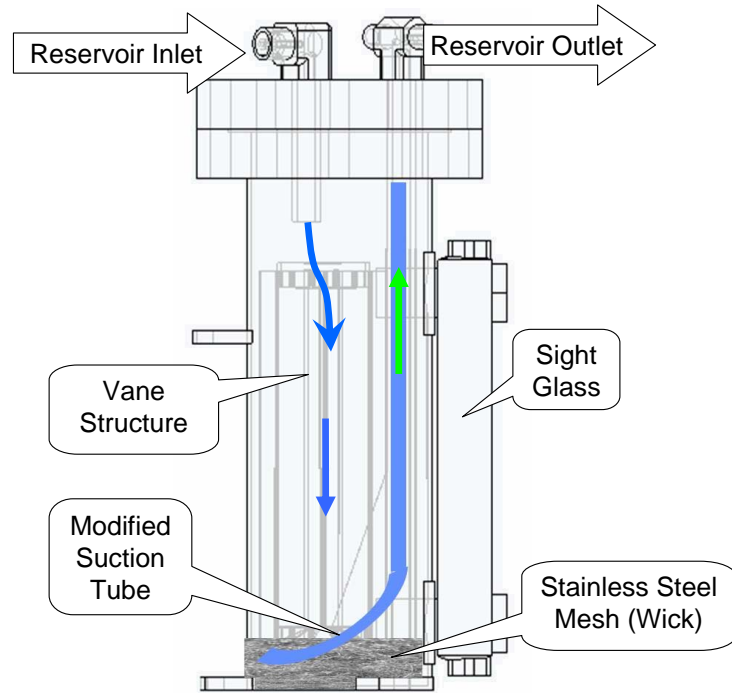


Figure 2.3: Stainless Steel Vane Structure: (a) Design and Cross-Section; (b) Micro-Gravity Operation.

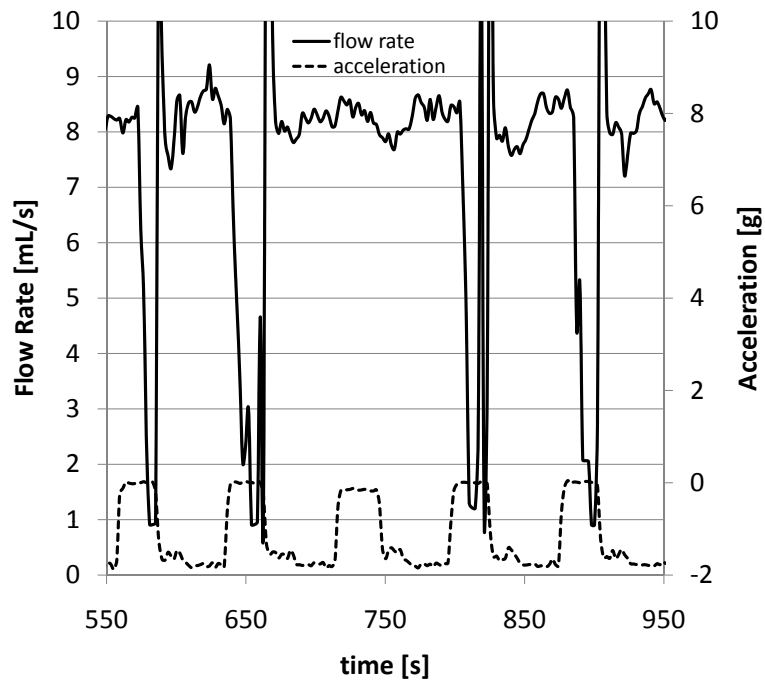
after it passed along the vane's central axis during sloshing, allowing for a continuous liquid feed, but was not positioned directly beneath the vane structure core. The reservoir inlet tube was a significant distance away from the vane structure which induced a nozzle cone effect, which didn't concentrate inlet fluid onto the vane core. This design introduced more flow instability than the previous reservoir, as shown in Figure 2.4(b).

Finally, as shown in Figure 2.5, the stainless steel reservoir was changed to allow the fluid inlet to make direct contact with the inlet of the vane structure. This modification removed the disconnection between the fluid entering the reservoir and the inlet of the vane structure resulting in flow expansion before reaching the vane. With an inlet tube that made direct contact with the vane structure, this problem should be minimized. The fourth generation of the reservoir did not undergo any flight testing.

The final liquid-vapor separator configuration, mounted within the variable-gravity array spray cooling experiment, Figure 2.7, contained a very high surface area vane structure, as shown Figure 2.6. This vane structure was designed using three-dimensional modeling software and generated using an ABS plastic rapid prototyping machine. To verify proper operation, the vane was housed within a transparent acrylic tube with caps on each end, allowing for flow visualization that was synchronized with the flight data. The top cap had an inlet port that injected fluid (mostly liquid) onto the center of the vane structure, allowing surface tension forces to hold the liquid central to the circular reservoir, as shown in Figure 2.8(a). This capillary action subsequently forced the vapor within the entrained fluid to exit radially through small pores in the inner tube of the vane structure to an open space between the vanes and the inner wall of the reservoir. At the end of this vane structure was the bottom end-cap which was funnel-shaped to an exit port that fed nearly 100% liquid to the nozzle. During operation under elevated gravity, the liquid-vapor separator functioned like any other terrestrial reservoir with the inlet on the top and outlet on the bottom. During micro-gravity, the liquid-vapor separator collected the liquid in the center as it traveled to the exit port leaving the vapor to fill the surrounding volume. Figure 2.8(a) displays, for a



(a)



(b)

Figure 2.4: Third Generation Reservoir: (a) Cross-Sectional View; (b) Raw Test Data.

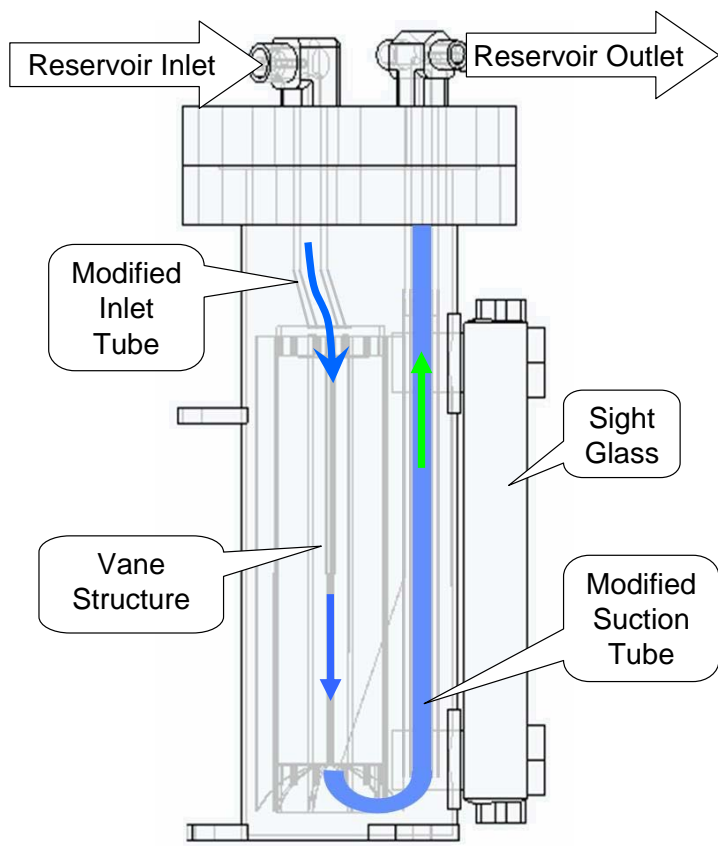


Figure 2.5: Final Stainless Steel Liquid-Vapor Separator Iteration.

flow rate of $\dot{m} = 8 \text{ [g/s]}$, stable operation during micro-gravity and elevated gravity.

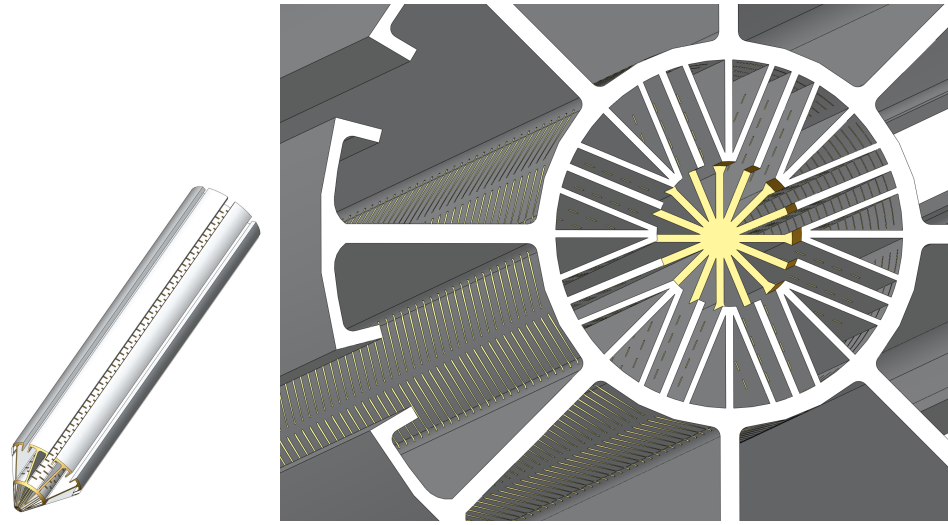


Figure 2.6: Liquid-Vapor Separator Internal Vane Structure (Isometric and Top Views).

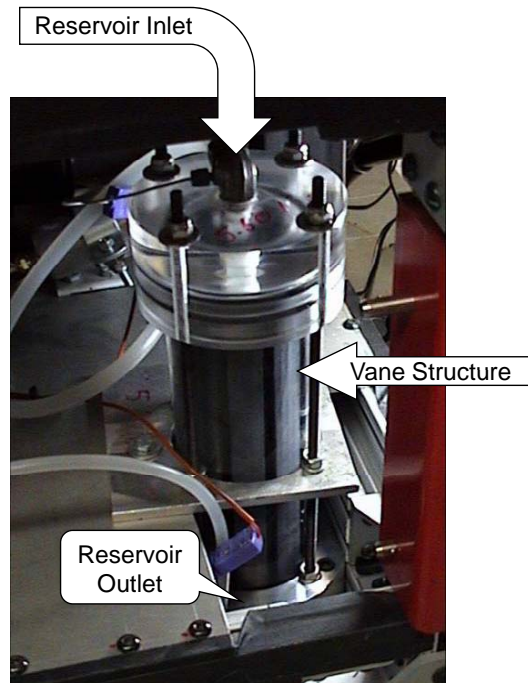
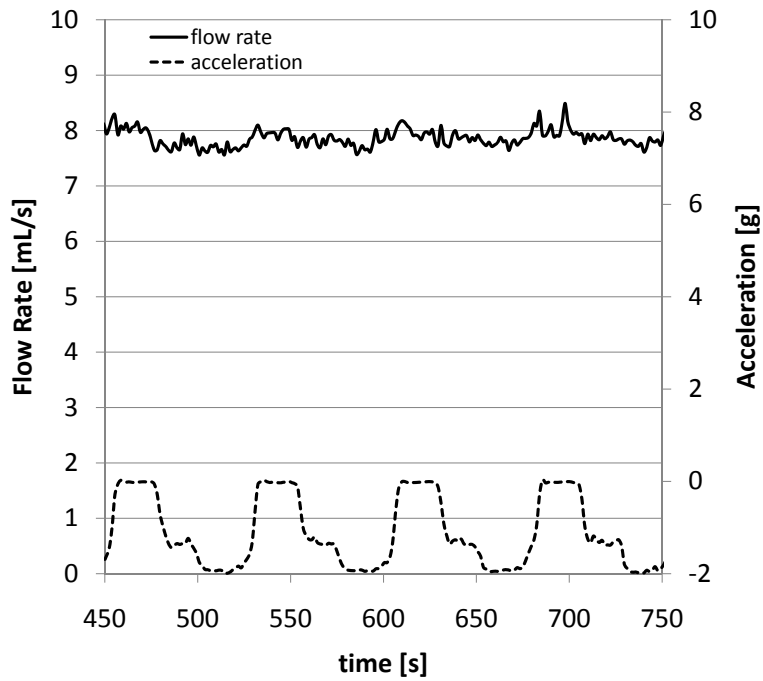
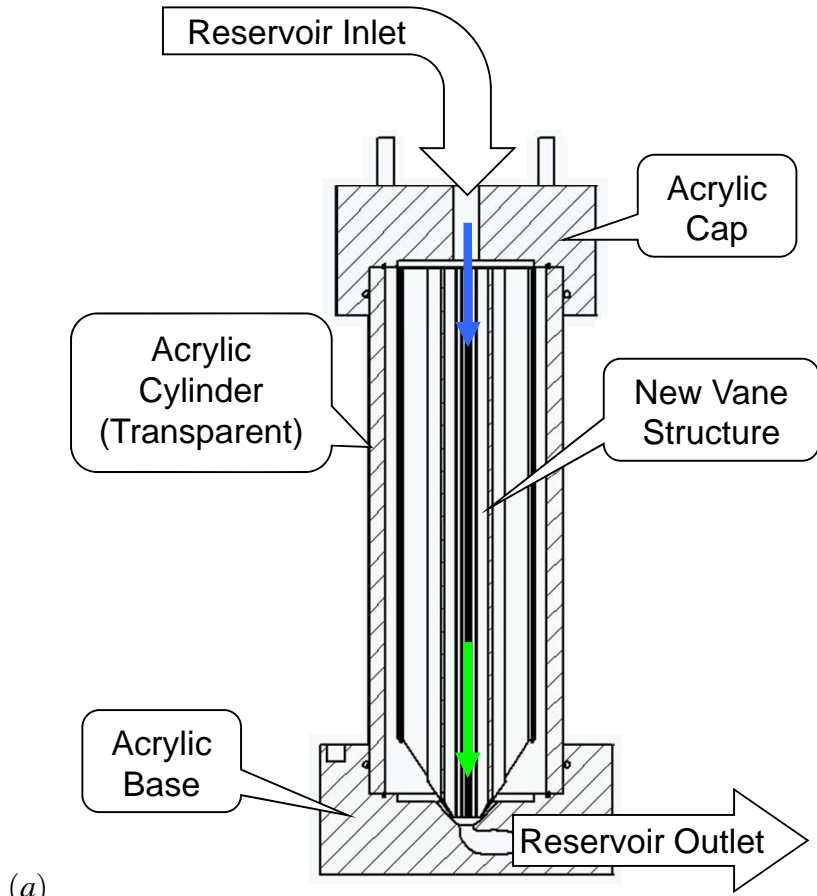


Figure 2.7: Final Liquid-Vapor Separator Mounted.



(b)

Figure 2.8: Final Reservoir: (a) Cross-Sectional View; (b) Raw Test Data.

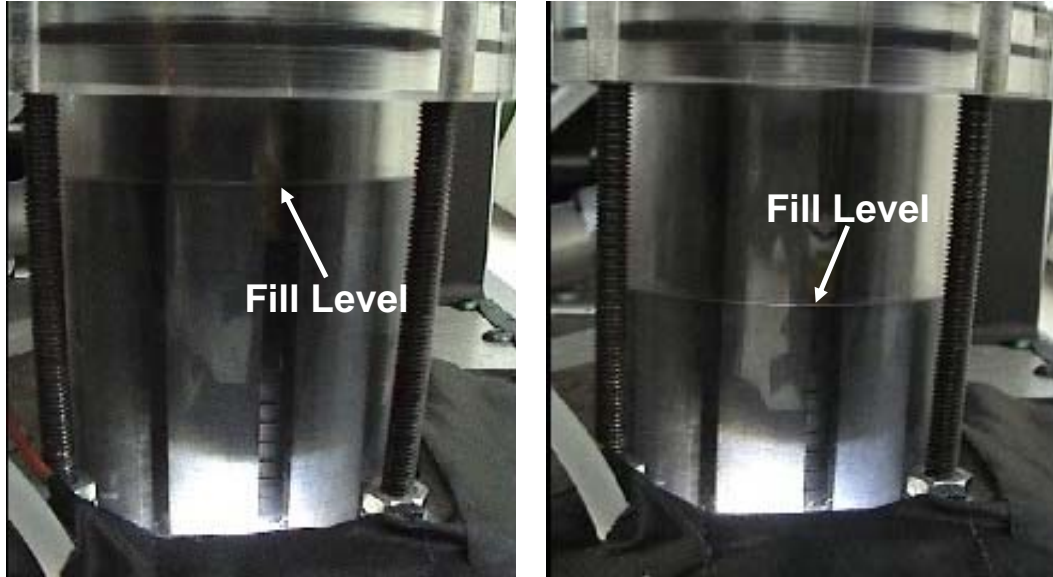


Figure 2.9: Reservoir Fill, Flight 3 (left) and Flight 4 (right).

2.3 Results and Discussion

Flight testing the liquid-vapor separator was completed using NASA's C-9 Reduced Gravity Aircraft. Flights 3 and 4 (corresponding to the last two flights in the June 2007 flight week) investigated the effect of reservoir liquid fill on the sustained operability of the nozzle pump. The flow rate was recorded during each parabola to verify stable operation. The spray system was drained of some working fluid to allow additional vapor space in the reservoir for the Flight 3 experiments. In addition, prior to Flight 4 the system was further drained to increase the amount of vapor space in the reservoir. Figure 2.9 shows the approximate fill level for Flight 3 and Flight 4.

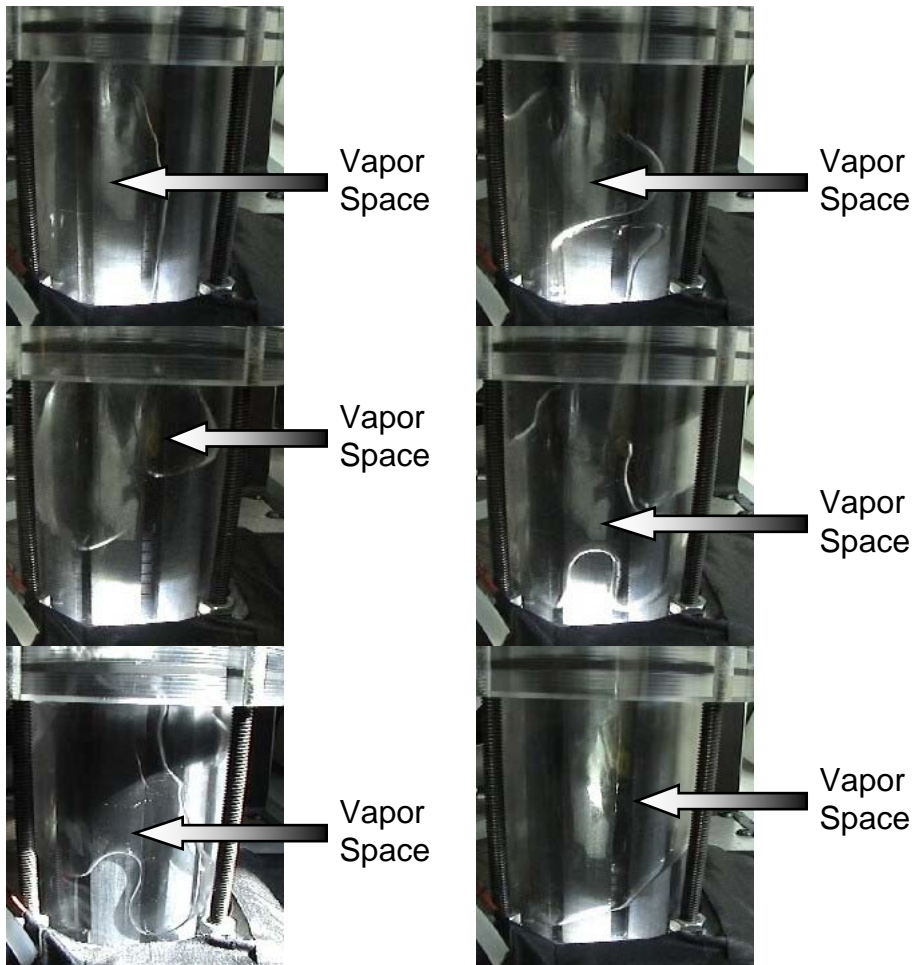
Flow rates were varied throughout the course of a flight in which the system experienced micro, terrestrial, and elevated gravity. Testing was completed at four different flow rate settings for each reservoir fill (Flight 3, 4). The flow rates examined were: $\dot{m} \approx 14, 17.5, 21, \text{ and } 30 \text{ [g/s]}$. Additionally, two reservoir fills were examined: $\sim 66\%$ and $\sim 33\%$, determined by a qualitative visual inspection. Also, the array heater was turned off for these tests, but the nozzle preheater was operated at prescribed inlet temperatures.

Although the flight trajectories for the reservoir tests included both micro-gravity, ter-

restrial, and elevated gravity data, only micro-gravity data was analyzed. This was due to the fact that when the induced gravity was at or above terrestrial, liquid-vapor separation was driven by the gravitational body force and capillary/surface tension forces did not play a significant role. Each parabola contained approximately eleven to fourteen data points. The average and standard deviation of each parabola's data points were calculated to compare flow stability.

Figures 2.10 and 2.11 show the reservoir volume being occupied by vapor space in a micro-gravity environment. Due to the inconsistencies in flight testing and uncontrollable dynamics, the exact same acceleration vector could not be maintained for each parabola. This inconsistency is reflected in the variation of reservoir vapor space shown in Figures 2.10 and 2.11. The camera was positioned on the aft side of the reservoir, because micro-gravity acceleration vector typically pointed forward, to photograph the vapor space and its fluctuation due to acceleration, flow rate, and fill level.

Figures 2.12-2.15 show samples of flow stability through a group of parabolas for specified flow rate regimes ($\dot{m} \approx 14, 17.5, 21, \text{ and } 30$ [g/s]). It can be seen that for the lowest flow setting, $\dot{m} \approx 14$ [g/s] shown in Figure 2.12, the flow rate was very consistent for both of the tested fill levels, with the approximate fill level pictured to the right of each plot. When the flow rate increased to $\dot{m} \approx 17.5$ [g/s], shown in Figure 2.13, occasional flow dropouts occurred. The flow rate dropouts had a longer duration in the lower fill case. As the flow further increases to $\dot{m} \approx 21$ [g/s], shown in Figure 2.14, more frequent dropouts occurred and the effect of the reservoir fill displayed a more prominent role. At the reduced fill level, Flight 4, nearly every micro-gravity segment produced a flow rate dropout, where in the higher fill level, Flight 3, dropouts occurred less frequently with shorter loss-of-flow durations. The highest tested flow rate setting, $\dot{m} \approx 30$ [g/s] shown in Figure 2.15, produced very consistent flow rate dropouts in the micro-gravity portion of each parabola. The flow rate recovered during the micro-gravity portion of the parabolas more consistently at the higher fill level, although the lower fill level showed a sustained flow for a longer time at



Note: Pictures are presented to show where the vapor space typically resided and are not shown as a sequence of events.

Figure 2.10: Micro-Gravity Vapor Space in Reservoir, Flight 3.

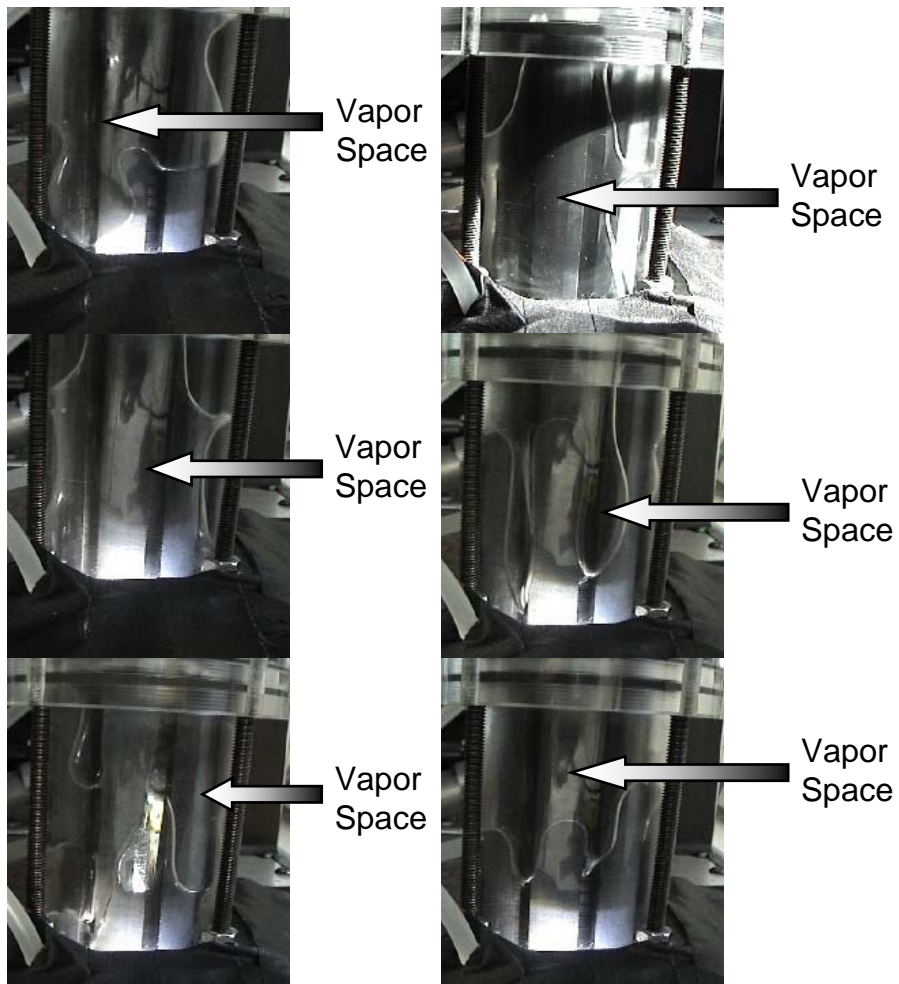


Figure 2.11: Micro-Gravity Vapor Space in Reservoir, Flight 4.

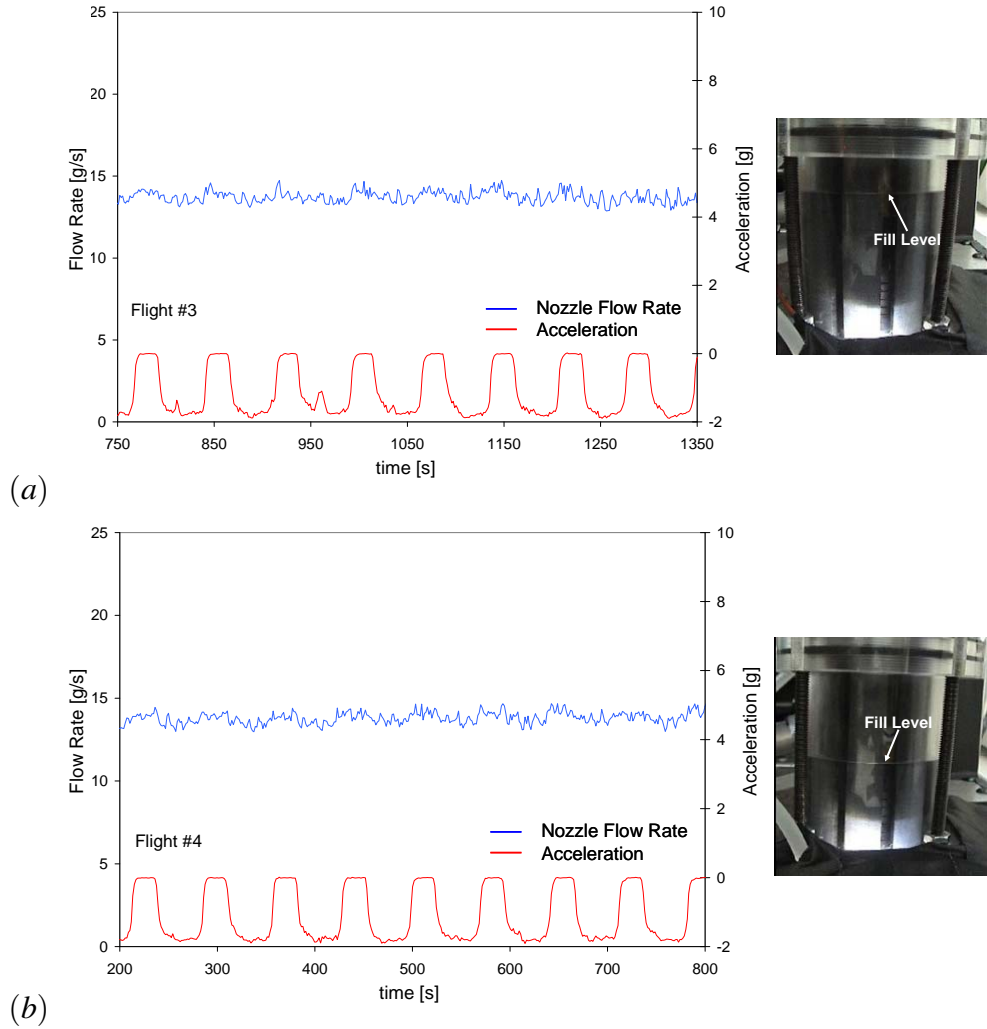
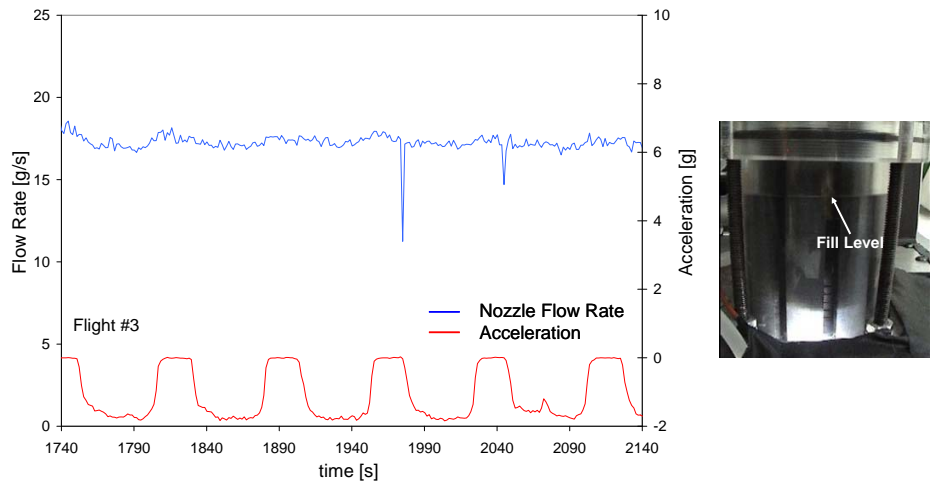


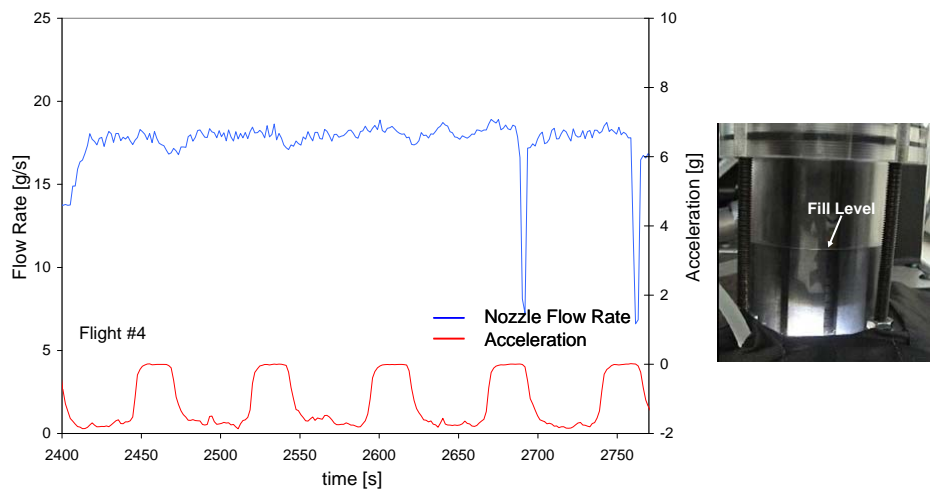
Figure 2.12: Flow Stability in a Transient Gravitational Environment ($\dot{m} \approx 14$ [g/s]): (a) Flight 3; (b) Flight 4.

the onset of each parabola.

Figure 2.16 further describes the flow rate stability as a function of flow rate and fill level in micro-gravity. The average and standard deviation of each parabola's data set are plotted to demonstrate flow rate variation. When a dropout occurred the standard deviation increased significantly, but the flow rate average also decreased, thus shifting the target flow rate to the left. Figure 2.16 demonstrates that for the low flow rate case, $\dot{m} = 14$ [g/s], the flow rate was very stable in higher fill case (Flight 3) and was suitably stable in the lower fill case (Flight 4). The flow stability for medium and high flow rates, $\dot{m} = 17.5$ and 21 [g/s],



(a)



(b)

Figure 2.13: Flow Stability in a Transient Gravitational Environment, ($\dot{m} \approx 17.5$ [g/s]): (a) Flight 3; (b) Flight 4.

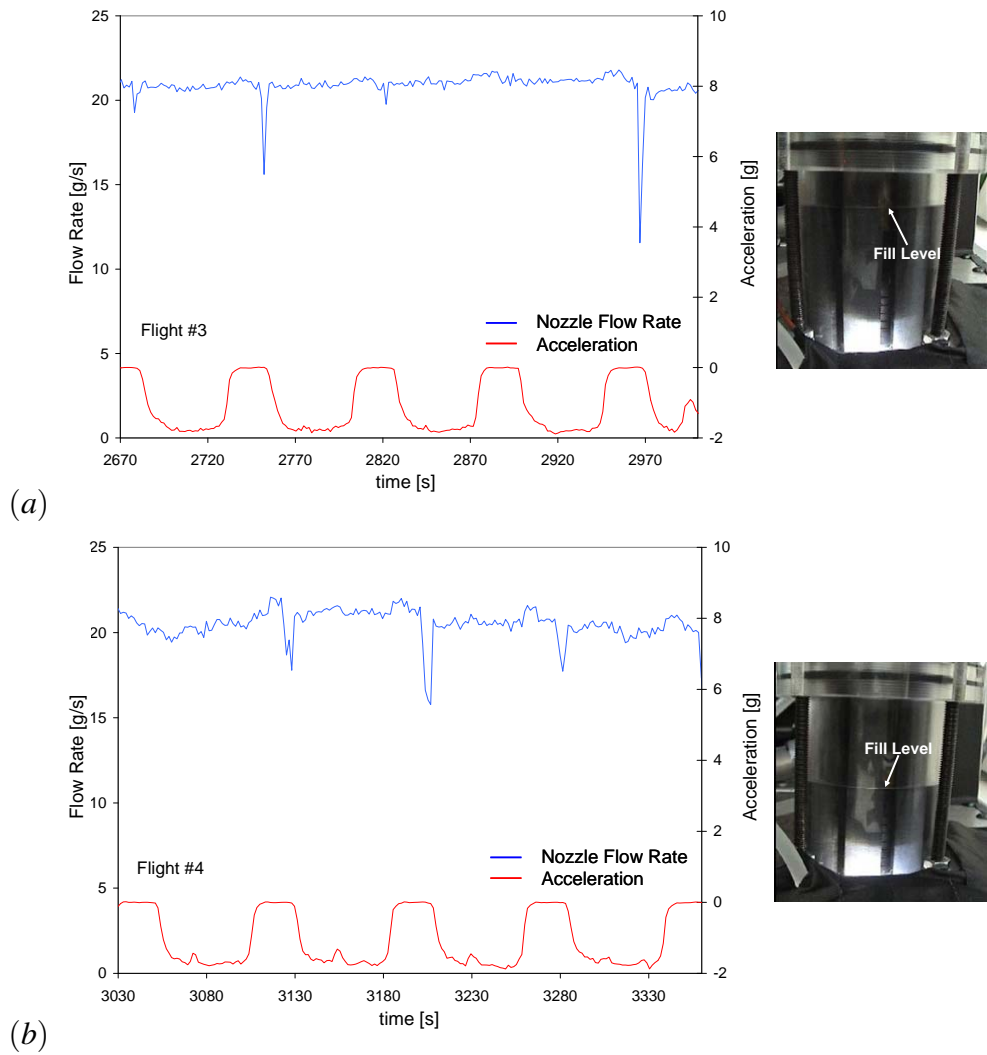


Figure 2.14: Flow Stability in a Transient Gravitational Environment, ($\dot{m} \approx 21$ [g/s]): (a) Flight 3; (b) Flight 4.

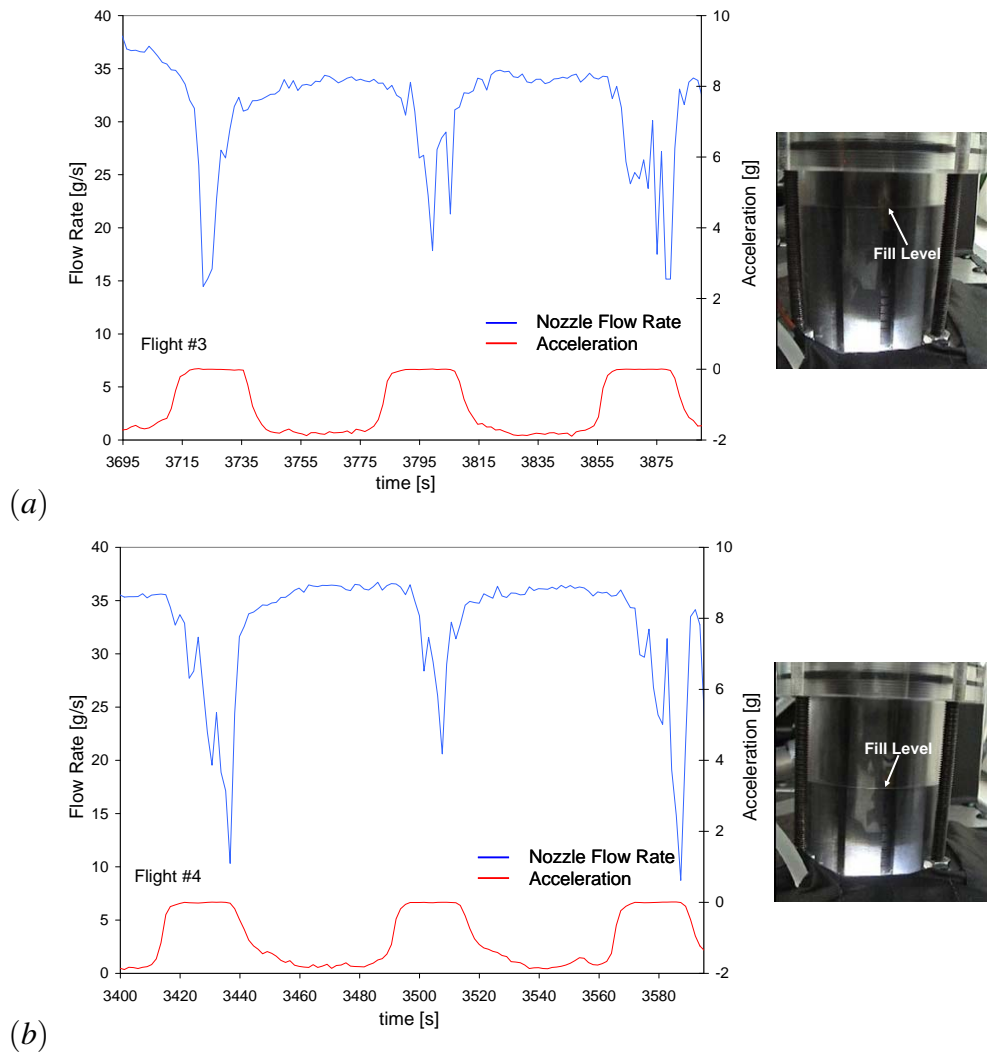


Figure 2.15: Flow Stability in a Transient Gravitational Environment, ($\dot{m} \approx 30$ [g/s]): (a) Flight 3; (b) Flight 4.

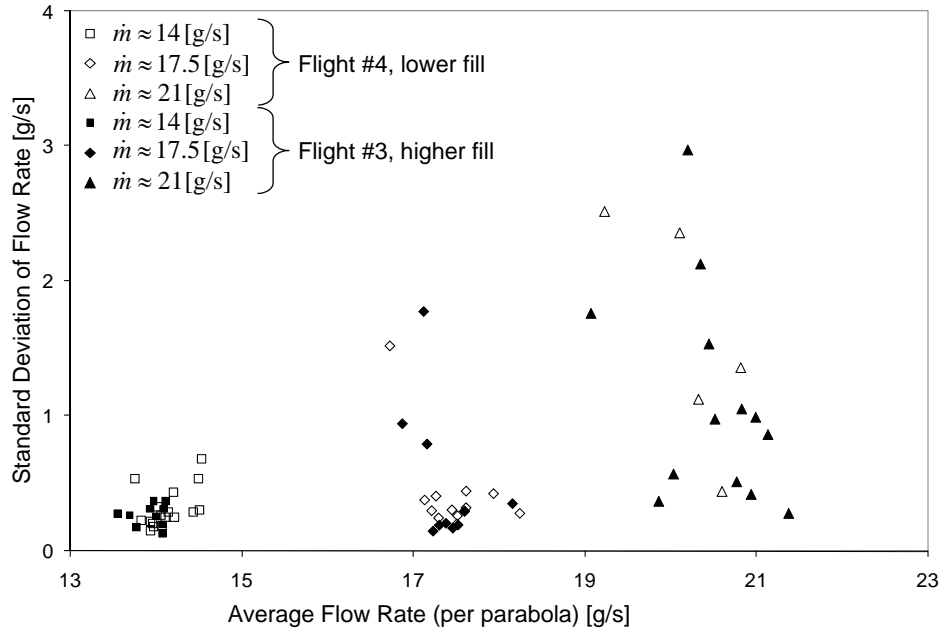


Figure 2.16: Flow Stability as a Function of Flow Rate and Fill Level

showed a decrease in flow stability for both fill cases (Flights 3 and 4) in which the micro-gravity flow stability was not as dependent on flow rate as other factors, such as parabola duration, liquid return flow rate (to reservoir), and acceleration inconsistencies.

2.4 Conclusions

The effectiveness of a liquid-vapor separator for a two-phase spray-cooling thermal management system was examined. The vapor (or liquid) percentage entering pumps and nozzle heads has a significant impact on the flow rate and cooling performance. The ABS plastic core of the reservoir enabled steady operation, in terms of flow rate, of the spray cooling system during gravitational transients and micro-gravity conditions. In some cases, the reservoir would drain during micro-gravity without refilling during each 25 [s] parabola, resulting in loss of flow conditions toward the end of each parabola, which was magnified at higher flow rates. The separator was evaluated at multiple vapor space fill levels and demonstrated steady operation for the lower flow rates.

2.5 Future Work

Improvements through future work would include optimization of the vane structure using analytical and numerical modeling. Weislogel et al. [36–39] has done modeling work to suggest that tapered geometries would increase flow stability during pump surges/dropouts while allowing for high flow rates driven by capillary forces. Additionally, since the vane structure was created using a rapid prototyping machine (ABS plastic) there was a certain amount of surface roughness perpendicular to the vane structure length that may induce pinning of the meniscus. Surface modifications could be made to reduce this effect while enhancing overall operability.

Bibliography

- [1] Mudawar, I., “Assessment of High-Heat-Flux Thermal Management Schemes,” *IEEE Transactions on Components and Packaging Technologies*, Vol. 24, No. 2, 2001, pp. 122–141.
- [2] Lee, H. S., Merte, H., and Chiamonte, F., “Pool Boiling Curve in Microgravity,” *Journal of Thermophysics and Heat Transfer*, Vol. 11, No. 2, 1997, pp. 216–222.
- [3] Gu, J., Kawaji, M., and Futamata, R., “Effects of Gravity on the Performance of Pulsating Heat Pipes,” *Journal of Thermophysics and Heat Transfer*, Vol. 18, No. 3, 2004, pp. 370–378.
- [4] Kim, J., “Review of Reduced Gravity Boiling Heat Transfer: US Research,” *Journal of the Japanese Society of Microgravity Application*, Vol. 20, No. 4, 2003, pp. 264–271.
- [5] Glassman, B., Kuravi, S., Du, J., Lin, Y., Zhao, G., and Chow, L., “A Fluid Management System for a Multiple Nozzle Array Spray Cooler,” *37th AIAA Thermophysics Conference*, AIAA Paper No. 2004-2574, 2004.
- [6] Kim, J., “Spray Cooling Heat Transfer: The State of the Art,” *International Journal of Heat and Fluid Flow*, Vol. 28, No. 4, 2007, pp. 753–767.
- [7] Ortiz, L. and Gonzalez, J. E., “Experiments on Steady-State High Heat Fluxes Using Spray Cooling,” *Experimental Heat Transfer*, Vol. 12, 1999, pp. 215–233.
- [8] Johnson, J. E., Selvam, R. P., and Silk, E. A., “Spray Cooling Modeling: Droplet Sub-Cooling Effect on Heat Transfer,” *Space Technology and Applications International Forum (STAIF)*, Vol. 969, 2008, pp. 104–111.
- [9] Selvam, R. P. and Ponnappan, R., “Numerical Modeling of Nucleation Boiling in Thin Film and Effect of Droplet Impact,” *Thermal and Fluids Analysis Workshop (TFAWS)*, 2004.
- [10] Selvam, R. P., Lin, L., and Ponnappan, R., “Computational Modeling of Spray Cooling: Current Status and Future Challenges,” *Space Technology and Applications International Forum (STAIF)*, Vol. 746, 2005, pp. 55–63.

- [11] Selvam, R. P., Sarkar, M., and Ponnappan, R., “Modeling of Spray Cooling: Effect of Droplet Velocity and Liquid to Vapor Density Ratio on Heat Transfer,” *Thermal and Fluids Analysis Workshop (TFAWS)*, 2005.
- [12] Selvam, R. P., Sarkar, M., Sarkar, S., and Ponnappan, R., “Effect of Vapor Bubble Size in Heat Transfer in Spray Cooling,” *AIP Space Technology and Applications International Forum (STAIF)*, Vol. 813, 2006, pp. 145–152.
- [13] Selvam, R. P., Sarkar, S., and Ponnappan, R., “Modeling of Spray Cooling: Convective Flow Effect on Vapor Bubble Dynamics and Heat Transfer,” *9th AIAA/ASME Joint Thermophysics and Heat Transfer Conference*, AIAA Paper No. 2006-3411, 2006.
- [14] Puterbaugh, R. L., Yerkes, K. L., Michalak, T. E., and Thomas, S. K., “Cooling Performance of a Partially-Confined FC-72 Spray: The Effect of Dissolved Air,” *45th AIAA Aerospace Sciences Meeting and Exhibit*, AIAA Paper No. 2007-199, 2007.
- [15] Puterbaugh, R. L., *The Effect of Dissolved Air on the Cooling Performance of a Partially-Confined FC-72 Spray*, Master’s thesis, Department of Mechanical and Materials Engineering, Wright State University, Dayton, OH, 2008.
- [16] Kreitzer, P. J. and Kuhlman, J. M., “Visualization of Electrohydrodynamic Effects and Time Scale Analysis for Impinging Spray Droplets of HFE-7000,” *AIP Space Technology and Applications International Forum (STAIF)*, Vol. 969, 2008, pp. 86–93.
- [17] Kreitzer, P. J., *Experimental Testing of Convective Spray Cooling with the Aid of an Electrical Field Using the Coulomb Force*, Master’s thesis, Department of Mechanical and Aerospace Engineering, West Virginia University, Morgantown, WV, 2006.
- [18] Kreitzer, P. J., Kuhlman, J. M., Mehra, D., Gray, D., and Yerkes, K. L., “Effects of Contact Charging on Spray Impingement Heat Transfer Performance and Spray Behavior,” *39th AIAA Thermophysics Conference*, AIAA Paper No. 2007-4269, 2007.
- [19] Glaspell, S. L., *Effects of the Electric Kelvin Force on Spray Cooling Performance*, Master’s thesis, Department of Mechanical and Aerospace Engineering, West Virginia University, Morgantown, WV, 2006.
- [20] Chow, L. C., Sehmbe, M. S., and Pais, M. R., “Critical Heat Flux in Spray Cooling,” *AIAA 34th Aerospace Sciences Meeting and Exhibit*, AIAA Paper No. 96-0727, 1996.
- [21] Lin, L. and Ponnappan, R., “Heat Transfer Characteristics of Spray Cooling in a Closed Loop,” *International Journal of Heat and Mass Transfer*, Vol. 46, 2003, pp. 3737–3746.
- [22] Lin, L. and Ponnappan, R., “Two-Phase High Capacity Spray Cooling Loop - Nozzle Orientation Effects and Performance Results,” *3rd AIAA International Energy Conversion Engineering Conference*, AIAA Paper No. 2005-5733, 2005.

- [23] Lin, L., Ponnappan, R., Yerkes, K. L., and Hager, B., “Large Area Spray Cooling,” *42nd AIAA Aerospace Sciences Meeting and Exhibit*, AIAA Paper No. 2004-1340, 2004.
- [24] Lin, L., Harris, R., Lawson, J., and Ponnappan, R., “Spray Cooling with Methanol and Water Mixtures,” *9th AIAA/ASME Joint Thermophysics and Heat Transfer Conference*, AIAA Paper No. 2006-3410, 2006.
- [25] Sone, K., Yoshida, K., Oka, T., Abe, Y., Mori, Y., and Nagashima, A., “Spray Cooling Characteristics of Water and FC-72 Under Reduced and Elevated Gravity for Space Application,” *International Energy Conversion Engineering Conference*, Vol. 2, 1996, pp. 1500–1505.
- [26] Yoshida, K., Abe, Y., Oka, T., Mori, Y., and Nagashima, A., “Spray Cooling Under Reduced Gravity Condition,” *Journal of Heat Transfer*, Vol. 123, 2001, pp. 309–318.
- [27] Baysinger, K. M., Yerkes, K. L., Michalak, T. E., Harris, R. J., and McQuillen, J., “Design of a Microgravity Spray Cooling Experiment,” *42nd AIAA Aerospace Sciences Meeting and Exhibit*, AIAA Paper 2004-0966, 2004.
- [28] Baysinger, K. M., *Experimental Testing and Numerical Modeling of Spray Cooling Under Terrestrial Gravity Conditions*, Master’s thesis, Department of Mechanical and Materials Engineering, Wright State University, Dayton, OH, 2005.
- [29] Yerkes, K. L., Michalak, T. E., Baysinger, K. M., Puterbaugh, R., Thomas, S. K., and McQuillen, J., “Variable-Gravity Effects on a Single-Phase Partially Confined Spray Cooling System,” *Journal of Thermophysics and Heat Transfer*, Vol. 20, No. 3, 2006, pp. 361–370.
- [30] Michalak, T. E., Yerkes, K. L., Puterbaugh, R., Thomas, S. K., and McQuillen, J., “Cooling Performance of a Partially-Confined FC-72 Spray: The Effect of Variable Gravity,” *45th AIAA Aerospace Sciences Meeting and Exhibit*, AIAA Paper No. 2007-198, 2007.
- [31] Yaniec, J. S. and Del Rosso, D., *NASA JSC Reduced Gravity Program User’s Guide*, Aircraft Operations Division, AOD 33899, 2007.
- [32] Shoemaker, J. M. and Schrage, D. S., “Microgravity Fluid Separation Physics - Experimental and Analytical Results,” *35th AIAA Aerospace Sciences Meeting and Exhibit*, AIAA Paper No. 97-0886, 1997.
- [33] Schrage, D. S., Shoemaker, J. M., and McQuillen, J., “Passive Two-Phase Fluid Separation - A Dynamic Simulation Model,” *36th AIAA Aerospace Meeting Sciences and Exhibit*, AIAA Paper No. 1998-731, 1998.
- [34] Barbu, A., Ellis, M., Kurwitz, C., and Best, F., “Acoustic Gauge Monitoring of Fluid Inventory in a Microgravity Vortex Separator,” *Measurement Science and Technology*, Vol. 17, 2006, pp. 403–410.

- [35] Kuravi, S., Glassman, B., Lin, Y., Du, J., Zhao, G., Chow, L., and Rini, D., “Design of a Two-Phase Separator for Variable Gravity Applications,” *37th AIAA Thermophysics Conference*, AIAA Paper No. 2004-2288, 2004.
- [36] Weislogel, M. M. and Lichter, S., “Capillary Flow in Interior Corners,” *Journal of Fluid Mechanics*, Vol. 373, 1998, pp. 349–378.
- [37] Weislogel, M. M., Collicott, S., Gotti, D., Bunnell, C., Kurta, C., and Goliher, E., “The Capillary Flow Experiments: Handheld Fluids Experiments for International Space Station,” *42nd AIAA Aerospace Sciences Meeting and Exhibit*, AIAA Paper No. 2004-1148, 2004.
- [38] Weislogel, M. M., Bunnell, C., Kurta, C., Goliher, E., Green, R., and Hickman, J., “Preliminary Results from the Capillary Flow Experiment Aboard ISS: The Moving Contact Line Boundary Condition,” *43rd AIAA Aerospace Sciences Meeting and Exhibit*, AIAA Paper No. 2005-1439, 2005.
- [39] Weislogel, M. M., Jenson, R. M., Klatte, J., and Dreyer, M. E., “The Capillary Flow Experiments Aboard ISS: Moving Contact Line Experiments and Numerical Analysis,” *Space Technology and Applications International Forum*, AIAA Paper No. 2008-0816, 2008.
- [40] Weislogel, M. M., “Some Analytical Tools for Fluids Management in Space: Isothermal Capillary Flows Along Interior Corners,” *Advances in Space Research*, Vol. 32, No. 2, 2003, pp. 163–170.

Appendix A

Experimental Setup: Additional Figures

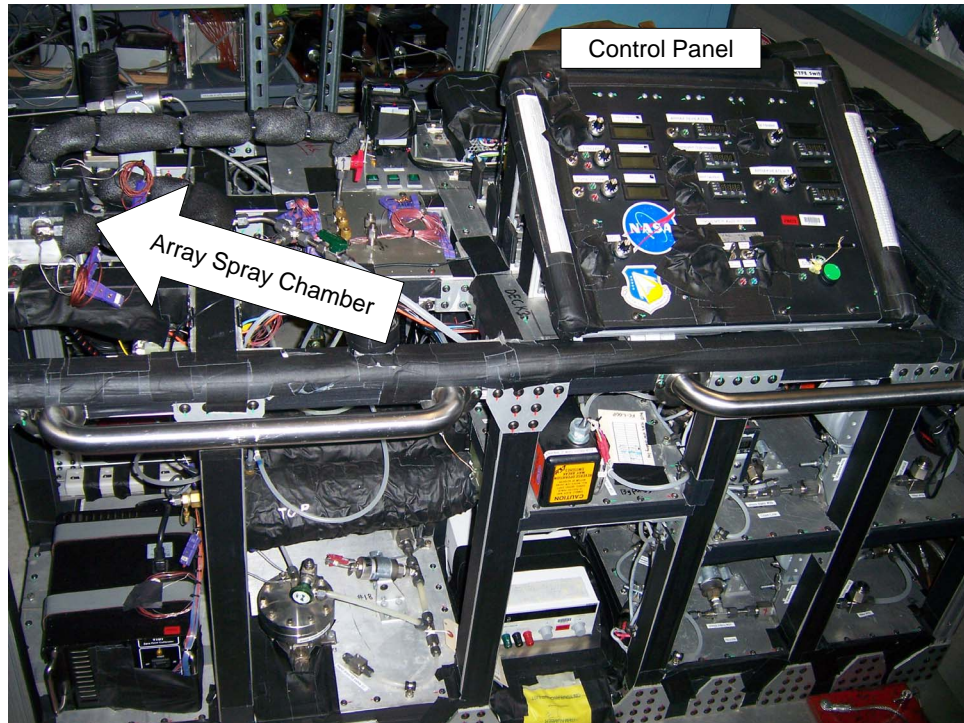


Figure A.1: Experimental Test Setup

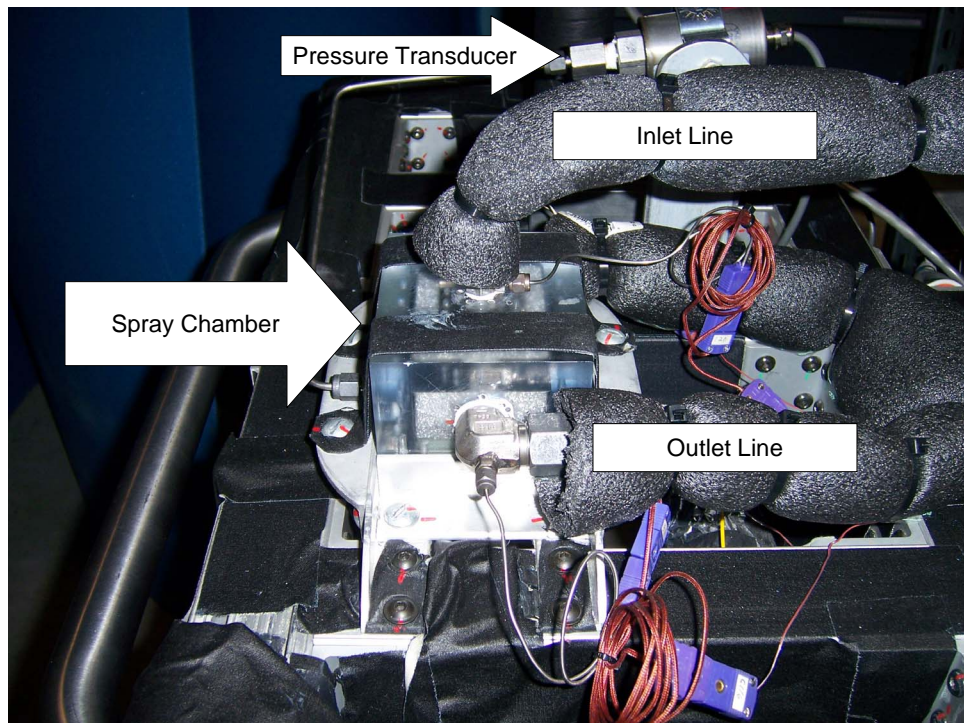


Figure A.2: Array Spray Chamber Mounted to Experiment

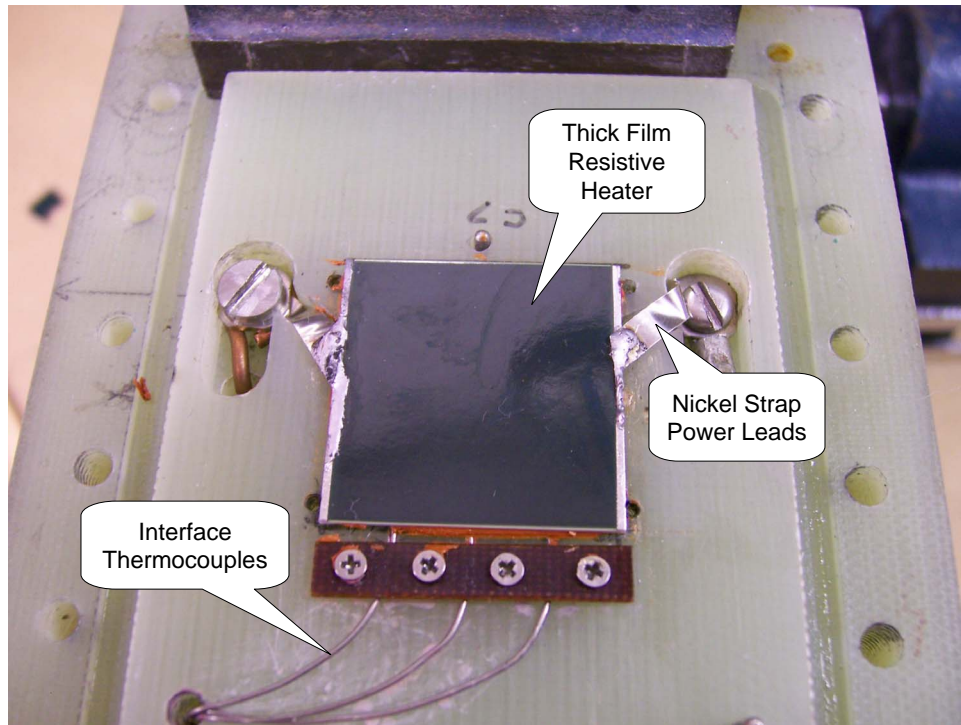


Figure A.3: Thick Film Resistive Heater Mounted

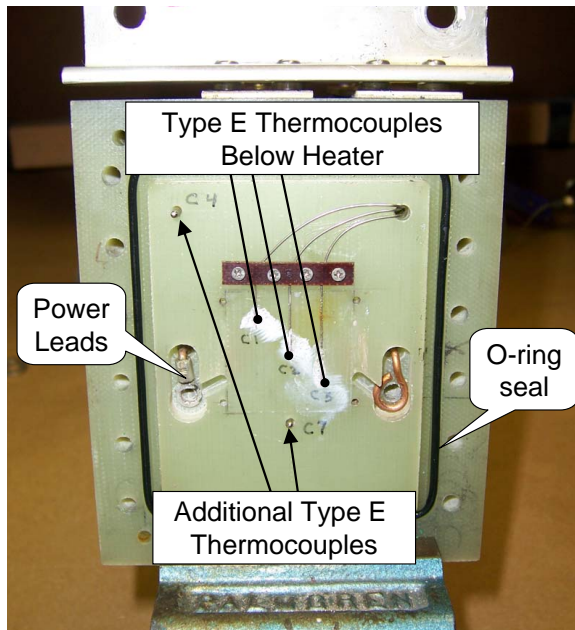


Figure A.4: Thermocouple Placement Underneath Heater

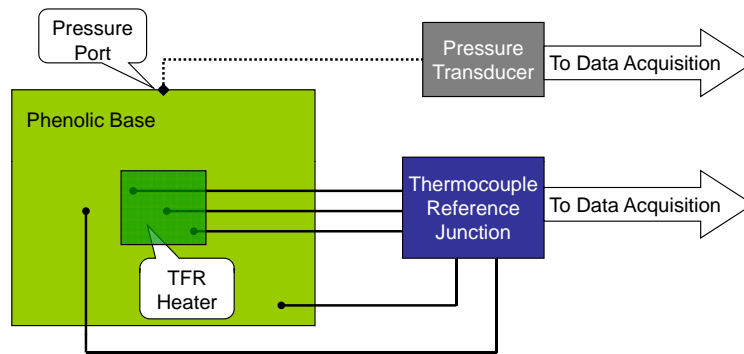


Figure A.5: Chamber Instrumentation Diagram

TC Name	TC1	TC2	TC3	TC4	TC5
Placement	Heater	Heater	Heater	Chamber	Phenolic
Description	Interface Temperature	Interface Temperature	Interface Temperature	Fluid Temperature	12.7 mm below TFR
TC Name	TC6	TC7	TC8	TC9	TC10
Placement	Phenolic	Chamber	Drain	Drain	Nozzle Inlet
Description	6.35 mm below TFR	Fluid Temperature	Chamber Outlet Temperature	Chamber Outlet Temperature	Nozzle Inlet Temperature

Table A.1: Chamber Thermocouple Locations

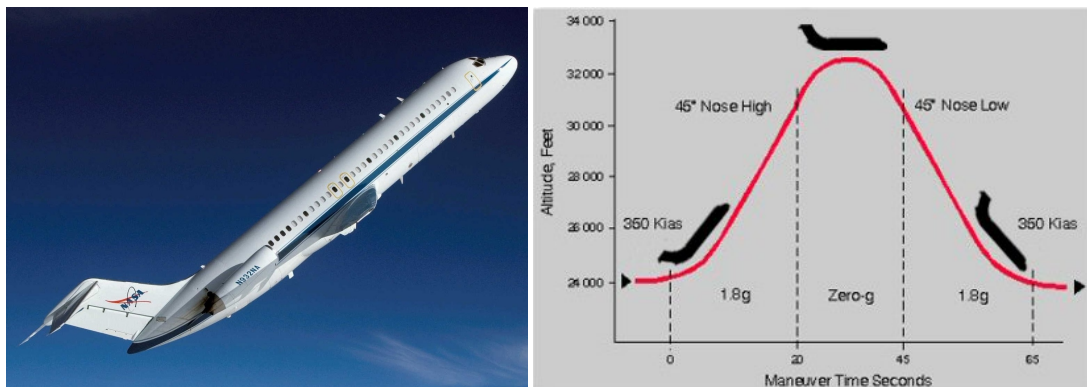


Figure A.6: NASA's C-9 Reduced Gravity Aircraft and In-flight Trajectory

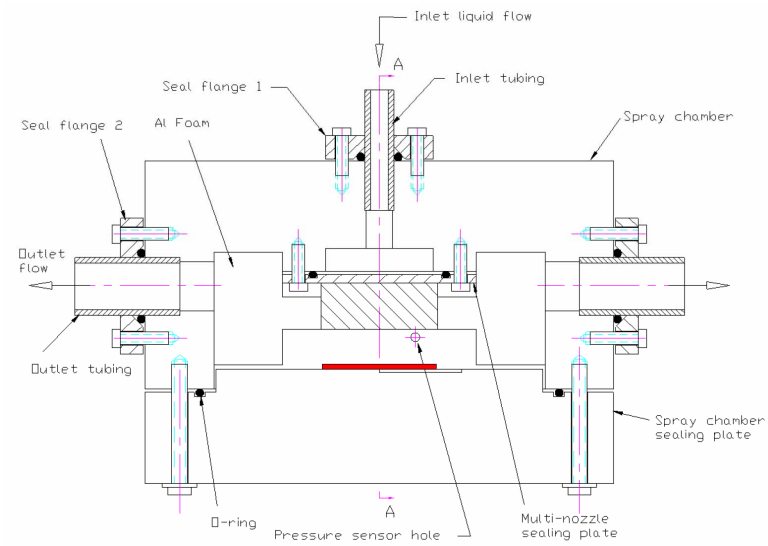


Figure A.7: Section View Design of Array Spray Chamber

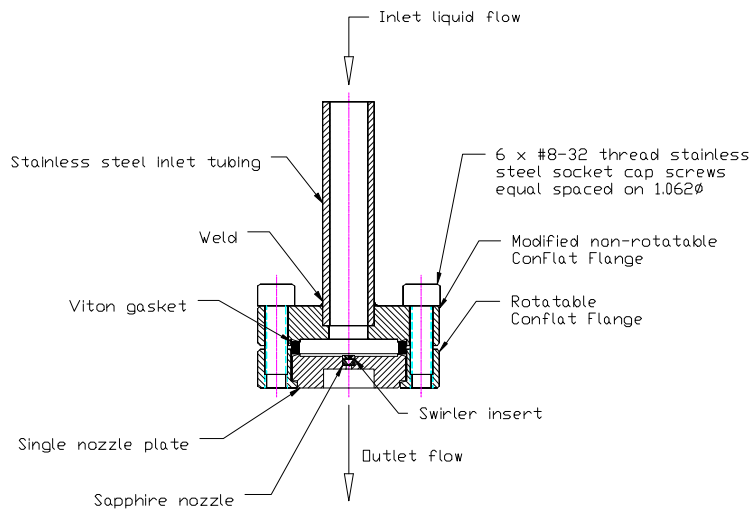


Figure A.8: Single Nozzle Design

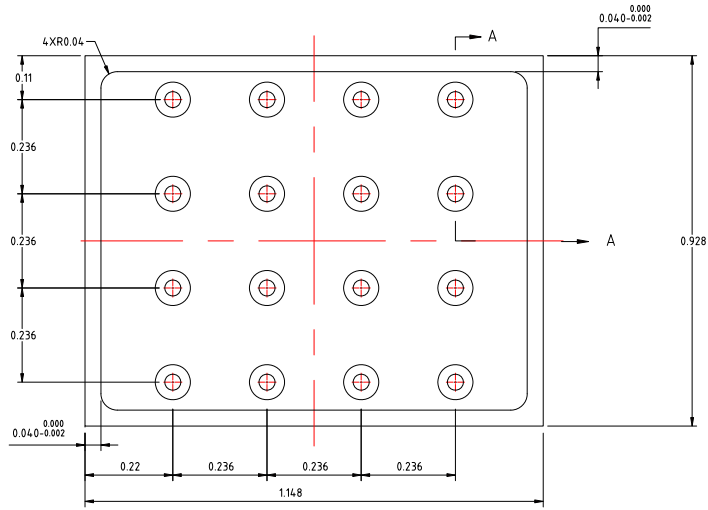


Figure A.9: 16-Nozzle Array Layout

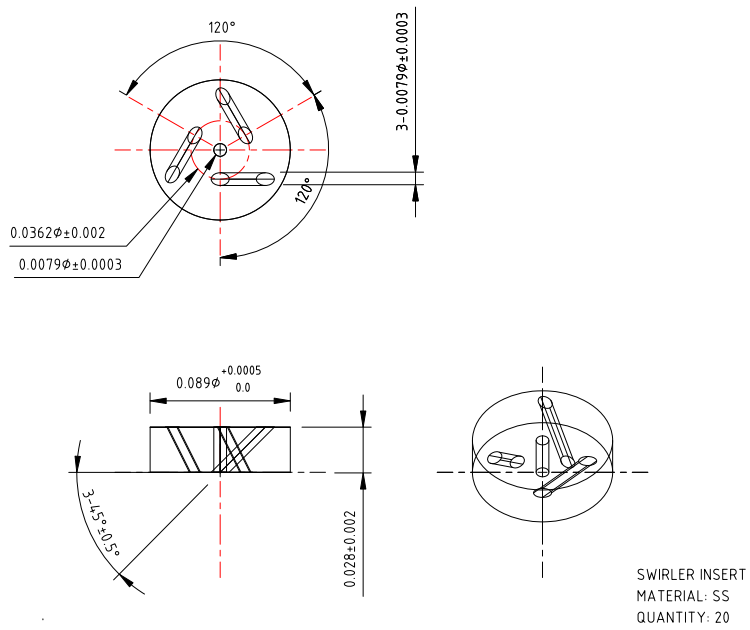


Figure A.10: Swirler Insert Design

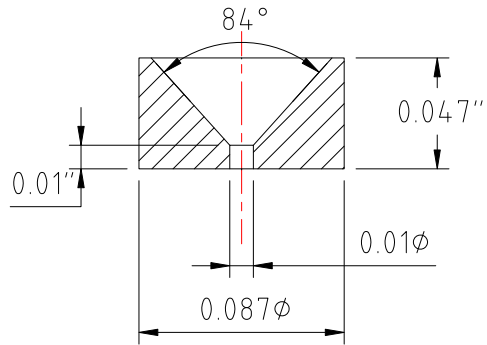


Figure A.11: Sapphire Orifice Design

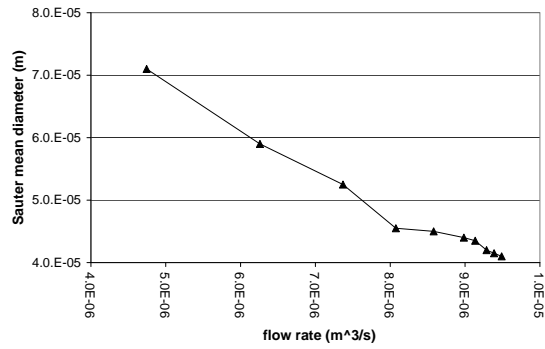


Figure A.12: Single Nozzle Characterization - Sauter Mean Diameter vs. Flow Rate

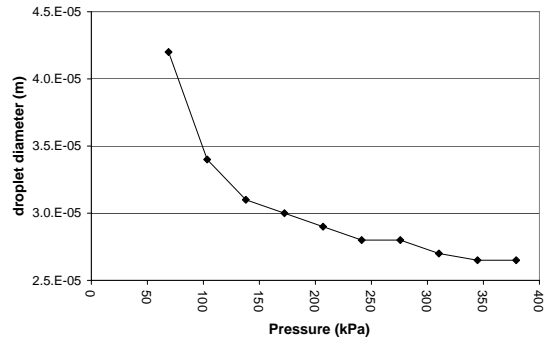


Figure A.13: Single Nozzle Characterization - Droplet Diameter vs. Pressure Drop

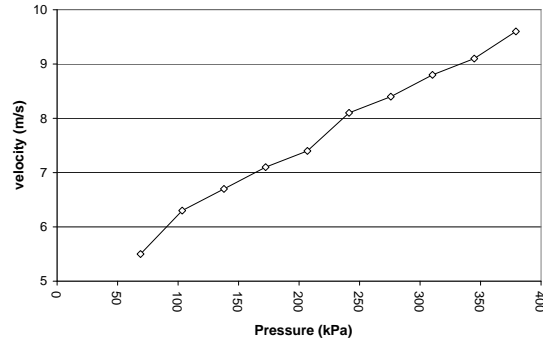


Figure A.14: Single Nozzle Characterization - Velocity vs. Pressure Drop

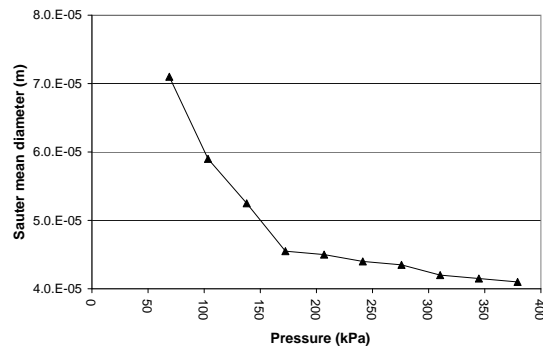


Figure A.15: Single Nozzle Characterization - Sauter Mean Diameter vs. Pressure Drop

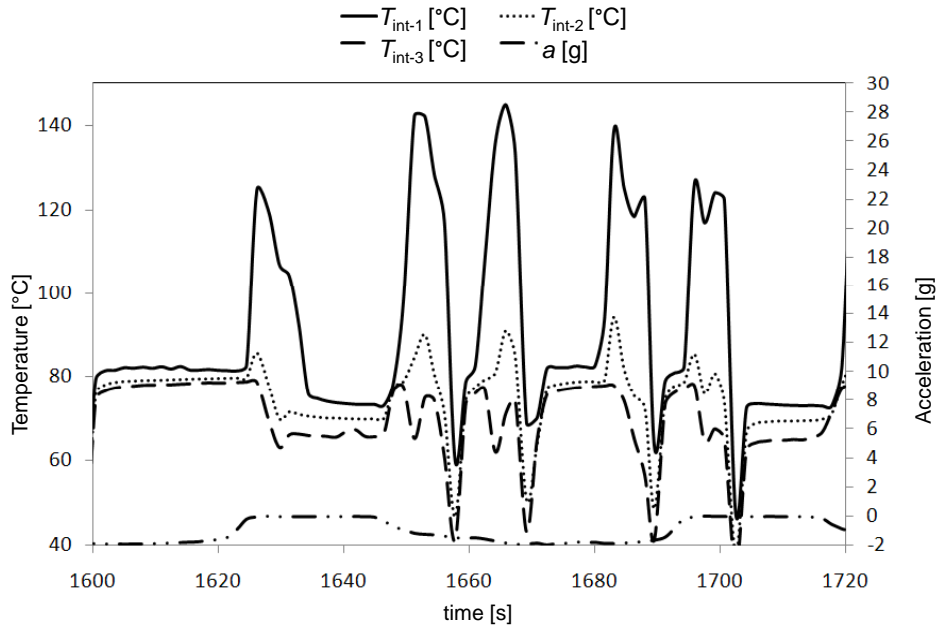


Figure A.16: Interface Thermocouple Variation Near CHF ($(1-f)q'' = 21.4 \pm 0.04$ [W/cm²], $\dot{m} = 8.00 \pm 0.19$ [g/s])

Appendix B

Calibration and Uncertainty Analysis

B.1 Flow Meter

B.1.1 Calibration Setup

The calibration of the flowmeter was performed using a simple stopwatch, 3000 mL flask, 100mL graduated cylinder, and a Mettler PL4400 scale. The Tuthill magnetically coupled gear pump, model DDS.99PPPV2NN37000, pumps the fluid, air saturated FC-72, through a 15 micron in-line filter. Then, fluid flows through a Sponsler MF90-CB-PH-A-4X-V flow meter which is attached to a signal conditioner. The Omega, FTB9504, signal conditioner converts the frequency signal to a voltage (0-10 VDC) that can be read by an Agilent 34970A data acquisition unit. After the flowmeter, the fluid is then rerouted out of the rig and to a large flask which acts as a reservoir. From that flask, the fluid then is return to the above mentioned gear pump. The flow schematic for the calibration is shown in Figure B.1.

B.1.2 Calibration Procedure

To begin the setup, a large flask was filled with approximately 3.5 liters of FC-72 and placed next to an empty 100 mL graduated cylinder. An inlet and outlet tube were placed

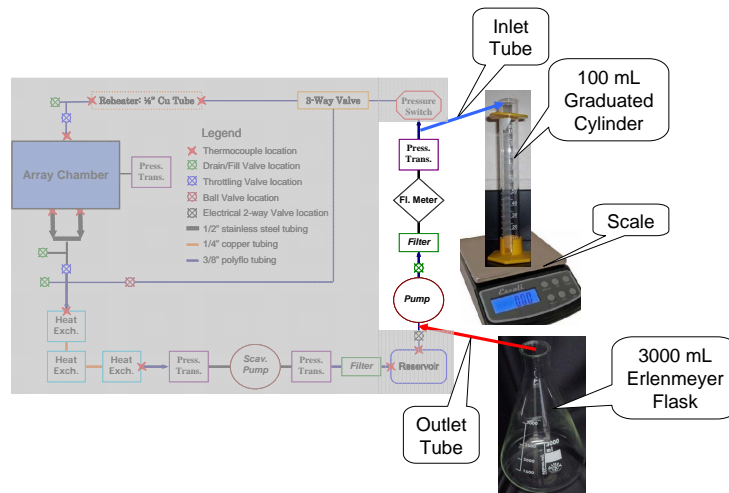


Figure B.1: Flowmeter Calibration Setup

inside the flask of FC-72. The outlet tube pulled FC-72 out of the flask, and sent it through the flow loop. The same fluid was then put back into the flask via the inlet tube. To begin the experiment, a desired flow rate was chosen. Then, the pump was adjusted to achieve a flow rate as close as possible to the desired flow rate, according to the data logger software on the laptop connected to the spray cooling system. Once the flow rate seemed to be fairly stable and near the desired rate, the data acquisition scan was started on the laptop. Within the next couple of seconds, the spray tube was removed from the flask and quickly placed into the graduated cylinder, at which time the stopwatch was started. After a length of time, dependent upon the desired fill mark on the graduated cylinder and therefore the magnitude of the flow rate, the inlet tube was returned to the flask and the time was stopped. The data acquisition was stopped and saved approximately ten seconds after the return of the spray tube to the flask. Then, the volume and mass of the FC-72 in the graduated cylinder were measured and recorded, along with the trial name and number, exact time duration, desired flow rate, and data acquisition file name. Then, the measured flow rate, average computer voltage, and average computer flow rate were calculated and recorded. The FC-72 from the graduated cylinder was poured back into the flask and the experiment was repeated. Trials for desired flow rates from 2.1 to 13.67 mL/s (2 to 13 gph) were performed, with five trials

per desired flow rate. The uncertainty of readability for the graduated cylinder is ± 5 mL. The uncertainty of readability for the scale is $\pm .05$ g. The uncertainty in the stopwatch recording is $\pm .5$ s.

B.1.3 Uncertainty Analysis

Although many factors were considered to try to reduce the amount of uncertainty in the flowmeter and thermocouple calibrations, there is still enough error that a detailed analysis must be completed. The uncertainty associated with the flowmeter calibration is attributed to:

1. Time-human reaction/stopwatch
2. Volume-graduated cylinder error and readability
3. Mass-scale error
4. Regression-difference between linear fit and data points

The error associated with the mass flow rate is:

$$\Delta \dot{m}_{total} = \Delta \dot{m}_{mass/time} + \Delta \dot{m}_{regression} \quad (\text{B.1})$$

$$\dot{m} = \frac{m}{t} \quad (\text{B.2})$$

which gives the uncertainty for the mass and time error:

$$\Delta \dot{m}_{mass/time} = \sqrt{\left[\left(\frac{\partial \dot{m}}{\partial m} \right) dm \right]^2 + \left[\left(\frac{\partial \dot{m}}{\partial t} \right) dt \right]^2} \quad (\text{B.3})$$

where

$$\frac{\partial \dot{m}}{\partial m} = \frac{1}{t} \quad (\text{B.4})$$

time (s)	mass (kg)	mass flow rate (kg/s)	recorded mass flow rate (kg/s)	Eqn B.6 (kg/s)	Eqn B.3 (kg/s)	$\Delta\dot{m}_{total}$ Eqn. B.1 (kg/s)	% error
210.0	1.4908	.007099	.00716	6.05 e-5	1.707 e-5	7.75 e-5	1.09%
135.0	1.4470	.010719	.01082	1.040 e-4	3.987 e-5	1.438 e-4	1.34%
105.9	1.5547	.014671	.01418	4.955 e-4	6.938 e-5	5.649 e-4	3.85%
74.99	1.3906	.018544	.017661	8.825 e-4	1.238 e-4	1.006 e-3	5.43%
65.02	1.4495	.022293	.02125	1.04 e-3	1.716 e-4	1.211 e-3	5.43%

Table B.1: Mass Flow Rate Calibration Example

and

$$\frac{\partial \dot{m}}{\partial t} = -\frac{m}{t^2} \quad (\text{B.5})$$

The instrument errors are:

$$dm = \pm .5g = \pm .0005kg$$

$$dt = \pm .5s$$

To determine flow rate linear regression:

$$\Delta\dot{m}_{regression} = | \dot{m}_{actual} - \dot{m}_{predicted} | \quad (\text{B.6})$$

Sample calibration data are shown in Table B.1. The maximum total error, $\Delta\dot{m}_{total}$, is 6.3%. This error percentage is taken pervasively as a conservative approach. Figure B.2 shows the mass flow rate uncertainty containing error bars at 6.3%.

The error associated with the volumetric flow rate is:

$$\Delta\dot{V}_{total} = \Delta\dot{V}_{volume/time} + \Delta\dot{V}_{regression} \quad (\text{B.7})$$

$$\dot{V} = \frac{V}{t} \quad (\text{B.8})$$

which gives the uncertainty for the mass and time error:

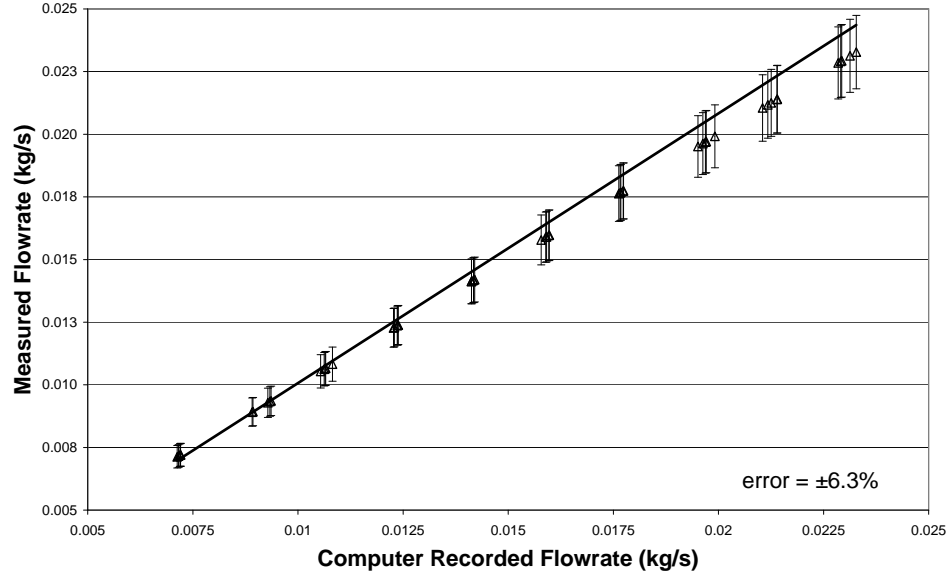


Figure B.2: Mass Flow Rate Calibration Uncertainty

$$\Delta \dot{V}_{\text{volume/time}} = \sqrt{\left[\left(\frac{\partial \dot{V}}{\partial V} \right) dV \right]^2 + \left[\left(\frac{\partial \dot{V}}{\partial t} \right) dt \right]^2} \quad (\text{B.9})$$

where

$$\frac{\partial \dot{V}}{\partial V} = \frac{1}{t} \quad (\text{B.10})$$

and

$$\frac{\partial \dot{V}}{\partial t} = -\frac{V}{t^2} \quad (\text{B.11})$$

The instrument errors are:

$$dV = \pm 5\text{mL} = \pm .000005\text{m}^3$$

$$dt = \pm .5\text{s}$$

To determine flow rate linear regression:

$$\Delta \dot{V}_{\text{regression}} = | \dot{V}_{\text{actual}} - \dot{V}_{\text{predicted}} | \quad (\text{B.12})$$

time (s)	volume (m^3)	volumetric flow rate ($\frac{m^3}{s}$)	recorded volumetric flow rate ($\frac{m^3}{s}$)	Eqn B.12 ($\frac{m^3}{s}$)	Eqn B.9 ($\frac{m^3}{s}$)	$\Delta\dot{V}_{total}$ Eqn. B.7 ($\frac{m^3}{s}$)	% error
210.0	8.85 e-4	4.21 e-6	4.25 e-6	3.59 e-8	2.58 e-8	6.17 e-8	1.47%
135.0	8.59 e-4	6.36 e-6	6.43 e-6	6.17 e-8	4.39 e-8	1.06 e-7	1.66%
105.9	9.28 e-4	8.76 e-6	8.46 e-6	2.96 e-7	6.27 e-8	3.59 e-7	4.09%
74.99	8.29 e-4	1.11 e-5	1.06 e-5	4.85 e-7	9.94 e-8	5.85 e-7	5.29%
65.02	8.66 e-4	1.33 e-5	1.27 e-5	6.21 e-7	1.28 e-7	7.49 e-7	5.62%

Table B.2: Mass Flow Rate Calibration Example

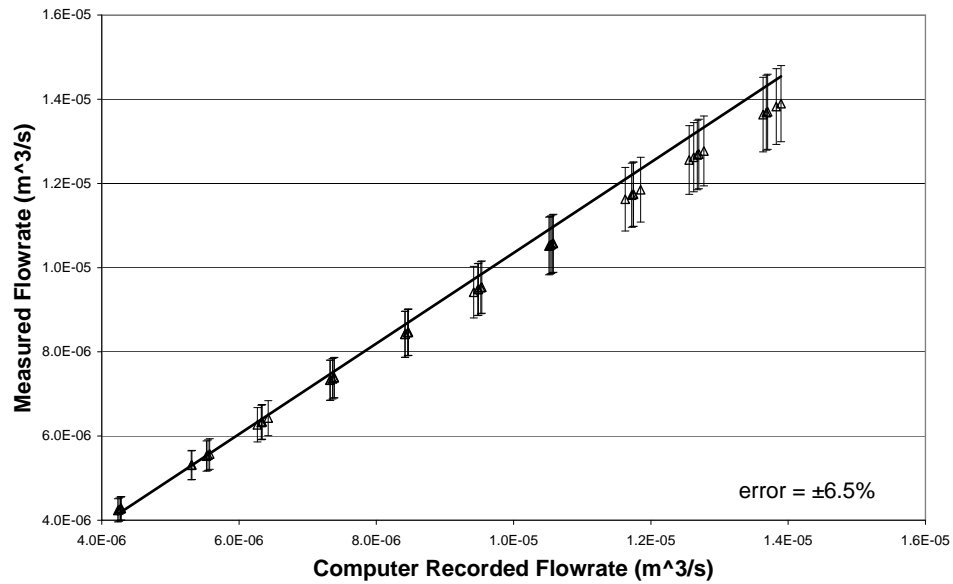


Figure B.3: Volumetric Flow Rate Calibration Uncertainty

Sample calibration data are shown in Table B.2. The maximum total error, $\Delta\dot{V}_{total}$, is 6.5%. This error percentage is taken pervasively as a conservative approach. Figure B.3 shows the mass flow rate uncertainty containing error bars at 6.5%.

B.2 Thermocouples

B.2.1 Calibration Setup

The significant thermocouples were calibrated using a Hart Scientific Ice Point Calibrator (model # 9101), a Hart Scientific Calibration Bath (model # 6330), and a Hart Scientific Precision platinum RTD (5628 and 1502A). The ice point was used as a precision reference that would be exactly the same no matter the ambient environment. The calibration bath was filled with silicon oil and was controlled using the rig's laptop with an RS-232 connection. An additional RS-232 connection to the RTD was read-only. This value was taken as the absolute temperature and this temperature was used to calibrate the other thermocouples as well as determine the bath's steady state.

Each thermocouple within the test chamber was calibrated before its installation. In addition, the thermocouples in the preheater, the chamber inlet, and the chamber outlet lines were also calibrated.

B.2.2 Calibration Procedure

To perform the calibration, a program, using a temperature ramp and decay, was written using Visual Basic for Applications by Richard Harris of University of Dayton Research Institute. This program would interface with the rig's data acquisition unit, the calibration bath, and the RTD, all through the laptop computer. The basic logic of the software was written in such a way as to reduce the program's complexity, whilst keeping the data accurate. A temperature was set on the calibration bath; not a precise setting, but held constant for a time long enough to reach steady state, then a data point was taken for all thermocouples and the RTD. After 2.5 hours, enough time to reach steady state, the RTD and all thermocouples in the calibration bath would record a final data point for that temperature setting. Next, the temperature bath would increase in temperature to the next set point and this process would repeat all the way to 120°C. Afterwards, a very similar process took

place during the cooling portion of the calibration. The last data point before the calibration bath set temperature was changed and the $\frac{\Delta T}{\Delta t}$ for the last time increment was recorded for the calibration. The data was fitted linearly and associated residuals were calculated. If any connections were changed/modified or if a thermocouple needed replaced, this procedure was redone.

B.2.3 Uncertainty Analysis

The uncertainty associated with the thermocouple calibration comes from:

1. RTD-instrument error
2. Steady State-temperature gradients (bath, thermocouples, RTD)

The error associated with the thermocouple calibration is:

$$\Delta T_{total} = \Delta T_{RTD} + \Delta T_{readout} + \Delta T_{regression} \quad (\text{B.13})$$

where

$$\Delta T_{RTD} = .006^{\circ}C \quad (\text{B.14})$$

$$\Delta T_{readout} = .009^{\circ}C \quad (\text{B.15})$$

and

$$\Delta T_{regression} = | T_{predicted} - T_{RTD} | \quad (\text{B.16})$$

Table B.3 shows a sample thermocouple calibration data set. The RTD temperature and computer recorded temperature are used to achieve a linear fit for the data.

$$T_{predicted} = mT_{recorded} + b \quad m = slope \quad b = intercept \quad (\text{B.17})$$

Then, the original recorded temperature is plugged into the linear fit equation to generate an equation predicted temperature. The difference between the predicted temperature and

the RTD temperature is recorded as the regression error, Eqn B.16. Eqns B.14, B.15, and B.16 are added to equal the total thermocouple error, Eqn B.13.

RTD Temperature ($^{\circ}\text{C}$)	Recorded Temperature ($^{\circ}\text{C}$)	Predicted Temperature ($^{\circ}\text{C}$)	Regression Error B.16 ($^{\circ}\text{C}$)	Total Error B.13 ($^{\circ}\text{C}$)
34.75	34.82	34.77	0.0123	0.027
39.75	39.83	39.77	0.0195	0.035
44.74	44.80	44.73	0.0031	0.018
49.74	49.80	49.74	0.0016	0.017
54.72	54.78	54.70	0.0198	0.035
59.71	59.77	59.69	0.0156	0.031
64.72	64.83	64.75	0.0273	0.042
69.69	69.76	69.68	0.0104	0.025
74.71	74.79	74.70	0.0028	0.018
79.69	79.81	79.72	0.0236	0.039
84.67	84.78	84.68	0.0058	0.021
89.69	89.77	89.67	0.0181	0.033
94.66	94.78	94.67	0.0176	0.033
99.68	99.79	99.68	0.0047	0.020
104.65	104.76	104.65	0.0029	0.018
109.64	109.76	109.64	0.0079	0.023
114.67	114.80	114.67	0.0020	0.017
119.63	119.74	119.61	0.0164	0.031
99.67	99.80	99.69	0.0128	0.028
74.71	74.78	74.69	0.0121	0.027
53.09	53.13	53.06	0.0297	0.045

Linear fit equation (Eqn B.17): $T_{predicted} = .999125334T_{recorded} - .024029693$

Table B.3: Sample Thermocouple Calibration Data Set

B.3 Heat Flux to Spray

The heater power is determined via the use of two voltmeters. The first voltmeter, V_1 , measures the voltage drop across the heater. The second voltmeter, V_2 , measures the voltage drop across a precision resistor that is in series with the heater. V_2 is used to calculate the current, I . Therefore, the heat (power) generated (consumed) by the heater is:

$$\dot{Q} = V_1 I = V_1 \frac{V_2}{R} \quad (\text{B.18})$$

$$q'' = \frac{V_1 V_2}{A_{heater} R} \quad (\text{B.19})$$

$$q''_{spray} = (1 - f) q'' = (1 - f) \frac{V_1 V_2}{A_{heater} R} \quad (\text{B.20})$$

where (from Eqn C.30)

$$f = -.0002144 q'' + .0588504 \quad (\text{B.21})$$

$$q''_{spray} = [1 - (-.0002144 q'' + .0588504)] q'' \quad (\text{B.22})$$

simplifying and substituting in for q''

$$q''_{spray} = .0002144 (q'')^2 + .9411496 q'' \quad (\text{B.23})$$

$$q''_{spray} = .0002144 \left(\frac{V_1 V_2}{A_{heater} R} \right)^2 + .9411496 \left(\frac{V_1 V_2}{A_{heater} R} \right) \quad (\text{B.24})$$

So, the uncertainty with the heat removed by the spray is comprised of the error in measurement.

$$\Delta q''_{spray, total} = \Delta q''_{measurement} \quad (\text{B.25})$$

The measurement error is calculated by

$$\Delta q''_{measurement} = \sqrt{\left[\left(\frac{\partial q''_{spray}}{\partial V_1} \right) dV_1 \right]^2 + \left[\left(\frac{\partial q''_{spray}}{\partial V_2} \right) dV_2 \right]^2 + \left[\left(\frac{\partial q''_{spray}}{\partial R} \right) dR \right]^2 + \left[\left(\frac{\partial q''_{spray}}{\partial A_{heater}} \right) dA_{heater} \right]^2} \quad (\text{B.26})$$

where

$$\frac{\partial q''_{spray}}{\partial V_1} = .0004288V_1 \left(\frac{V_2}{A_{heater}R} \right)^2 + .9411496 \left(\frac{V_2}{A_{heater}R} \right) \quad (B.27)$$

and the data acquisition measurement error, from Agilent, is a function of the voltage and full scale error shown as

$$dV_1 = \pm (.002V_1 + .0006(100V)) V \quad (B.28)$$

$$\frac{\partial q''_{spray}}{\partial V_2} = .0004288V_2 \left(\frac{V_1}{A_{heater}R} \right)^2 + .9411496 \left(\frac{V_1}{A_{heater}R} \right) \quad (B.29)$$

$$dV_2 = \pm (.0015V_2 + .0004(10V)) V \quad (B.30)$$

$$\frac{\partial q''_{spray}}{\partial R} = -.0004288 \frac{1}{R^3} \left(\frac{V_1V_2}{A_{heater}} \right)^2 - .9411496 \left(\frac{V_1V_2}{A_{heater}R^2} \right) \quad (B.31)$$

$$dR = \pm .02\% = \pm .00002\Omega \quad (B.32)$$

$$\frac{\partial q''_{spray}}{\partial A_{heater}} = -.0004288 \frac{1}{A_{heater}^3} \left(\frac{V_1V_2}{R} \right)^2 - .9411496 \left(\frac{V_1V_2}{A_{heater}^2 R} \right) \quad (B.33)$$

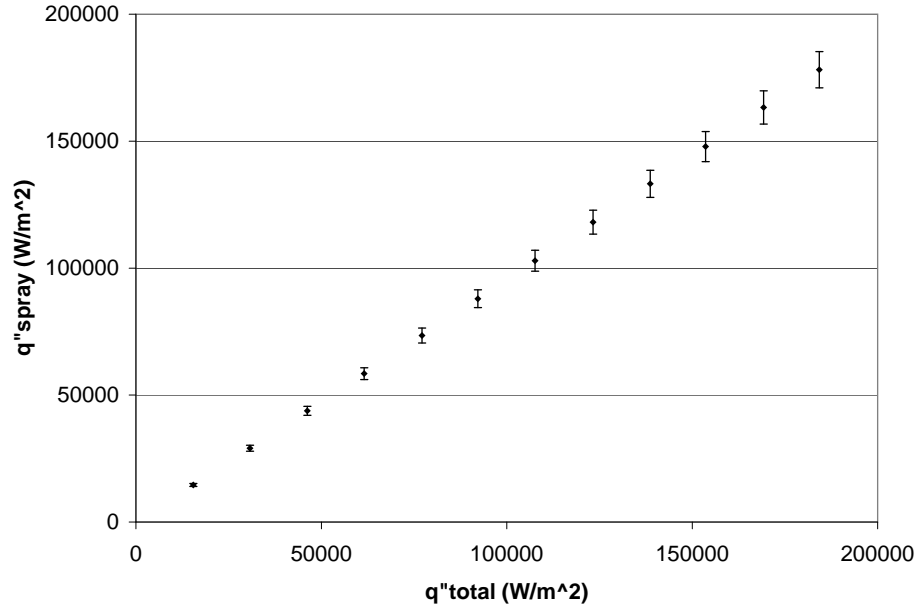
$$dA_{heater} = \pm 1.8339e^{-6} m^2 \text{ from Eqn B.44} \quad (B.34)$$

Table B.4 shows the calculation for determining the total heat as well as the values for determining the heat transferred to the spray and its associated uncertainty, further explained in Figure B.4.

V_1 (Volts)	V_2 (Volts)	R (ohms)	f	$q''_{total} \frac{W}{m^2}$	$q''_{spray} \frac{W}{m^2}$	$\Delta q''_{total} \frac{W}{m^2}$	% error
10.218	0.0985	0.1	5.67%	15450	14574	627	4.30%
14.423	0.1389	0.1	5.46%	30752	29075	907	3.12%
17.688	0.1702	0.1	5.24%	46212	43791	1134	2.59%
20.418	0.1964	0.1	5.03%	61539	58447	1333	2.28%
22.873	0.2198	0.1	4.81%	77154	73445	1517	2.07%
25.010	0.2402	0.1	4.60%	92178	87941	1684	1.91%
27.036	0.2594	0.1	4.38%	107642	102926	1847	1.79%
28.939	0.2775	0.1	4.16%	123245	118114	2004	1.70%
30.706	0.2943	0.1	3.95%	138676	133202	2154	1.62%
32.327	0.3096	0.1	3.74%	153607	147864	2296	1.55%
33.940	0.3249	0.1	3.52%	169245	163287	2441	1.49%
35.420	0.3390	0.1	3.31%	184251	178151	2577	1.45%

Examples values for V_1 and V_2 are taken from a baseline test (21May07).

Table B.4: Heat Transferred to Spray Calculation and Uncertainty



error bars = 4% (minimum power=10W)

Figure B.4: Uncertainty of Heat Transferred to Spray

B.3.1 Uncertainty Analysis

The area and associated area uncertainty used in the uncertainty calculation for q'' was also derived.

$$A = L \cdot W \quad (\text{B.35})$$

$$\Delta A = \sqrt{\left[\left(\frac{\partial A}{\partial L}\right) dL\right]^2 + \left[\left(\frac{\partial A}{\partial W}\right) dW\right]^2} \quad (\text{B.36})$$

$$L = W \quad (\text{B.37})$$

$$A = L^2 \quad (\text{B.38})$$

$$\Delta A = \sqrt{\left[\left(\frac{\partial A}{\partial L}\right) dL\right]^2 + \left[\left(\frac{\partial A}{\partial L}\right) dL\right]^2} = \sqrt{2 \left[\left(\frac{\partial A}{\partial L}\right) dL\right]^2} \quad (\text{B.39})$$

$$\frac{\partial A}{\partial L} = 2L \quad (\text{B.40})$$

$$dL = .0000254m \quad (\text{B.41})$$

$$L = 1.005in = .025527 m \quad (\text{B.42})$$

$$A = .00065163 m^2 \quad (\text{B.43})$$

$$\Delta A = \sqrt{2[(2 \cdot .025527) \cdot .0000254]^2} = 1.8339e^{-6} m^2 \quad (\text{B.44})$$

Appendix C

Heater Losses: One-Dimensional Heat Conduction Model

C.1 Description/Motivation

The experimental spray chamber, which houses the heater, does not remove heat from the thick film resistive heater purely by the spray. There are heat losses due to the conductivity, although very low, of the phenolic (G6) that the heater is mounted on. This phenolic base not only transfers heat to the ambient air through its thickness, but also via contact with the mixing post-spray fluid outside of the heater area and the outer edges of the phenolic as well, described in better detail in Figure C.1.

The thermocouples instrumented into the chamber and simplification were the main reasons why a 1-D analytical solution was needed to determine the heater downward losses, Q_d . In addition, no thermocouples were placed laterally through the phenolic base to determine the side losses, Q_s . Q_u , the upward heat loss/gain between the phenolic base and fluid entrained in the aluminum foam, was taken to be zero due to, once again, lack of thermocouples as well as a low heat transfer coefficient with $T - T_\infty$ near 0.

There is an array of 3 thermocouples sandwiched between the interface of the heater

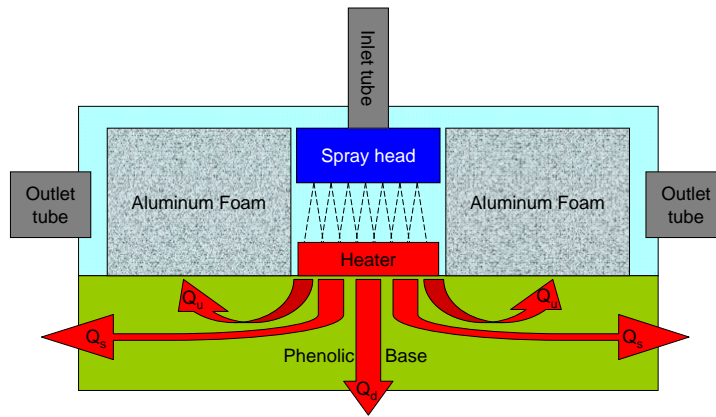


Figure C.1: Possible Heat Losses Not Due to Spray

Layer	Position	Thickness (mm)	Thermal Conductivity (W/m-K)
Ceramic Substrate	top (sprayed surface)	0.643	≈ 27
Resistive Layer (heater)	middle	0.008	≈ 1.04
Glass Cover	bottom	0.040	≈ 1.04

Table C.1: Resistive Heater Properties

and the phenolic base which can be averaged to get an approximate interface temperature. There are 2 thermocouples in the phenolic below the heater, spaced 6.35 [mm] (0.25 [in.]) and 12.7 [mm] (0.5 [in.]) beneath the bottom surface of the heater.

C.2 One-Dimensional Analytical Model

The thick film resistive heater is made of 3 layers, a ceramic substrate, a thin resistive film, and a glass cover plate. The details of each layer are presented in Table C.1.

A 1-D conduction model was needed to calculate a spray surface temperature that could be used to calculate the heat transfer coefficient associated with the spray nozzles. The analysis was broken into 3 layers; ceramic, resistive, and glass. An assumed fraction, f , of the input heat was determined to be lost downward, while the remaining heat, $Q(1 - f)$, is assumed to be taken away by the spray.

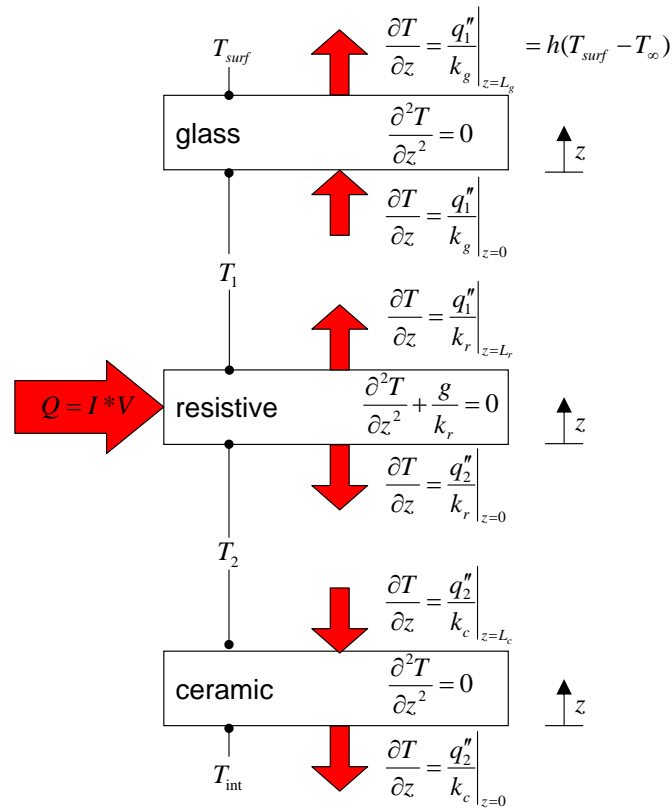


Figure C.2: 1-D Model Governing Equations and Boundary Conditions

The governing equations and boundary conditions are detailed in Figure C.2.

The temperature distribution through the ceramic layer is derived from:

$$\frac{\partial^2 T}{\partial z^2} = 0 \quad (C.1)$$

which gives a linear distribution of the form

$$T_c(z) = c_1 z + c_2 \quad (C.2)$$

and

$$\frac{\partial T_c}{\partial z} = c_1 \quad (C.3)$$

applying boundary conditions

$$\frac{\partial T_c}{\partial z}(z = L_c) = q_2'' = \frac{fQ}{k_c A_c} = c_1 \quad (\text{C.4})$$

$$T_c(z = 0) = T_{int} = c_2 \quad (\text{C.5})$$

combining C.4 and C.5

$$T_c(z) = \frac{fQ}{k_c A_c} z + T_{int} \quad (\text{C.6})$$

evaluating at $T_c(z = L_c) = T_2$ gives

$$T_2 = \frac{fQ}{k_c A_c} L_c + T_{int} \quad (\text{C.7})$$

The temperature distribution through the resistive layer is derived from:

$$\frac{\partial^2 T}{\partial z^2} + \frac{g}{k_r} = 0 \quad (\text{C.8})$$

which gives a parabolic distribution of the form

$$T_r(z) = c_1 z^2 + c_2 z + c_3 \quad (\text{C.9})$$

and

$$\frac{\partial^2 T}{\partial z^2} = 2c_1 \quad (\text{C.10})$$

but, from the governing equation

$$\frac{\partial^2 T}{\partial z^2} = -\frac{g}{k} = -\frac{Q}{k \cdot V} \quad (\text{C.11})$$

which gives

$$c_1 = -\frac{Q}{2k_r \cdot V} = \quad (\text{C.12})$$

simplifying

$$c_1 = -\frac{Q}{2k_r L_r A_r} \quad (\text{C.13})$$

c_2 can now be found using

$$\frac{\partial T_r}{\partial z} = 2c_1 z + c_2 \quad (\text{C.14})$$

applying boundary conditions

$$\frac{\partial T_r}{\partial z}(z=0) = \frac{q_2''}{k_r} = \frac{fQ}{k_r A_r} = c_2 \quad (\text{C.15})$$

c_3 can be found using using C.7 from above

$$T_r(z=0) = T_2 = \frac{fQ}{k_c A_c} L_c + T_{int} = c_3 \quad (\text{C.16})$$

combing C.13, C.15, and C.16

$$T_r(z) = -\frac{Q}{2k_r L_r A_r} z^2 + \frac{fQ}{k_r A_r} z + \frac{fQ}{k_c A_c} L_c + T_{int} \quad (\text{C.17})$$

evaluating at $T_r(z = L_r)$ gives

$$T_1 = -\frac{QL_r}{2k_r A_r} + \frac{fQL_r}{k_r A_r} + \frac{fQ}{k_c A_c} L_c + T_{int} \quad (\text{C.18})$$

The temperature distribution through the glass layer is derived from:

$$\frac{\partial^2 T}{\partial z^2} = 0 \quad (\text{C.19})$$

which gives a linear distribution of the form

$$T_g(z) = c_1 z + c_2 \quad (\text{C.20})$$

and

$$\frac{\partial T_g}{\partial z} = c_1 \quad (\text{C.21})$$

applying boundary conditions

$$\frac{\partial T_g}{\partial z}(z=0) = -q_2'' = -\frac{(1-f)Q}{k_g A_g} = c_1 \quad (\text{C.22})$$

$$T_g(z=0) = T_1 = -\frac{QL_r}{2k_r A_r} + \frac{fQL_r}{k_r A_r} + \frac{fQL_c}{k_c A_c} + T_{int} = c_2 \quad (\text{C.23})$$

inserting C.22 and C.23

$$T_g(z) = -\frac{(1-f)Q}{k_g A_g} z - \frac{QL_r}{2k_r A_r} + \frac{fQL_r}{k_r A_r} + \frac{fQL_c}{k_c A_c} + T_{int} \quad (\text{C.24})$$

evaluating at $T_g(z=L_g) = T_{surf}$ gives

$$T_{surf} = -\frac{(1-f)QL_g}{k_g A_g} - \frac{QL_r}{2k_r A_r} + \frac{fQL_r}{k_r A_r} + \frac{fQL_c}{k_c A_c} + T_{int} \quad (\text{C.25})$$

The solution to surface temperature is further simplified when

$$A_c = A_r = A_g = A \quad (\text{C.26})$$

giving

$$T_{surf} = -\frac{(1-f)QL_g}{k_g A} - \frac{QL_r}{2k_r A} + \frac{fQL_r}{k_r A} + \frac{fQL_c}{k_c A} + T_{int} \quad (\text{C.27})$$

and simplifying gives the final solution

$$T_{surf} = \frac{Q}{A} \left(-\frac{(1-f)L_g}{k_g} - \frac{L_r}{2k_r} + \frac{fL_r}{k_r} + \frac{fL_c}{k_c} \right) + T_{int} \quad (\text{C.28})$$

C.3 Determination of the Heat Loss Fraction

To determine the fractional heat loss downward through the heater, a simple 1-D calculation shows the heat flow by using a linear difference between the two thermocouples within the phenolic. These thermocouples, spaced 6.35 [mm] (0.25 [in.]) apart (z-direction), provide a basis for this analysis.

The values/properties needed for this analysis are:

1. phenolic thermal conductivity $k_{phen} = 0.29 \frac{W}{m-K}$
2. cross sectional area of phenolic base $A_{phen} = 13.51 in^2$ (.008716m²)
3. distance between thermocouples $\Delta z = 1/4''$ (.00635m)
4. downward temperature difference $\Delta T(C)$
5. total heat input $\dot{Q}(W)$

To generate a correlation between the heat loss fraction and the heat input, a steady state temperature difference must be found for each heat input. A baseline data set, terrestrial gravity, was used instead of flight test data because baseline data runs allowed the chamber to reach a near steady state condition, ΔT was plotted against time to determine steady state values for heater powers ranging from 0 – 120W (Figure C.3). Next, using equation C.29, an assumed downward heat loss was calculated for each steady state point, shown in Table C.2.

$$q'' = -k \frac{\Delta T}{\Delta z} \quad (C.29)$$

When $\dot{Q} = 0$, $d\Delta T \neq 0$, therefore a correction of .15°C was added to each ΔT in Table C.2. To generate a correlation between the heat input, Q , and the downward heat loss percentage f , they were plotted against each other to demonstrate a linear relationship, shown in Figure C.4.

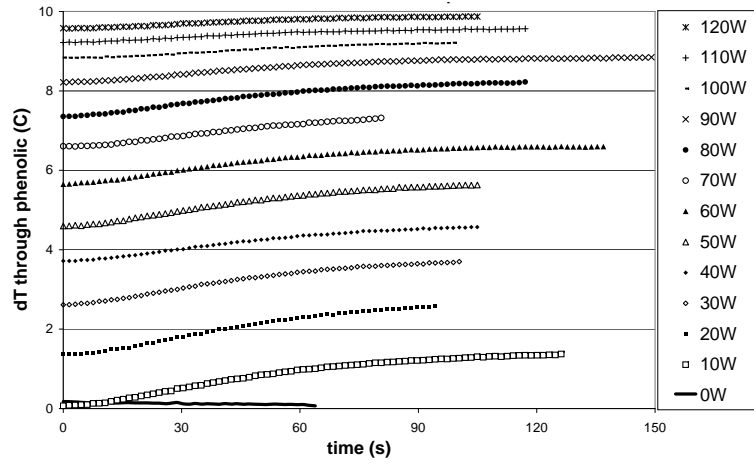
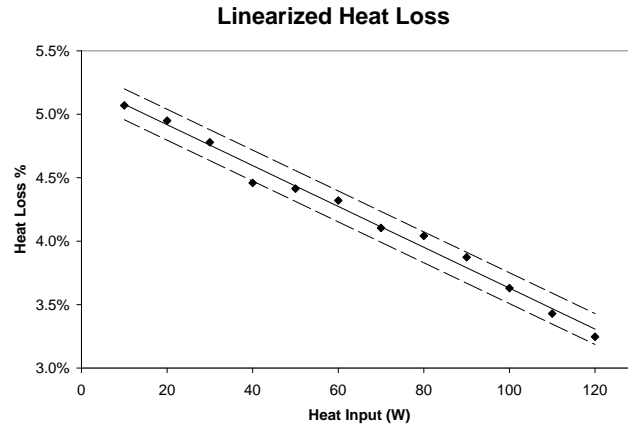


Figure C.3: Heat Loss Indicator (dT vs. time)

$Q_{input} (W)$	$\Delta T (^{\circ}C)$	$Q_{down} (W)$	$\%_{loss}$
0	.08		
10	1.27	.51	5.07%
20	2.49	.99	4.95%
30	3.60	1.43	4.78%
40	4.48	1.78	4.46%
50	5.54	2.21	4.41%
60	6.51	2.59	4.32%
70	7.22	2.87	4.10%
80	8.12	3.23	4.04%
90	8.76	3.49	3.87%
100	9.12	3.69	3.63%
110	9.48	3.77	3.43%
120	9.79	3.90	3.25%

Table C.2: Downward Heat Loss



Error band = 3 standard deviations = .122%

Figure C.4: Linear Correlation Between Total Heat and Downward Heat Loss

$$f = -.00016101\dot{Q}(W) + .05239716 \quad (C.30)$$

Equation C.30 can be applied to C.28 to give an estimation for T_{surf} .

Appendix D

Nondimensionalization

D.1 Nondimensional Heat Input

The terms used for non-dimensionalization for heat input were determined as follows:

$$b = \text{lengthscale} = \frac{W}{2} = \text{half width of heater}$$

$$A = W^2$$

$$g = \frac{Q}{V} = \frac{Q}{L_r A} = \frac{Q}{L_r W^2}$$

$$\Delta = \frac{L_r}{b} = \frac{2L_r}{W}$$

$$G = \frac{gb^2}{k_r(T_{sat} - T_{\infty,wall})} = \frac{Q\left(\frac{W}{2}\right)^2}{L_r W^2 k_r(T_{sat} - T_{\infty,wall})} = \frac{Q}{4L_r k_r(T_{sat} - T_{\infty,wall})}$$

The nondimensional heat input is:

$$G\Delta = \frac{Q}{4L_r k_r(T_{sat} - T_{\infty,wall})} \frac{2L_r}{W} = \frac{\frac{1}{2}Q}{k_r W(T_{sat} - T_{\infty,wall})}$$

D.2 Nondimensional Ratio of Inertia and Acceleration to Viscous Forces

Inertial Force:

$$F_{inertial} = \rho v^2 D^2$$

Gravitational Force:

$$F_{gravitational} = \rho a D^3$$

Viscous Force:

$$F_{viscous} = \mu v D$$

grouping

$$\frac{(F_{inertial})^{\frac{3}{4}} (F_{gravitational})^{\frac{1}{4}}}{F_{viscous}} \Rightarrow \frac{(\rho v^2 D^2)^{\frac{3}{4}} (\rho a D^3)^{\frac{1}{4}}}{\mu v D}$$

rearranging

$$\frac{\rho v^{\frac{1}{2}} D^{\frac{5}{4}} a^{\frac{1}{4}}}{\mu} \Rightarrow \left(\frac{\rho^2 v D^{\frac{5}{2}} a^{\frac{1}{2}}}{\mu^2} \right)^{\frac{1}{2}} \Rightarrow \left(\left(\frac{v^2}{aD} \right)^{\frac{1}{2}} \frac{\rho^2 D^3 a}{\mu^2} \right)^{\frac{1}{2}}$$

where

$$Fr = \frac{v^2}{aD} \quad \text{and} \quad Ga = \frac{\rho^2 D^3 a}{\mu^2}$$

therefore

$$\left(Fr^{\frac{1}{2}} Ga \right)^{\frac{1}{2}} = \left(\left(\frac{v^2}{aD} \right)^{\frac{1}{2}} \frac{aD^3 \rho^2}{\mu^2} \right)^{\frac{1}{2}}$$

D.3 Other Nondimensional Terms

The nondimensional temperature is:

$$\theta = \frac{(T - T_{\infty, wall})}{(T_{sat} - T_{\infty, wall})}$$

The Weber number is used as a nondimensional flow rate:

$$We = \frac{\rho v^2 D}{\sigma}$$

Appendix E

Procedures for Experimentation

E.1 FC-72 Fill Procedure

1. Start up the rig.
2. Before purging, the valve positions should be:
 - (a) drain closed
 - (b) toggle between normal flow and bypassed flow
 - (c) nozzle pump open
 - (d) toggle between bottom and top sump valves
 - (e) toggle between bottom and top nozzle
3. Purge the system: inlet nitrogen into drain/fill valve A near drain pump using tube A
4. Open drain/fill valve B for nitrogen exit.
5. Hook the roughing vacuum pump to the following locations using tube B:
 - (a) drain/fill valve A
 - (b) drain/fill valve B

(c) 3/8" 4-way joint connection on chamber

6. Turn the valves to the following positions:

- (a) drain open
- (b) toggle between top and bottom nozzle
- (c) top sump open
- (d) nozzle pump open
- (e) toggle between normal flow and bypass
- (f) bottom sump open
- (g) hand valves open

7. Turn on the roughing vacuum pump and let it run until most of the liquid is out of the system. Let it run overnight if need be. Close the hand valves and remove the roughing pump. For the rest of the valves, refer to the roughing pump valve positions.

8. Connect the turbo vacuum pump the same way the roughing pump was connected. Turn the pump on and press the start switch. Let the pump run until it's reading around 1×10^{-3} Torr.

9. Before filling, turn the valves to the following positions:

- (a) drain closed
- (b) bottom nozzle
- (c) top sump closed
- (d) nozzle pump open
- (e) bypass on
- (f) bottom sump closed
- (g) hand valves open

10. Close valve 3 and open valves 1, 2, and 4. Refer to Figure E.1 for valve clarification.

11. Turn the hot plate on high. As the FC-72 approaches its boiling point, turn the heater down to low.

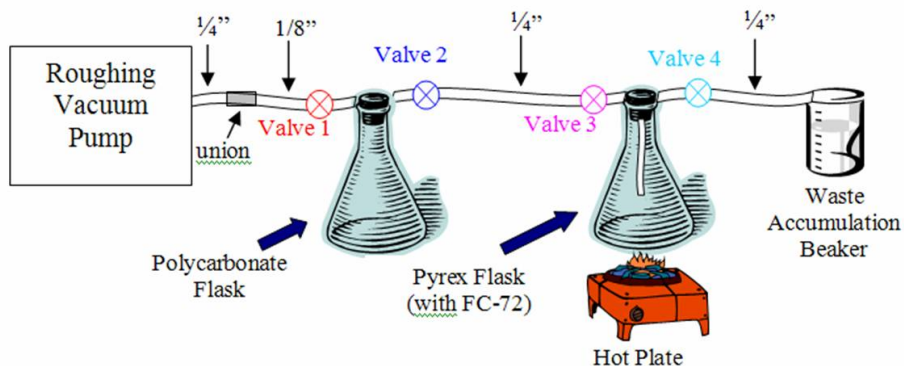


Figure E.1: Fill Procedure Setup/Schematic A

12. Boil the FC-72 for three minutes, then turn on the roughing pump. After boiling, turn off the hot plate.
13. Close valves 1 and 4. Open valve 3. Leave valve 2 as is. Turn off the roughing pump.
14. Allow the FC-72 liquid to siphon into the polycarbonate flask. Then, close valves 2 and 3. Open valve 4. This will prevent a pressure build up in the Pyrex flask
15. Using Figure E.2, connect the polycarbonate flask to the turbo pump and the top shelf of the rig.
16. Valve 1, valve 3, and the hand valve located below the drain/fill location should be closed. Valve 2 should be open. Turn the turbo pump on.
17. Close valve 2. Invert the polycarbonate flask. Open valve 1, valve 3, and the hand valve. FC-72 from the flask will begin to siphon into the system.
18. Once the FC-72 stops going in, close valve 1 and valve 3. Turn off the turbo pump, remove the tube assembly, and pour leftover FC-72 into the black FC-72 barrel.

E.2 Test Cards and Test Plan Matrix

Test cards, shown in Figure E.3, and the test plan matrix, shown in E.4; outline the format of the test plan and experimental operating conditions that will be targeted during experimental testing.

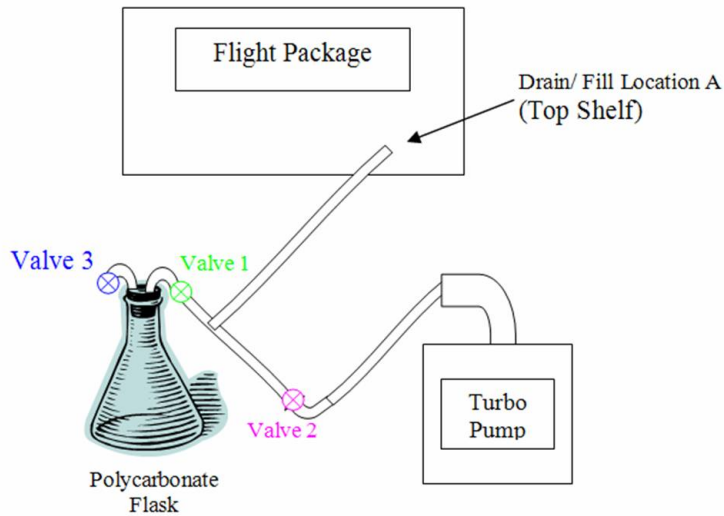


Figure E.2: Fill Procedure Setup/Schematic B

CARD NO: SPAR-1	RUN NO: Array-06192007-1	Variable Gravity Array Spray Cooling Experiment	
Operating Conditions 1. Flow rate (gph): 8, 10, 12 2. Subcooling (C): 15 3. Nozzle reheat (C): 25-30 4. Chamber pressure (psia): 8.5-9.0 5. Heat input range to CHF (W): 20-160 6. Working fluid: FC-72 7. Air content: ~10% 8. Saturation Temp (C): 42.5 9. _____ : _____ 10. _____ : _____			
Date: 19 June 07			
TEST POINT CONDITIONS			
1 st 10 Para	2 nd 10 Para	3 rd 10 Para	4 th 10 Para
Heater Power (W) 20-100 (8gph)	Heater Power (W) 120-CHF (8gph)	Heater Power (W) 20-100 (10gph)	Heater Power (W) 120-CHF (10gph)
5 th 10 Para	6 th 10 Para	2.0-g Turns	
Heater Power (W) 20-100 (12gph)	Heater Power (W) 120-CHF (12gph)	Heater Power (W) 1. 100-130 (8gph) 2. 120-150 (8gph) 3. 110-150 (10gph) 4. 140-147 (10gph)	
Flight Conditions			
Parabola# 1-57 + Turns		Acceleration (g) 0.001-2.0	
Flyers:			
	Name	Organization	
1.	Kirk Yerkes	AFRL/PRP	
2.	Rebekah Puterbaugh	AFRL/PRPS	
3.	Lt Chris Del La Pena	AFRL/PRPS	
RUN NO: Array-06192007-1 Flight Information Tail Number: N932NA Estimated Take-off time: 0930 Estimated Landing time: 1200 Estimated Flight time: 2.7 hr Estimated # of Parabolas: 57		Test Procedure Comments: 1. Each heat setting lasts 2-3 parabolas (typically 40 parabolas...if more, heat load steps and frequency are adjusted accordingly to CHF) 2. Multiple heat loads can be made during an extended 2.0-g turn 3. Hand recorded experimental data records are taken continuously to record parabola number, flow rate, heat load, etc.	
Responsible PI:		Classification	
TAA:		Data: Unclassified Video: Unclassified	

Figure E.3: Example Test Card

Proposed Test Plan Matrix June Flight Week-Array

	Flight 1 40-60 parabolas	Flight 2 40-60 parabolas	Flight 3 40-60 parabolas	Flight 4 40-60 parabolas
1. Heater orientation	Vertical			
2. Mass flow rate, (gal/hr)	8, 10, 12			
3. Heater power, W (run until steady periodic conditions satisfied)	0-160 (~ 2-20W increments)			
4. Subcooling	10°C	15°C	5°C	5-15°C
5. Vapor Sat. Temp. (°C)	30-60°C			

Figure E.4: Example Test Plan Matrix

E.3 Experimental Test Procedure

The Standard Operating Procedure (SOP), as outlined in Appendix E.3.1, for the test equipment is subdivided into six areas comprised of:

1. Loading checklist
2. Pre-test checklist
3. Testing checklist
4. Post-test checklist
5. Leak shut down procedure
6. Emergency shut down procedure.

NASA is responsible for proper mounting of the test equipment in the aircraft with assistance from Air Force personnel, as requested, to address specific experimental requirements. Prior to each series of experiments during a flight, the pre-test checklist is executed and the system air content is adjusted by either venting air into the system or by using a vacuum pump to extract the air from the system. Partial pressure calculations can be used

to quantify the air content in addition to the extraction of working fluid samples (refer to Appendix E.4) for post flight analysis of air content. In addition, prior to each flight the experiment is powered up to a standby mode allowing for the ice point reference to become temperature stabilized and to verify system conditions prior to flight. When possible, and with NASA permission, the experimental apparatus is allowed to remain in this standby mode to minimize the time required to initiate experiments during flight.

The experimental procedure is initiated once the aircraft reaches an appropriate altitude. This consists of mounting cameras, data laptop, and executing the testing checklist. Operation of the experimental apparatus requires a primary operator, back-up operator and data recorder, and support personnel to operate video recording apparatus and to serve as backup operators. Real time flight test data consisting of flow rates, three-axis accelerometers, heater temperatures, saturation pressure, flow system pressures, and heat loads are obtained with an integrated data acquisition system and laptop. Experiments are controlled manually by varying the heat load while maintaining flow rate and subcooling through a control panel affixed to the experiment. Hand recorded data, shown in Appendix E.3.3, consisting of critical flow rates and temperatures are also taken during the course of the experiment. When available, video is taken by using a high speed video system and digital cameras affixed to the experimental apparatus. Initially, the data acquisition system and video are time queued and allowed to remain on throughout the flight test.

A typical aircraft flight path will consist of multiple parabolas consisting of a reduced-g, high-g (1.8 g) portion, and an occasional turn (Since there are multiple experiments, the NASA pre-flight will stipulate the total parabola goal, range, and any experiment specific requirements during the flight, including high-g turns. This is repeated until the fuel reserve conditions are met.). The number of parabolas prior to a turn is determined by the wind, air traffic, and parabola type. During this flight path, the flight test will consist of varying the heat load in predetermined increments (Test Plan Matrix, Appendix E.2) over the course of a single or multiple parabola(s) until a steady-periodic condition is observed. At a fixed

heat load, the flow rate and subcooling is monitored and controlled as required to meet the pre-flight objectives. The heat load is increased until a CHF event occurs at which point the heat load is decreased and incrementally increased at a finer increment until another CHF event occurs. The number of heat load increments prior to a turn is approximated such that several parabolas prior to a turn a CHF event occurred. In this manner extended 2.0-g turns allow high-g data to be obtained at or near a CHF event.

At the conclusion of the experimental procedure, the post-test checklist is executed. Once the test equipment is shutdown, the cameras and data laptop are stowed appropriately for aircraft landing.

The air content of the system can be adjusted between flights, if needed, by executing the FC-72 Membrane Filter Procedure as outlined in Appendix E.5. This procedure is used to quickly adjust the air content an undetermined amount up or down. After such an adjustment, the Fluid Sample Extraction Procedure (Appendix E.4) is once again initiated.

E.3.1 Standard Operating Procedure

1. Loading Checklist

- (a) Verify that all mounting bolts are tight.
- (b) Verify power connections, 115 VAC 60 Hz.

2. Pre-test Checklist

- (a) Ascertain that the coolant and water systems are filled with sufficient liquids.
- (b) Plug in cords for the four AC circuits, 20 amp capacity for circuits 1 and 3 and 15 amp capacity for circuits 2, and 4.
- (c) Turn on Breakers 1, 2, 3 and 4, verify green indicators for each.
- (d) Verify that all toggle switches are in the off (down) position and all potentiometers are at 0 (fully counterclockwise).

- (e) Press the Start button and verify red indicators for the pumps and target heaters and red and blue indicators for the flow bypass.

3. Testing Checklist

- (a) Turn on the laptop computer, log in and start the data acquisition program.
- (b) Verify system pressures are appropriate for coolant temperature.
- (c) Turn on the water pump and set the flow rate as indicated on the computer display using the potentiometer; verify green indicator.
- (d) Turn on the coolant pumps and set the flow rates as indicated on the computer display using the potentiometers; verify green indicators and flow rate on the digital readouts.
- (e) Switch the bypass toggle switches to the up position and verify spray in the chamber.
- (f) Set the preheater PID controllers to the desired temperature and set the alarm cutout temperatures.
- (g) Switch the PID controllers on; verify green indicators.
- (h) When the fluids are at operating temperature, the preheater indicators will be cycling.
- (i) Verify that the over-temperature PID controller alarm settings are correctly adjusted.
- (j) Turn on the video cameras and place them in record mode.
- (k) Turn on the target heater switches and verify green indicators.
- (l) Set the target heater wattage using the potentiometers.
- (m) Take data as appropriate to the flight test plan.

4. Post-test Checklist

- (a) Switch off target heaters and set potentiometers to the 0 position.
- (b) Switch off preheater switches.
- (c) Switch bypass toggle switches to the down position.
- (d) Switch off all pumps and set potentiometers to the 0 position.
- (e) Switch off video cameras.

- (f) Stop data acquisition and shut down computer.
- (g) Switch off the four Breakers.

5. Leak Shut Down Procedure

- (a) Identify the location of the leak and use the pump to isolate FC-72 away from leak into either the chamber or the fluid reservoir and close the appropriate valves.
- (b) Hit Panic button to shutdown the system and allow the system to come to a low pressure equilibrium.
- (c) Assess source of leak for fixability. If fixable, (e.g., wrong valve is open), seal leak; otherwise.
- (d) Use either absorbent PIGs or Kimwipes to mop-up leak. Place wet materiel into zip lock baggie or vent tank.

6. Emergency Shut Down Procedure

- (a) Hit Panic button.
- (b) Ensure all power is off.
- (c) Visually verify and contain any leaks using absorbent PIGs or Kimwipes. Place wet materiel into zip lock baggie or vent tank.

E.3.2 Emergency Procedure

The fluid flow and heating power of the system will be shut off when the “Emergency Off” push-button switch on the right hand side of the control panel is depressed. Power will not be restored to the system until this switch is manually reset and the “Start” button is pressed.

All heater circuits are protected from an over-temperature situation with analog relays that have been calibrated to a defined temperature. In the event of a relay failure in a

valve arm back toward the hand drain (see Figure E.7). Unscrew the syringe and remove it from the three-way valve.

7. Return the nozzle flow switch on the control panel to normal flow.
8. Connect the syringe to the three-way valve on the Aire-ometer, shown in Figure E.8. Turn the blue three-way valve arm on the Aire-ometer toward the unused channel. The open line on the Aire-ometer is indicated by the green dot on the stopcock. The drain line is open when the green dot is pointed upwards, while the inlet line is open when the dot is pointed downwards. Open the drain line, which is attached to the calibrated goose neck.
9. Turn the hand crank in the counterclockwise direction, allowing the mercury to rise to the bottom of the stopcock. Place the stopcock in the horizontal, or closed, position.
10. Open the inlet line. Draw a sample of FC-72 by turning the hand crank clockwise. After drawing approximately 0.5 mL of fluid, open the drain line. The current sample has been exposed to air located in the inlet tube, and must be discarded. Turn the hand crank counterclockwise to return the mercury line to the bottom of the stopcock, removing the waste FC-72. Place the stopcock in the closed position, and then reopen the inlet line.
11. Turn the hand crank clockwise, drawing in FC-72 until the mercury level is approximately 1.3 cm below the 1 mL calibrated mark. Open the drain line. Turn the hand crank counterclockwise, bringing the mercury level up to the 1.0 mL mark. Close the stopcock. Read the pressure gauge, noting the reference pressure.
12. Turn the hand crank clockwise, bringing the mercury level down to 4.0 mL. Let the system equilibrate for 1 minute, then turn the hand crank counterclockwise until the pressure gauge is once again reading the reference pressure. Repeat step 12 two more times, ensuring all the air has been removed from the FC-72. When reading the manometer to determine the percentage of air present in the sample, the major graduations indicate 0.1 mL, or 10% increments, while the minor graduations indicate 0.02 mL, or 2% increments. Take the reading from the bottom of the FC-72 meniscus.
13. Open the drain line and turn the hand crank counterclockwise, returning the mercury level to the bottom of the stopcock. Place the stopcock in the horizontal position. For additional samples, repeat steps 11-13.

E.5 FC-72 Membrane Filter Procedure

1. See Figure E.9 for membrane filter set up and connection to flight package. On the membrane filter cylinder, the side labeled “Vacuum” should be connected to the

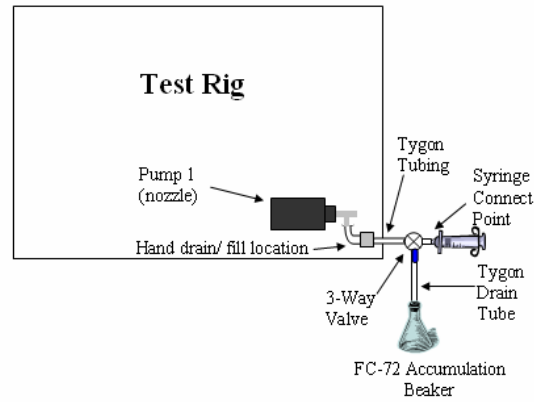


Figure E.7: Sample Extraction Schematic-A



Figure E.8: Aire-ometer used for measuring air content percentage.

roughing pump. The side labeled “In” should be attached to the hand drain/fill location on the bottom shelf of the rig, and the side labeled “Out” should be connected to the hand drain/fill location on the top shelf of the rig.

2. Start up the rig.
3. Rig Valve Positions:
 - (a) Drain Closed
 - (b) Bottom Nozzle
 - (c) Top Sump Closed
 - (d) Nozzle Pump Open
 - (e) Normal Flow
 - (f) Bottom Sump Open
4. Turn on Pump 1 (nozzle) and Pump 3 (scav).
5. Turn on the roughing pump.
6. Open the plug valves attached to the membrane filter.
7. Open the flow valves on the rig, located below the hand drain/fill locations.
8. To read the flow rate, use the drain flow rate reading as well as the nozzle flow rate reading.

E.6 Heater Replacement Procedure

Items needed:

1. Combination wrenches $7/8''$, $13/16''$, $1/2''$, $9/16''$, $7/16''$
2. Allen wrench $5/32''$
3. Gaffers tape
4. Phillips screwdriver

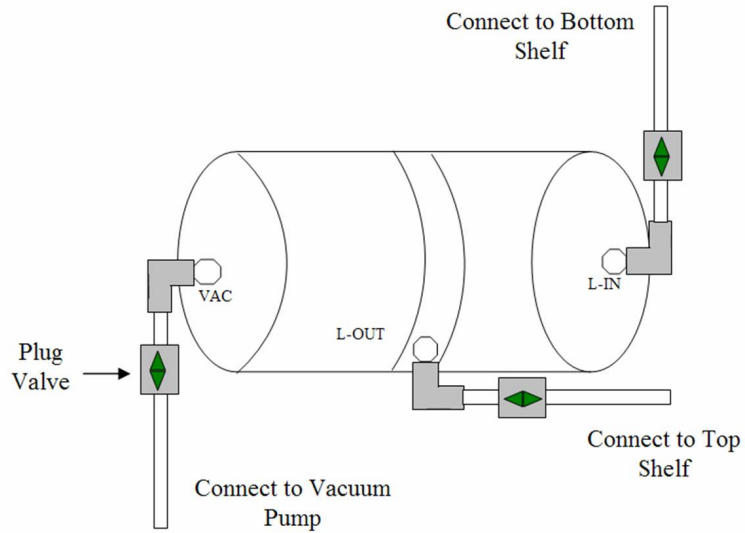


Figure E.9: Membrane Filter Diagram

5. Small flat screwdriver
6. Replacement heater
7. Exacto knife
8. High temp. solder
9. Soldering Flux
10. Q-tips
11. High heat soldering iron
12. Nickel strap (.004" x .125", x 3")
13. High temp. RTV silicon
14. Vacuum grease
15. Plugs 1/2"x2
16. Plug 1/4"
17. Heater set screws x4

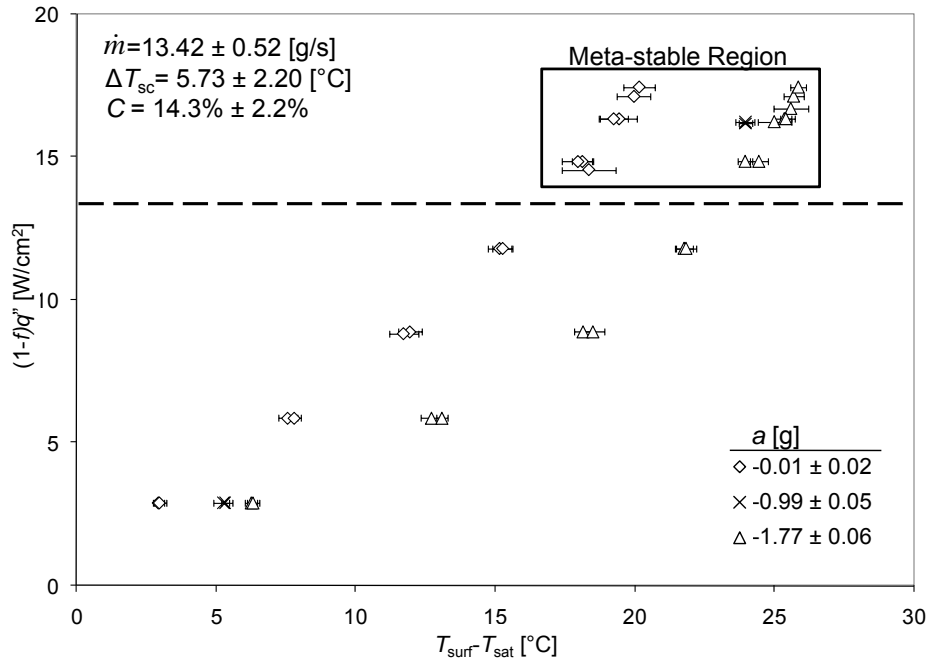
Procedure

1. Unbolt the heater unit from the flight package and disconnect the thermocouples attached to the heater unit.
2. Turn the valves to the following positions:
 - (a) drain closed
 - (b) array nozzle closed
 - (c) top sump closed
 - (d) nozzle pump closed
 - (e) normal flow on
 - (f) bottom sump closed
3. Cap off the nozzle inlet and outlets on the heater unit.
4. Remove heater unit from the flight package and place on a bench top.
5. Disassemble array chamber and disconnect power leads on the heater array.
6. Remove heater by cutting away the RTV silicon carefully in order to not harm the thermocouples underneath heater. Clean off excess RTV silicon from the heater.
7. Solder new connections for replacement heater's power leads.
8. Position four screws near each corner of the replacement heater and reapply RTV silicon. Remove the four screws after the RTV silicon is reapplied.
9. Reconnect the new heater's power leads.
10. Reassemble array block together and apply a new layer of vacuum grease along groove in array chamber.
11. Reinstall the heater unit to the flight package, reconnecting the inlet and outlet leads.
12. Connect membrane filter and pump/remove air from the heater system. See FC-72 Filter Membrane Procedure.

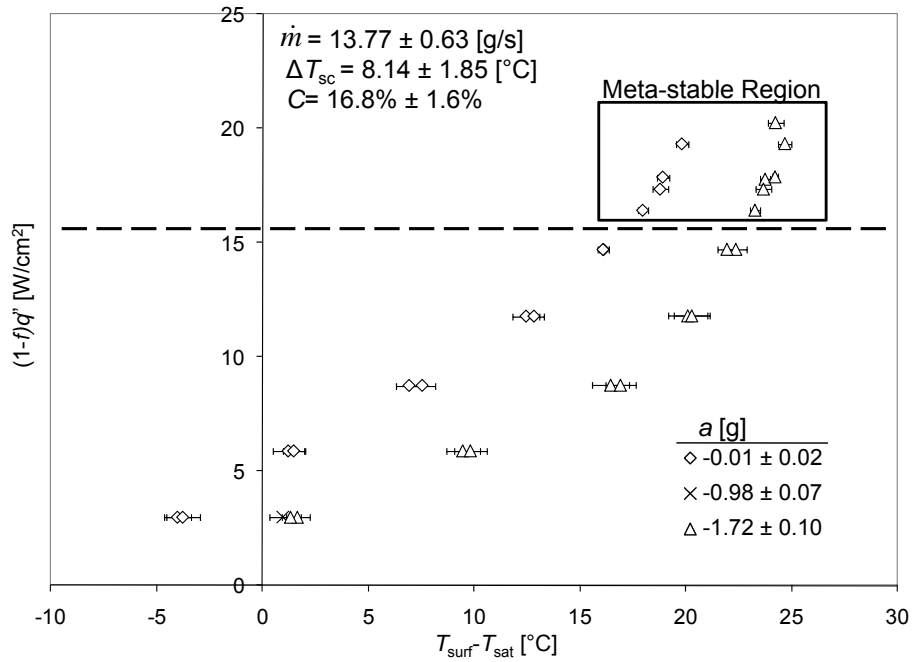
Appendix F

Additional Experimental Plots

The following plots are very similar to those found in Chapter 1.3, but were not included to minimize main body length.



(a)



(b)

Note: Only steady-state data points are shown. CHF occurred at gravitational transients for heat fluxes above dotted line.

Figure F.1: Meta-Stable CHF Regions, Heat Flux Input vs. Surface Temperature Difference: (a) Cases 45-47; (b) Cases 69-72.

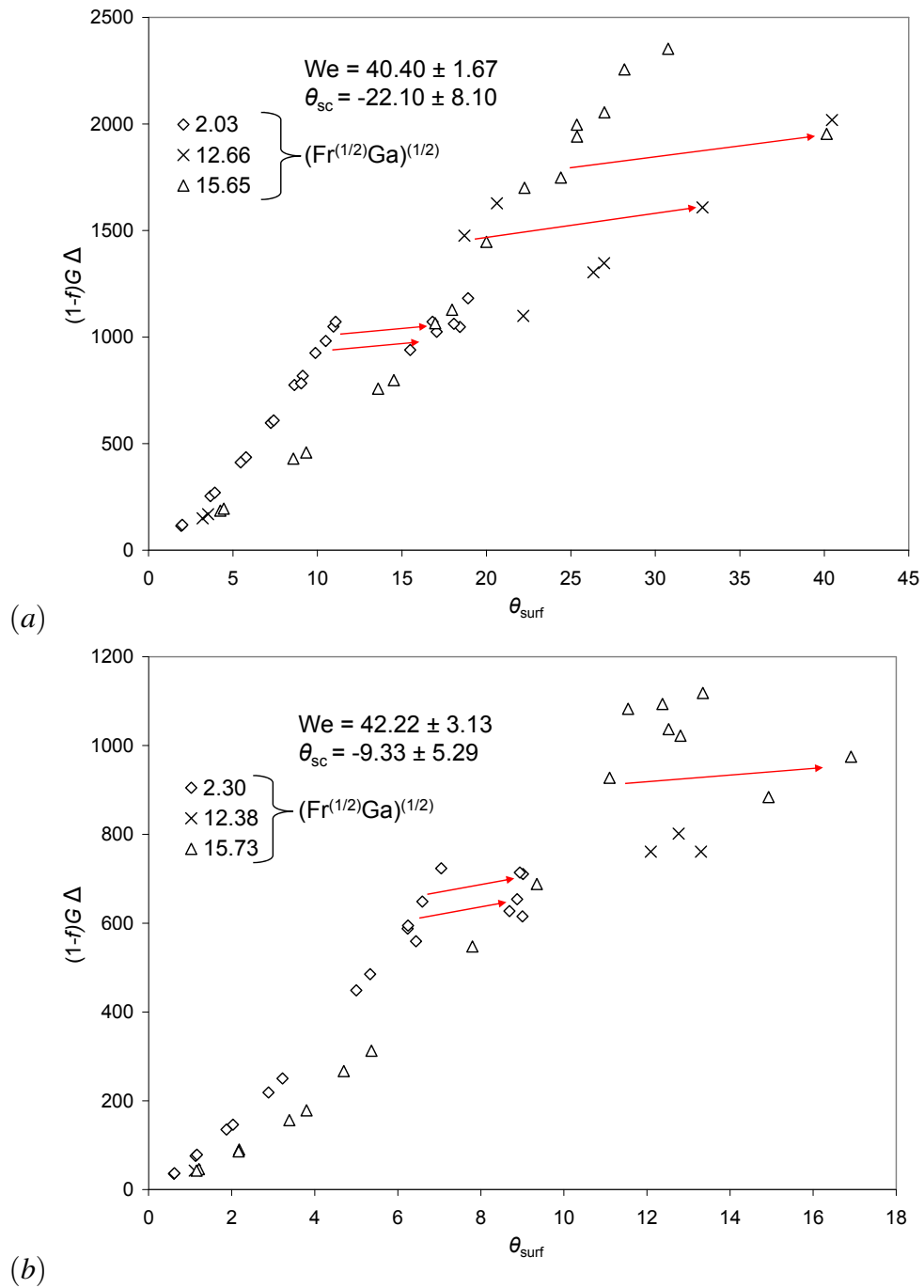


Figure F.2: Meta-Stable CHF Regions, Dimensionless Heat Flux Input vs. Dimensionless Surface Temperature Difference: (a) Cases 45-47; (b) Cases 69-72.

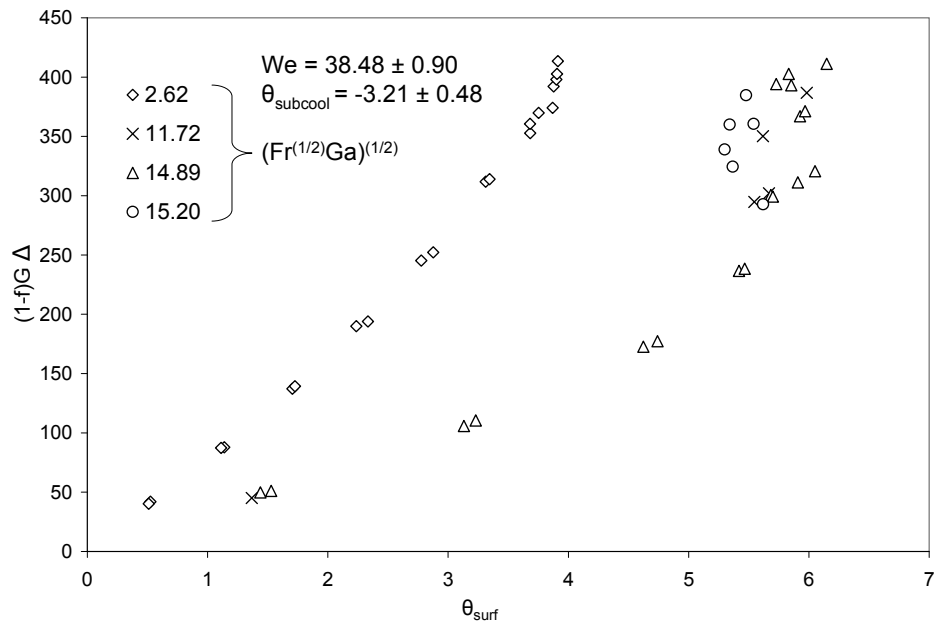
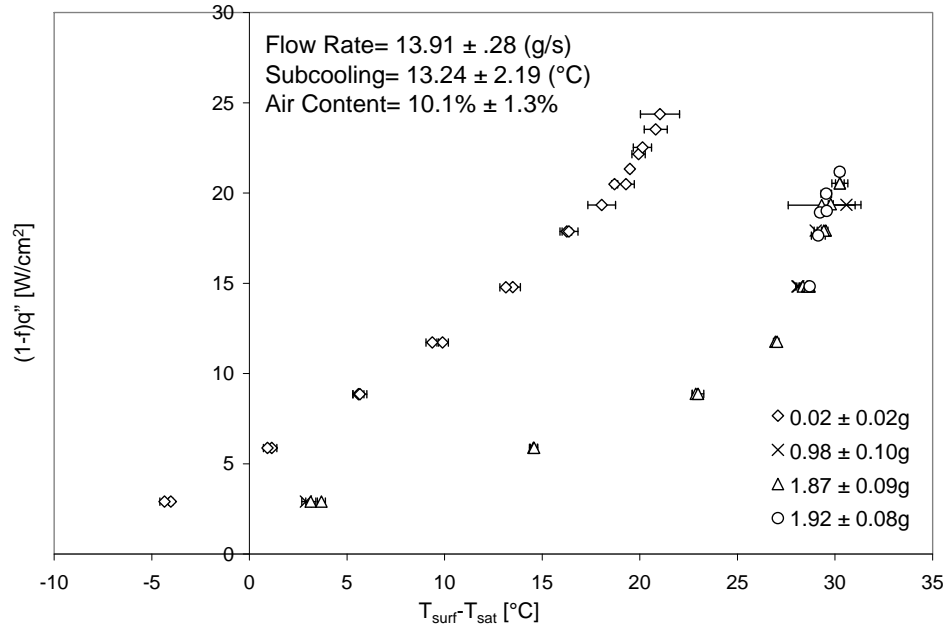


Figure F.3: Dimensional and Non-dimensional Steady State Heat Flux Transferred to Spray for Micro, Terrestrial and Elevated Gravity for Cases 01-04

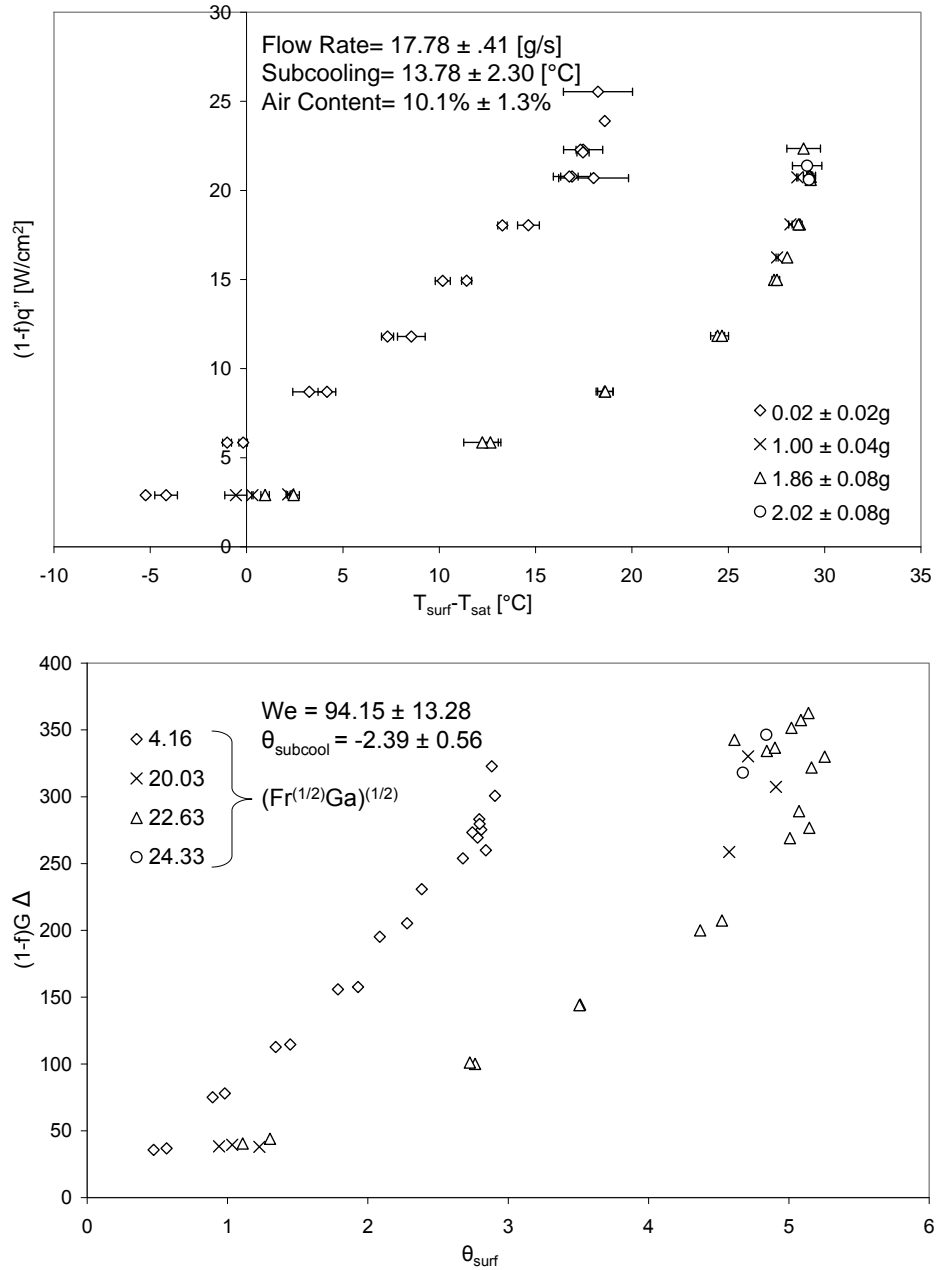


Figure F.4: Dimensional and Non-dimensional Steady State Heat Flux Transferred to Spray for Micro, Terrestrial and Elevated Gravity for Cases 05-08

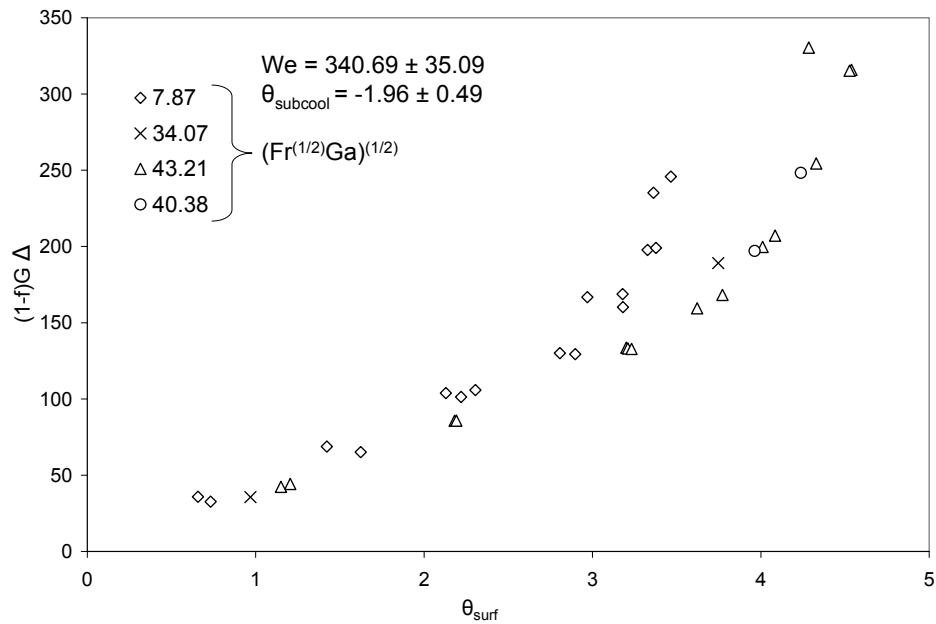
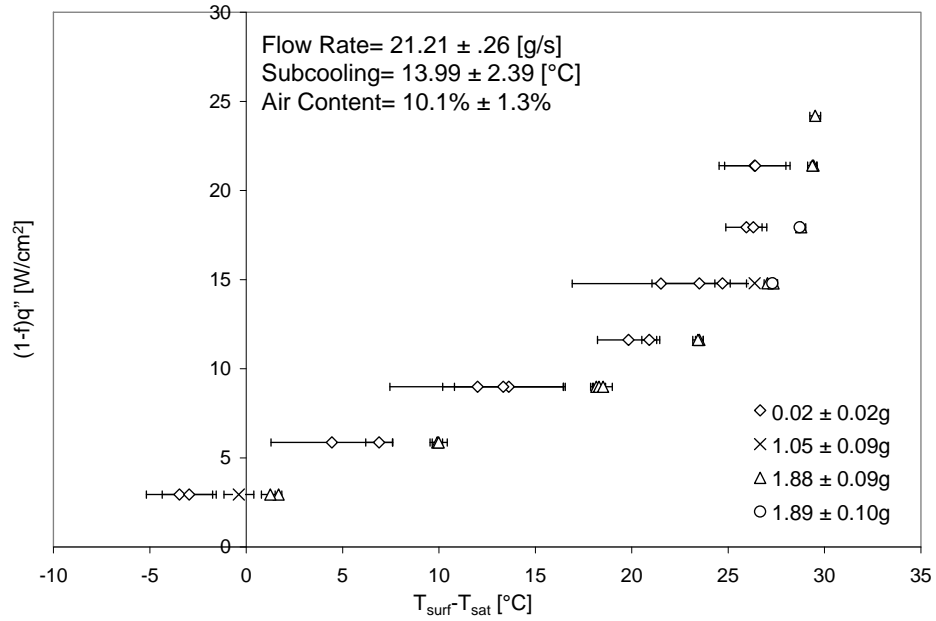


Figure F.5: Dimensional and Non-dimensional Steady State Heat Flux Transferred to Spray for Micro, Terrestrial and Elevated Gravity for Cases 09-12

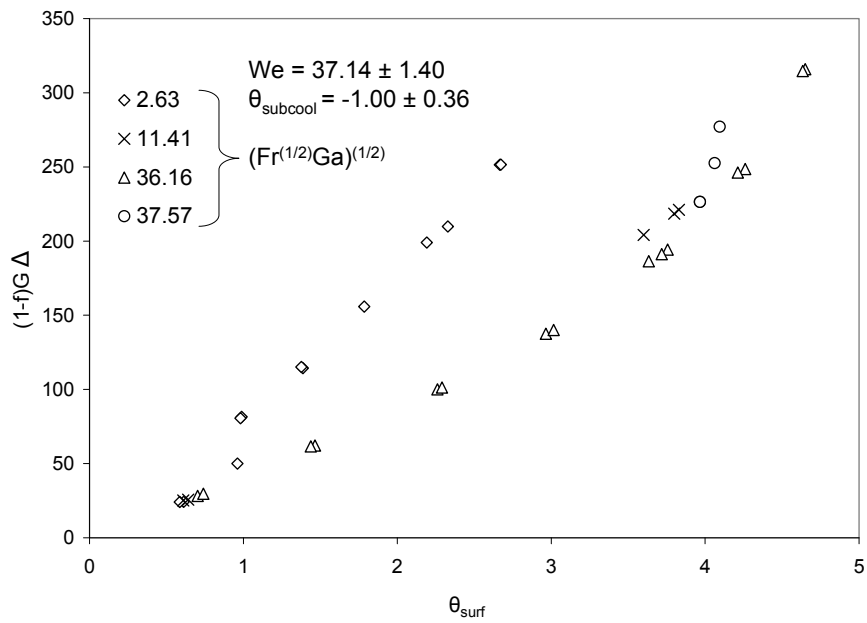
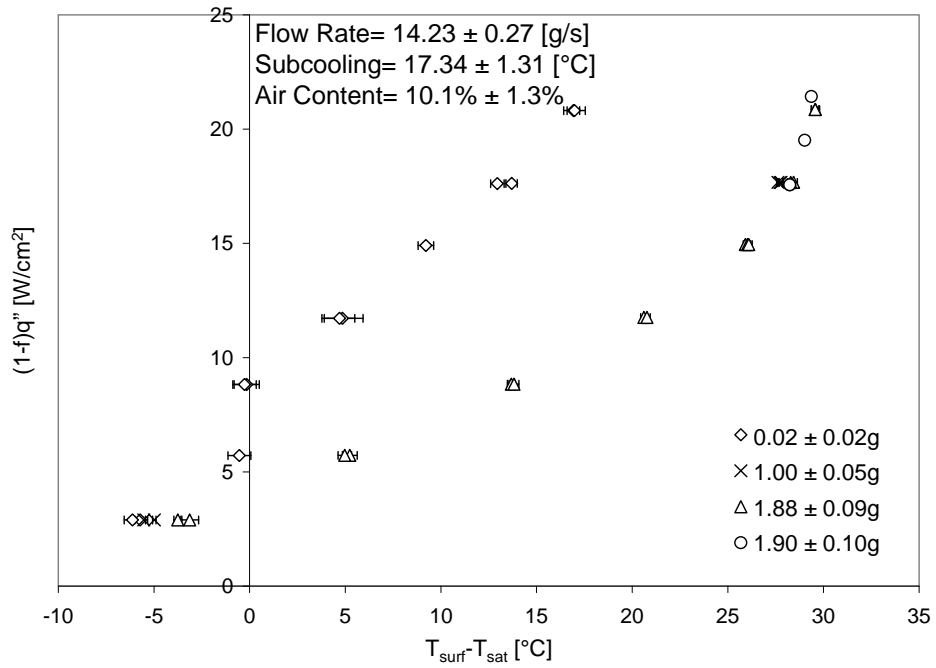


Figure F.6: Dimensional and Non-dimensional Steady State Heat Flux Transferred to Spray for Micro, Terrestrial and Elevated Gravity for Cases 13-16

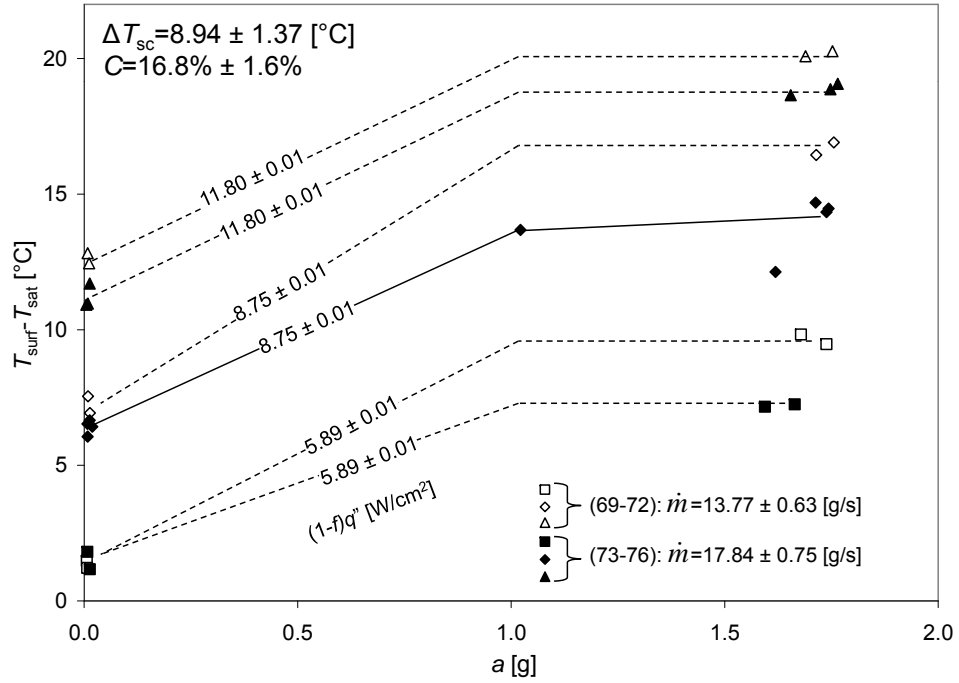
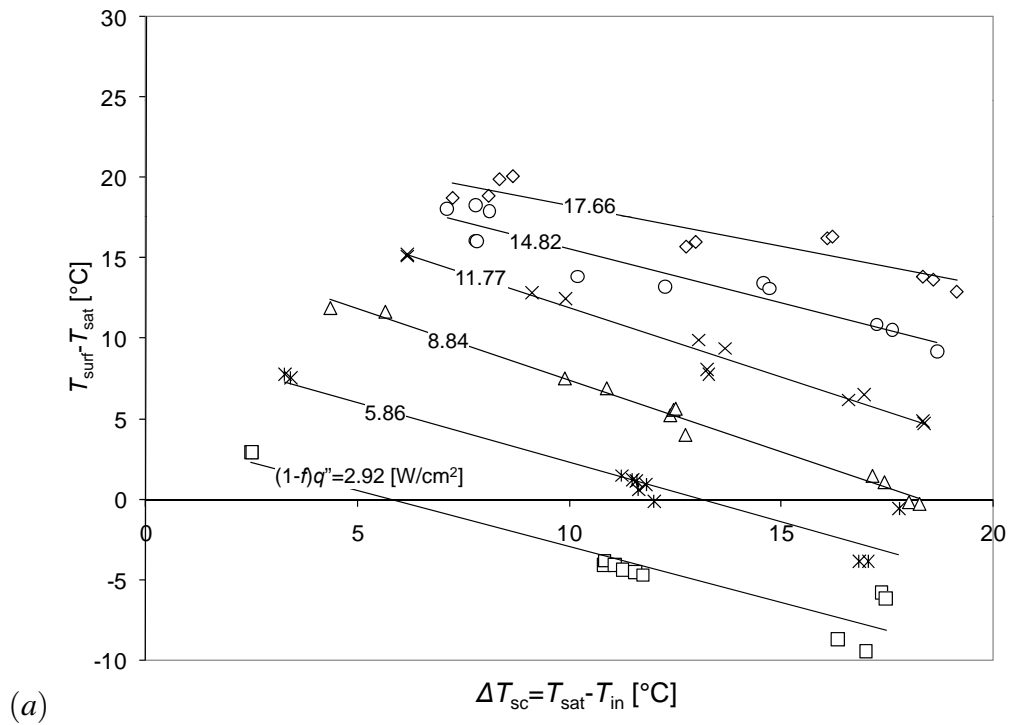
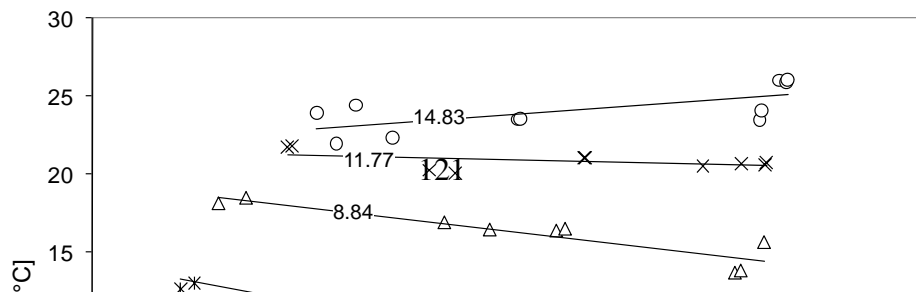
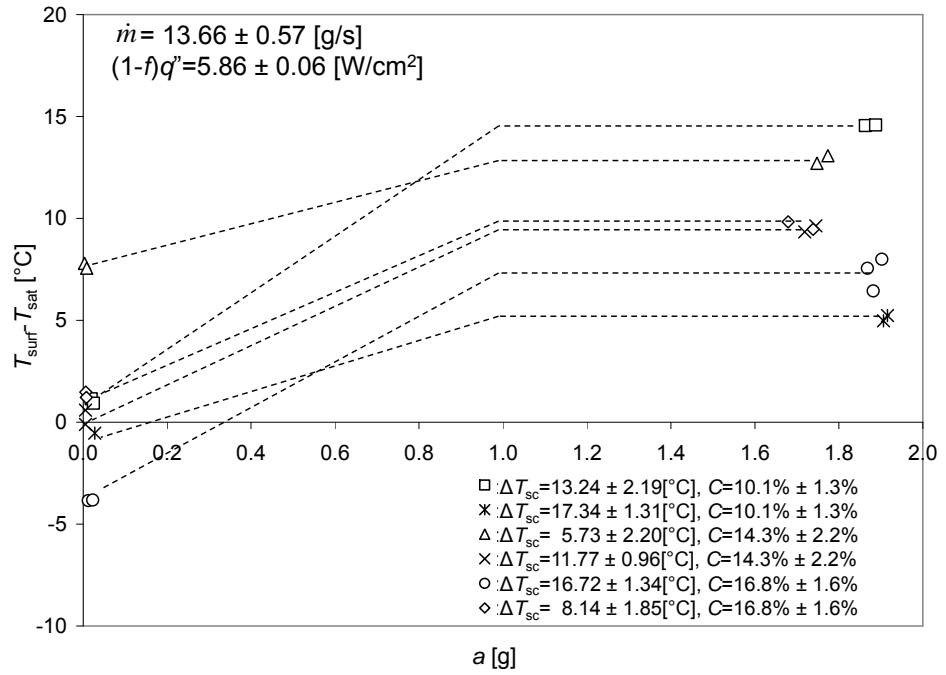


Figure F.7: Effect of Acceleration and Flow Rate on the Surface Temperature Difference ($\Delta T_{sc} = 8.94 \pm 1.37 \text{ [}^\circ\text{C]}$).

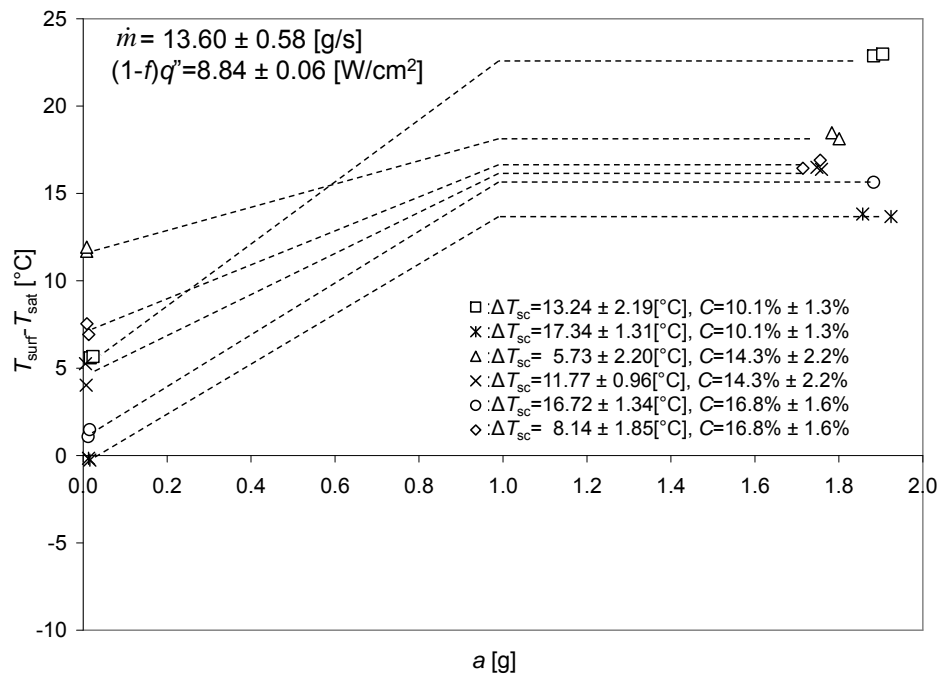


(a)



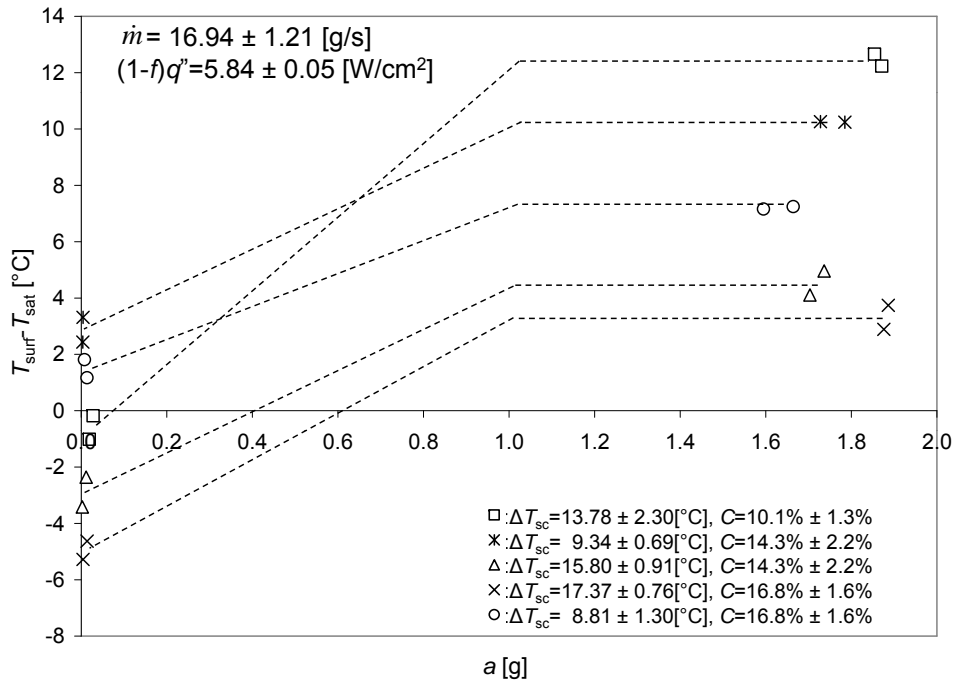


(a)

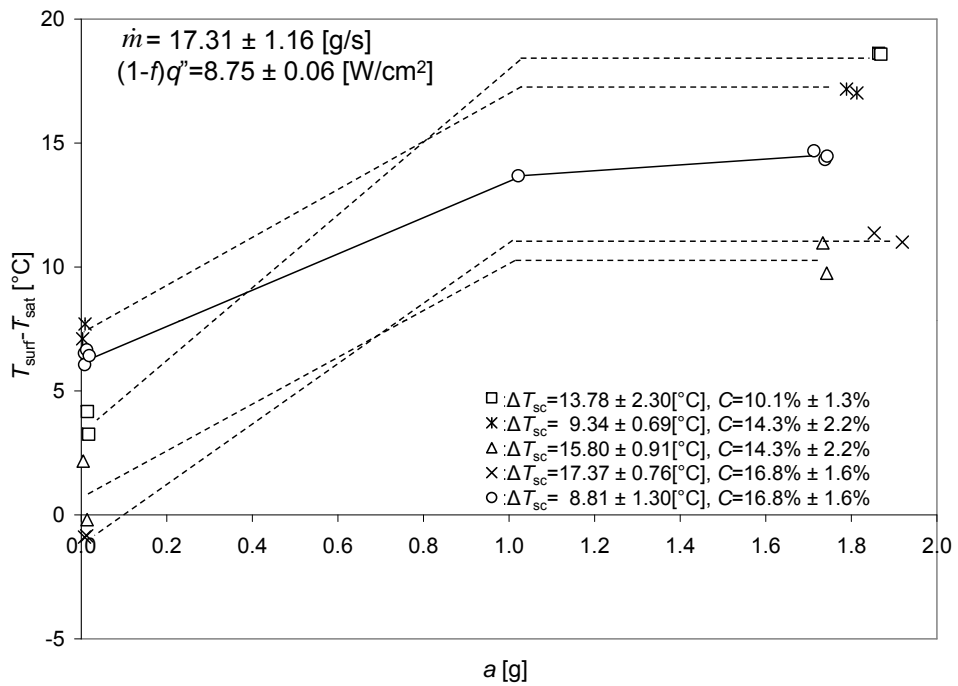


(b)

Figure F.8: Effect of Subcooling on Cooling Performance: (a) $\dot{m} = 13.66 \pm 0.57$ [g/s]; (b) $\dot{m} = 13.60 \pm 0.58$ [g/s].

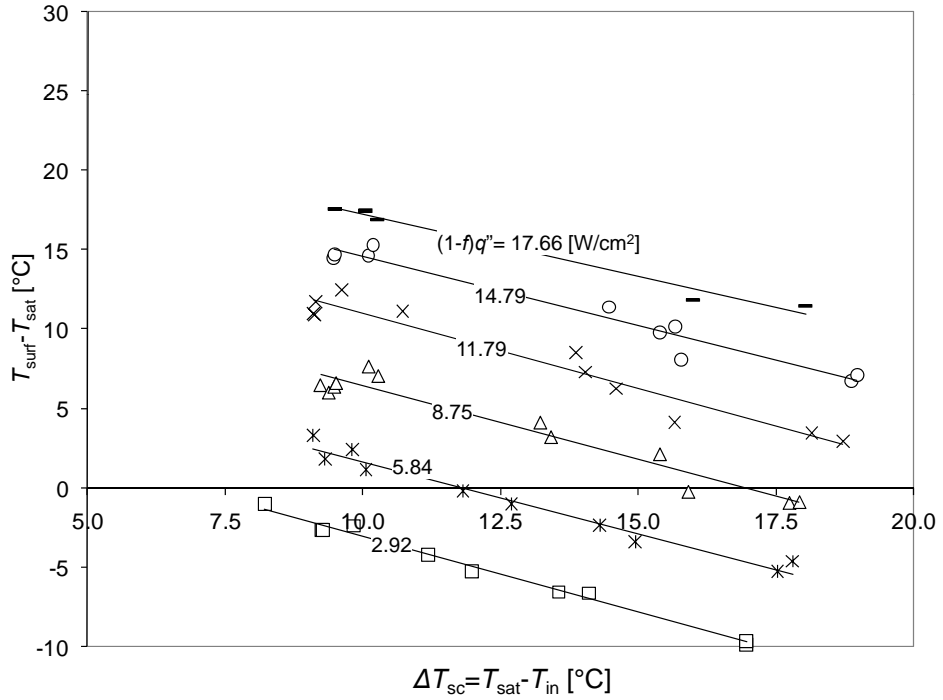


(a)

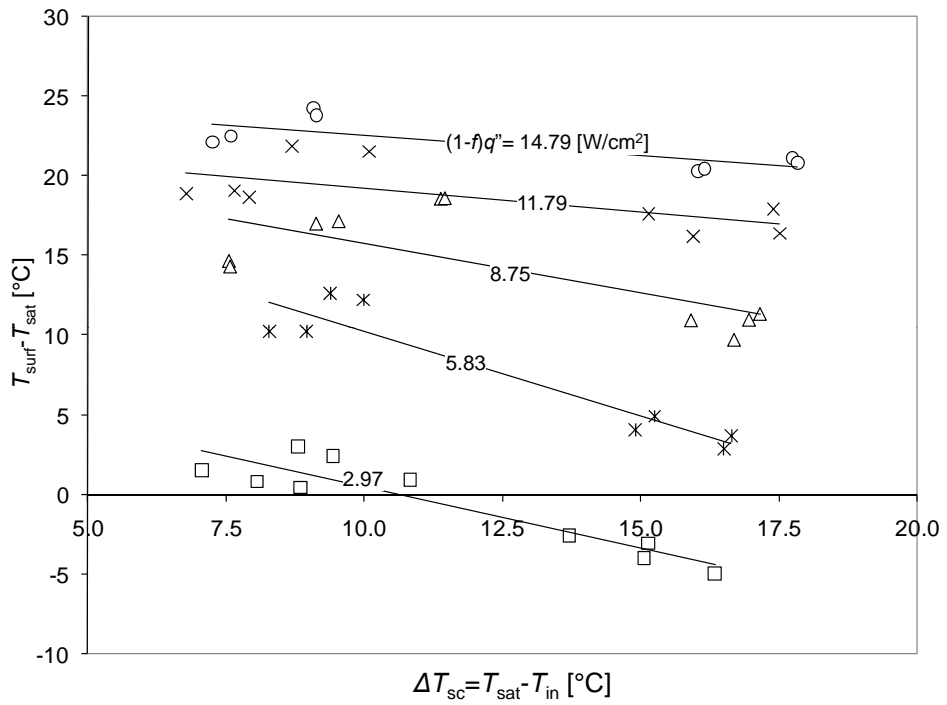


(b)

Figure F.9: Effect of Subcooling on Cooling Performance: (a) $\dot{m} = 16.94 \pm 1.21$ [g/s]; (b) $\dot{m} = 17.31 \pm 1.16$ [g/s].



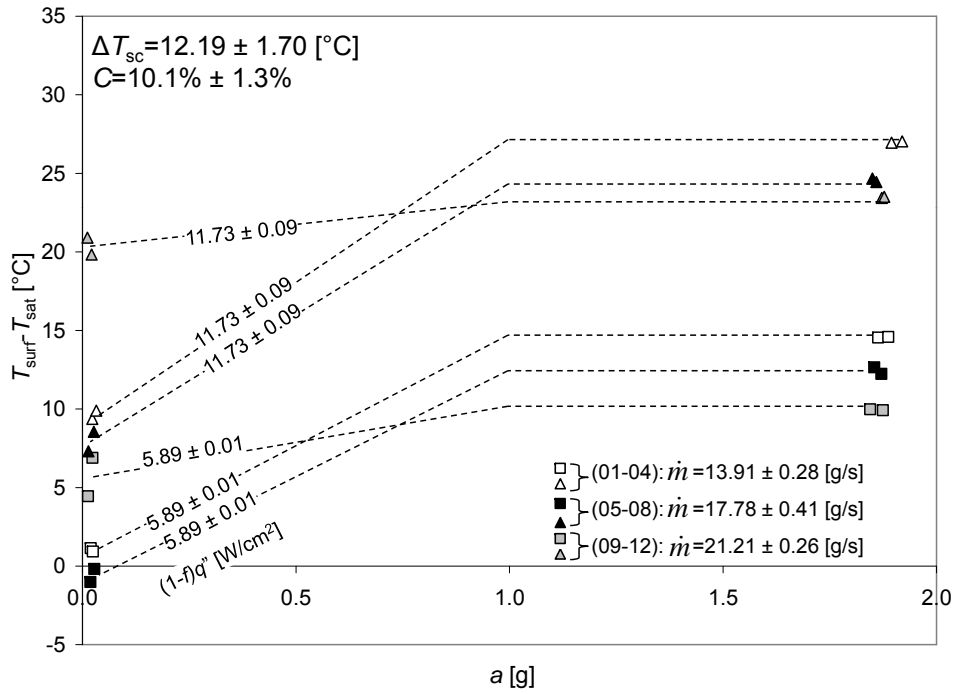
(a)



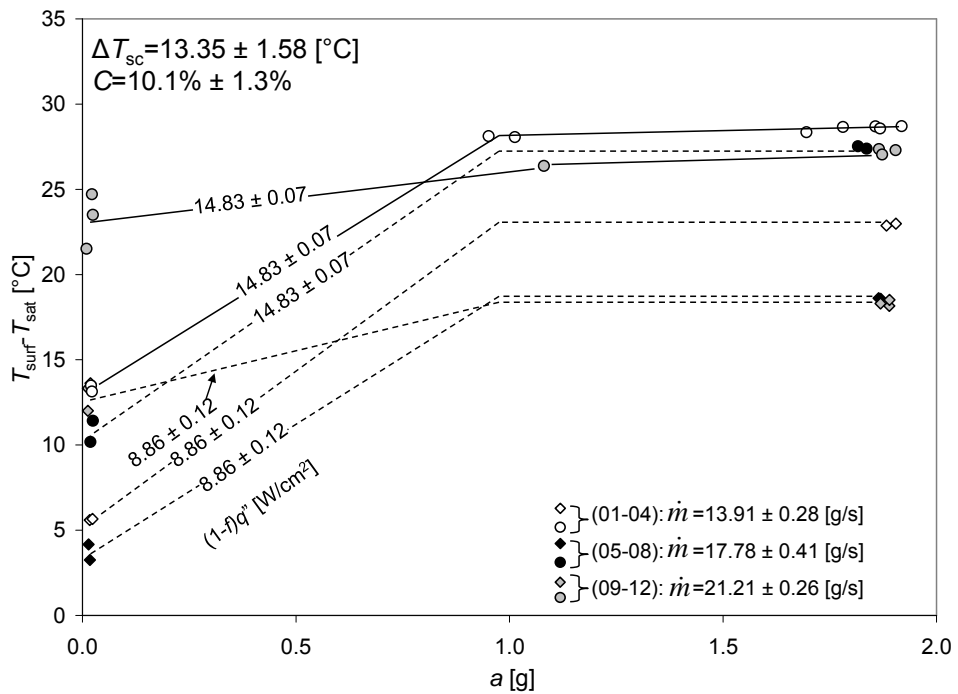
(b)

Note: Above data contains information with $C = 10.1\%$, 14.3% , and 16.8% .

Figure F.11: Variation of Surface Temperature Difference with Subcooling ($\dot{m} = 17.29 \pm 1.22$ [g/s]): (a) $a = 0.01 \pm 0.01$ [g]; (b) $a = 1.79 \pm 0.08$ [g].

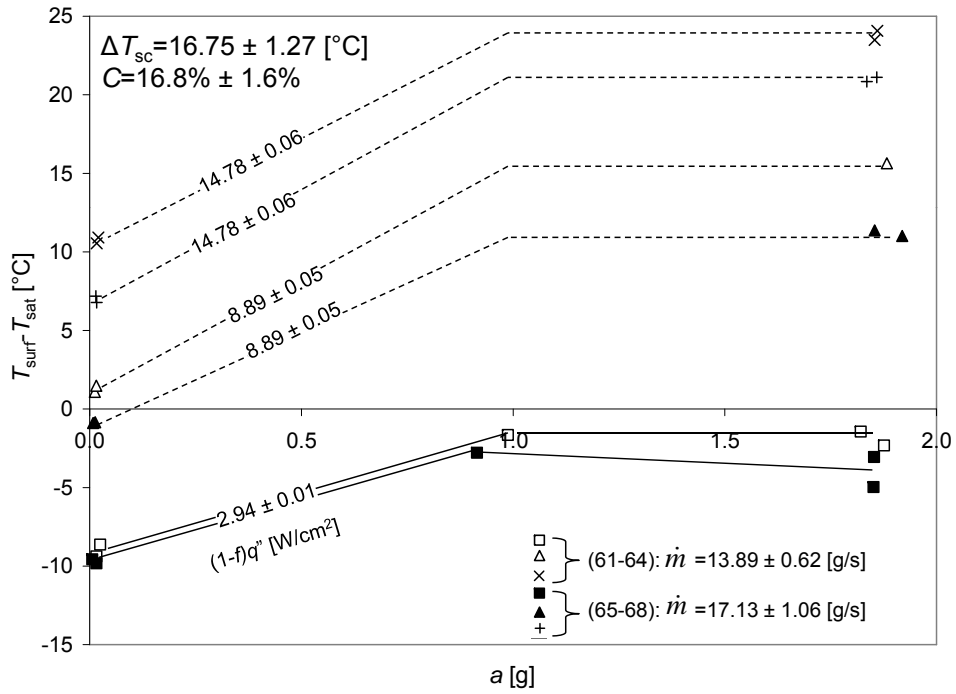


(a)

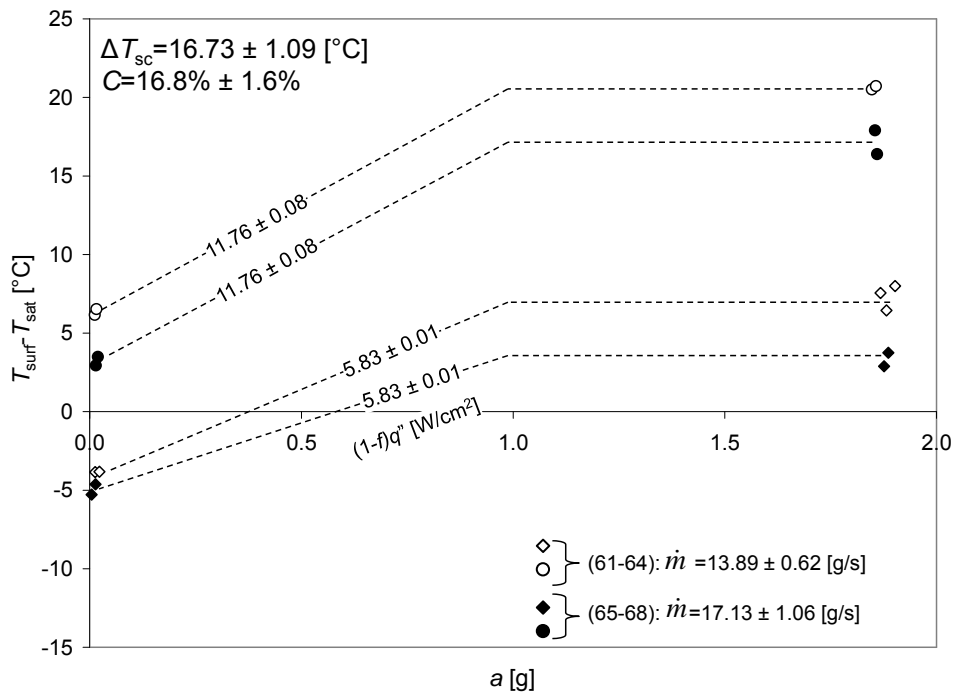


(b)

Figure F.12: Effect of Acceleration and Flow Rate on the Surface Temperature Difference: (a) $\Delta T_{sc} = 12.19 \pm 1.70 \text{ [}^\circ\text{C]}$; (b) $\Delta T_{sc} = 13.35 \pm 1.58 \text{ [}^\circ\text{C]}$.



(a)



(b)

Figure F.13: Effect of Acceleration and Flow Rate on the Surface Temperature Difference: (a) $\Delta T_{sc} = 16.75 \pm 1.27 [^{\circ}\text{C}]$; (b) $\Delta T_{sc} = 16.73 \pm 1.09 [^{\circ}\text{C}]$.

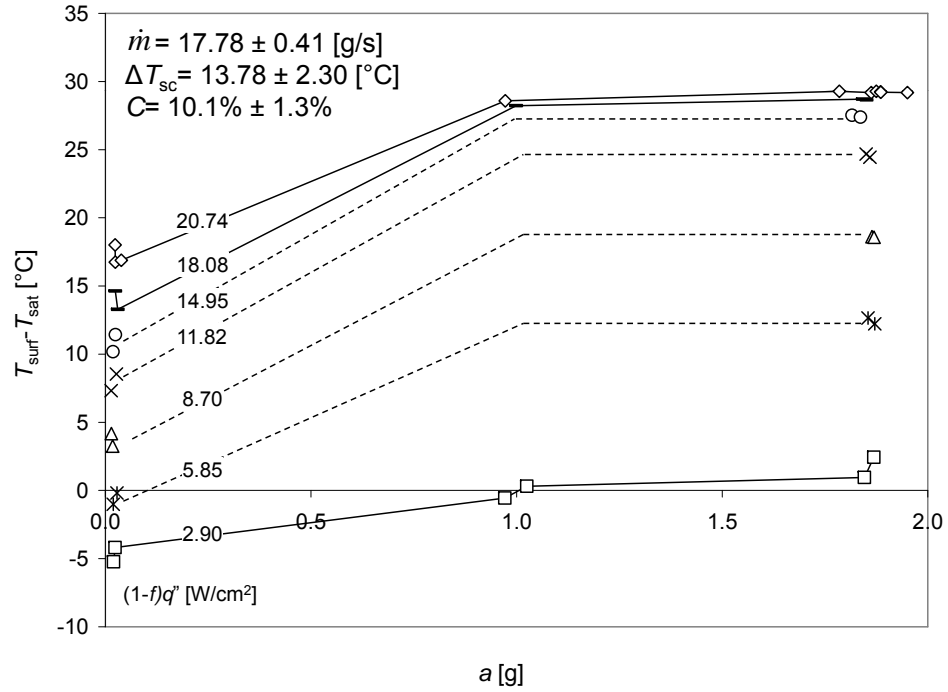
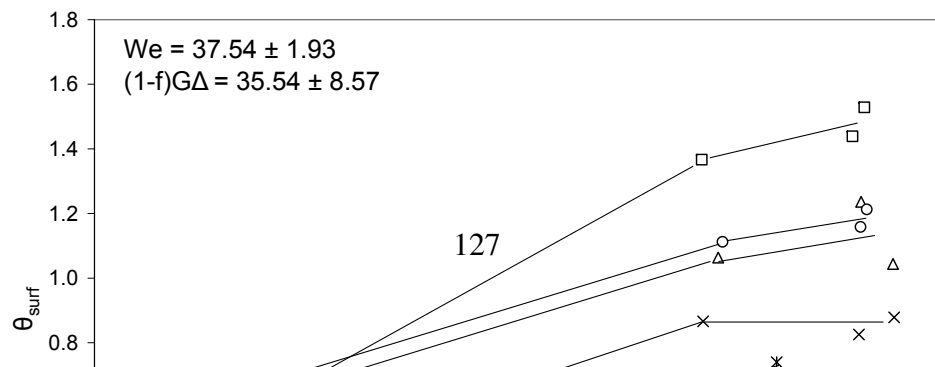
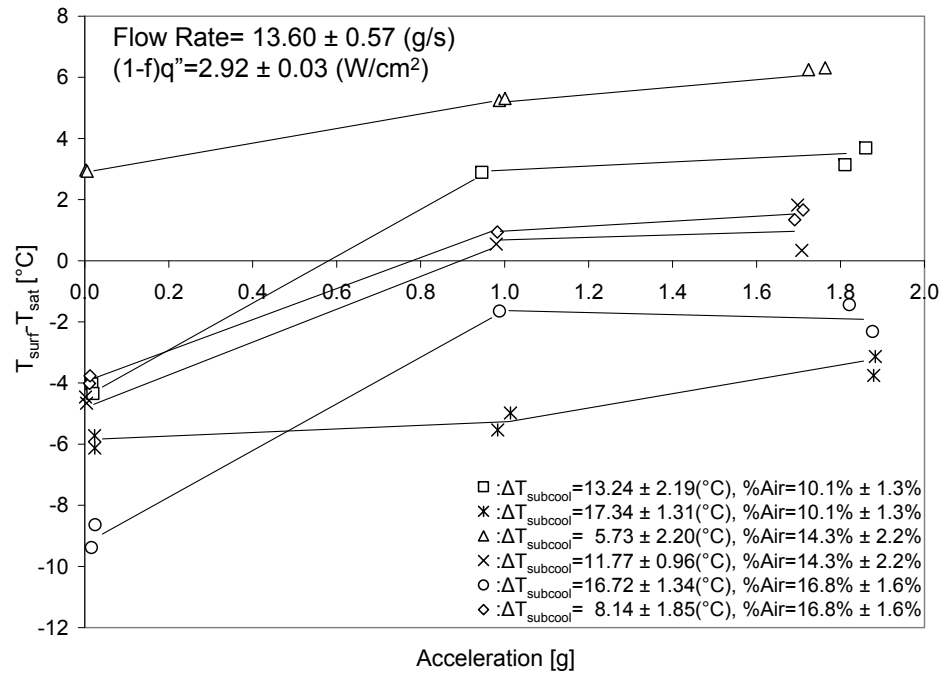


Figure F.14: Surface Temperature Difference vs. Acceleration.



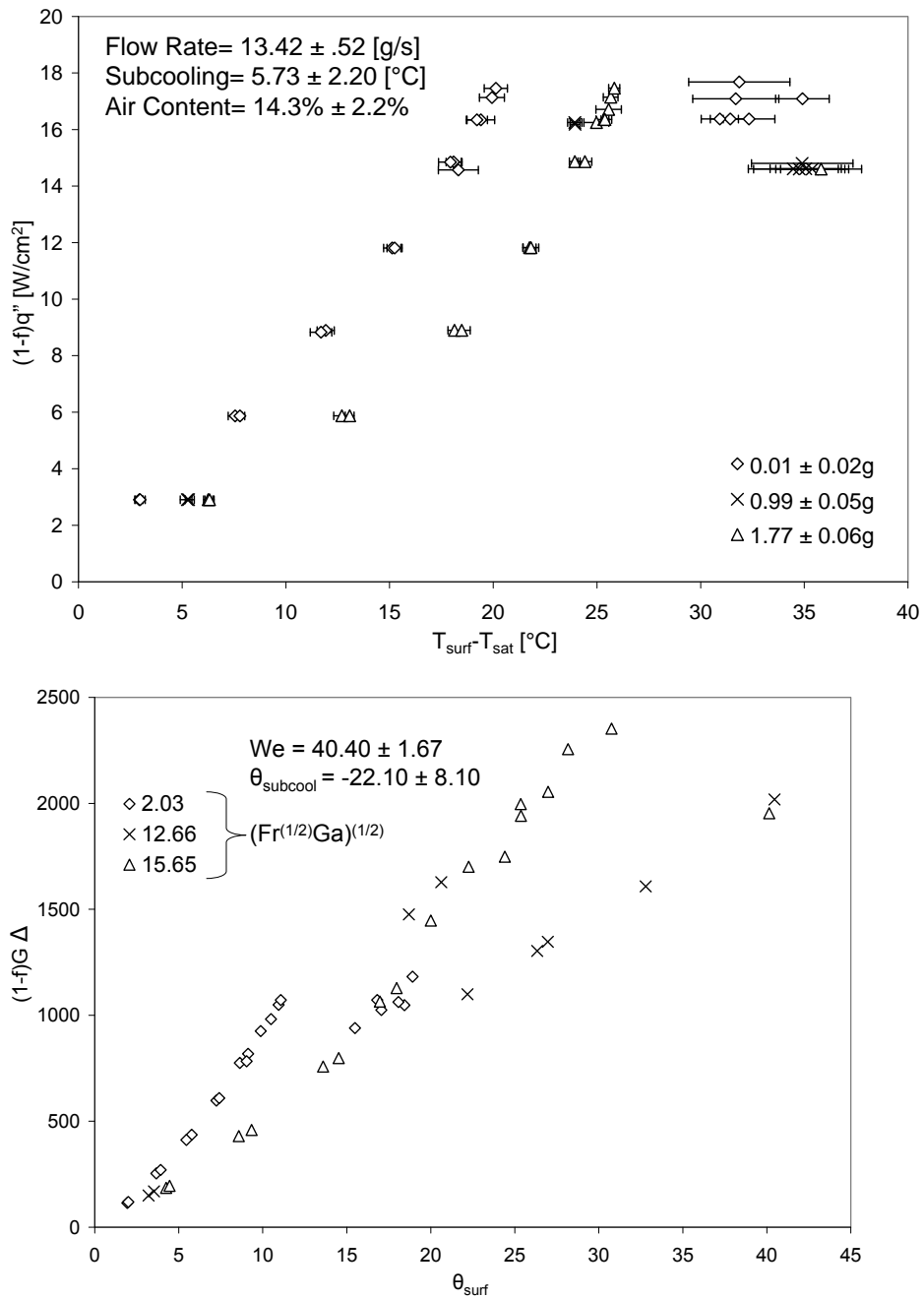


Figure F.15: Dimensional and Non-dimensional Steady State Heat Flux Transferred to Spray for Micro, Terrestrial and Elevated Gravity for Cases 45-47

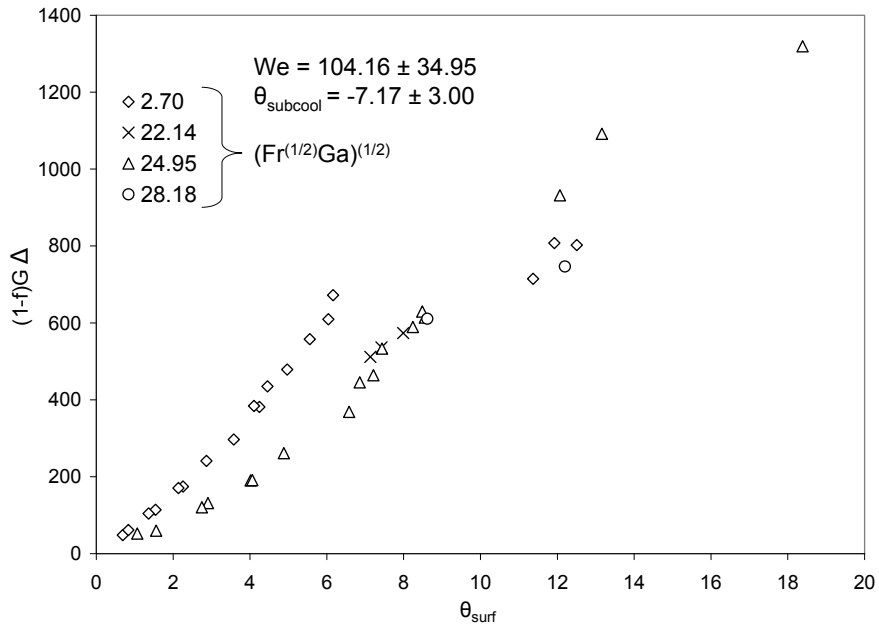
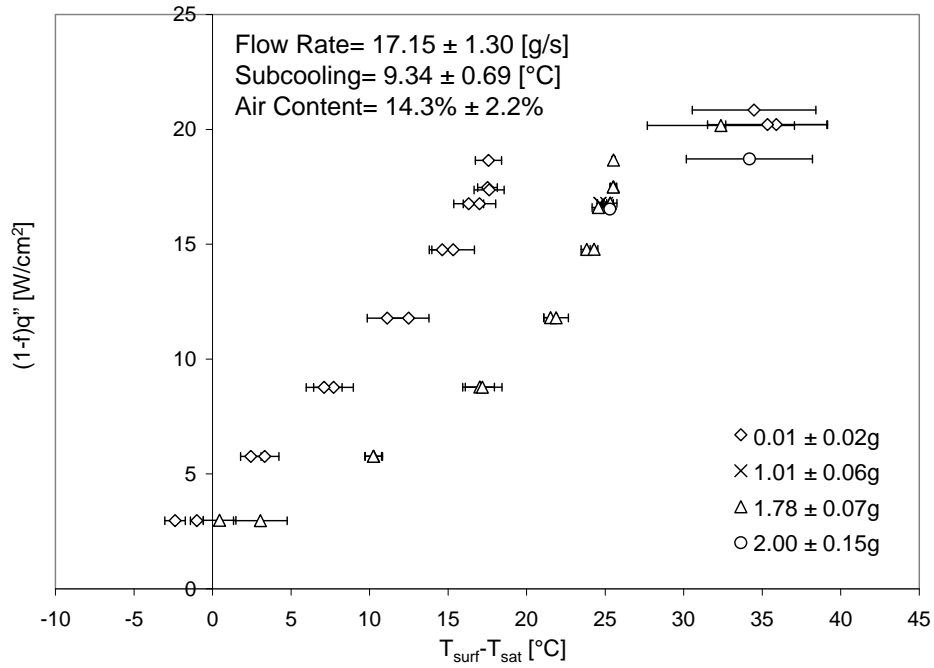


Figure F.16: Dimensional and Non-dimensional Steady State Heat Flux Transferred to Spray for Micro, Terrestrial and Elevated Gravity for Cases 49-52

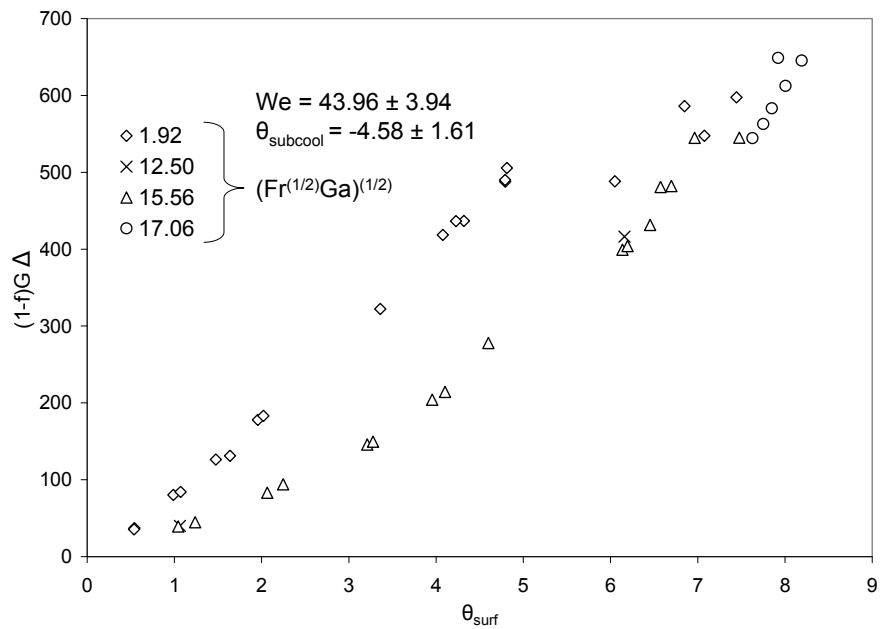
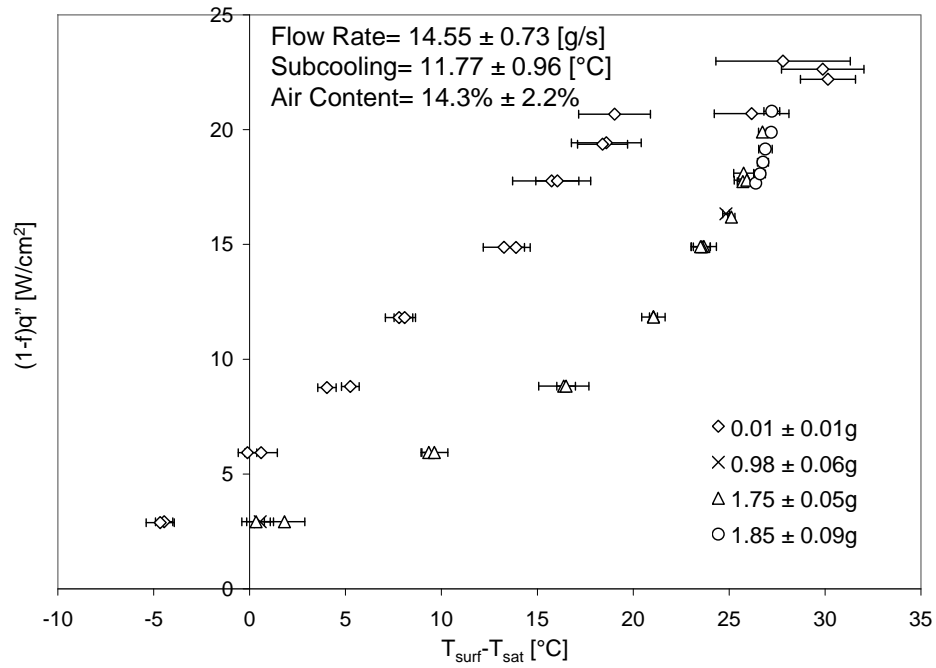


Figure F.17: Dimensional and Non-dimensional Steady State Heat Flux Transferred to Spray for Micro, Terrestrial and Elevated Gravity for Cases 53-56

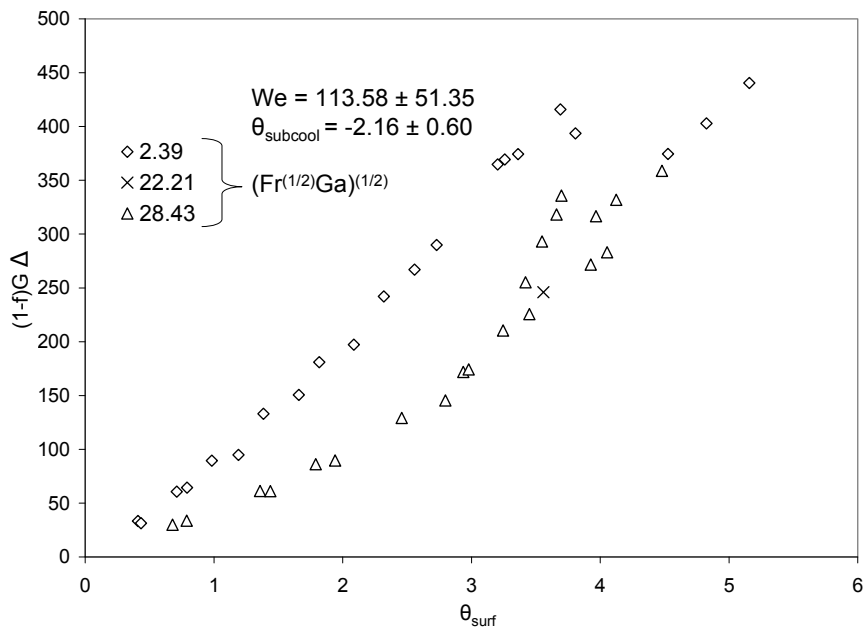
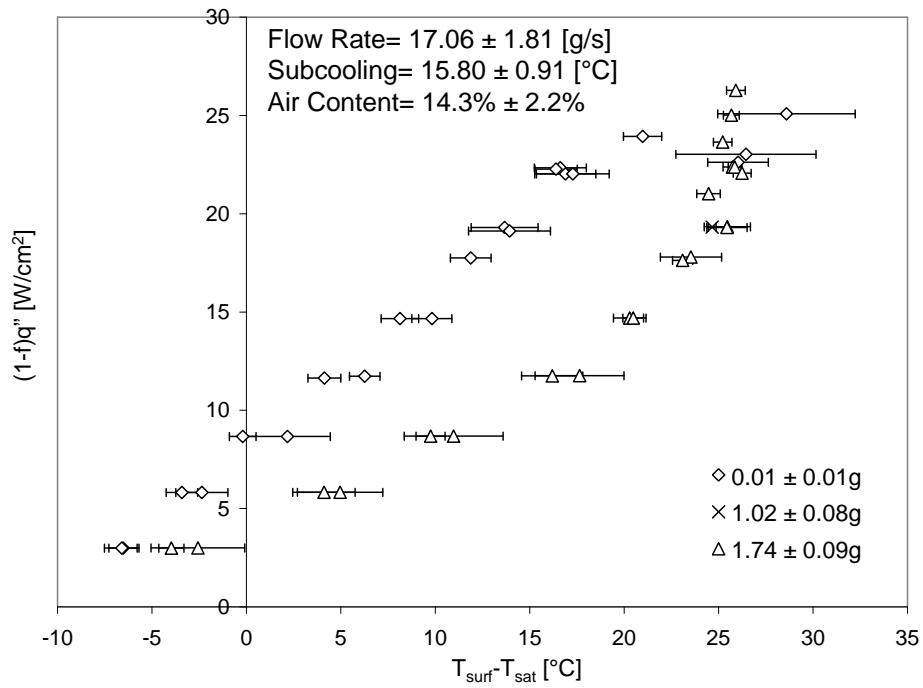


Figure F.18: Dimensional and Non-dimensional Steady State Heat Flux Transferred to Spray for Micro, Terrestrial and Elevated Gravity for Cases 57-59

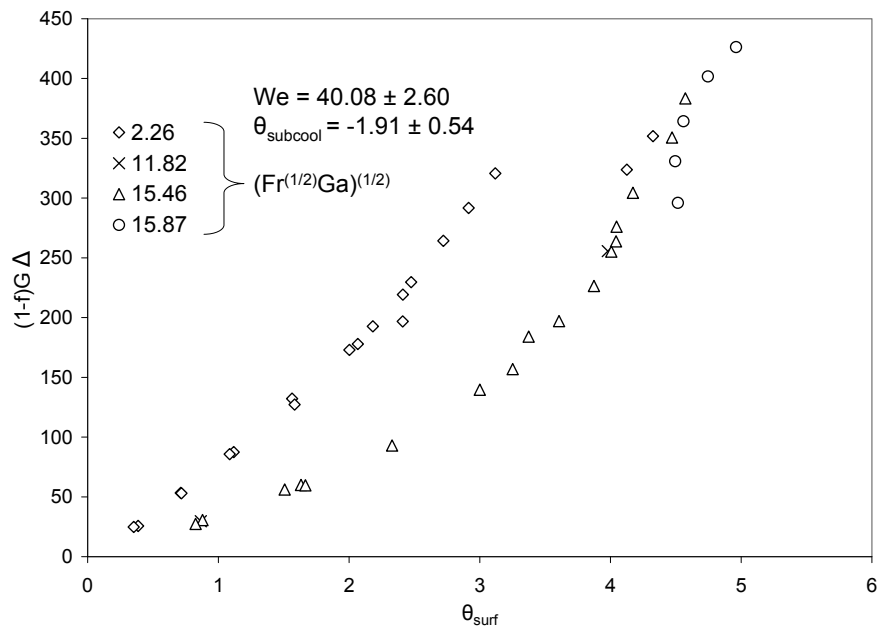
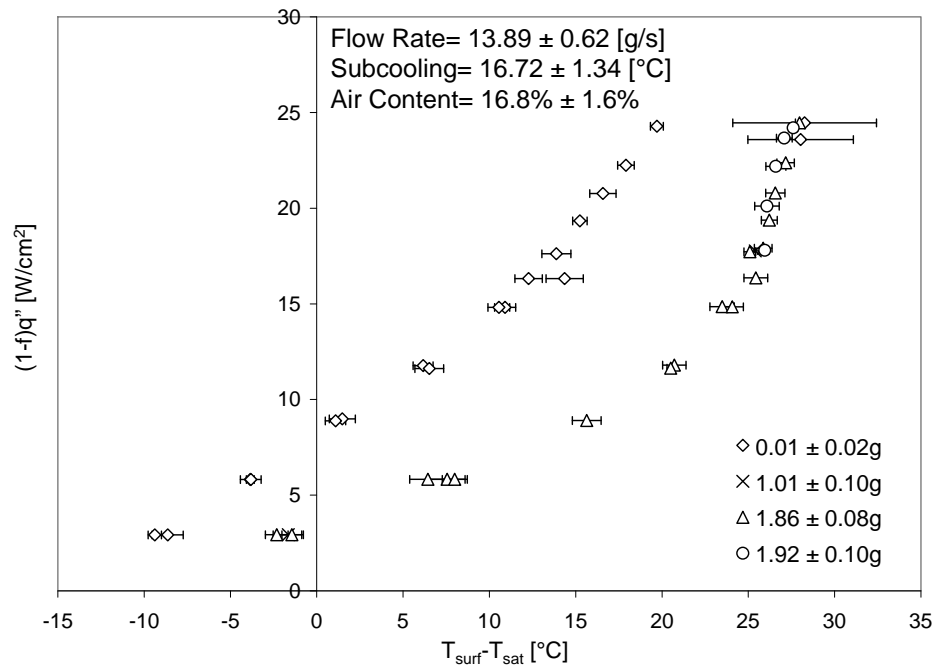


Figure F.19: Dimensional and Non-dimensional Steady State Heat Flux Transferred to Spray for Micro, Terrestrial and Elevated Gravity for Cases 61-64

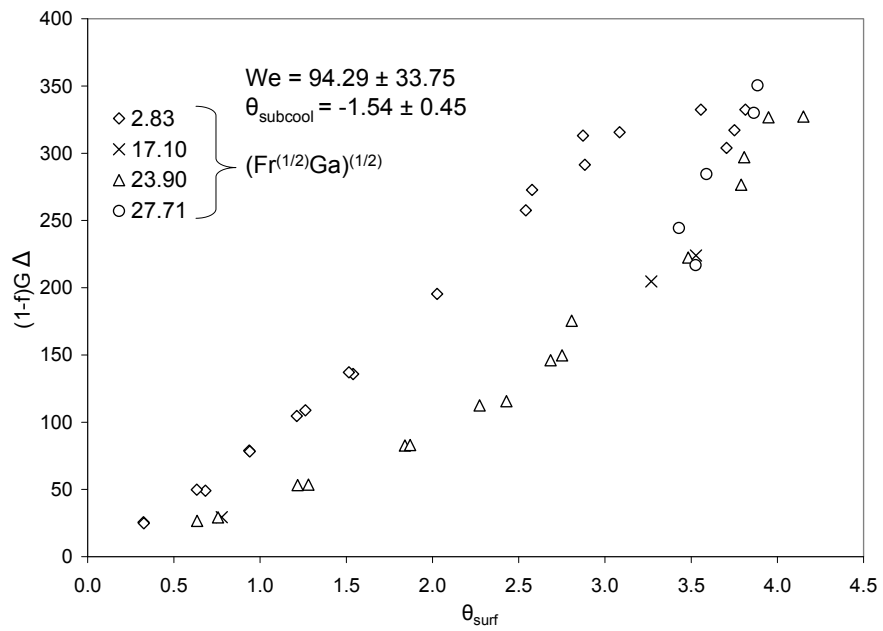
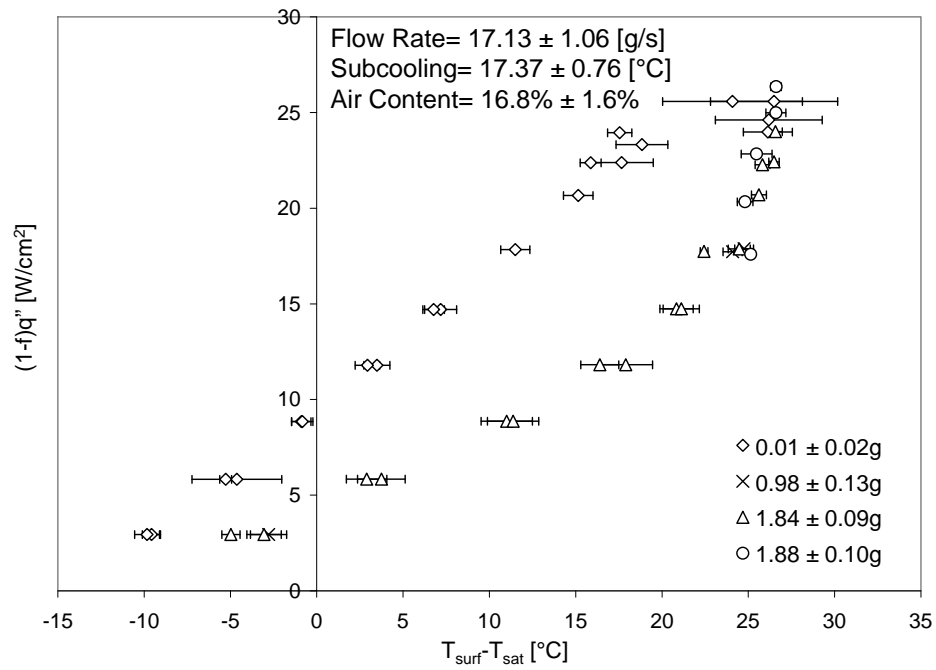


Figure F.20: Dimensional and Non-dimensional Steady State Heat Flux Transferred to Spray for Micro, Terrestrial and Elevated Gravity for Cases 65-68

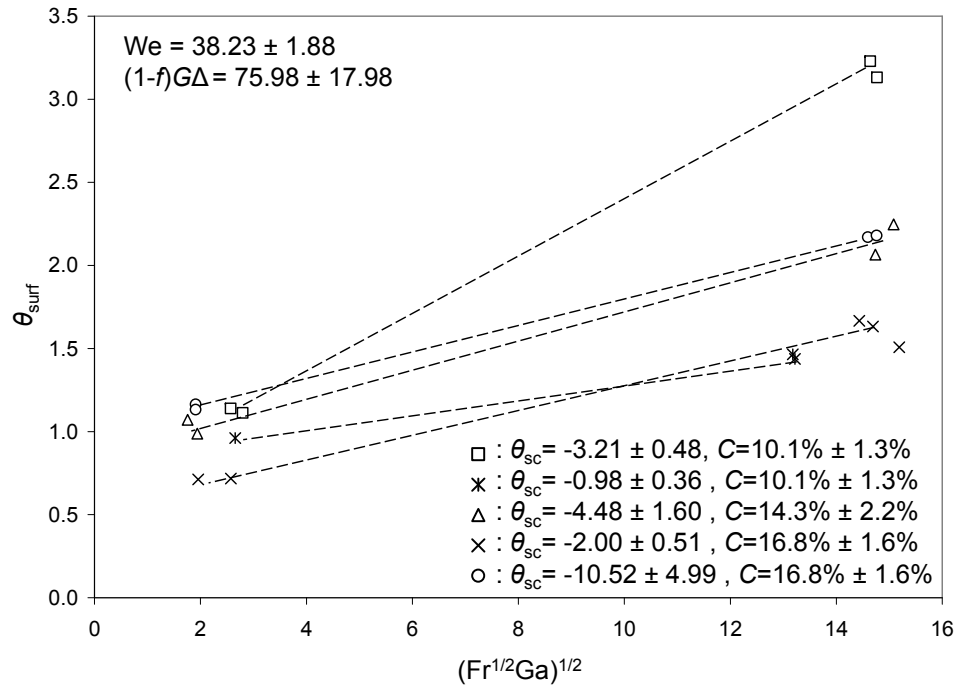
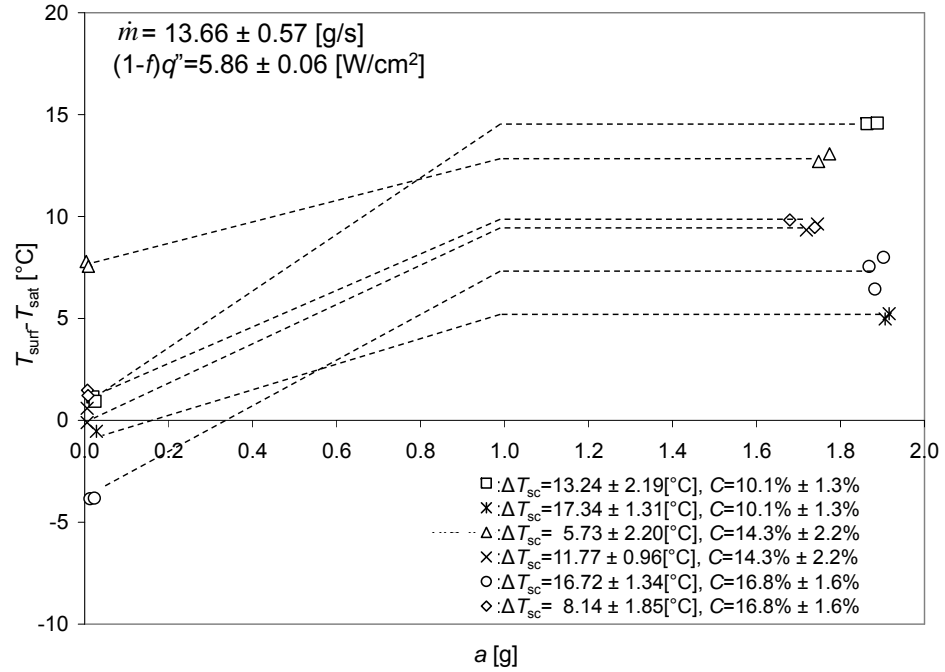


Figure F.22: Dimensional and Non-dimensional Steady State Surface Temperature for Micro, Terrestrial and Elevated Gravity

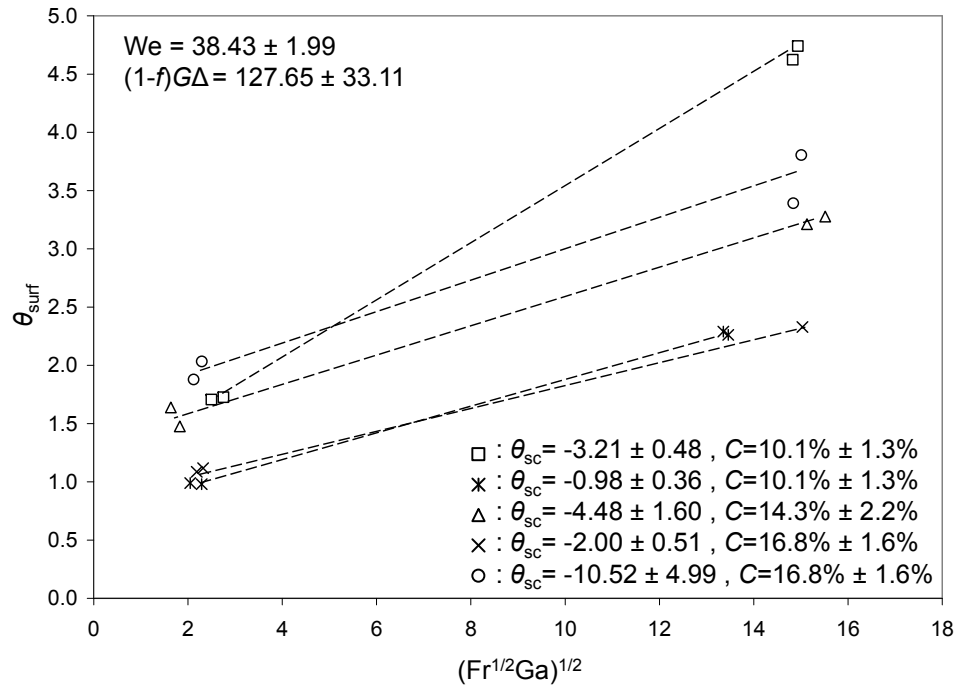
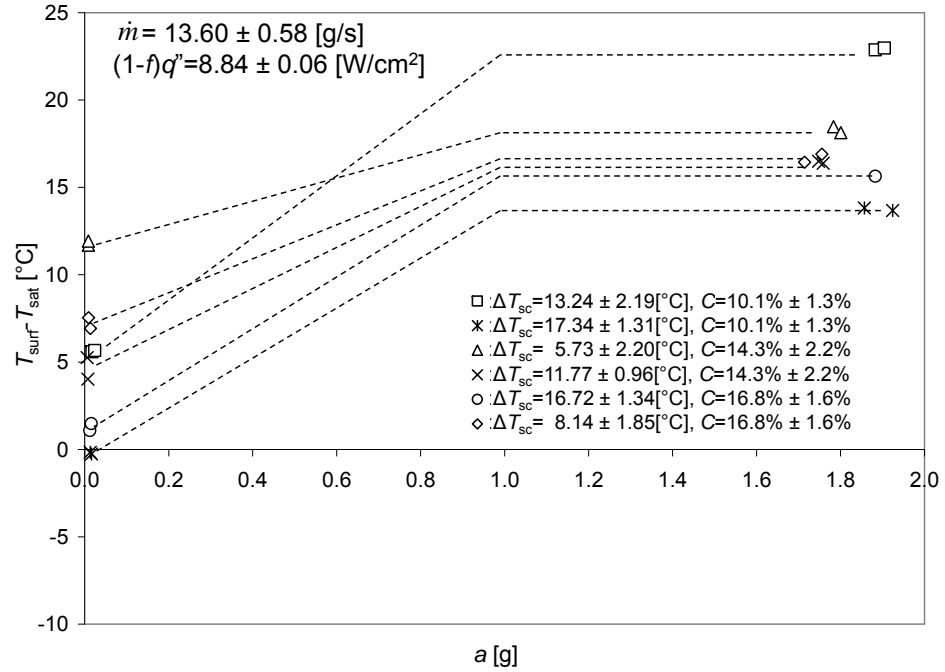


Figure F.23: Dimensional and Non-dimensional Steady State Surface Temperature for Micro, Terrestrial and Elevated Gravity

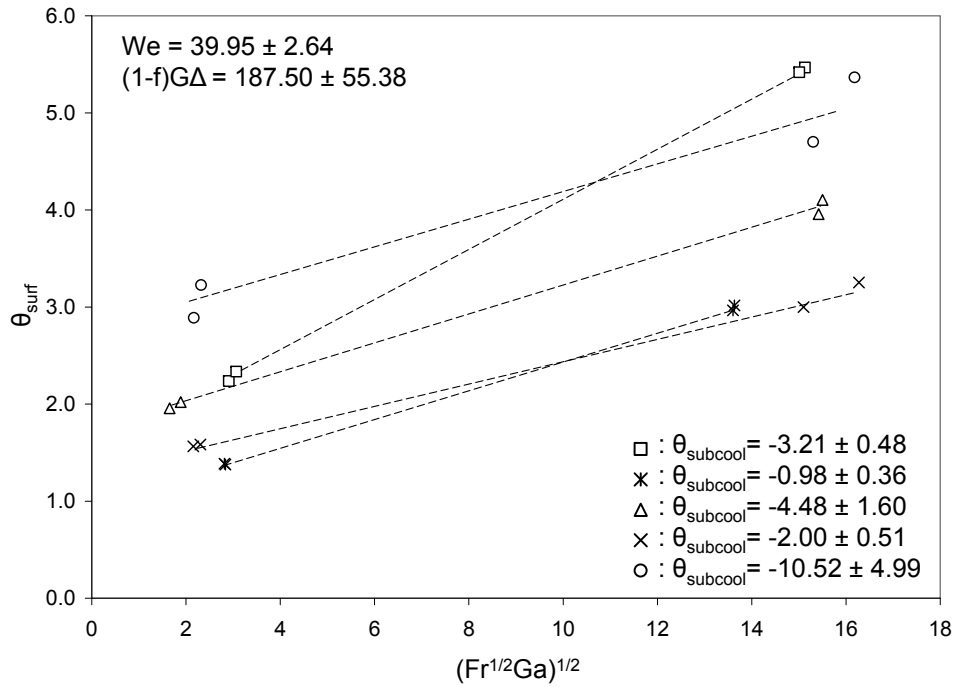
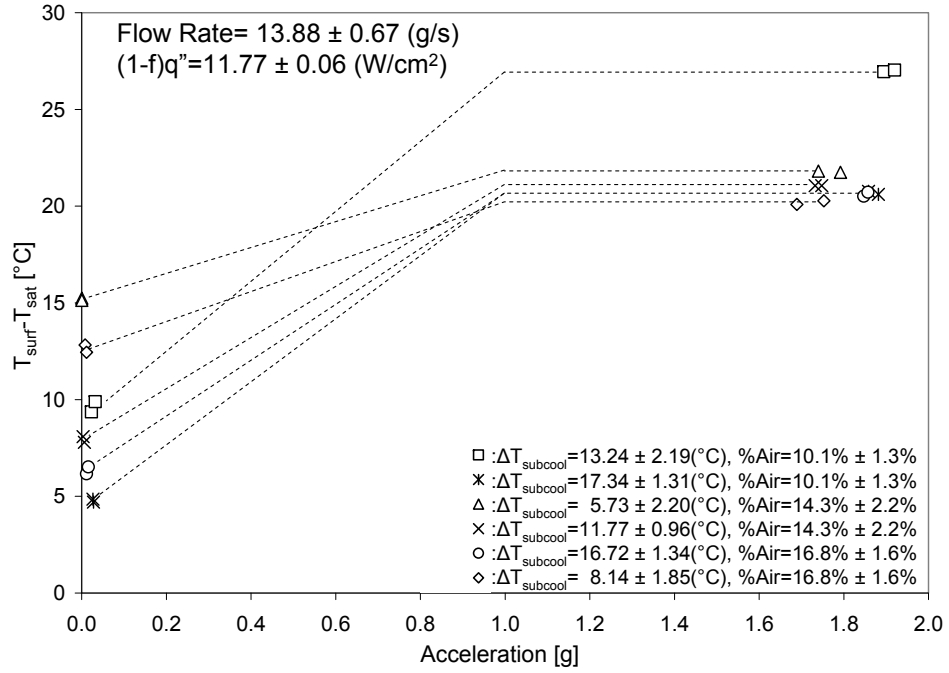


Figure F.24: Dimensional and Non-dimensional Steady State Surface Temperature for Micro, Terrestrial and Elevated Gravity

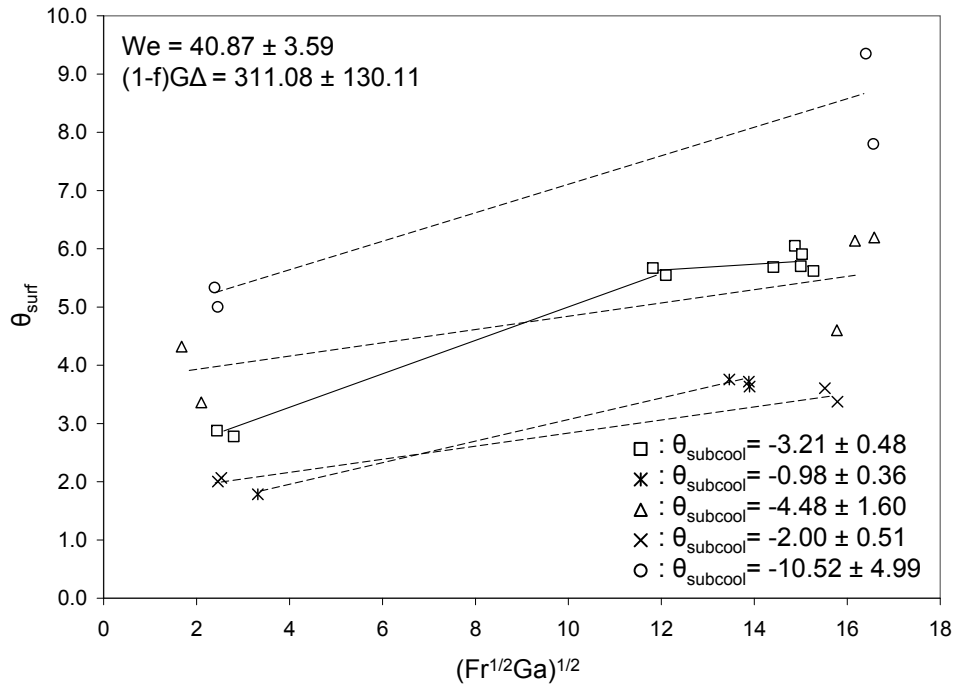
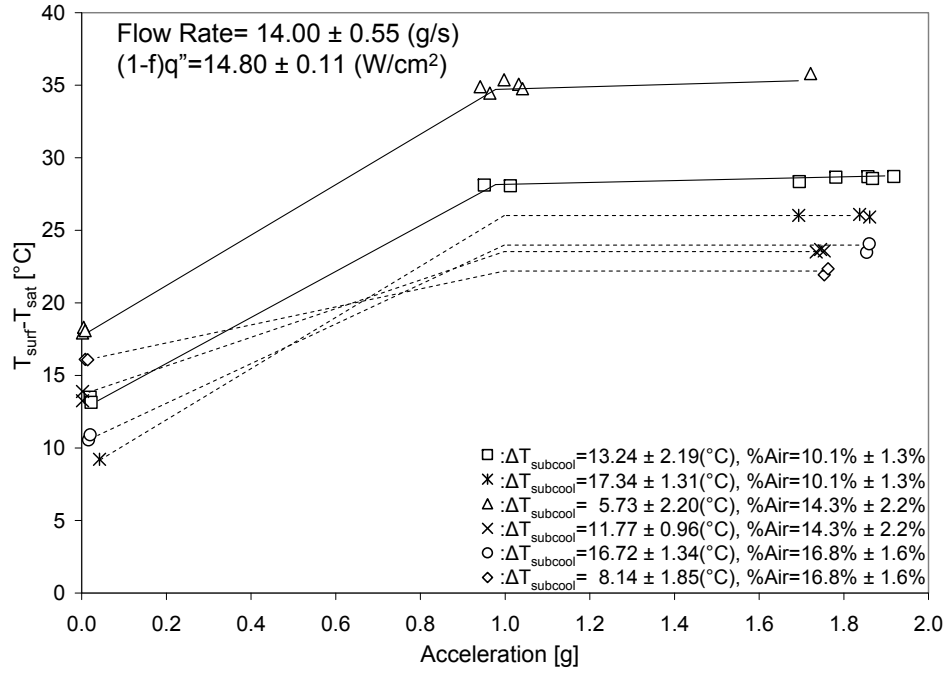


Figure F.25: Dimensional and Non-dimensional Steady State Surface Temperature for Micro, Terrestrial and Elevated Gravity

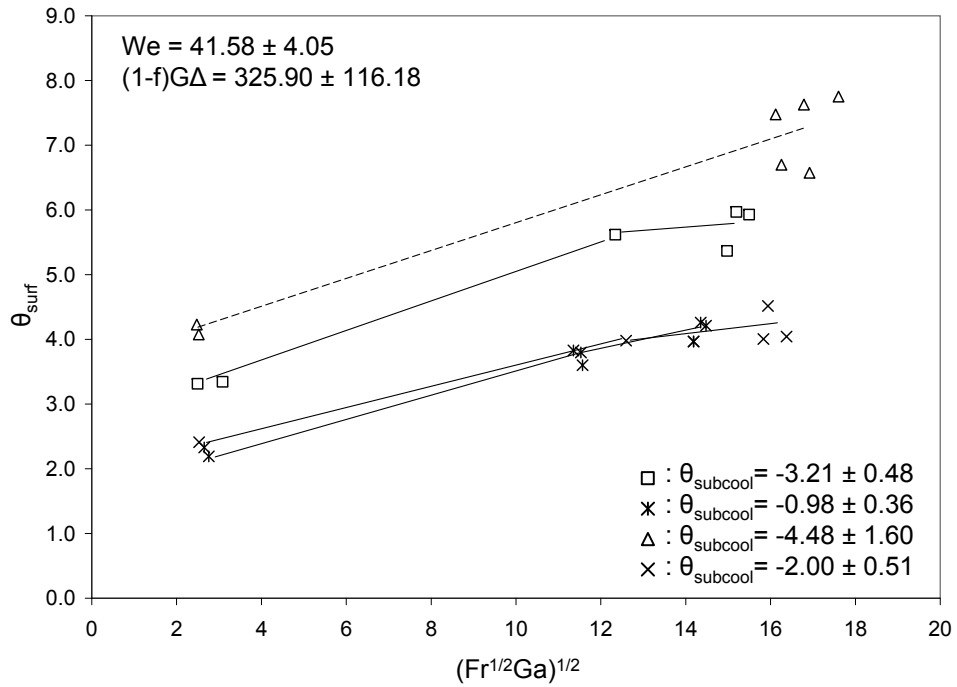
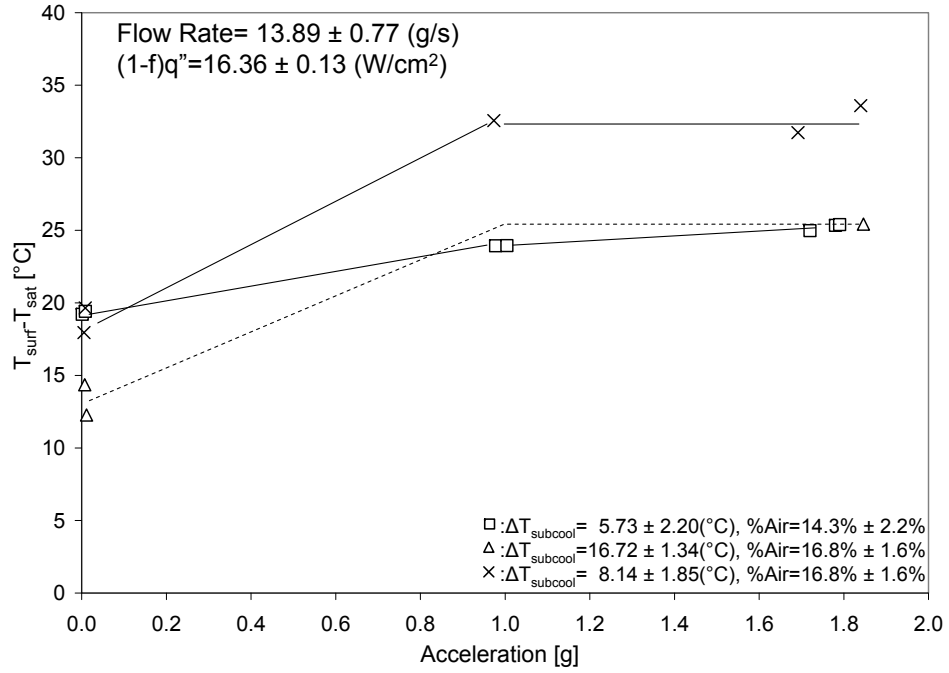


Figure F.26: Dimensional and Non-dimensional Steady State Surface Temperature for Micro, Terrestrial and Elevated Gravity

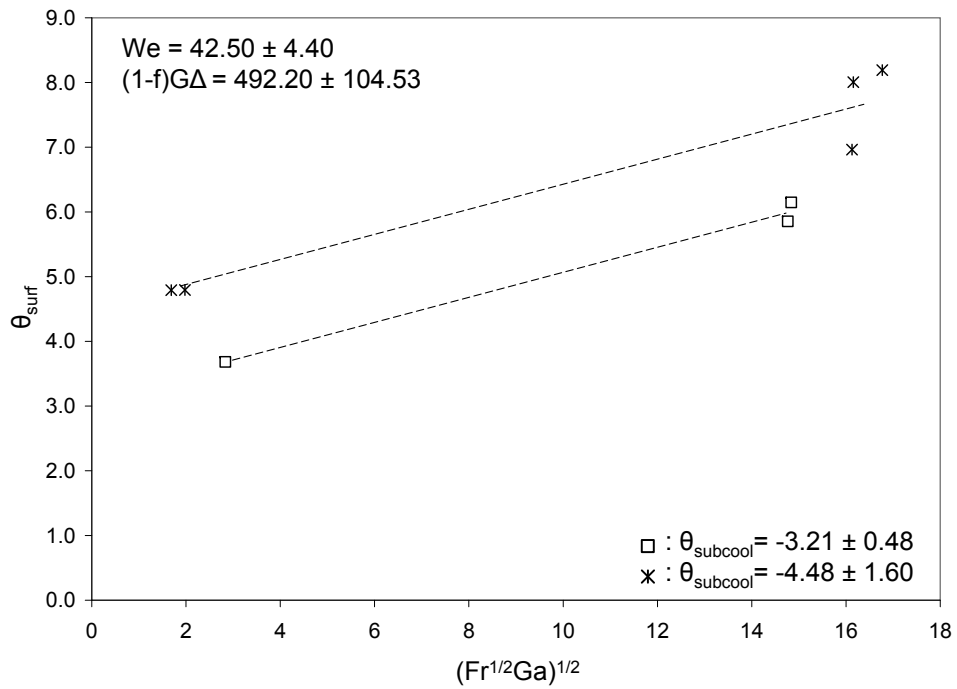
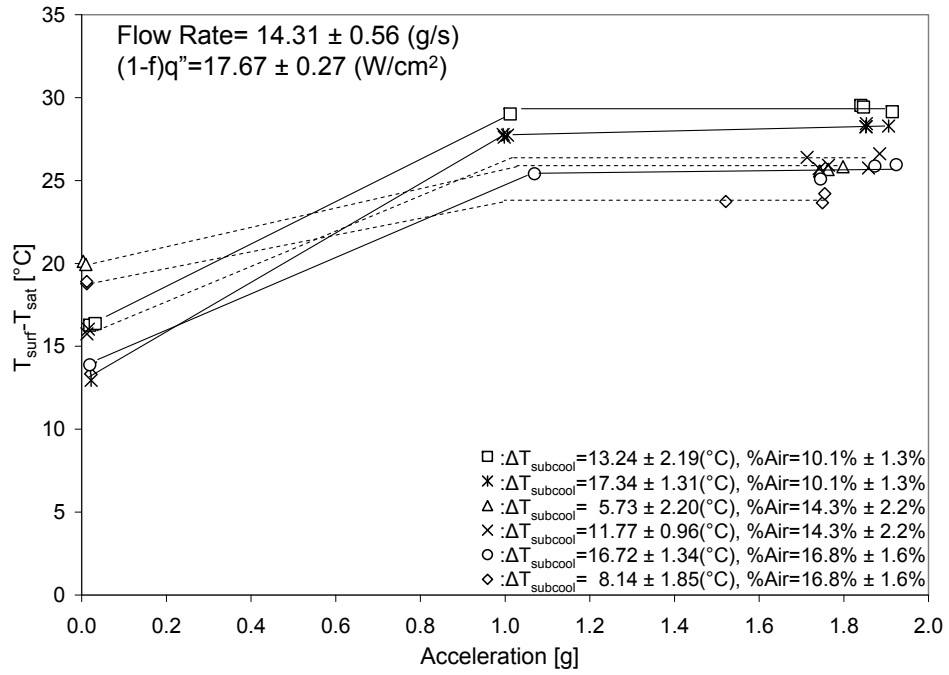


Figure F.27: Dimensional and Non-dimensional Steady State Surface Temperature for Micro, Terrestrial and Elevated Gravity

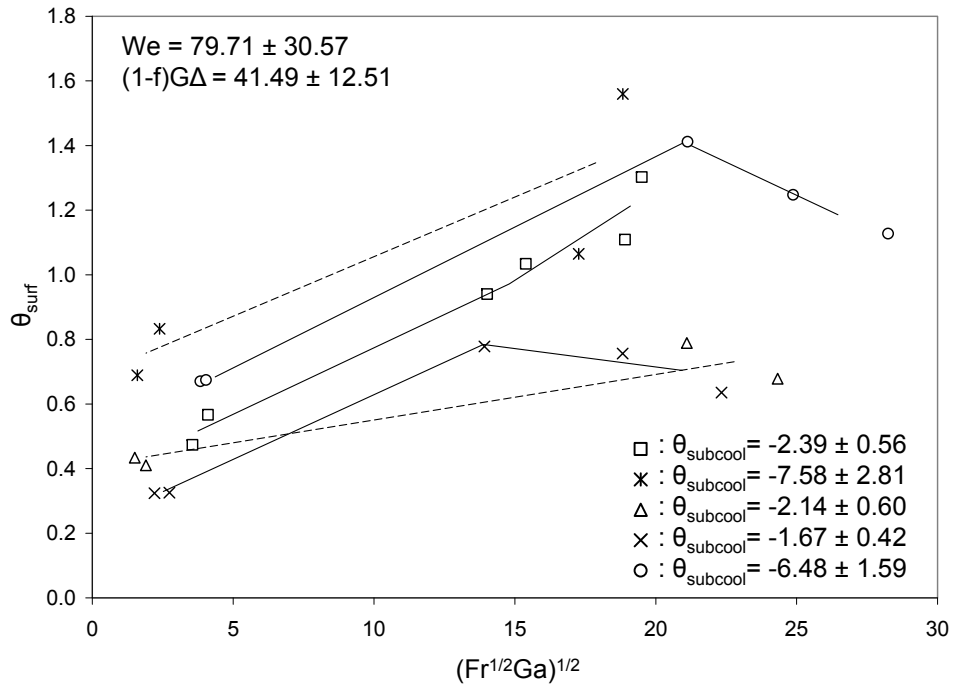
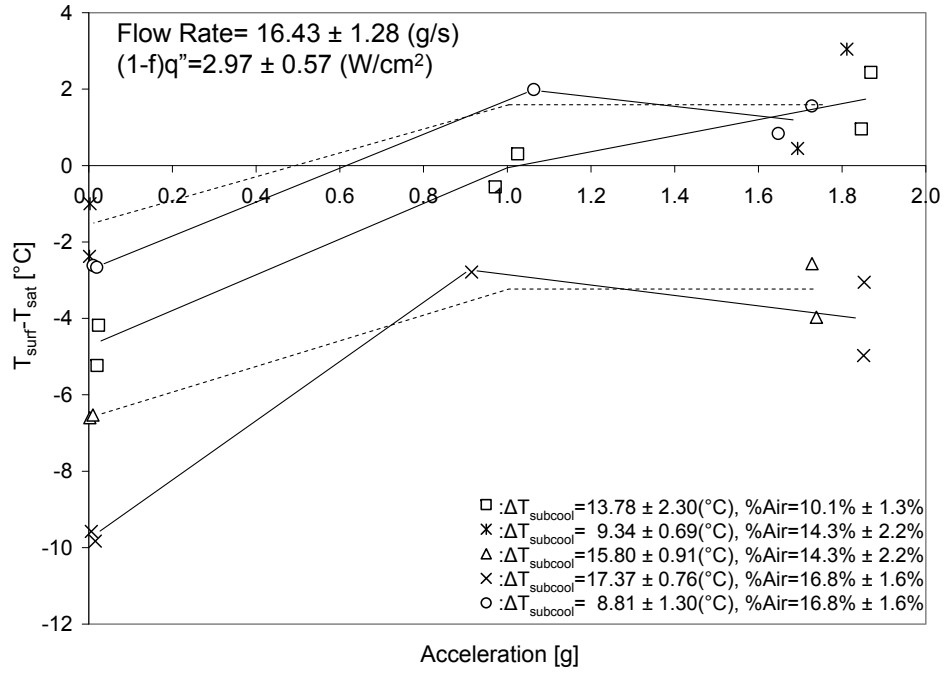


Figure F.28: Dimensional and Non-dimensional Steady State Surface Temperature for Micro, Terrestrial and Elevated Gravity

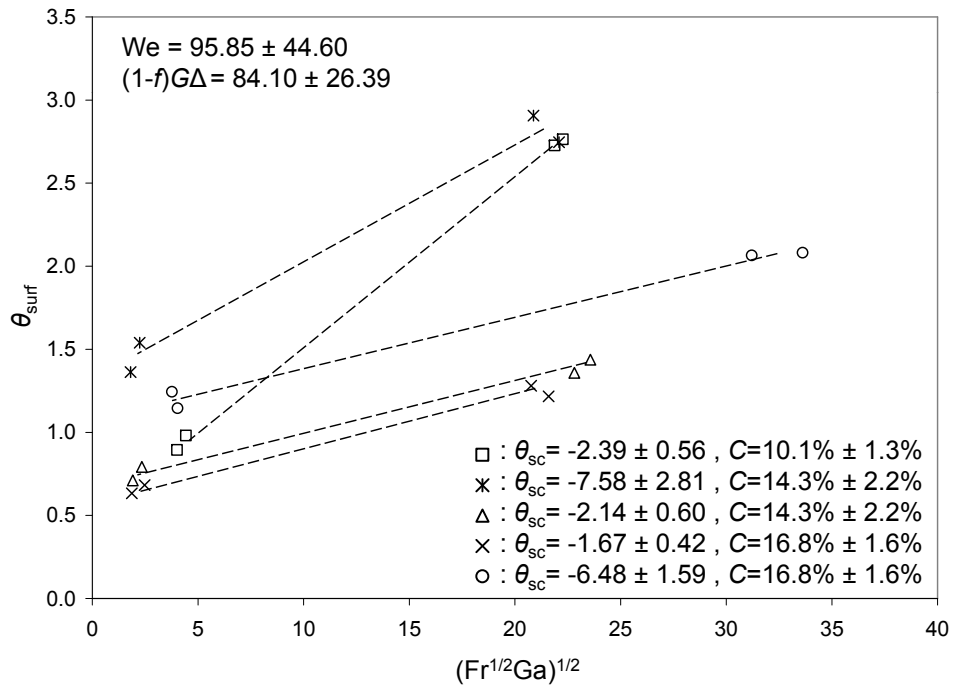
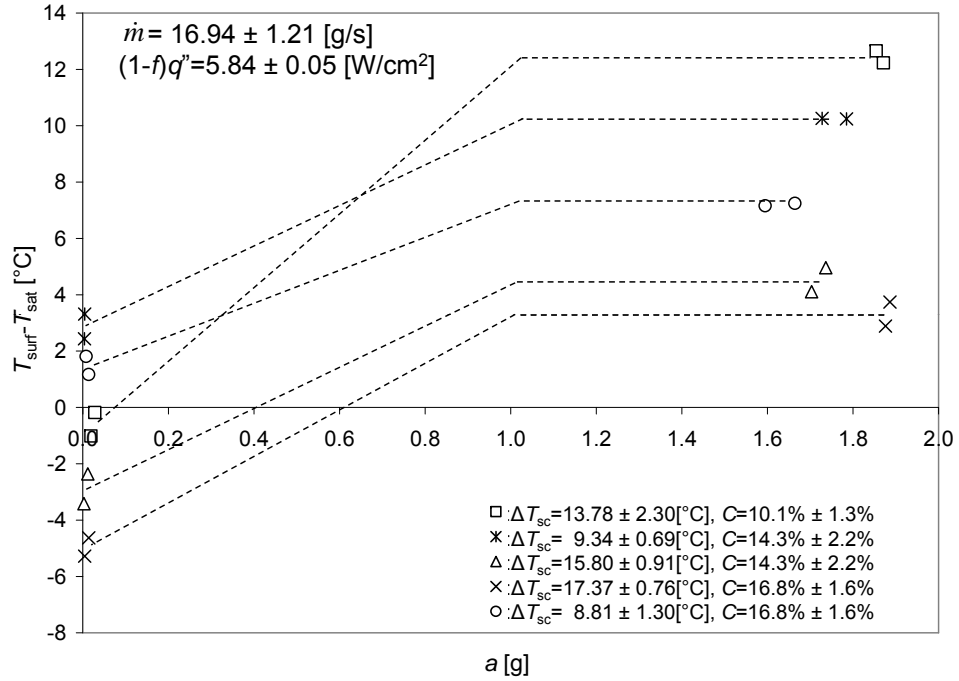


Figure F.29: Dimensional and Non-dimensional Steady State Surface Temperature for Micro, Terrestrial and Elevated Gravity

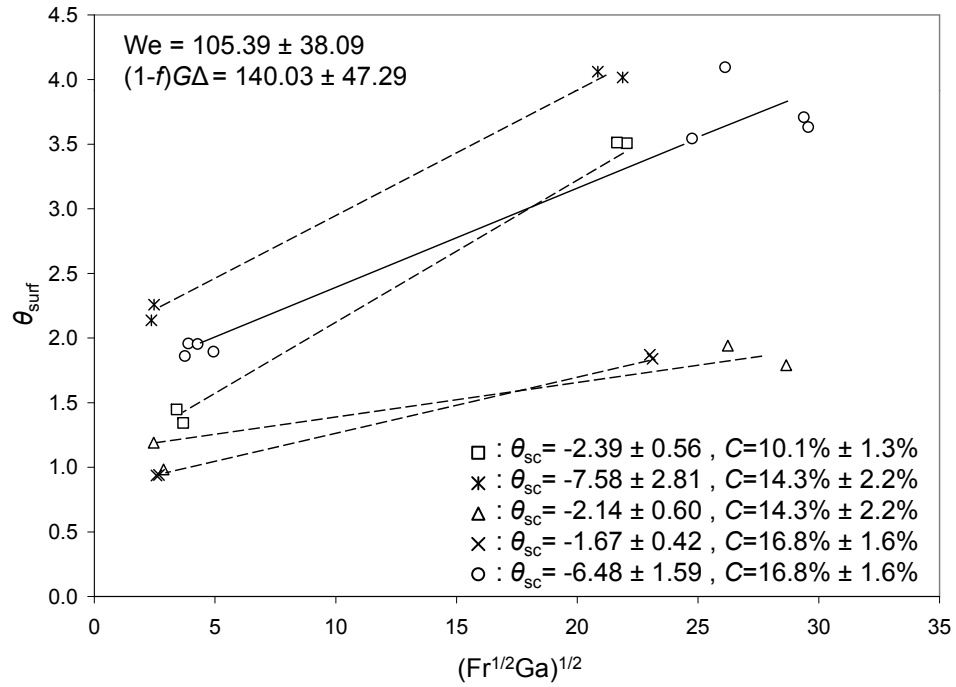
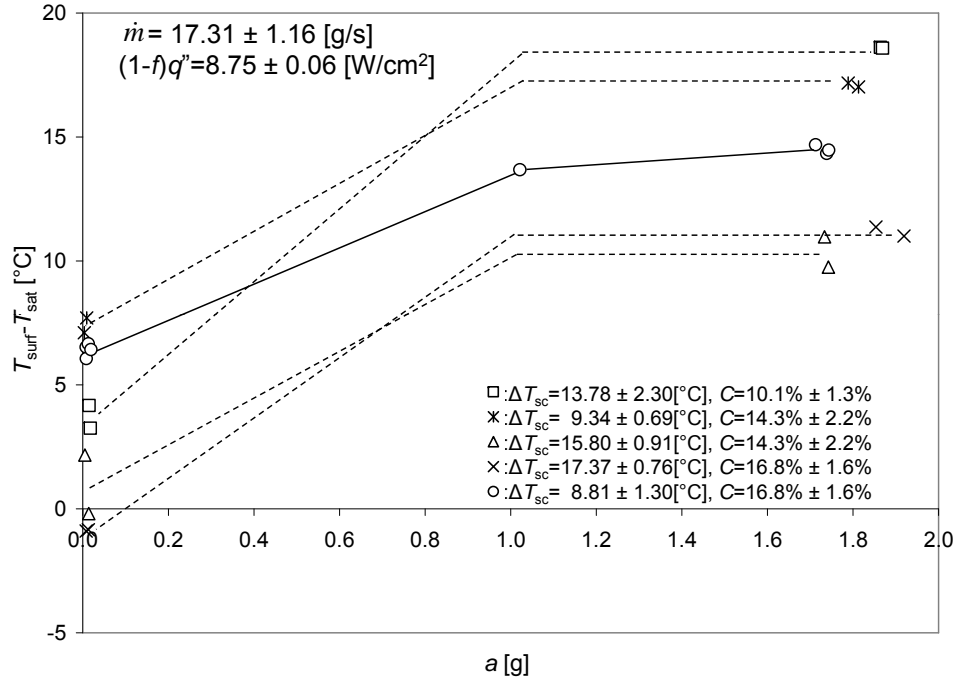


Figure F.30: Dimensional and Non-dimensional Steady State Surface Temperature for Micro, Terrestrial and Elevated Gravity

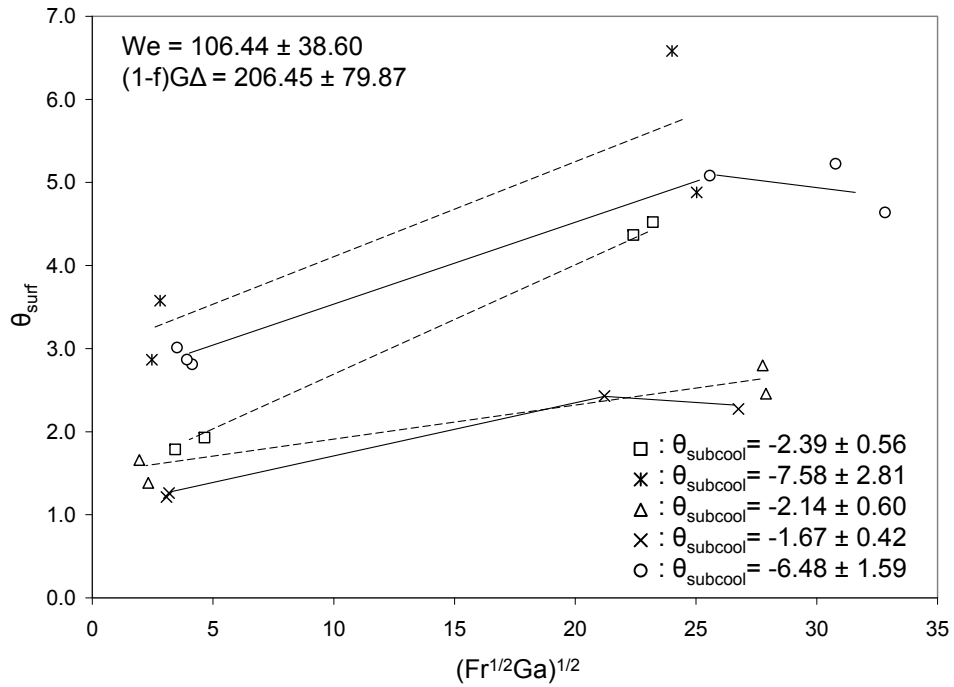
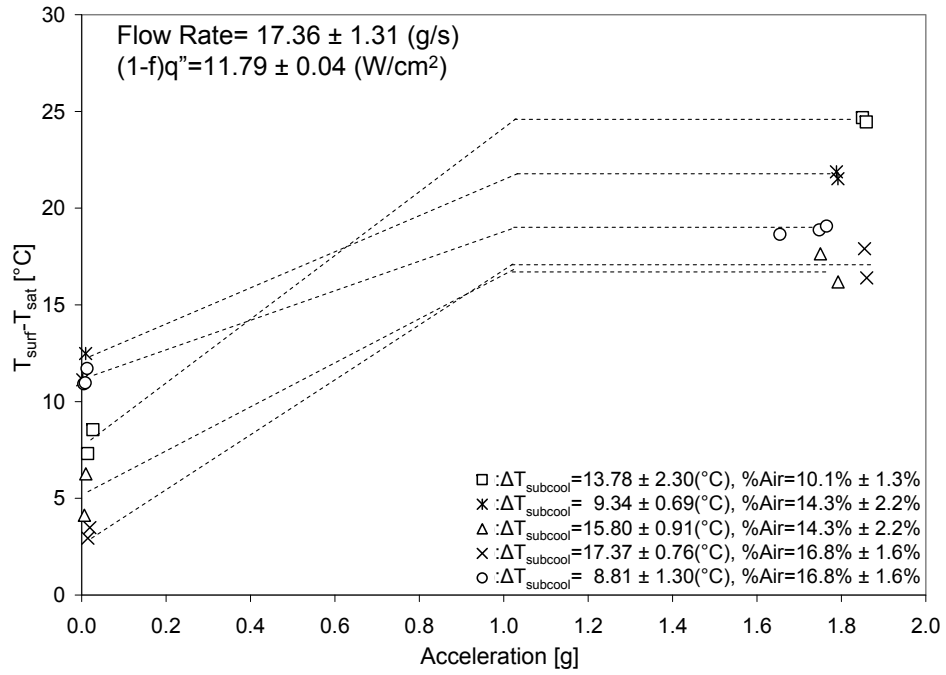


Figure F.31: Dimensional and Non-dimensional Steady State Surface Temperature for Micro, Terrestrial and Elevated Gravity

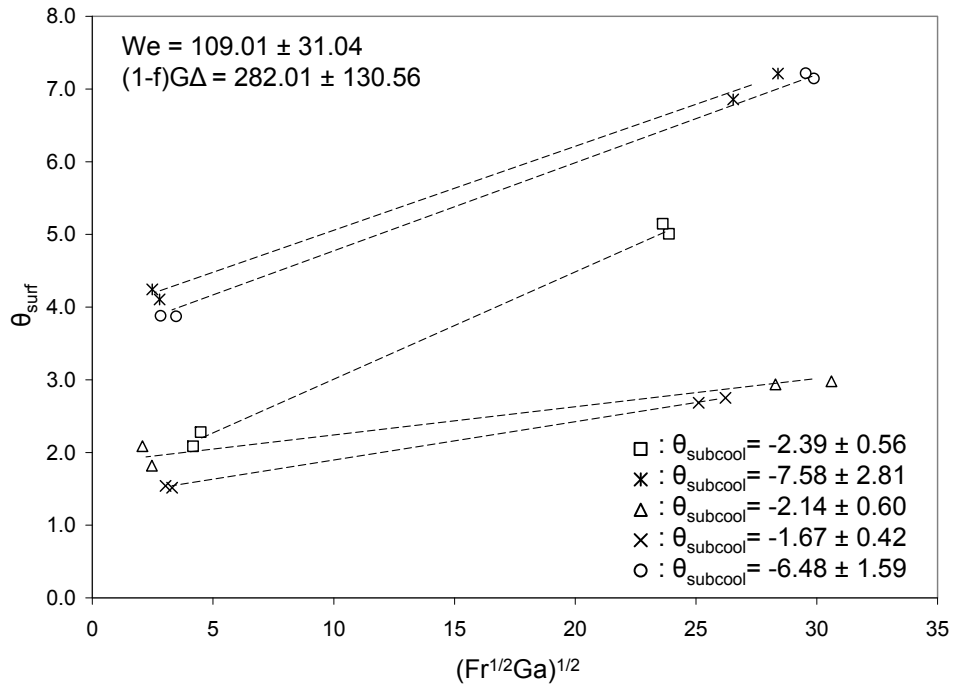
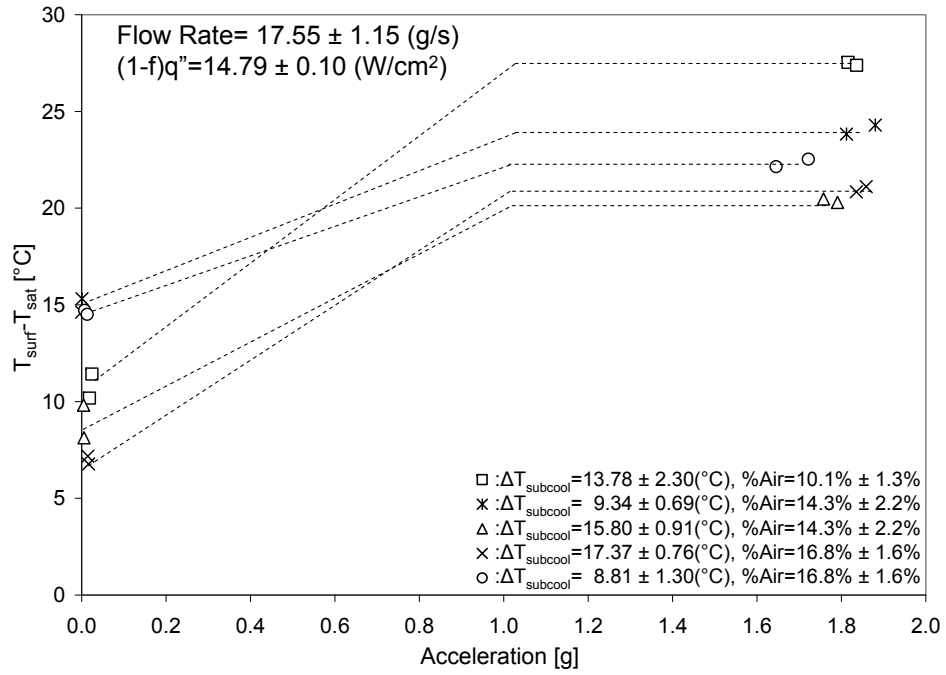


Figure F.32: Dimensional and Non-dimensional Steady State Surface Temperature for Micro, Terrestrial and Elevated Gravity

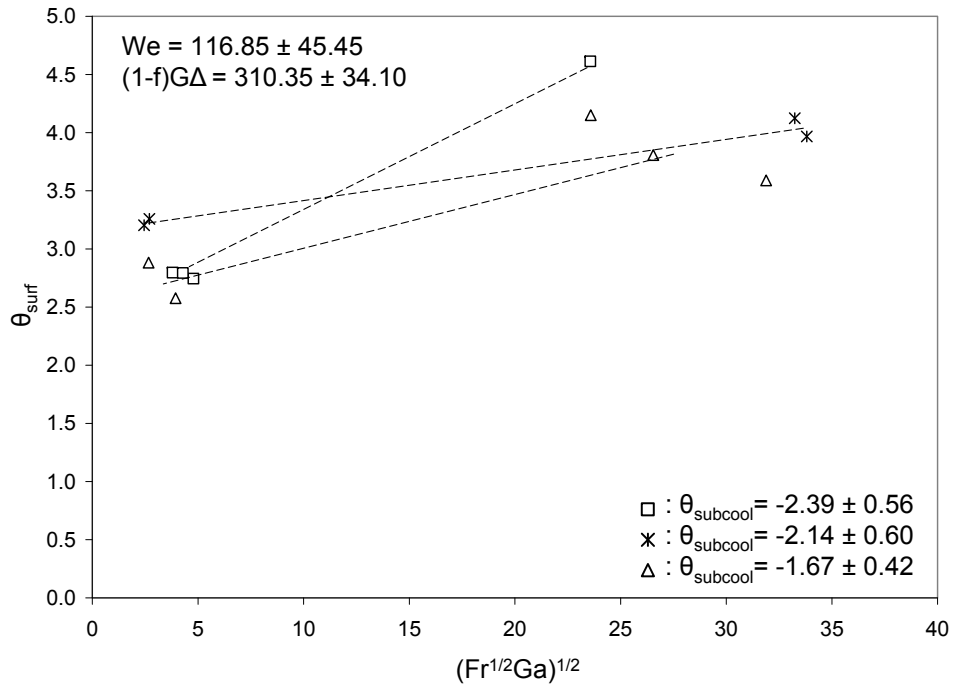
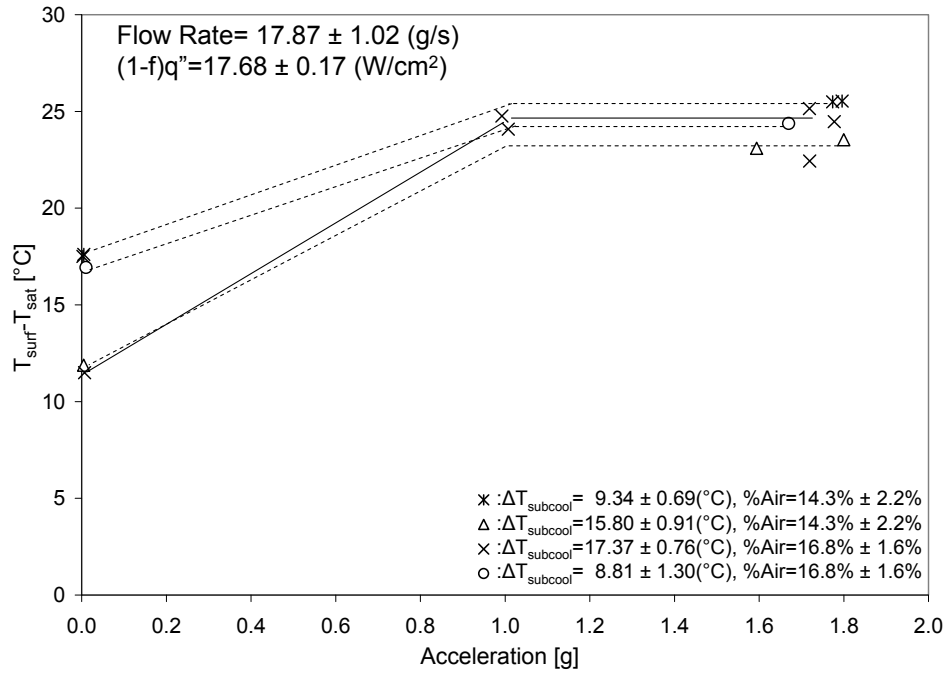


Figure F.33: Dimensional and Non-dimensional Steady State Surface Temperature for Micro, Terrestrial and Elevated Gravity

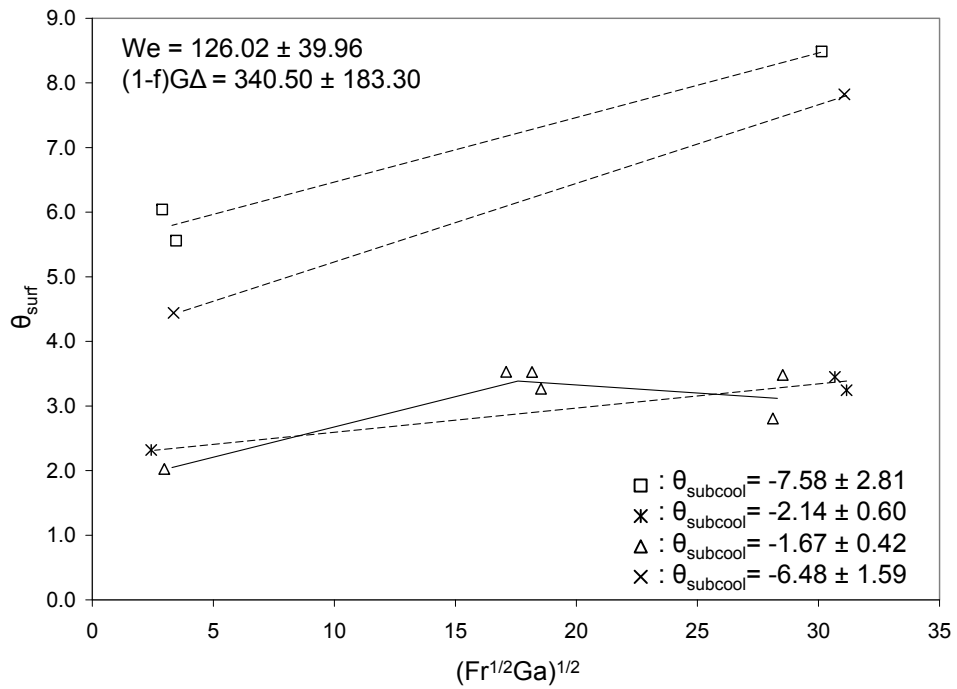
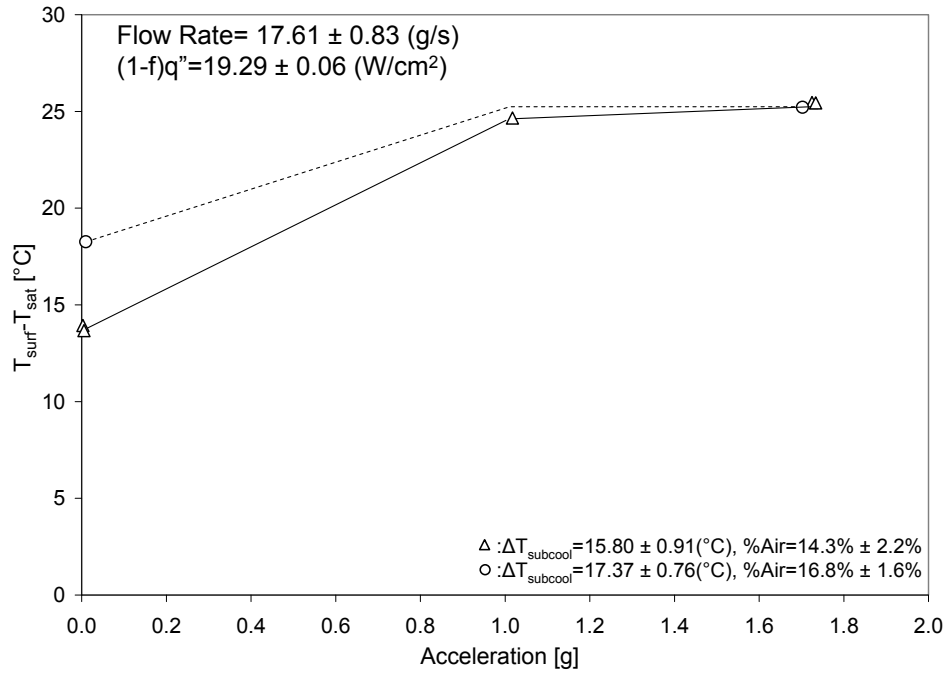


Figure F.34: Dimensional and Non-dimensional Steady State Surface Temperature for Micro, Terrestrial and Elevated Gravity

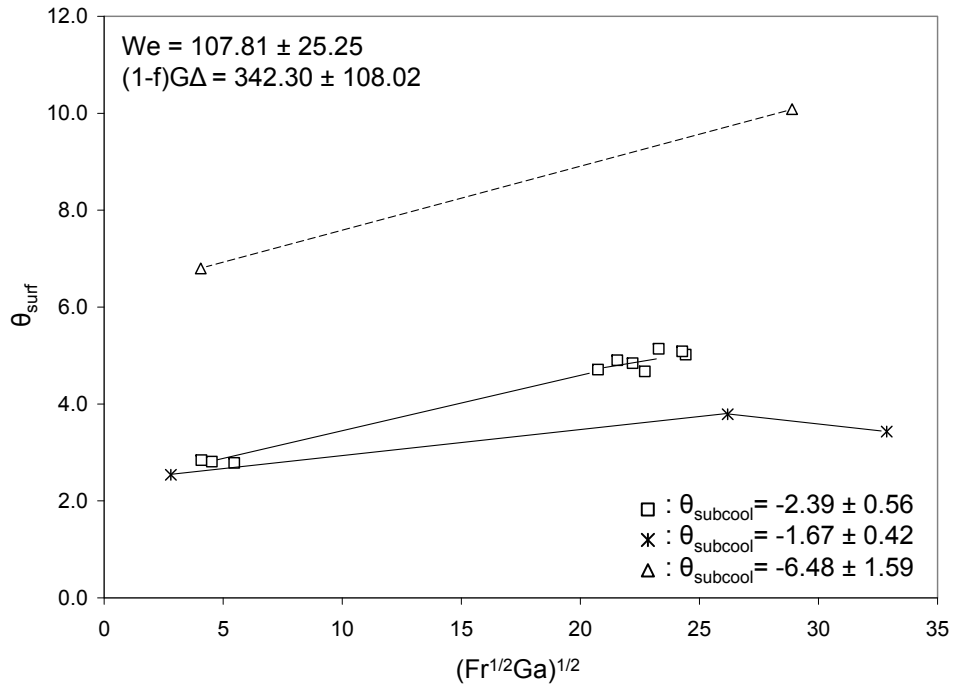
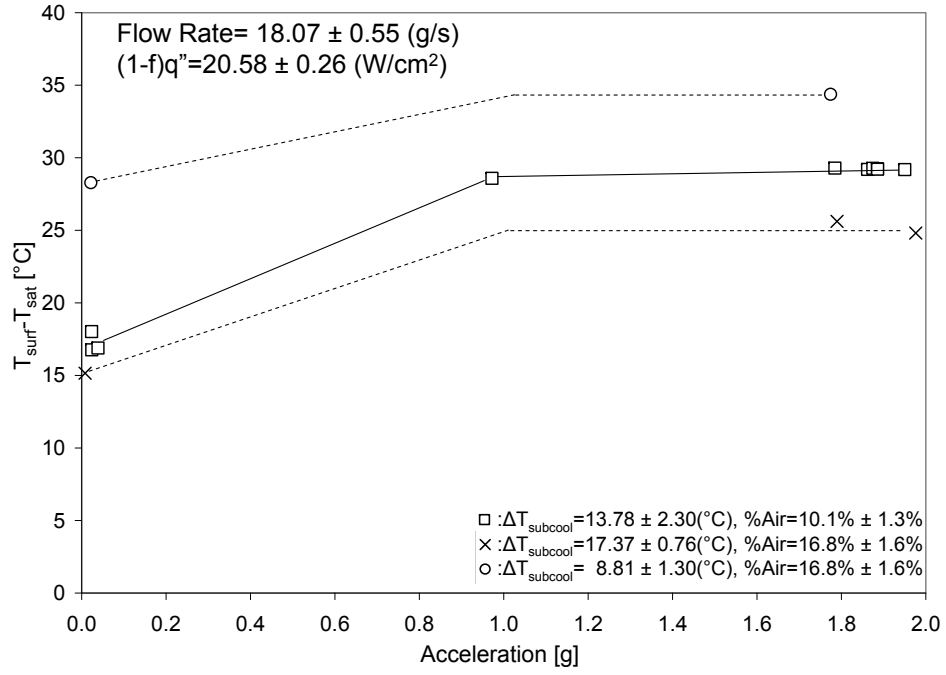


Figure F.35: Dimensional and Non-dimensional Steady State Surface Temperature for Micro, Terrestrial and Elevated Gravity

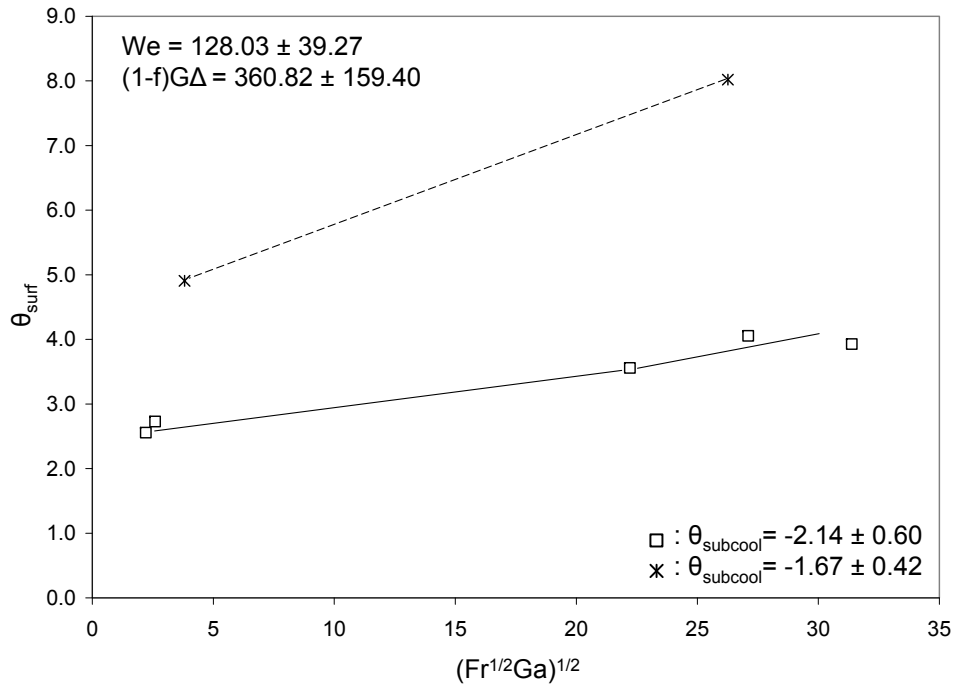
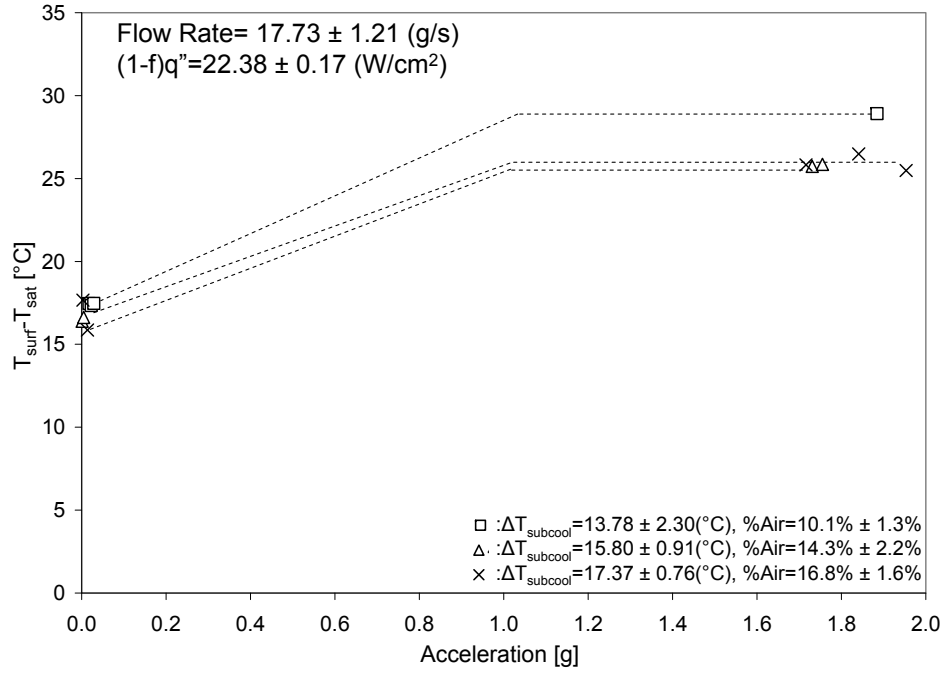
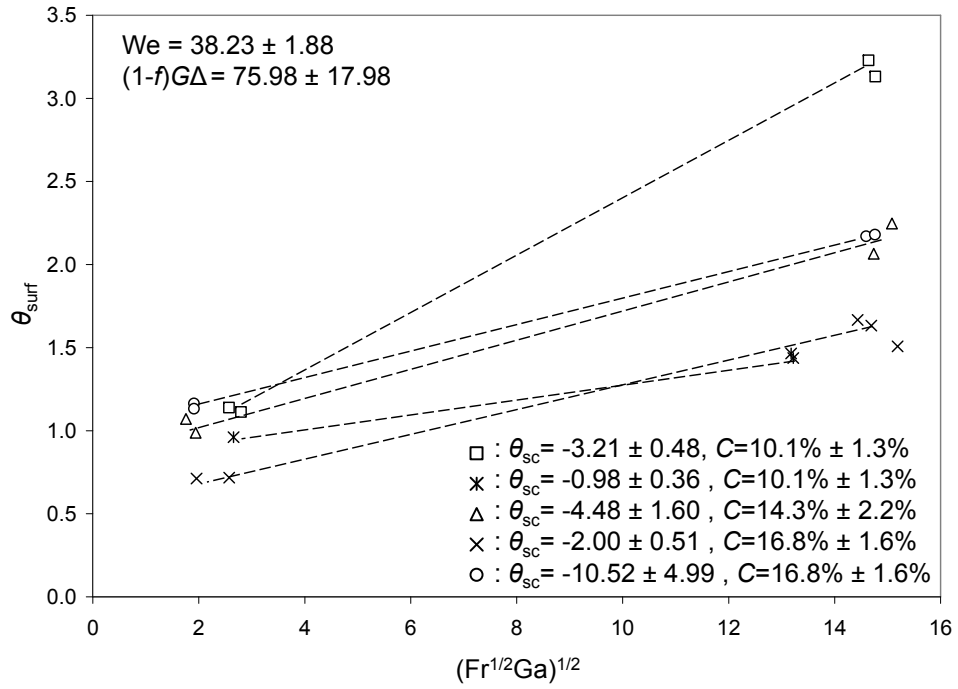
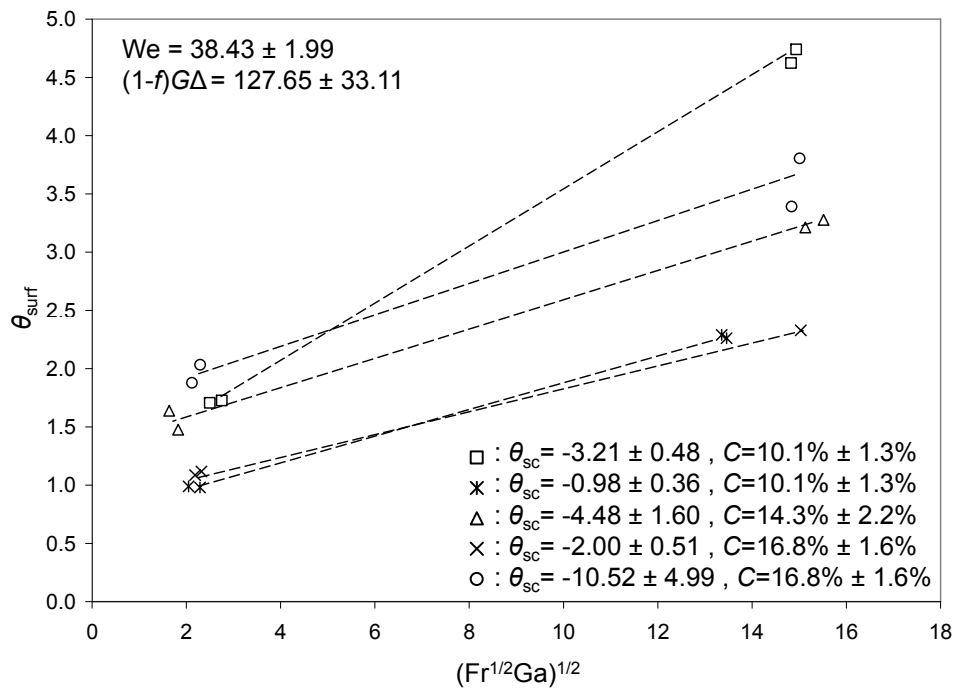


Figure F.36: Dimensional and Non-dimensional Steady State Surface Temperature for Micro, Terrestrial and Elevated Gravity

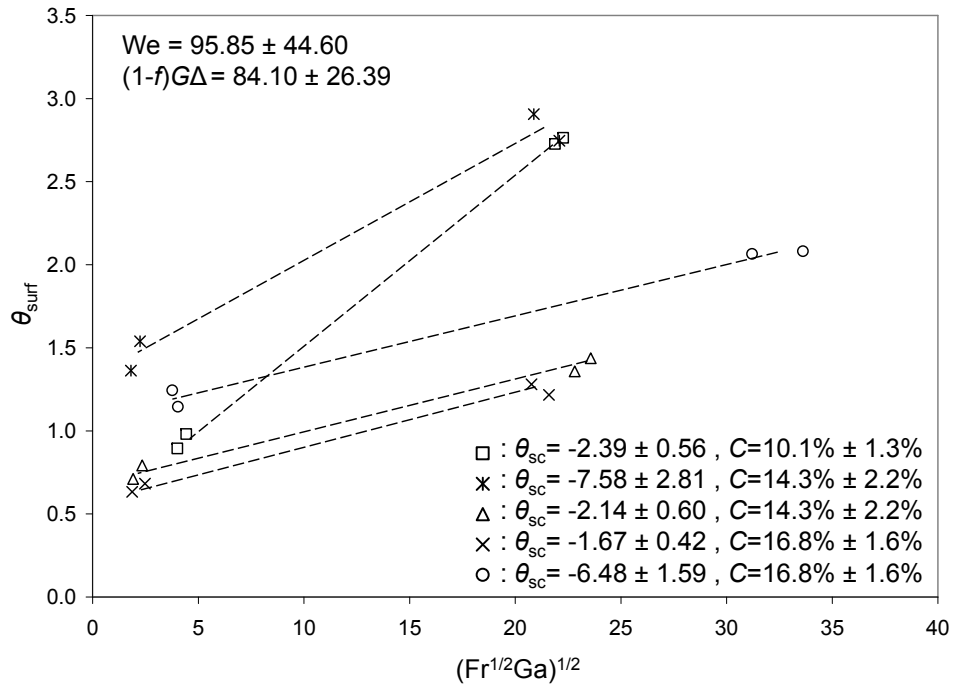


(a)

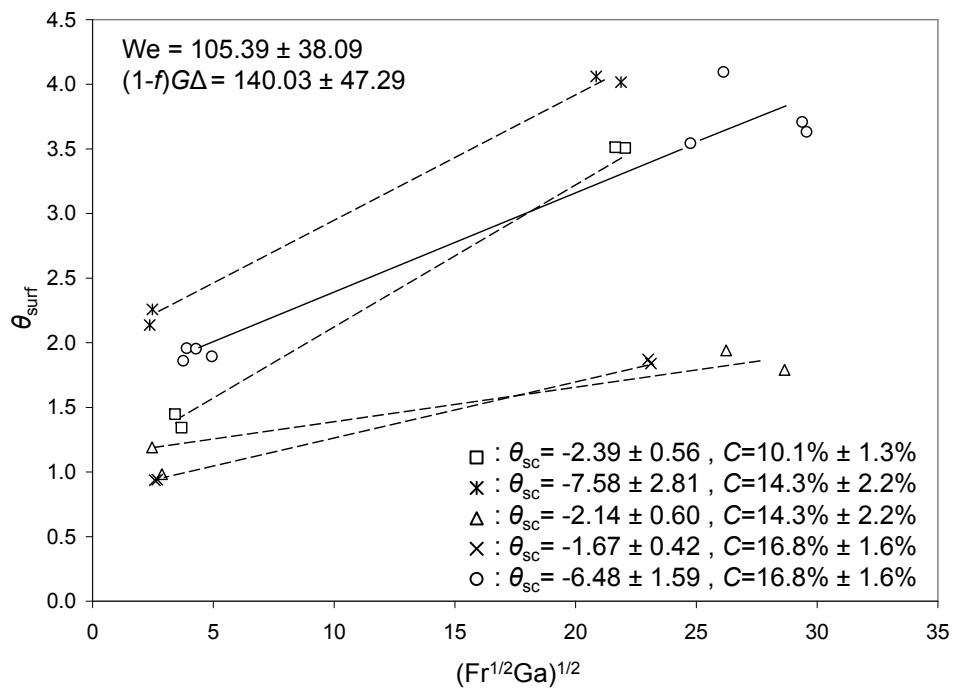


(b)

Figure F.37: Effect of Dimensionless Subcooling on Cooling Performance: (a) $We = 38.23 \pm 1.88$; (b) $We = 38.43 \pm 1.99$.



(a)



(b)

Figure F.38: Effect of Dimensionless Subcooling on Cooling Performance: (a) $We = 95.85 \pm 44.60$; (b) $We = 105.39 \pm 38.09$.

Appendix G

Test Equipment Data Package

This section contains the document that had to be generated to get approval from NASA officials six weeks prior to flight testing. It is shown in a direct version; exactly how it was presented to NASA officials.

**TEST EQUIPMENT DATA PACKAGE
FOR
THE VARIABLE GRAVITY
SPRAY COOLING ARRAY EXPERIMENT**

Kirk Yerkes, Levi Elston
Air Force Research Laboratory, Propulsion Directorate
Wright Patterson Air Force Base
1950 Fifth Street
WPAFB, OH 45433-7251
PH (937) 656-4428
FAX (937) 656-7529
E-mail: kirk.yerkes@wpafb.af.mil, levi.elston@us.af.mil

25 July 2007

Change Record

Version	Date	Owner	Description
Basic	7 May 2007	Levi Elston	Initial release
Rev 2	25 July 2007	Levi Elston	Added triple temperature cutoff circuit

Revisions

Rev. 2 - 25 July 2007

System Weight

Original TEDP listed weight as 642 pounds. Upon arrival at GRC, rig weighed in at 742 pounds. Additional items were placed on rig including brackets, 80/20 channel, wiring, laptop power supply, and handle bars. Several structural

Rev 1 pg #	Rev 2 pg #	Change
N/A	i	Added Change Record and Revisions Sheet
i	iii	Changed flight dates to 10 Sept 07 – 14 Sept 07
i	iii	Removed John Nairus from Flyer Names List and added Casandra Applin
i	iii	Removed request for high speed camera support
1	1	Removed John Nairus from Flight Manifest and added Casandra Applin
17	17	Corrected missing reference of Figure 16 to Figure CGG
34	34	Corrected confusing direction for Leak Procedure, added “proceed to step 4”
N/A	46	Added “Array Triple Over-temp Cutoff Circuit” Diagram
93	92	Adjusted “Calibration Work Instruction” pressure calibration limit from 14.7 psia to 100 psia

C-9 Quick Reference Data Sheet

Principle Investigator: Kirk Yerkes, PhD

Contact Information: AFRL/PRP
1950 Fifth Street
WPAFB, OH 45433-7251
PH: (937) 255-6186
FAX: (937) 656-7529
E-mail: kirk.yerkes@wpafb.af.mil

Experiment Title: Variable Gravity Spray Cooling Array Experiment

Flight Dates: 10 Sept 07 – 14 Sept 07

Overall Assembly Weight: 705 lbs (see pg. 14)

Assembly Dimensions: 44"×64.5"×44"

Equipment Orientation Requests: Lengthwise along axis of aircraft

Floor Mounting Strategy: Bolts

Gas Cylinder Requests: No

Overboard Vent Requests: No

Power Requirements: 115 VAC, 60 Hz (see pg. 17)

Free Float Experiment: No

Flyer Names for Each Proposed Flight Day:

Kirk Yerkes, AFRL
Travis Michalak, AFRL
Levi Elston, AFRL
Rebekah Puterbaugh, AFRL
Lt. Chris De La Pena, AFRL
Lt. Leah Swanson, AFRL
Lt. Casandra Applin
John McQuillen, NASA GRC
(see Flight Manifest for flying schedule, pg. 1)

Camera Pole and/or Video Support: No

Table of Contents

C-9 Quick Reference Data Sheet	i
Table of Contents	iv
List of Tables	v
List of Figures	v
Flight Manifest.....	1
Experiment Background	1
Experiment Description	1
Equipment Description	2
Reduced Gravity Flight Equipment	2
Proposed Layout of Equipment	3
Special Handling Requirements.....	4
Items to Be Taken On-board.....	5
Special Requirements.....	5
Structural Verification	5
Load Factors.....	5
Frame Components	5
FC-72 Reservoir.....	5
Component Table.....	7
Rig Frame Analysis.....	8
Shelves	11
Pull Testing	13
Analysis of Microgravity Experiment Rig as One Object	14
Electrical Analysis	16
Electrical Schematic.....	16
Electrical Load	16
Electrical Emergency Flow Shutdown Switch	16
Loss of Electrical Power	17
Pressure System	17
Flow Schematic.....	17
Flow Component Listing	19
Fluid Containment Plan	20
Laser Certification	21
Parabola Details and Crew Assistance.....	21
Institutional Review Board	21
C-9 Hazards Analysis	21
Tool Requirements.....	32
Photo Requirements	32
Aircraft Loading.....	32
Ground Support Requirements	32
Hazardous Materials	32
Material Safety Data Sheets.....	32
Test Procedures.....	33
Loading Checklist.....	33
Pre-test Checklist	33

Testing Checklist	33
Post-test Checklist.....	34
Leak Shut Down Procedure	34
Emergency Shut Down Procedure	34
Appendix A: Electrical Schematic.....	35
Appendix B: 2020 Joint Fastener Static Testing.....	47
Appendix C: Experiment Drawings and Flow Schematic	57
Appendix D: Pressure Certification.....	71
Appendix E: Material Safety Data Sheet	77
Appendix F: Calibration Work Instruction.....	87

List of Tables

Table 1: Flight Manifest.....	1
Table 2: Component Analysis.....	8
Table 3: Experiment Rig Loads and Moments	9
Table 4: Extrusion Properties.....	9
Table 5: Joint Strength Values.....	9
Table 6: Shelf Loading.....	12
Table 7: Shelf Margins of Safety	13
Table 8: Pull Test Results	14
Table 9: Assembly Weight and Moment Arm.....	14
Table 10: Component Requirements	17
Table 11: Flow Components.....	19
Table B1: Corner Bracket Loads	49
Table B2: Tee Bracket Loads	49
Table B3: Corner Bracket Loads	54
Table B4: Tee Bracket Loads	54

List of Figures

Figure 1: Experimental Rig Structure and Base Plate	2
Figure 2: Spray Test Chamber	2
Figure 3: Flow Loop Schematic.....	3
Figure 4: Equipment Orientation	4
Figure 5: Operator Locations.....	4
Figure 6: Reactions to 9g Forward Load Factor—FC-72 Reservoir	7
Figure 7: Reactions to 9g Forward Load Factor—Rig Frame	11
Figure 8: Reactions to 9g Forward Load Factor—Shelf.....	13
Figure 9: Reactions to 9g Forward Load Factor—Assembly	15
Figure 10: Reservoir Drawing	18
Figure B1: Corner Joint	47
Figure B2: Corner Joint	48
Figure B3: Corner Joint Load Point.....	49
Figure B4: Tee Joint.....	50
Figure B5: Tee Joint Point Load.....	51

Figure B6: Corner Joint	52
Figure B7: Corner Joint	53
Figure B8: Corner Joint Load Point.....	54
Figure B9: Tee Joint.....	55
Figure B10: Tee Joint Point Load.....	55
Figure C1: Side View of Rig	58
Figure C2: Top View of Rig.....	59
Figure C3: Rear View of Rig	60
Figure C4: Three-dimensional View of Rig	61
Figure C5: Three-dimensional View of Rig	62
Figure C6: Three-dimensional View of Rig	63
Figure C7: Three-dimensional View of Rig	64
Figure C8: Three-dimensional View of Chamber	65
Figure C9: Wire Frame View of Exploded Test Chamber	67
Figure C10: Flow Schematic	69

Flight Manifest

Name	Affiliation	Preferred Days of Flight	Previous Flyer
Kirk Yerkes	AFRL	Tu-F	Yes, Jun 2007
Travis Michalak	AFRL	Tu-F	Yes, Jun 2007
Levi Elston	AFRL	Tu-F	Yes, Jun 2007
Rebekah Puterbaugh	AFRL	Tu-F	Yes, Jun 2007
Lt Chris De La Pena	AFRL	Tu-F	Yes, Jun 2007
Lt Leah Swanson	AFRL	Tu-F	Yes, Jun 2007
Lt Casandra Applin	AFRL	Tu-F	No
John McQuillen	NASA GRC	Alternate	Yes

Table 1: Flight Manifest

Experiment Background

Two-phase spray cooling is an example of a thermal management technique that may be utilized in high heat flux acquisition and high thermal energy transport concepts. It is one of many possible alternatives to the prevalent passive thermal management technologies, such as heat pipes and capillary pumped loops, which are currently used in space applications. Many researchers have investigated the utility of two-phase sprays for the thermal management of devices generating high heat fluxes. However, there has been little research addressing the physics and ultimate performance of two-phase spray cooling in the micro-gravity environment. This research is supported by John McQuillen at the NASA Glenn Research Center.

Experiment Description

The experiment consists of two primary components as shown in the equipment drawings. The first component is a rotatable spray test chamber containing the spray nozzles, heaters, primary condenser surface, and sump configuration to collect the liquid and condensate. The second component is the flow loop system that consists of two flow loops to manage the working fluid, FC-72, and a water loop to cool the spray test chamber. The experiment will be operated by applying electrical power to the Indium Tin Oxide (ITO) heaters or thick film resistance heaters, to generate heat, and spray cooling the heaters. Data will be collected on the heat transfer performance and thermophysics of spray cooling of the heaters in both high-g and micro-g environments.

Equipment Description

Reduced Gravity Flight Equipment

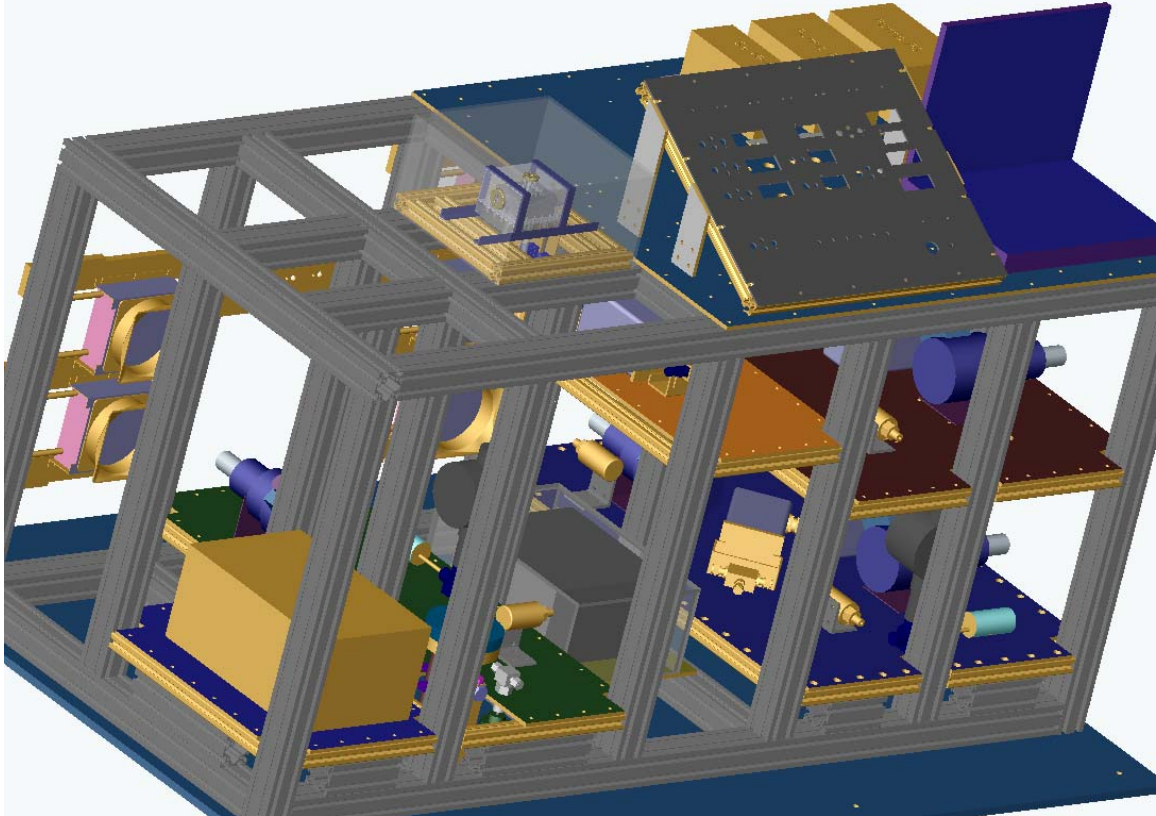


Figure A: Experimental Rig Structure and Base Plate

The entire experiment is constructed of an aluminum framework made of “8020” with a 0.5-inch thick aluminum base plate which serves as the mounting plate and a containment pan should any fluid leaks develop during flight tests (see Figure A). The experimental rig is 44” wide by 64.5” long by 44” high and weighs 705 lbs. All hardware used is of type experimental.

The spray test chamber, made of acrylic and phenolic, is very small and will be attached to the rig during a flight test (see Figure B). The spray test chamber consists of a 16 nozzle array, a resistive heater, and a fluid sump system. The inside of the chamber contains a foam wick structure as the primary condensation surface for the condensate liquid to return to the sump system. Liquid is collected in the sump and returned to the fluid

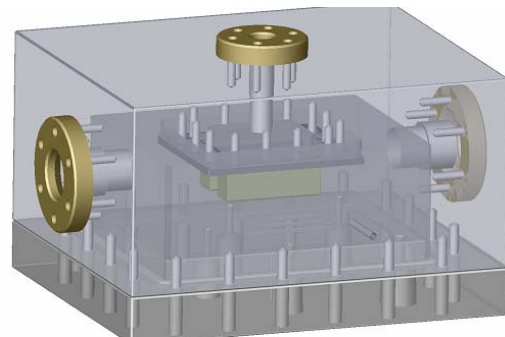


Figure B: Spray Test Chamber

delivery loop. Thermocouples mounted in the chamber are used to determine the heat transfer in and around the heater.

The flow loop consists of the pumps, flow meters, pressure and temperature transducers, pressure relief switches, reservoirs, electrical valves, liquid-air heat exchangers, re-heaters, and associated plumbing (see Figure C). These components serve to move the cooling water and the FC-72 working to and from the spray test chamber while monitoring flow rate, temperatures, and pressure. Various power supplies are also mounted to the experimental framework to provide electrical power to the various fluid motive components in the flow loop, heaters, and, instrumentation transducers.

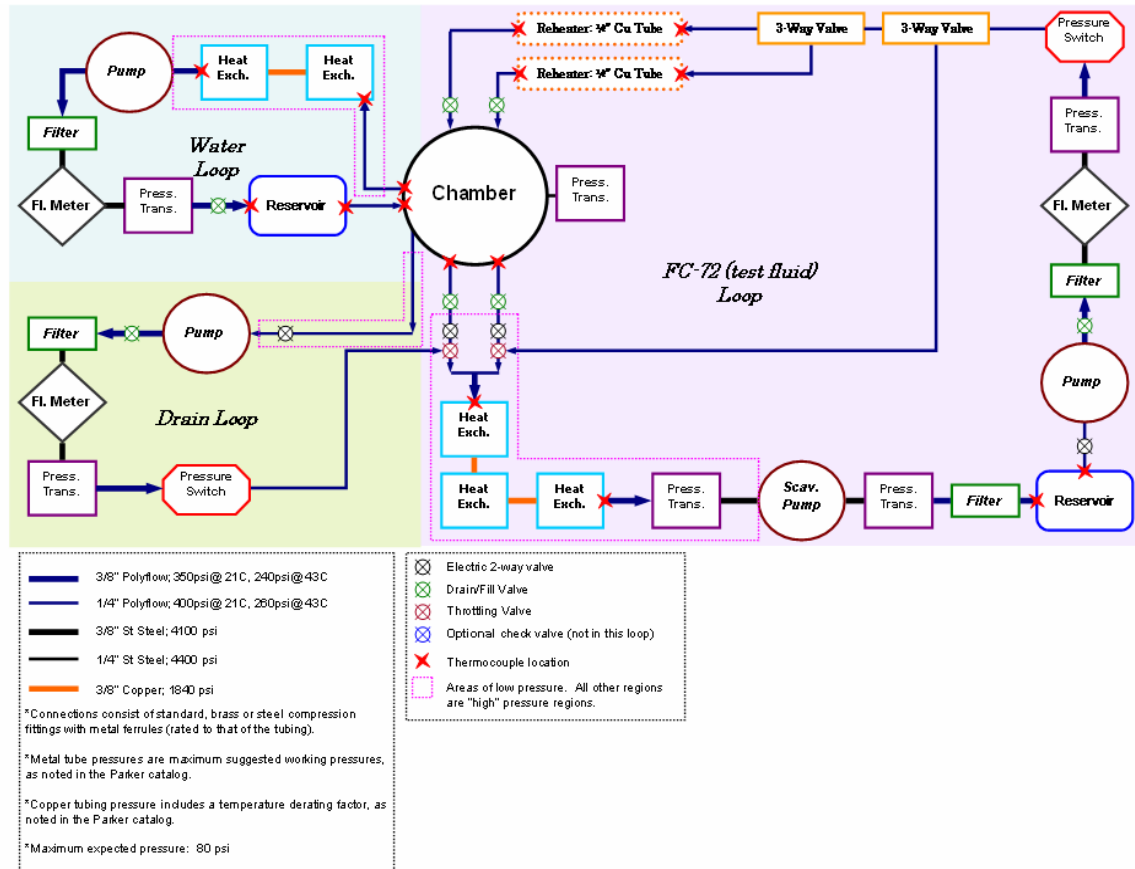


Figure C: Flow Loop Schematic

The experiment will be operated and monitored via a control panel and data acquisition system. The data acquisition system consists of a laptop coupled to an HP Data Acquisition/Switch Unit. Various safety features limit the maximum heater temperature and system pressure in order to maintain the experiment within safe operating parameters during the flight test. Both software and mechanical safety features allow for the safe shutdown in the event of a temperature or pressure excursion above allowable limits.

Proposed Layout of Equipment

The experimental hardware is configured to be installed on the C-9 with the long axis of the experiment rig parallel to the longitudinal axis of the aircraft. Figure D illustrates the

axis/orientation that will be used in this test series. A layout of the hardware during parabolas, including the location of operators, is shown in Figure E.

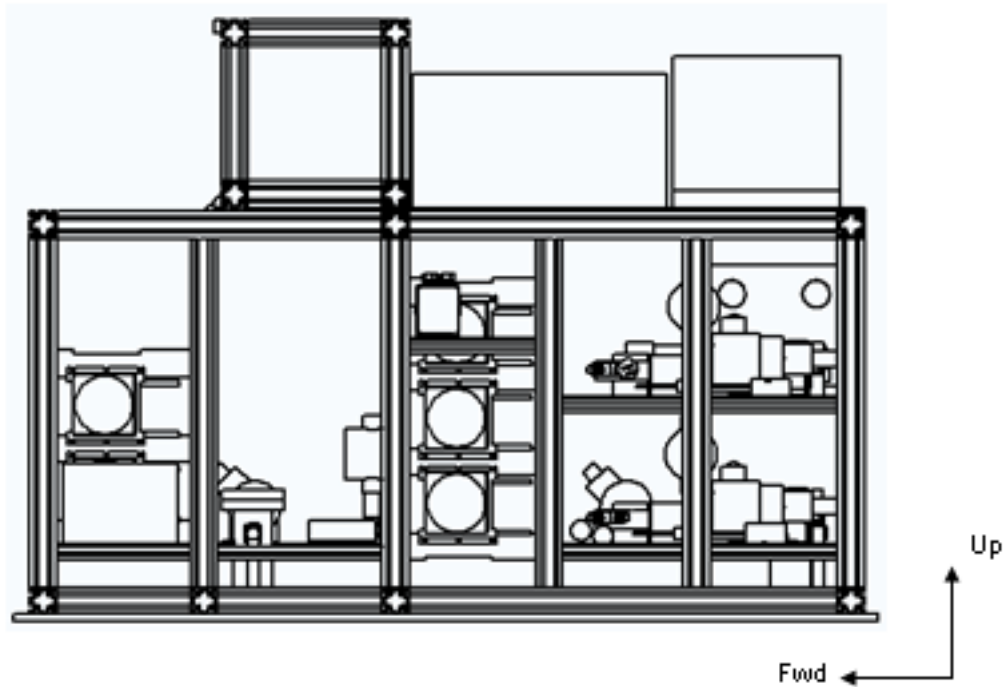


Figure D: Equipment Orientation

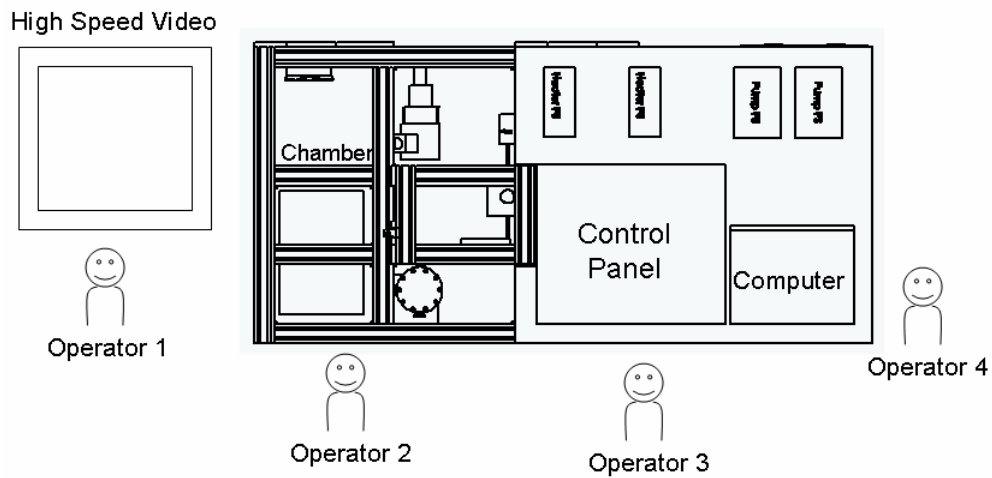


Figure E: Operator Locations

Special Handling Requirements

This experiment does not have components with any special handling requirements or any special hazards.

Items to Be Taken On-board

The following items will be taken on-board the C-9 aircraft: laptop, flashlights, spill kit, video cameras, digital still camera, notebooks, clipboards, gaffer's tape.

Special Requirements

This experiment does not have any special requirements (in-flight or ground based). This experimental setup will not free-float at any time during flight.

Structural Verification

Load Factors

This report analyzes the effects of emergency load factors specified by the *JSC Reduced Gravity Program User's Guide*. The components are analyzed with emergency load factors in all appropriate orientations.

Direction	Load Factor
Forward	9g
Aft	3g
Lateral	2g
Up	2g
Down	6g

Frame Components

Provided is the detailed analysis to the extent that the component warranted. This will serve as an example as to how the other components in Table 2 were analyzed.

FC-72 Reservoir

The FC-72 reservoir is mounted to the base plate and a shelf with four ¼-20 bolts and weighs 5.60 lbs. when filled with FC-72 to its operational level. Figure F shows the 9g forward load factor results.

Applied g loading:

Direction	Load (lbs)
Forward	50.4
Aft	16.8
Up/Lateral	11.2
Down	33.6

Tensile/shear loading: The independent tensile/shear loading per bolt was calculated as shown here:

$$\frac{(\text{applied load})}{\# \text{ of bolts}}$$

Direction	Load (lbs/bolt)
Forward	12.6
Aft	4.2
Up/Lateral	2.8
Down	8.4

Margins of Safety: The ultimate tensile margin of safety is calculated as shown here:

$$MS_{UT} = \frac{F_{UT}}{(applied\ load)(FS)} - 1$$

Where,

F_{UT} = Ultimate tensile failure load (other options include F_{YT} = Yield tensile failure load, F_{SU} = Ultimate shear failure load, and F_{SY} = Yield shear failure load)

FS = Factor of safety

Established NASA factors of safety are 2.0 or greater for all structural or fracture critical elements.

The tensile and shear loads for a grade 8 1/4-20 bolt are:

$$F_T = 4770\ lbs \quad F_S = 2860\ lbs$$

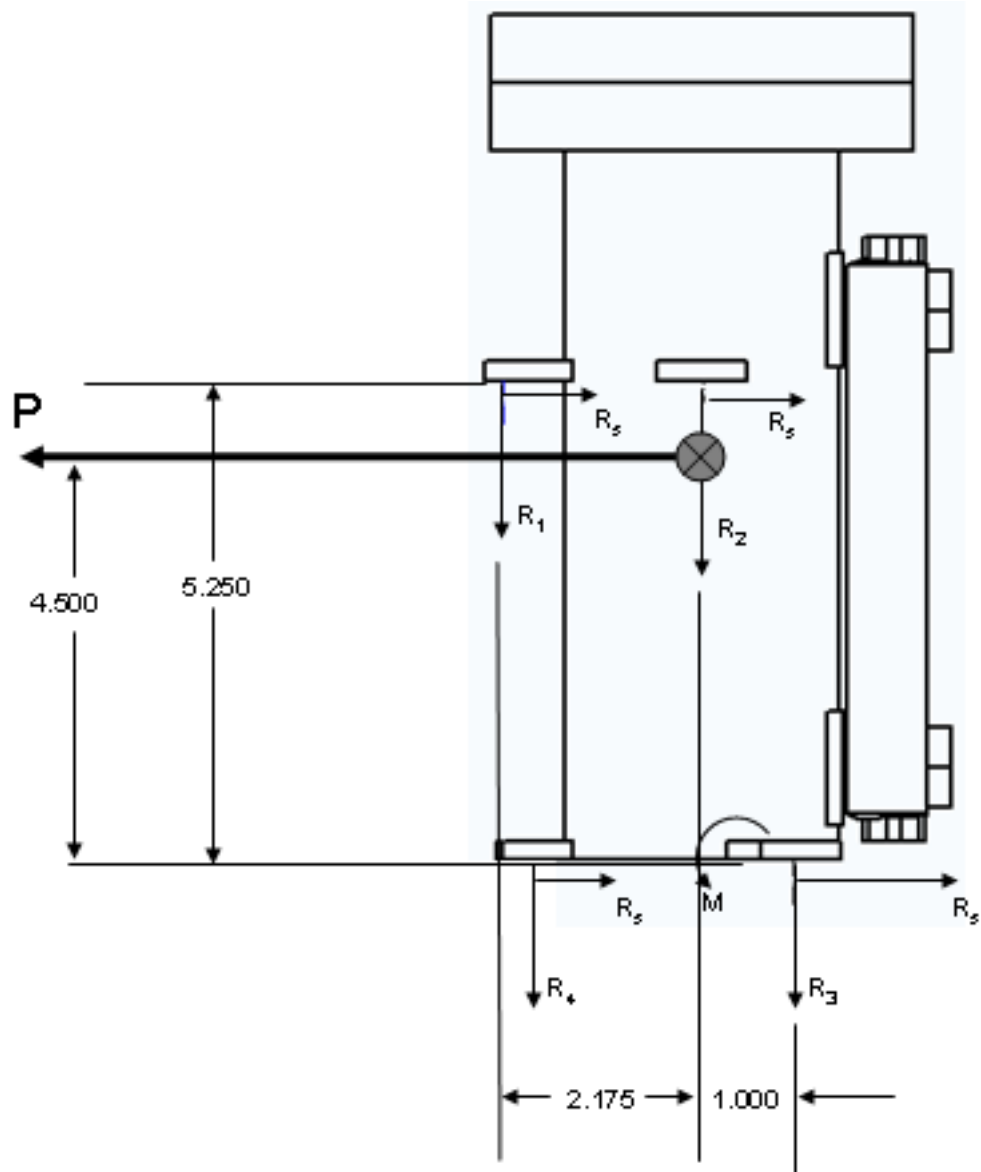


Figure F: Reactions to 9g Forward Load Factor—FC-72 Reservoir

Shear ultimate margin of safety:

$$MS_s = \frac{2860}{(12.6)(2)} - 1 = 112$$

With a margin of safety of 112, it is clear that the applied g-loads in any direction are small in comparison with the failure or yield loads for the bolts. All tensile/shear loads are two orders of magnitude below the failure loads and thus indicate large margins of safety for any force acting on this component.

Component Table

Table 2 contains all data pertinent to the analysis of the remaining frame components. It is evident from the ultimate tensile margins of safety that none of the components ap-

proach the failure loads of the bolts restraining them and therefore, no further analysis of these components is warranted.

Component	Weight (lbs)	Applied g-load (9g forward – lbs)	Bolt	Tensile/shear loading (lbs/bolt)	F_s (lbs)	MS F_s
Power Supply (480W)	3.85	34.7	10-32	8.7	1525	87
Power Supply (100W)	1.60	14.4	10-32	3.6	1525	210
Power Supply (chamber heater)	3.15	28.4	10-32	7.1	1525	106
Power Supply (1kW)	15.6	143.1	1/4-20	17.9	1525	41.5
Heat Exchanger Fan	3.35	30.2	10-32	5.0	1525	150
Heat Exchanger Assembly – Water Loop	10.5	94.5	MS51959	3.9	1525	192
Heat Exchanger Assembly – FC-72 Loop	14.2	127.8	MS51959	5.3	1525	142
Accelerometer	2.9	26.1	MS51959	6.5	1525	116
Water Reservoir	14.0	126.0	Grade 8 1/4-20	25.2	2860	55.8
Test Section	3.4	30.6	MS51959	3.8	1525	200

Table 2: Component Analysis

Rig Frame Analysis

This section will include a detailed analysis of the frame. The loads and moments acting on the rig frame base members are presented in Table 3. Therefore, the weight in Table 3 does not include the weight of the 80/20 extrusions below the lower joints and the center of gravity distance is measured from the top of those 80/20 extrusions.

The rig frame is constructed of 2020 extrusions from 80/20 Inc. All joints were assembled with their recommended bolt kits and all fasteners were torqued according to their specifications. The corner connections use the manufacturer’s 90° joining plates (P/N 4128) with two inside corner brackets (P/N 4114). Table 4 contains the extrusion properties and Table 5 has the joint strength values. 80/20 did not have documentation for the joints we are using with the 2020 extrusions. We performed static testing to develop our own figures and document the result in Appendix B. The frame is bolted to the base plate with MS51959-81 screws.

The total moment load resulting from the 9g forward load factor is reacted at eighteen joints connecting the vertical members to the base members (ignoring, conservatively, the effects of the eighteen joints at the top of the frame and the bracing that the shelves provide). The total moment load, as determined from the data of Table 3, is:

$$M_{Total} = 9g(\sum M) = 9(9649.51) = 86,845.59 \text{ in-lbs}$$

Dividing this total moment among the eighteen joints at the base of the frame yields a moment load per joint of 4824.76 in-lbs. Comparing this load to the joint ultimate strength:

$$MS_{Ult} = \frac{9700}{(4824.76)(1.5)} - 1 = .34$$

This gives us a positive margin of safety.

	Weight (lbs)	Z from top of 80/20 base (in)	Mz
Frame	111.60	18.25	2036.70
Shelf Supports	13.60	7.55	102.68
Shelves	50.70	8.11	411.18
Fasteners	41.30	12.00	495.60
Water Loop	10.50	14.99	157.40
FC72 Loop	14.20	12.29	174.52
Level One	49.90	5.47	272.95
Level Two	29.10	23.11	672.50
Level Three	2.60	20.50	53.30
Level Four	27.60	30.81	850.36
Test Section	3.40	30.81	104.75
Optical Mountings	1.50	21.01	31.52
Wiring & Connectors	43.00	18.25	784.75
Plumbing & Fittings	48.20	18.25	879.65
Miscellaneous	101.0	15.00	1515.0
Accelerometer	2.90	30.81	89.35
Power Supply (1kW)	15.60	3.50	54.60
Total	566.70	15.32	8686.8

Table 3: Experiment Rig Loads and Moments

	2020	1010
Material	6105-T5 Aluminum	6105-T5 Aluminum
Yield Strength	35000 psi	35000 psi
Tensile Strength	38000 psi	38000 psi
Elastic modulus	10,2000,000 psi	10,2000,000 psi
Moment of inertia (x-x and y-y)	.5513 in ⁴	.04413 in ⁴
Section area	1.223 in ²	.435in ²

Table 4: Extrusion Properties

	Double 90° Joining Plate with 90° Corner Brackets – 2020	Corner Bracket – 1010
Direct (shear) load		325 lb
Moment load	9700.0 in·lbs	375 in·lbs
Torsion load		180 in·lbs

Table 5: Joint Strength Values

With the tipping moment factored into the situation under 9gs forward, the tensile load on the bolts in the row farthest from the line of rotation will experience the highest load and that load can be calculated with this formula:

$$P_{t,\max} = \frac{FLd_k}{\sum_i nd_i^2}$$

Where

F = overturn load

L = vertical distance from overturn line to center of gravity

d_k = distance from overturn line to furthest bolt(s)

n = number of bolts in a row

d_i = distance from overturn line to row

The total rig, excluding the ½” aluminum base plate, weighs 566.7 lb and the center of gravity is 18.5 inches from the top of the base plate. This will result in the reactions illustrated in Figure G. Substituting the known values into this formula

$$P_{t,\max} = \frac{(9)(566.7)(18.5)(62)}{10(5^2 + 1.5^2 + 61^2 + 62^2) + 4(3^2 + 6^2 + 8^2 + 11^2 + 14^2 + 17^2 + 20^2 + 23^2 + 26^2) + \dots} = 27$$
$$\dots + 4(29^2 + 32^2 + 35^2 + 38^2 + 41^2 + 44^2 + 47^2 + 50^2 + 53^2 + 56^2 + 59^2) + \dots$$
$$\dots + 11(12.5^2 + 13.5^2 + 27^2 + 28^2) + 9(38.5^2 + 39.5^2)$$

$P_{t,\max}$ = tipping tensile load = 27 lbs/bolt

Margin of Safety: Using the margin of safety calculation stated earlier in this report, the ultimate and yield margins of safety in the tipping tensile load on the bolts in the row farthest from the line of rotation can be calculated by:

For MS51959 screws: $F_T = 2540$ lbs and $F_S = 1525$ lbs

$$MS_T = \frac{2540}{(27)(2)} - 1 \approx 46$$

With the large margins of safety, it is evident that the tensile load on the bolts in the row receiving the most tension during tipping will not be critical for bolt failure.

Combined Shear/Tensile Loading: The combined tipping shear and tensile loading is analyzed with the following formula:

$$\left(\frac{P_s}{F_s}\right)^3 + \left(\frac{P_t}{F_t}\right)^2 \leq 1$$

Where

P_s = applied shear load

F_s = shear failure load

P_t = applied tensile load (tipping)

F_t = tensile failure load

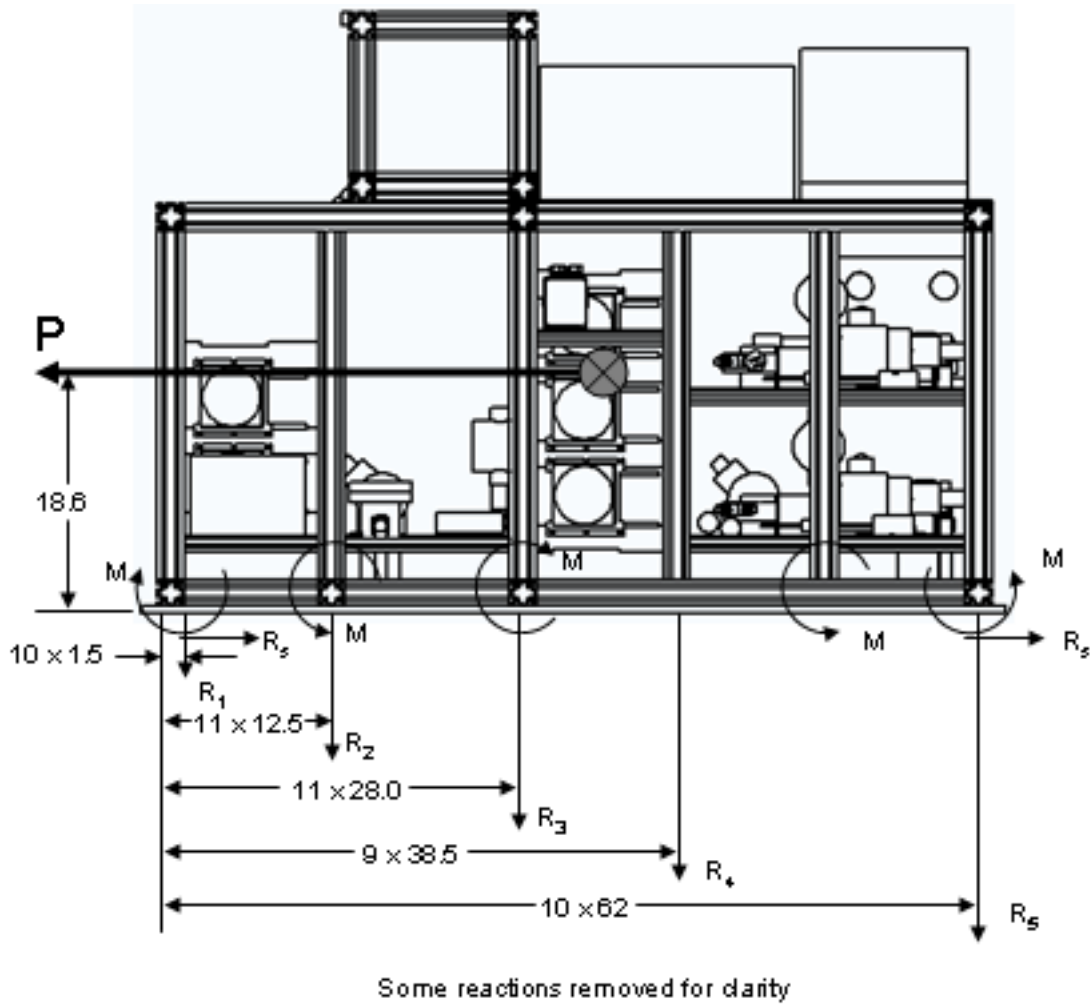


Figure G: Reactions to 9g Forward Load Factor—Rig Frame

The combined shear/tensile loading is analyzed below:

With a forward load of 572.6 at 9gs, which equals 5153.4 lbs, being held by 182 screws, the shear loading per screw is 28.3 lbs.

$$\left(\frac{28.3}{1525}\right)^3 + \left(\frac{27}{2540}\right)^2 = .00012 = .012\% \text{ of load carrying capacity used}$$

Shelves

Table 6 contains all data pertinent to the analysis of the shelves.

Shelf	Weight (including components – lbs)	Applied mass (9g forward – lbs)	Shear Loading (lbs/bolt)	Bolt	F _s (lbs)
1	17.8	160.2	7.0	¼-20	3300
2	17.2	154.8	5.2	¼-20	3300
3	10.1	90.9	4.1	¼-20	3300
4	36.5	328.5	8.0	¼-20	3300
5	29.2	262.8	6.0	¼-20	3300

Table 6: Shelf Loading

Shear Margin of Safety: The shear margin of safety for the first shelf is calculated as shown here:

$$MS_s = \frac{3300}{(7.0)(2)} - 1 \approx 235$$

With a margin of safety of 235, it is clear that the applied g-loads in any direction are small in comparison with the failure or yield loads for the bolts. All tensile/shear loads are two orders of magnitude below the failure loads and thus indicate large margins of safety for any force acting on this shelf.

Shelf Attachment to Frame: The shelves are attached to 1010 extrusions that are attached to the 2020 frame with corner brackets (P/N 4121 and 4122, right and left brackets respectively).

Shelf 4 is used to show the calculations for the shelves. It is supported by 8 extrusions and the 9g forward load factor results in reactions shown in Figure H. The 328.5 lb load spread over the 8 joints results in an individual loading of 41.06 lb. With a joint strength value of 325 lb, from Table 5, the margin of safety is:

$$MS = \frac{325}{41.06 \cdot 1.5} - 1 = 4.3$$

The center of gravity of the components on the shelf is at 2.75 in. This creates a moment load of:

$$M_{total} = 9g(36.5)(2.75) = 903.38$$

Dividing this total moment among the eight joints yields a moment load per joint of 112.9 in·lbs. This gives a margin of safety, using a joint strength value of 375 in·lbs from Table 5, of:

$$MS = \frac{375}{112.9 \cdot 1.5} - 1 = 1.2$$

By symmetry, the 3g aft and 2g lateral load factors are not considered critical for failure in the structure. The results of the calculations for the remaining shelves are shown in Table 7.

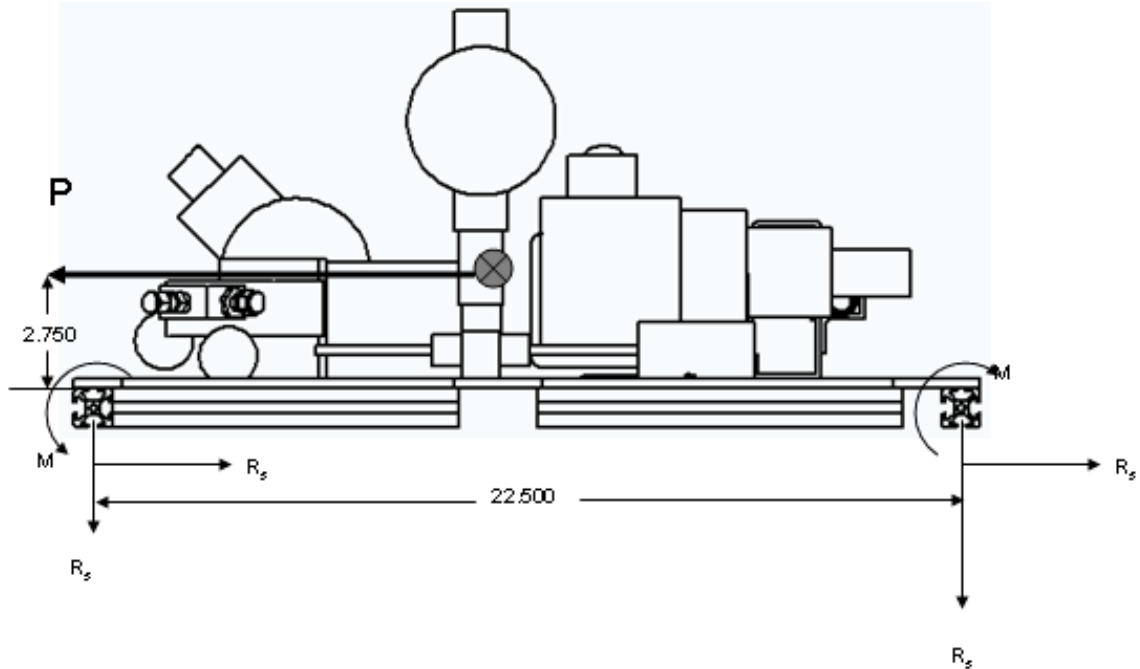


Figure H: Reactions to 9g Forward Load Factor—Shelf

Shelf	Weight (including components – lbs)	Applied mass (9g forward – lbs)	Shear load MS	Moment load MS
1	17.8	160.2	9.8	3.5
2	17.2	154.8	10.2	1.7
3	10.1	90.9	8.5	3.0
4	36.5	328.5	4.3	1.2
5	29.2	262.8	5.6	1.8

Table 7: Shelf Margins of Safety

Pull Testing

Components of the installation were pull tested using a Tenma Digital Force Gauge (operated by AFRL Research Engineers and calibrated by AF in-house Precision Measurement Equipment Laboratory). Data gathered from the pull tests are contained in Table 8. All components passed the pull test.

Component	Location	Weight (lbs)	Forward (lbs)	Aft (lbs)	Left (lbs)	Right (lbs)	Up (lbs)
Pump	Shelves 2,4,5	7.35	(132.3,135)	(44.1,135)	(29.4,135)	(29.4,135)	(29.4,60)
Flow meter	Shelves 2,4,5	3.75	(67.5,80)	(22.5,80)	(15,80)	(15,80)	(15,20)
2-way valve	Shelves 3,4,5	2.55	(45.9,60)	(15.3,60)	(10.2,60)	(10.2,60)	(10.2,15)
3-way valve	Shelves 4,5	2.85	(51.3,60)	(17.1,25)	(11.4,20)	(11.4,20)	(11.4,15)

Note: Format is (target, actual). All hold times are fifteen seconds.

Table 8: Pull Test Results

Analysis of Microgravity Experiment Rig as One Object

The weight and moment arm of the entire rig is in Table 9. It was calculated that the vertical center of gravity of the rig is 15.0 in. The base plate of the rig is bolted to the floor of the aircraft with 8 steel AN6 bolts. The independent shear/tensile load on the 8 bolts holding the base plate to the aircraft floor is calculated as:

Forward: 5538 lbs Up/Lateral: 1231 lbs

Description	Weight (lbs)	Z from aircraft floor (in)	Moment Arm (lbs·in)
Rig	543.5	17.6	9565.6
Reservoirs	23.2	4.5	104.40
Base Plate	139.1	0.25	34.78
Total	705.8	13.75	9704.75

Table 9: Assembly Weight and Moment Arm

The normal-gravity load per attach point is computed as 92.9 lb, well below the maximum allowable load of 200 lb. per attach point. The 9g forward load factor results in reactions shown in Figure I.

The tipping tensile load under 9gs forward on the bolts farthest from the line of rotation is calculated as:

$$P_{t,\max} = \frac{(9)(705.8)(13.75)(62.25)}{2(2.25^2 + 22.25^2 + 42.25^2 + 62.25^2)} = 441.3 \text{ lbs}$$

The shear load per bolt is:

$$P_s = \frac{(9)(705.8)}{8} = 794.0 \text{ lbs}$$

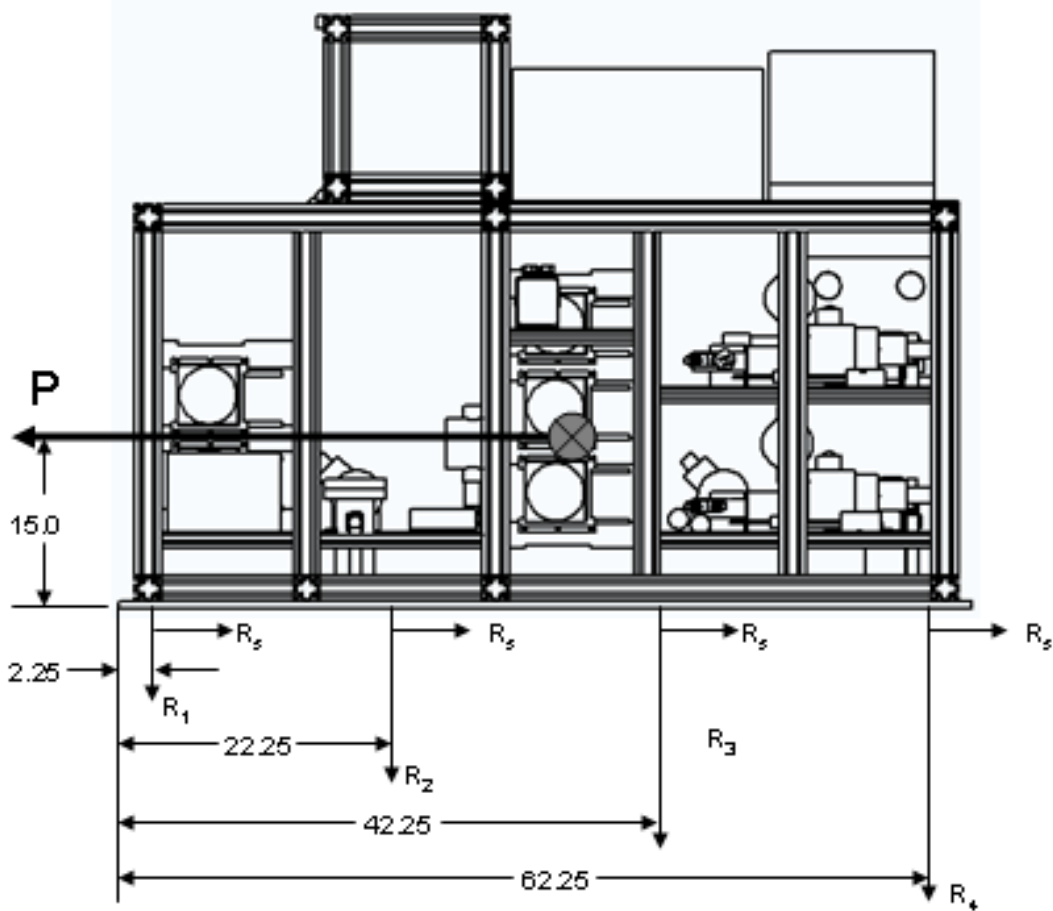


Figure I: Reactions to 9g Forward Load Factor—Assembly

Margin of Safety: Using the margin of safety calculation stated earlier in this report, the ultimate and yield margins of safety in the tipping tensile load on the bolts in the row farthest from the line of rotation can be calculated by:

For AN6 bolts: $F_{UT} = 10100$ lbs and $F_{YT} = 7740$ lbs

$$MS_{UT} = \frac{10100}{(441.3)(2)} - 1 = 10.44$$

$$MS_{YT} = \frac{7740}{(441.3)(2)} - 1 = 7.77$$

The ultimate shear strength for AN6 bolts is: $F_{SU} = 8280$ lbs. The margin of safety for shear loading is:

$$MS_{UT} = \frac{8280}{(794)(2)} - 1 = 4.21$$

With the large margins of safety, it is evident that the tensile load on the bolts in the row receiving the most tension during tipping will not be critical for bolt failure. The margin of safety for shear loading is large too.

Combined Shear/Tensile Loading: The combined tipping shear and tensile loading is analyzed with the following formula:

$$\left(\frac{794}{8280}\right)^3 + \left(\frac{441.3}{10100}\right)^2 = .002791 = .28\% \text{ of load carrying capacity used}$$

With the results above, the combined shear/tensile loading during 9gs forward, including tipping moment, is not critical for bolt failure.

As shown through this structural analysis, the Microgravity Experiment Rig will sustain the 9g forward loading with large margins of safety, indicating large margins in all other directions and planes.

Electrical Analysis

Electrical Schematic

Appendix A contains the electrical schematics for the microgravity experiment and shows the overall power distribution, fuses, and wire sizes.

Electrical Load

The Microgravity Spray Cooling Experiment requires 115 VAC, 60 Hz power for operation. The component requirements are in Table 10.

Electrical Emergency Flow Shutdown Switch

In the event that an emergency shutdown is required by failure of the test section or any other unforeseen circumstance, there is a large “emergency flow shutdown” switch that automatically shuts off power to all valves, heaters and pumps. This switch essentially shuts down the flow and the system can only be reset by pulling this button back up. The computer, display, and instrumentation are not affected by this emergency shutoff and thus permit the monitoring of the experiment if it is necessary.

In addition, individual items can be shut off by shutting off the main power switches on the control panel located on top of the frame.

Circuit	Power	Component	Load (amps)
1	115 VAC, 60 Hz	Water Heater	2
		FC Reheaters (2)	12
	Wire Gauge: 12		
	Max Outlet Current: 20 Amps	Total Circuit 1	14
2	115 VAC, 60 Hz	Power Supply	7
		Heater	4.5
	Wire Gauge: 12		
	Max Outlet Current: 15 Amps	Total Circuit 2	11.5
3	115 VAC, 60 Hz	1 kW Power Supply	10
		Heater	4.5
	Wire Gauge: 12		
	Max Outlet Current: 20 Amps	Total Circuit 3	14.5
4	115 VAC, 60 Hz	Power Supply	2
		Fans (5)	1
		Watt Transducers (2)	.004
		PID Controller (3)	.03
		Data Acquisition System	.5
			1
		Zero-Point Dry Well	1.5
		Laptop Computer	
	Wire Gauge: 12		
	Max Outlet Current: 15 Amps	Total Circuit 4	6.034

Table 10: Component Requirements

Loss of Electrical Power

In the event of a loss in electrical power, all valves, pumps, heaters and instrumentation will shut down. There will be no flow.

Pressure System

Flow Schematic

Appendix C contains the flow schematic, Figure CGG, for the microgravity experiment rig. Hose sizes are specified on the flow schematic. The bubbled numbers in Figure CGG correspond to the schematic reference numbers in Table 11.

Overpressure shutoff switches were set using the following rationale. Although it is not standard procedure, if the operating pressures are set at ground level, the gauge reading is converted into an absolute reading. Under normal operating conditions, cabin pressure is 11 to 12 psia. In the event of a rapid cabin depressurization, cabin pressure at altitude can fall to 4 psia. Therefore, the set pressure (SP) for the relief valves are set using the following function of the WP (in absolute pressure):

$$SP = 1.10 \cdot (WP - 4 \text{ psia}) = 1.1 \cdot (100 - 4) = 105.6 \text{ psia}$$

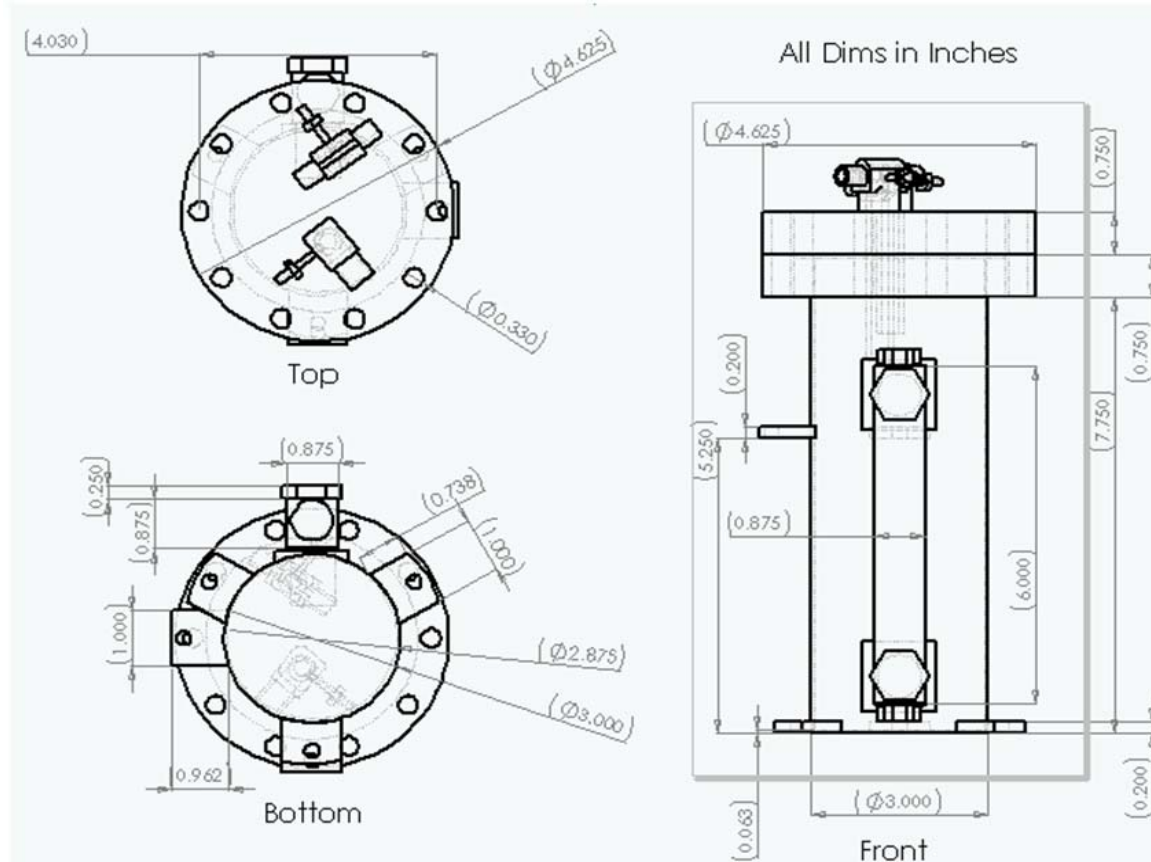


Figure J: Reservoir Drawing

The pneumatic pressure (PP) of components is set using the following equation:

$$PP = 1.25 \cdot 1.1 \cdot (WP - 4 \text{ psia}) + 14.7 \text{ psia} = 1.25 \cdot 1.1 \cdot (100 - 4) + 14.7 = 146.7$$

Both the set pressure and pneumatic pressure are differential pressures and the setting/testing occurs at a difference relative to ambient pressure.

The temperature within the test chamber will set the system pressure. The maximum temperature will be at the heater and is 100 °C. The maximum chamber temperature is set for 70 °C, which corresponds to a chamber pressure of 25 psiA. In order to drive flow through the spray nozzles, the pump needs to provide FC-72 at a pressure of 75 psiA.

Pressure switches will be set at 105 psiA and will shut off the heaters and pumps in the event of an overpressure situation. Shutting down the heaters and pumps will serve to remove the heat source and allow the pressure to equalize through the flow loop across the pumps resulting in a system pressure no more than 25 psiA. The volume of the chamber will also act as a fluid overflow reservoir to allow excess expansion of the FC-72.

All water flow components will be pressure tested to 111 psiG. All FC-72 flow components, including the test chamber, will be pressure tested to 132 psiG. Figure J shows a detailed drawing of the reservoir.

Pressure certification has been completed. Results are presented in Appendix D. In addition, the Variable Gravity Spray Cooling System’s Calibration Work Instruction, which shows the calibration methods and certified items used for calibration, has been attached in Appendix F.

Flow Component Listing

Table 11 contains a listing of the flow components. In-house MAWP items tested to max pneumatic pressure.

Table 11: Flow Components

Schematic Reference #	Component Description	MAWP (psig unless otherwise noted)	Manufacturer
<u>Water Loop</u>			
1	Heat Exchanger	250	Lytron
	Fan	n/a	Lytron
2	Heat Exchanger	250	Lytron
	Fan	n/a	Lytron
3	Pump	200	Tuthill
4	Filter	2150	Swagelock
5	Flow Meter	5000	Omega
	Pulse Amplifier	n/a	Omega
6	Pressure Transducer	100 (proof-200) psia	Omega
7	Reservoir/Sight Glass	290	MDC Vacuum/Lube Devices Inc.
8	Drain valve	1000	Swagelock
9	Pressure Switch	12000	United Electric Cont
<u>FC-72 Loop</u>			
10	Heat Exchanger	250	Lytron
	Fan	n/a	Lytron
11	Heat Exchanger	250	Lytron
	Fan	n/a	Lytron
12	Heat Exchanger	250	Lytron
	Fan	n/a	Lytron
13	Pump	200	Tuthill
14	Pump	250	Tuthill
15	Pump	250	Tuthill
16	Filter	2150	Swagelock
17	Filter	2150	Swagelock
18	Filter	2150	Swagelock
19	Flow Meter	5000	Omega
	Pulse Amplifier	n/a	Omega
20	Flow Meter	5000	Omega
	Pulse Amplifier	n/a	Omega
21	Pressure Transducer	200 (proof-400) psia	Omega
22	Pressure Transducer	200 (proof-400) psia	Omega
23	Pressure Transducer	200 (proof-400) psia	Omega
24	Pressure Transducer	100 (proof-200) psia	Omega
25	Reservoir	135	In-House
26	2-way valve	6000	Hoke/Simco Controls

Schematic Reference #	Component Description	MAWP (psig unless otherwise noted)	Manufacturer
	Actuator	n/a	Hoke/Simco Controls
27	2-way valve	6000	Hoke/Simco Controls
	Actuator	n/a	Hoke/Simco Controls
28	2-way valve	6000	Hoke/Simco Controls
	Actuator	n/a	Hoke/Simco Controls
29	2-way valve	6000	Hoke/Simco Controls
	Actuator	n/a	Hoke/Simco Controls
30	3-way valve	6000	Hoke/Simco Controls
	Actuator	n/a	Hoke/Simco Controls
31	3-way valve	6000	Hoke/Simco Controls
	Actuator	n/a	Hoke/Simco Controls
32	Drain valve	1000	Swagelock
33	Drain valve	1000	Swagelock
34	Drain valve	1000	Swagelock
35	Drain valve	1000	Swagelock
36	Drain valve	1000	Swagelock
37	Drain valve	1000	Swagelock
38	Pressure Switch	12000	United Electric Cont
39	Pressure Switch	12000	United Electric Cont
	Accelerometer	n/a	
Chamber	Chamber	135	In-House
40	Pressure Transducer	100 (proof-200) psia	Omega

Fluid Containment Plan

The test fluid is FC-72. FC-72 is a non-toxic and non-corrosive fluid. The total volume of FC-72 in the system is approximately 1.5 liters. The test chamber can hold 2.6 liters of FC-72, while the fluid reservoir between the two cut-off valves can hold approximately 1.5 liters. In the event of a leak in either the test chamber or the fluid reservoir, the FC-72 can be pumped into the other chamber. There are provisions to isolate the legs of the flow loop in the event of a leak.

There is a separate cooling loop which circulates water through a copper coil surrounding the test chamber to condense FC-72 vapor.

The junction between the rig and the baseplate has been sealed with RTV to contain any overnight leaks of fluid. Any penetrations through this plate, including those for test sections, tanks, etc, have also been sealed with RTV. The approximate volume, based on the height of the 80/20 channel and the enclosed area of the baseplate, is 44.75 liters. The base of the rig is divided into four cells. The smallest cell has an approximate volume of eight liters.

The majority of the plumbing within the flow loops is either metallic or polyflow and has been pressure certified to 1.25x (pneumatically) the Maximum Absolute Working Pressure (MAWP).

The experiment will be leak-checked prior to installation aboard the aircraft. After any test section or fluid change out, and prior to any flight, the rig will be leak-checked.

Absorbent PIGs, Kimwipes and Ziploc baggies will be strategically located around the rig to provide clean-up capability in the event of a leak. Used PIGs and Kimwipes will be sealed in the Ziploc baggies.

Laser Certification

No lasers will be used with this experiment.

Parabola Details and Crew Assistance

Forty parabolas per flight of 0.01g are requested. No modifications to either the timing between trajectories or the time duration of turns are anticipated.

Institutional Review Board

There are no plans to use human or animal test subjects and these tests are not of a biological nature.

C-9 Hazards Analysis

This section consists of AOD Forms 70 and 71.

HAZARD SOURCE CHECKLIST

Enumerate or mark N/A

- | | |
|-----|--|
| N/A | Flammable/combustible material, fluid (liquid, vapor, or gas) |
| 1 | Toxic/noxious/corrosive/hot/cold material, fluid (liquid, vapor, or gas) |
| 2 | High pressure system (static or dynamic) |
| N/A | Evacuated container (implosion) |
| N/A | Frangible material |
| N/A | Stress corrosion susceptible material |
| N/A | Inadequate structural design (i.e., low safety factor) |
| N/A | High intensity light source (including laser) |
| N/A | Ionizing/electromagnetic radiation |
| N/A | Rotating device |
| N/A | Extendible/deployable/articulating experiment element (collision) |
| N/A | Stowage restraint failure |
| N/A | Stored energy device (i.e., mechanical spring under compression) |
| N/A | Vacuum vent failure (i.e., loss of pressure/atmosphere) |
| 3 | Heat transfer (habitable area over-temperature) |
| 4 | Over-temperature explosive rupture (including electrical battery) |
| 5 | High/Low touch temperature |
| 6 | Hardware cooling/heating loss (i.e., loss of thermal control) |
| N/A | Pyrotechnic/explosive device |
| N/A | Propulsion system (pressurized gas or liquid/solid propellant) |
| N/A | High acoustic noise level |
| N/A | Toxic off-gassing material |
| N/A | Mercury/mercury compound |
| N/A | Other JSC 11123, Section 3.8 hazardous material |
| N/A | Organic/microbiological (pathogenic) contamination source |
| 7 | Sharp corner/edge/protrusion/protuberance |
| N/A | Flammable/combustible material, fluid ignition source (i.e., short circuit; under-sized wiring/fuse/circuit breaker) |
| 8 | High voltage (electrical shock) |
| N/A | High static electrical discharge producer |
| 9 | Software error or compute fault |
| N/A | Carcinogenic material |
| | Other: _____ |
| | Other: _____ |
| | Other: _____ |

DETAILED HAZARD DESCRIPTION

Use the following format for describing each identified hazard in detail.

Hazard Number: 1

Title:

Toxic fluid – FC-72

Hazard Description:

Water is not a health hazard.

FC-72 is non-toxic and inert; the quantity used in this experiment will not affect the aircraft environment

At room temperature: Eye contact--Contact with the eyes during product use is not expected to result in significant irritation. Skin contact--Contact with the skin during product use is not expected to result in significant irritation. Inhalation--No health effects are expected. Ingestion--No health effects are expected

At temperature >200°C: hydrogen fluoride and perfluoroisobutylene is generated.

Hazard Cause(s):

Leak, spill, or component failure causes release of test fluid from closed experimental system. Over temperature of FC-72 in excess of 200°C.

Hazard Control(s):

Pressure-testing of equipment of at least 1.25 times the operating pressure will ensure adequate containment of fluids.

Safety cut-out measures will monitor heater temperature, to not exceed 100°C, and shut down operation in potentially-hazardous circumstances.

Should a leak occur, the flow system is designed to be able to isolate the FC-72 either in the test chamber or the reservoir.

DETAILED HAZARD DESCRIPTION

Use the following format for describing each identified hazard in detail.

Hazard Number: 2

Title:

High pressure system

Hazard Description:

Over pressurization of flow system causes a component to fail; releasing test fluids and possibly injuring nearby personnel.

Hazard Cause(s):

Flow system blockage, or cabin depressurization causes unexpected pressure differential across an experiment component.

Hazard Control(s):

Test chamber: Temperature within the chamber will set the pressure. A maximum working temperature of 70 °C in the chamber will result in a maximum of 25 psiA.

FC-72 Nozzle inlet: Inlet pressure to the spray nozzle will be limited to 75 psiA

Water flow components will be pressure tested to 111 psiG.*

FC-72 flow components, including the test chamber, will be pressure tested to 132 psiG.*

Pressure switches will be set at 105 psiA and will shut off the heaters and pumps in the event of an over-pressure situation. Shutting down the heaters and pumps will serve to remove the heat source and allow the pressure to equalize through the flow loop across the pumps resulting in a system pressure no more than 25 psiA. The volume of the chamber will also act as a fluid overflow reservoir to allow excess expansion of the FC-72 or isolation of the FC-72 in the event of a leak.

*All noncommercial components will be pneumatically pressure tested to at least 1.25 times the maximum working pressure. Note: Maximum working pressure for FC-72 system is 100 psiA.

Maximum working pressure for water system is 75 psiA.

DETAILED HAZARD DESCRIPTION

Use the following format for describing each identified hazard in detail.

Hazard Number: 3

Title:

Heat transfer

Hazard Description:

Increase in temperature of habitable area surrounding experiment causes discomfort and/or burning in personnel on board

Hazard Cause(s):

Overheat on one or more components causes an increase in the temperature surrounding the experiment package.

Spill or leak of heated fluid causes an increase in the temperature surrounding the experiment package.

Hazard Control(s):

Maximum expected heater operating temperature of 100 °C and test chamber temperature of 70 °C – minimal heat load, will not significantly alter the environment surrounding the experiment package. This will allow high heat flux testing at the heater without significantly altering the chamber temperature.

Over-temperature controls and safety cut-out measures prevent overheating by shutting down the experiment.

DETAILED HAZARD DESCRIPTION

Use the following format for describing each identified hazard in detail.

Hazard Number: 4

Title:

Over temperature explosive rupture

Hazard Description:

Increase in temperature within the test cell will result in an increase in pressure. Should this increase in temperature result in a pressure exceeding the rating of the viewport to the test chamber, an explosive rupture may occur.

Hazard Cause(s):

The temperature in the chamber is balanced by the heat input from the heaters and the water coil around the chamber walls. The test chamber is controlled at a temperature consistent with a desired pressure. The maximum allowable chamber temperature is 70°C, which will result in a chamber pressure of 25 psiA.

Hazard Control(s):

The test chamber is constructed with 1-inch Lexan viewports mounted to the test chamber. In addition, over-temperature switches will shut off the heaters in the event of a temperature excursion in the test chamber. The Lexan viewports have been structurally analyzed to verify structural integrity in the event of a pressure excursion. The test chamber along with the FC-72 flow components will be tested to 132 psiG.

DETAILED HAZARD DESCRIPTION

Use the following format for describing each identified hazard in detail.

Hazard Number: 5

Title:

High touch temperature

Hazard Description:

Components or surfaces feel hot to the touch; may cause minor burns to personnel who come in contact with them.

Hazard Cause(s):

Improperly insulated surfaces expose personnel to hot surfaces.

Hazard Control(s):

High temperature components will be insulated or thermally shielded from the environment.

The test chamber, as well as potentially exposed components and surfaces, will be insulated.

DETAILED HAZARD DESCRIPTION

Use the following format for describing each identified hazard in detail.

Hazard Number: 6

Title:

Hardware cooling loss

Hazard Description:

Planned cooling measures fail, resulting in overheating of hardware, potentially resulting in hazardout temperatures in and around the experimental test package

Hazard Cause(s):

Line blockages

Pump failure

Heat exchanger fan failure

Hazard Control(s):

Safety cutout measures will ensure temperature control, < 70°C, including a manual emergency-shutdown-switch, which will shut down all potentially dangerous components.

DETAILED HAZARD DESCRIPTION

Use the following format for describing each identified hazard in detail.

Hazard Number: 7

Title:

Sharp corners

Hazard Description:

Sharp corners or other surfaces on experimental test package cause minor cuts/abrasions to personnel.

Hazard Cause(s):

Unintentional contact with sharp corners may cause minor cuts/abrasions.

Hazard Control(s):

A safety/grab rail will be installed along the perimeter of the experimental test package frame.

Any remaining exposed sharp edges or corners will be padded.

DETAILED HAZARD DESCRIPTION

Use the following format for describing each identified hazard in detail.

Hazard Number: 8

Title:

High voltage

Hazard Description:

Potentially lethal voltages will be used to power the experiment.

Hazard Cause(s):

1. Wire breaking and shorting to chassis.
 2. Shorting of voltage potential to ground.
 3. Breakdown of wire because of high current load.
-
-
-
-

Hazard Control(s):

1. All power lines are protected using circuit breakers and/or fuses.
 2. All voltage potentials are shielded and proper connectors are used.
 3. Experiment package is chassis grounded.
 4. All wiring is rated for operating currents.
-
-
-
-

DETAILED HAZARD DESCRIPTION

Use the following format for describing each identified hazard in detail.

Hazard Number: 9

Title:

Software error

Hazard Description:

Loss of experimental control (ie: temperature/pressure control) due to software error.

Hazard Cause(s):

Computer failure causes software not to work

Aircraft power loss/malfunction.

Hazard Control(s):

Computer operates on battery backup in case of power loss.

All safety cut-out measures will be controlled via hardware, rather than software.

Tool Requirements

Tools supplied by the Reduced Gravity Office should be sufficient for loading and removal of the experiment from the aircraft. In addition, we are also bringing our “FOD” rated tool kit, purchased from Snap-On, that has all the tools contained in foam cutouts within several zippered “packs”. An inventory sheet is attached with the tool kit that includes a CTK# that matches the etched number on each tool.

Photo Requirements

Request high-speed video camera for recording experimental results. The experiment contains sensitive non-classified information and therefore we request that pictures (from other researchers or NASA photographers) be directed away from our experiment so we are not in the background of any shots.

Aircraft Loading

The experiment can be loaded with a forklift and either directly on its own pallet or the lifting pallet/basket supplied by the Reduced Gravity Office. The experiment assembly contains casters that are removable. The experiment has a base plate of area 19.1 sq. ft. and weights 705 lbs which will result in a floor pressure of 36.91psi. The experiment will be loaded using four casters (10 lbs each) with two wheels on each. Therefore, the expected additional load carried by each caster will be 195.5 lbs and the additional load supported by each individual wheel will be 97.75 lbs. The caster wheels have a loaded contact area of approximately 0.5 sq. in. and the resulting floor pressure is expected to be 195.5 psi. Four jacks (10 lbs each) have a contact area of 12.75 sq. in. and are used to lower the experiment to the floor. The resulting floor pressure will be 15.33 psi.

Ground Support Requirements

It is necessary to have access to 115 VAC, 60 Hz in order to operate the assembly, either for final functional checks or the Test Readiness Review. No other ground requirements are necessary.

Hazardous Materials

FC-72 will be the primary working fluid. Temperatures exceeding 200 °C will result in FC-72 generating hazardous materials, hydrogen fluoride and perfluoroisobutylene. Because the heater temperatures will be limited to 100 °C there will be no hazardous material generation.

Material Safety Data Sheets

See Appendix E for the material safety data sheet (MSDS) for the FC 72.

Test Procedures

Transportation/Storage

1. Test rig and all support equipment will be transported via a box rental truck, driven by AFRL personnel.
2. AFRL requests an area inside the RGO's setup bay to store and run preliminary tests on the ground.

Loading Checklist

1. The use of a forklift is requested to load onto the aircraft.
2. Verify that all mounting bolts are tight.
3. Verify power connections, 115 VAC 60 Hz.

Pre-test Checklist

1. Ascertain that the coolant and water systems are filled with sufficient liquids.
2. Plug in cords for the four AC circuits, 20 amp capacity for circuits 1 and 3 and 15 amp capacity for circuits 2, and 4.
3. Turn on Breakers 1, 2, 3 and 4, verify green indicators for each.
4. Verify that all toggle switches are in the off (down) position and all potentiometers are at 0 (fully counterclockwise).
5. Press the Start button and verify red indicators for the pumps and target heaters and red and blue indicators for the flow bypass.

Testing Checklist

1. Turn on the laptop computer, log in and start the data acquisition program.
2. Verify system pressures are appropriate for coolant temperature.
3. Turn on the water pump and set the flow rate as indicated on the computer display using the potentiometer; verify green indicator.
4. Turn on the coolant pumps and set the flow rates as indicated on the computer display using the potentiometers; verify green indicators and flow rate on the digital readouts.
5. Switch the bypass toggle switches to the up position and verify spray in the chamber.
6. Set the reheater PID controllers to the desired temperature and set the alarm cutout temperatures.
7. Switch the PID controllers on; verify green indicators.
8. When the fluids are at operating temperature, the reheater indicators will be cycling.
9. Verify that the over-temperature PID controller alarm settings are correctly adjusted.
10. Turn on the video cameras and place them in record mode.
11. Turn on the target heater switches and verify green indicators.
12. Set the target heater wattage using the potentiometers.
13. Take data as appropriate to the flight test plan.

Post-test Checklist

1. Switch off target heaters and set potentiometers to the 0 position.
2. Switch off reheater switches.
3. Switch bypass toggle switches to the down position.
4. Switch off all pumps and set potentiometers to the 0 position.
5. Switch off video cameras.
6. Stop data acquisition and shut down computer.
7. Switch off the four Breakers.

Leak Shut Down Procedure

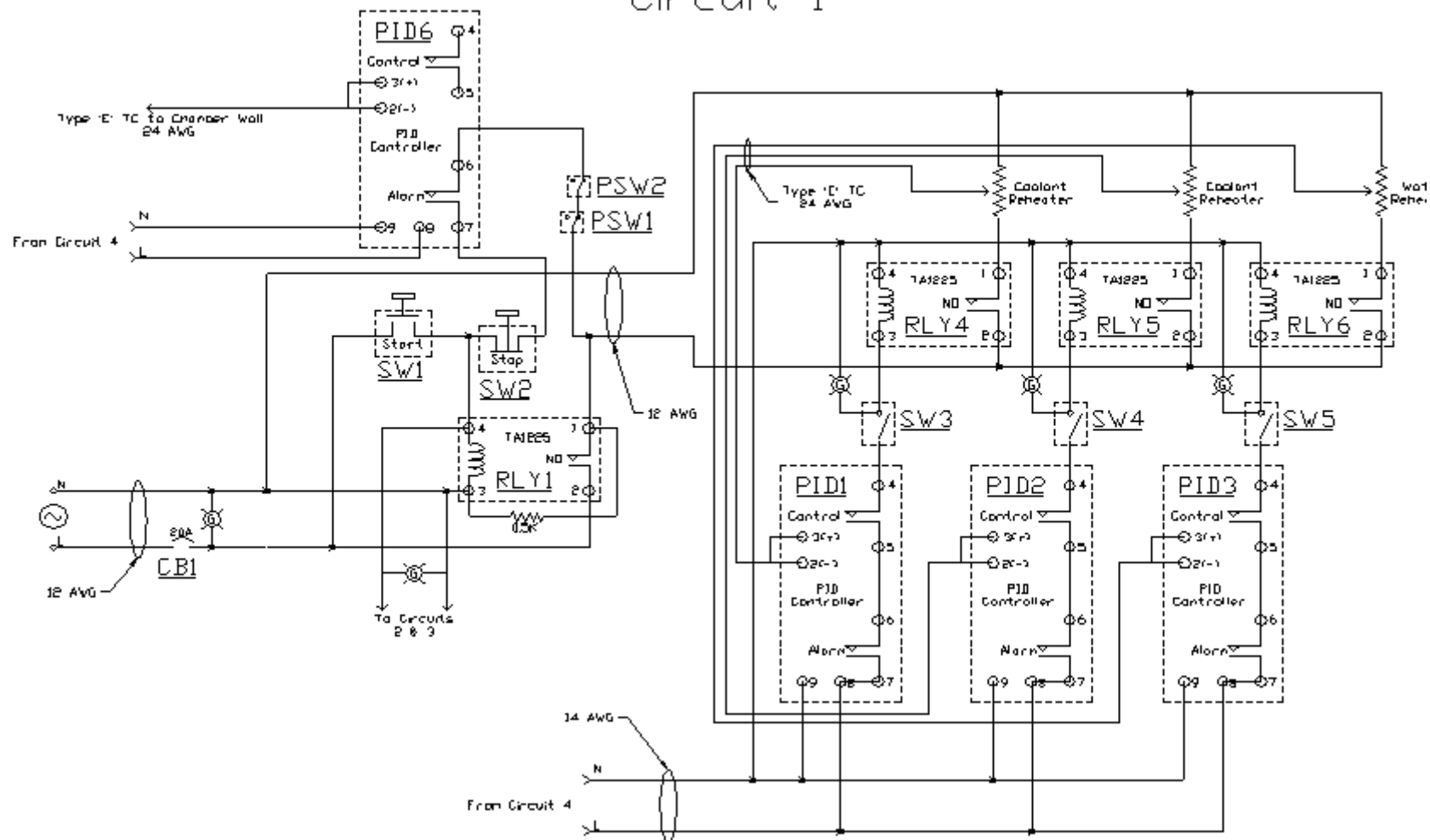
1. Identify the location of the leak and use the pump to isolate FC-72 away from leak into either the chamber or the fluid reservoir and close the appropriate valves.
2. Hit Panic button to shutdown the system and allow the system to come to a low pressure equilibrium.
3. Assess source of leak for fixability. If fixable, (e.g., wrong valve is open), seal leak; otherwise proceed to step 4.
4. Use either absorbent PIGs or Kimwipes to mop-up leak. Place wet materiel into zip lock baggie or vent tank.

Emergency Shut Down Procedure

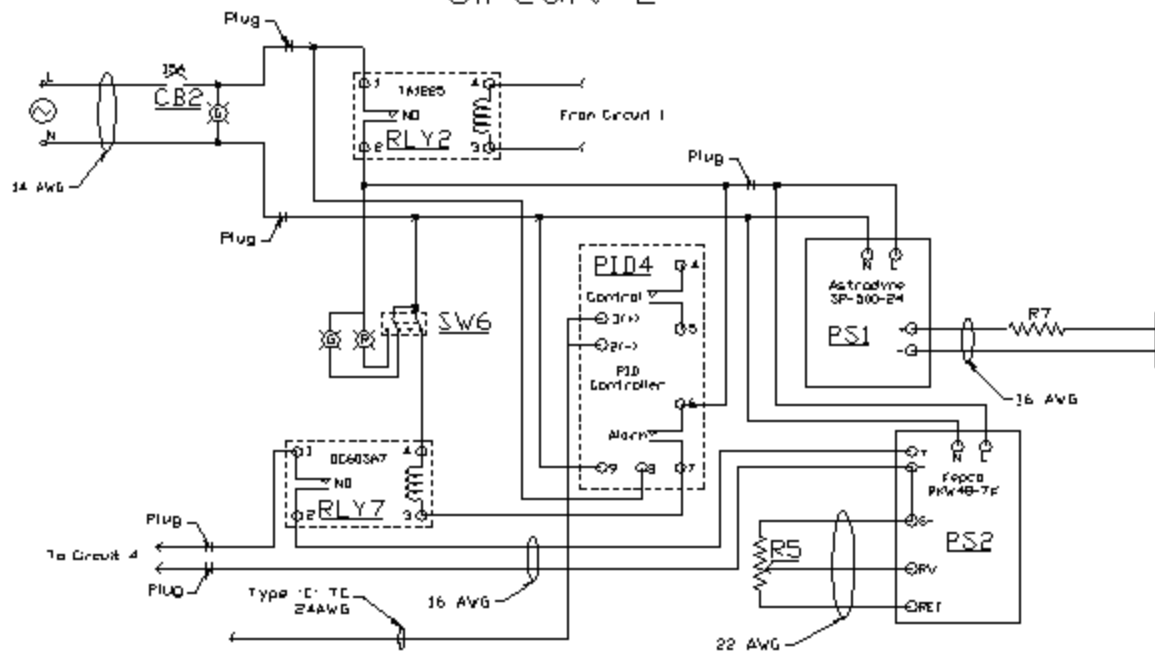
1. Hit Panic button.
2. Ensure all power is off.
3. Visually verify and contain any leaks using absorbent PIGs or Kimwipes. Place wet materiel into zip lock baggie or vent tank.

Appendix A: Electrical Schematic

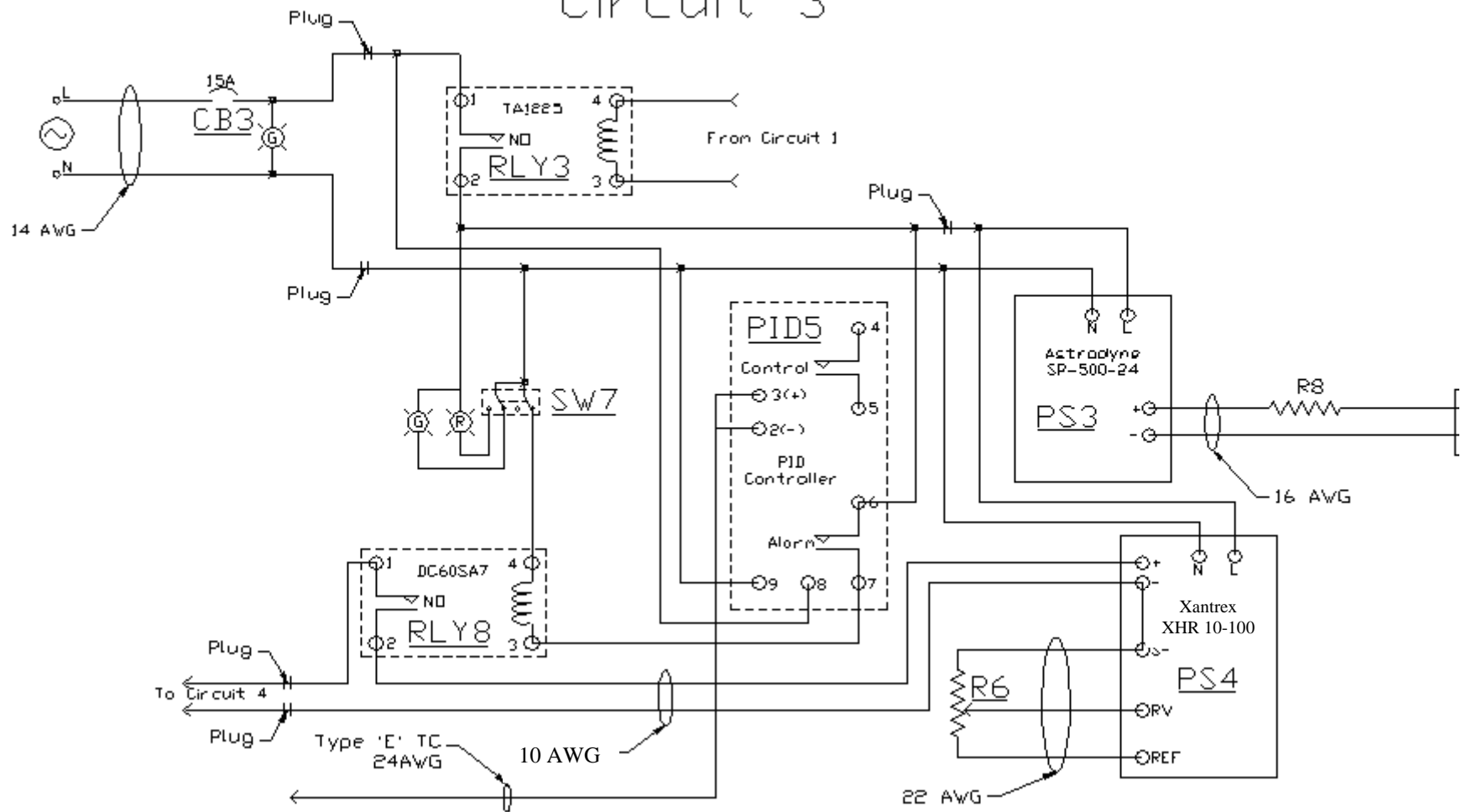
NASA Spray Experiment Circuit 1



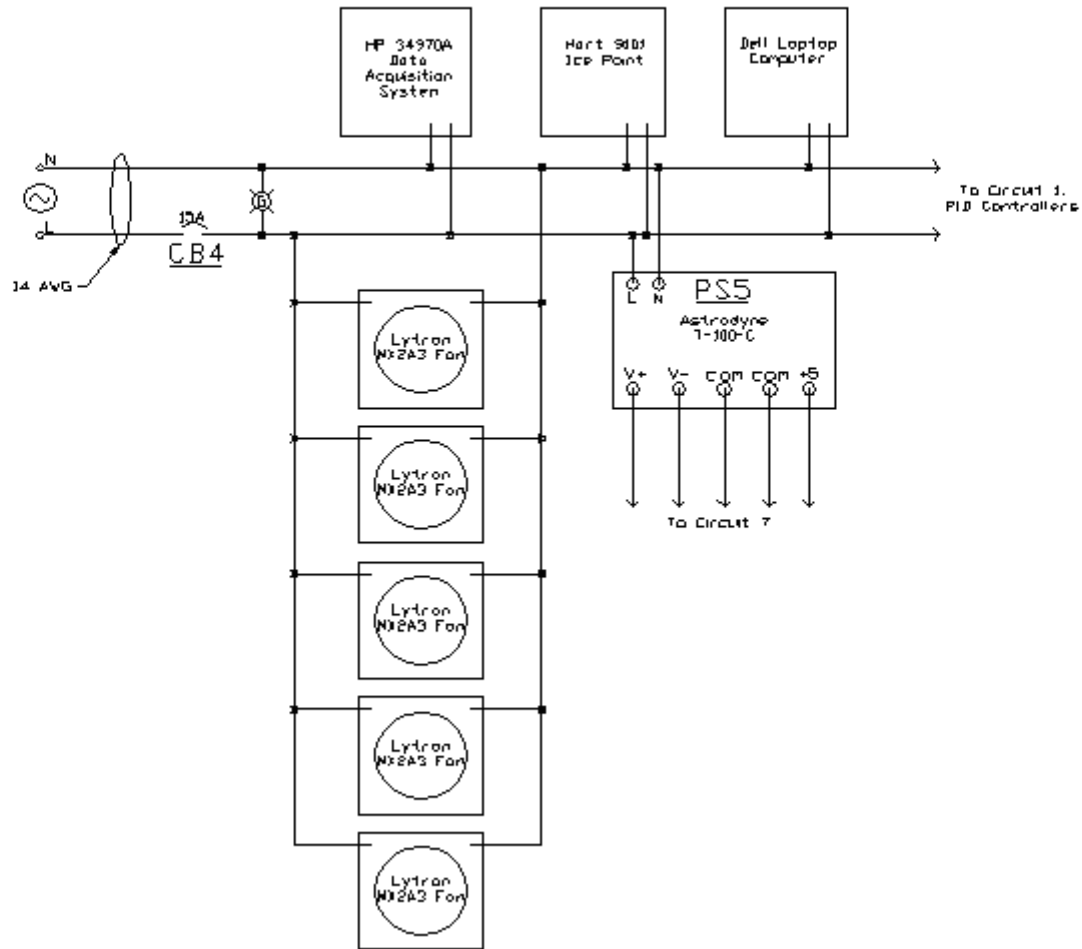
NASA Spray Experiment Circuit 2



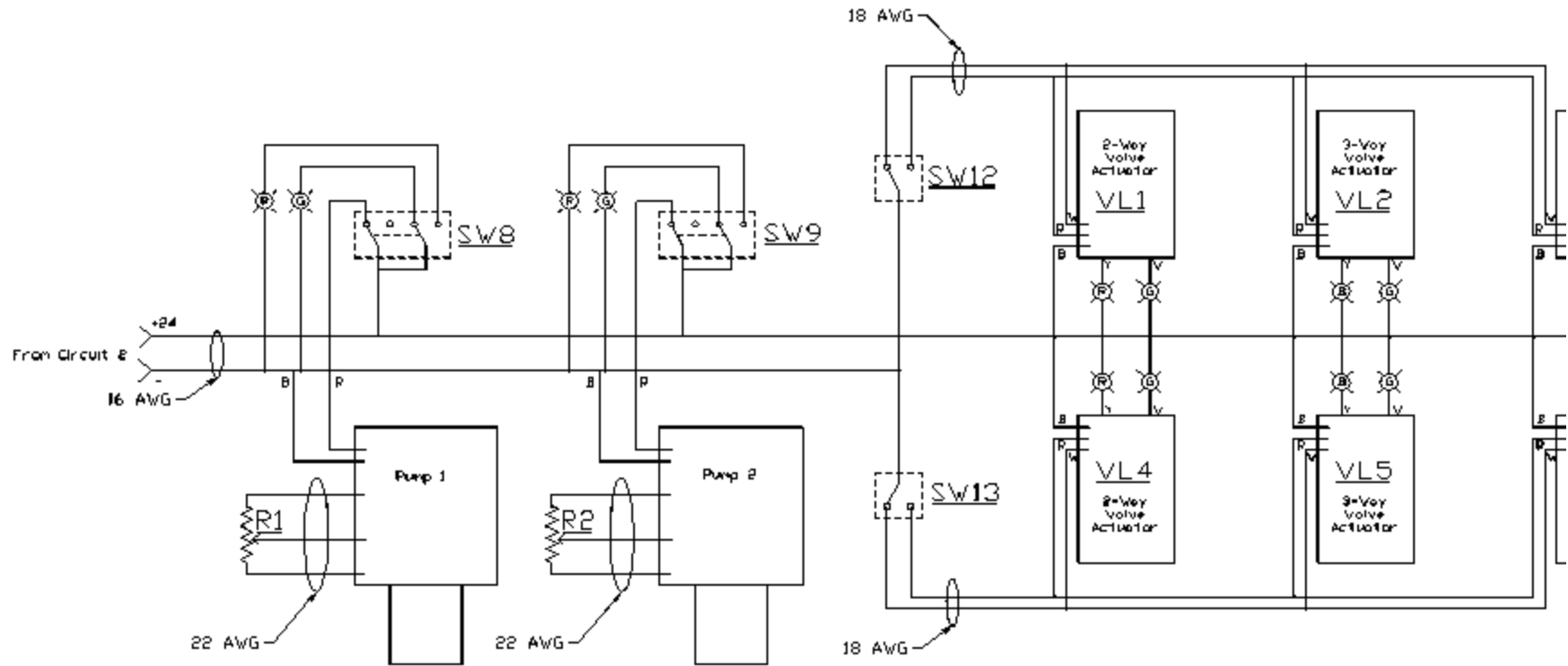
NASA Spray Experiment Circuit 3



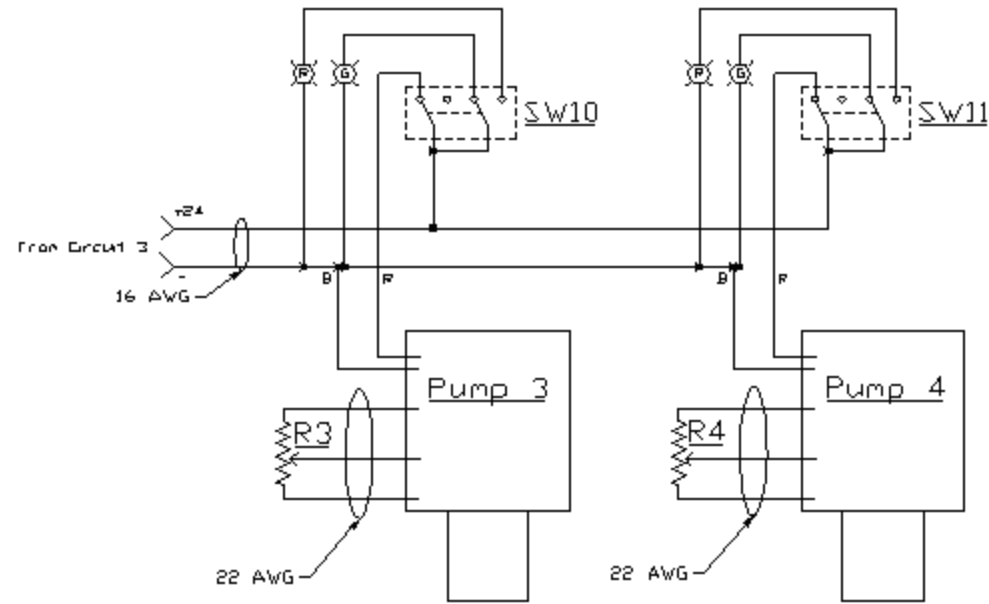
NASA Spray Experiment Circuit 4



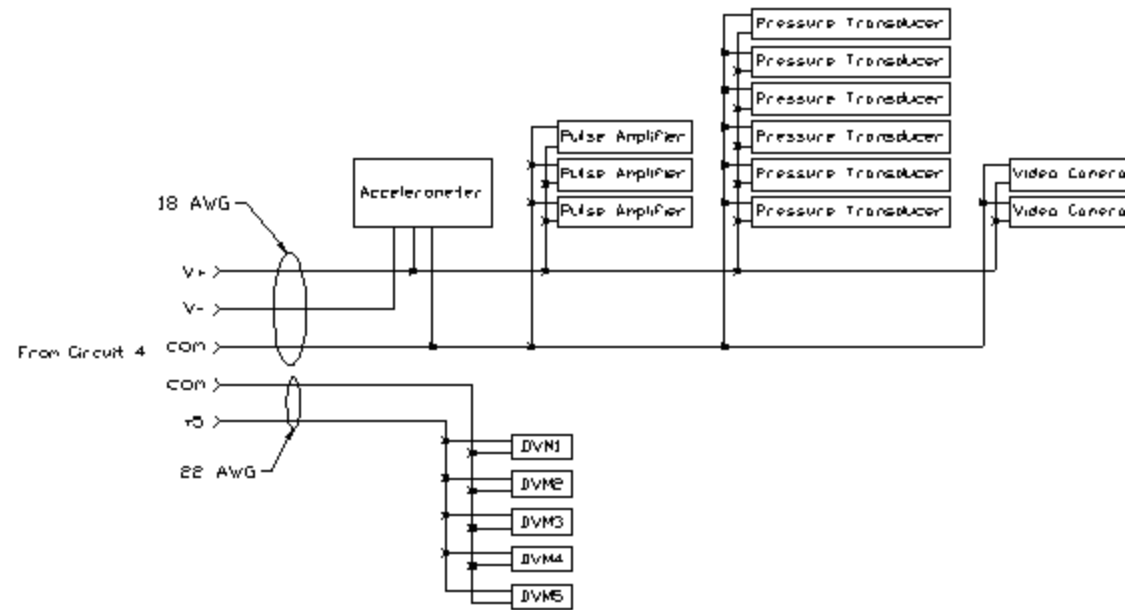
NASA Spray Experiment Circuit 5



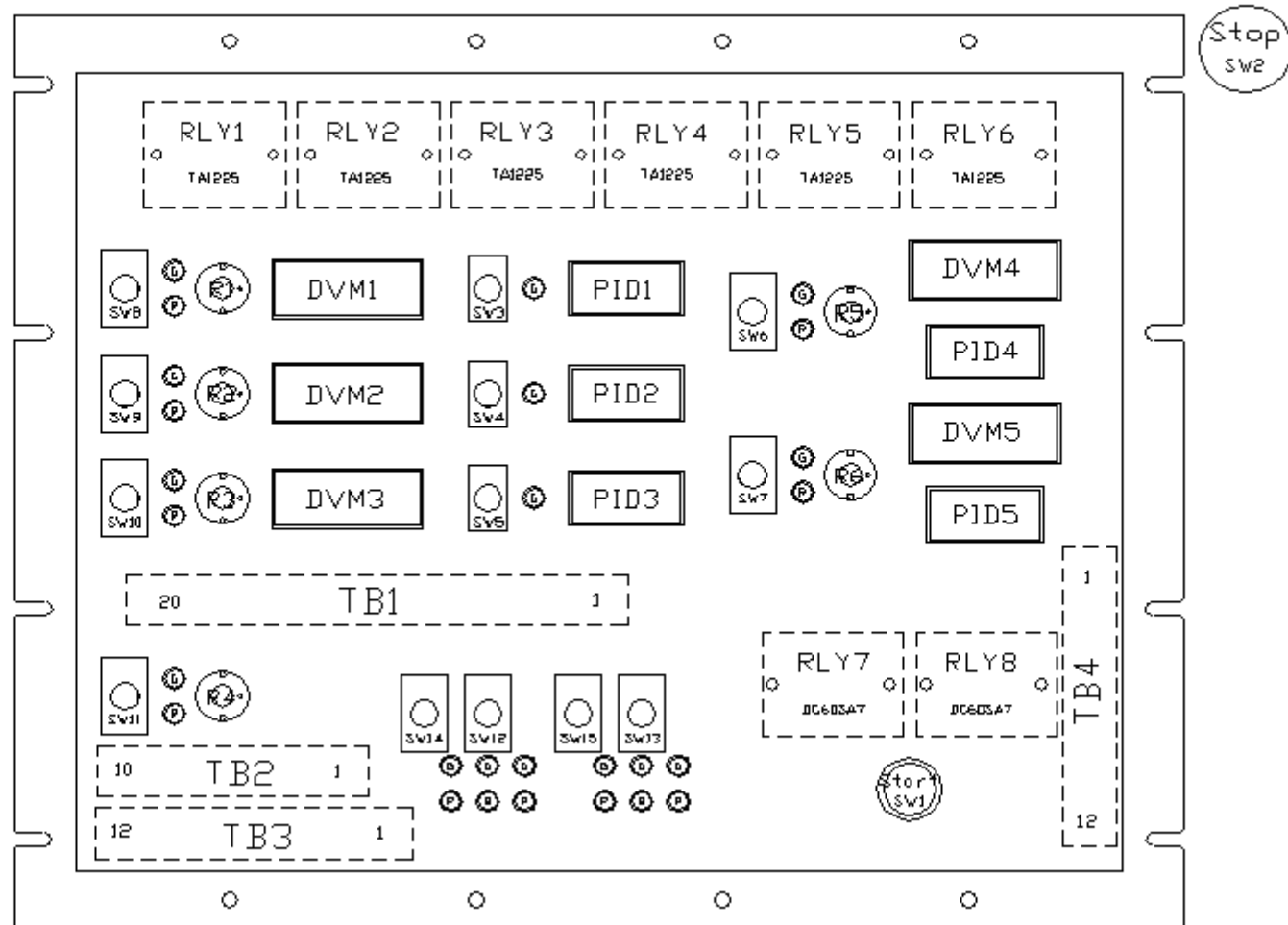
NASA Spray Experiment Circuit 6



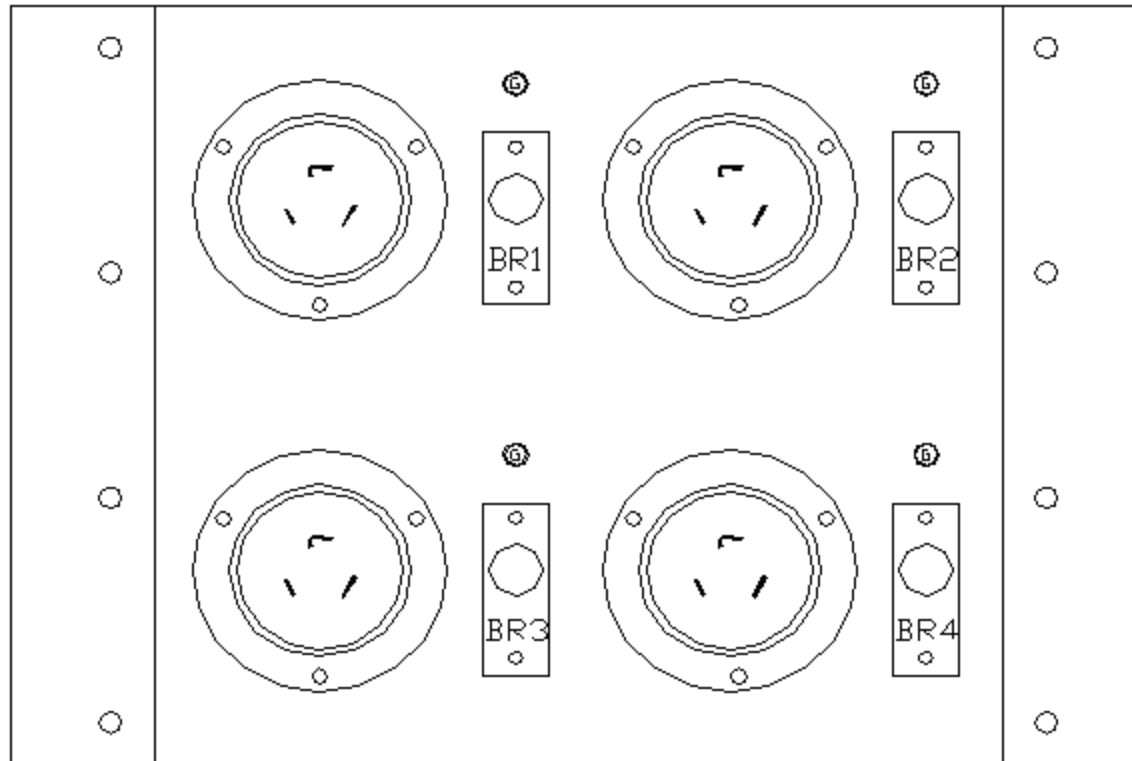
NASA Spray Experiment Circuit 7



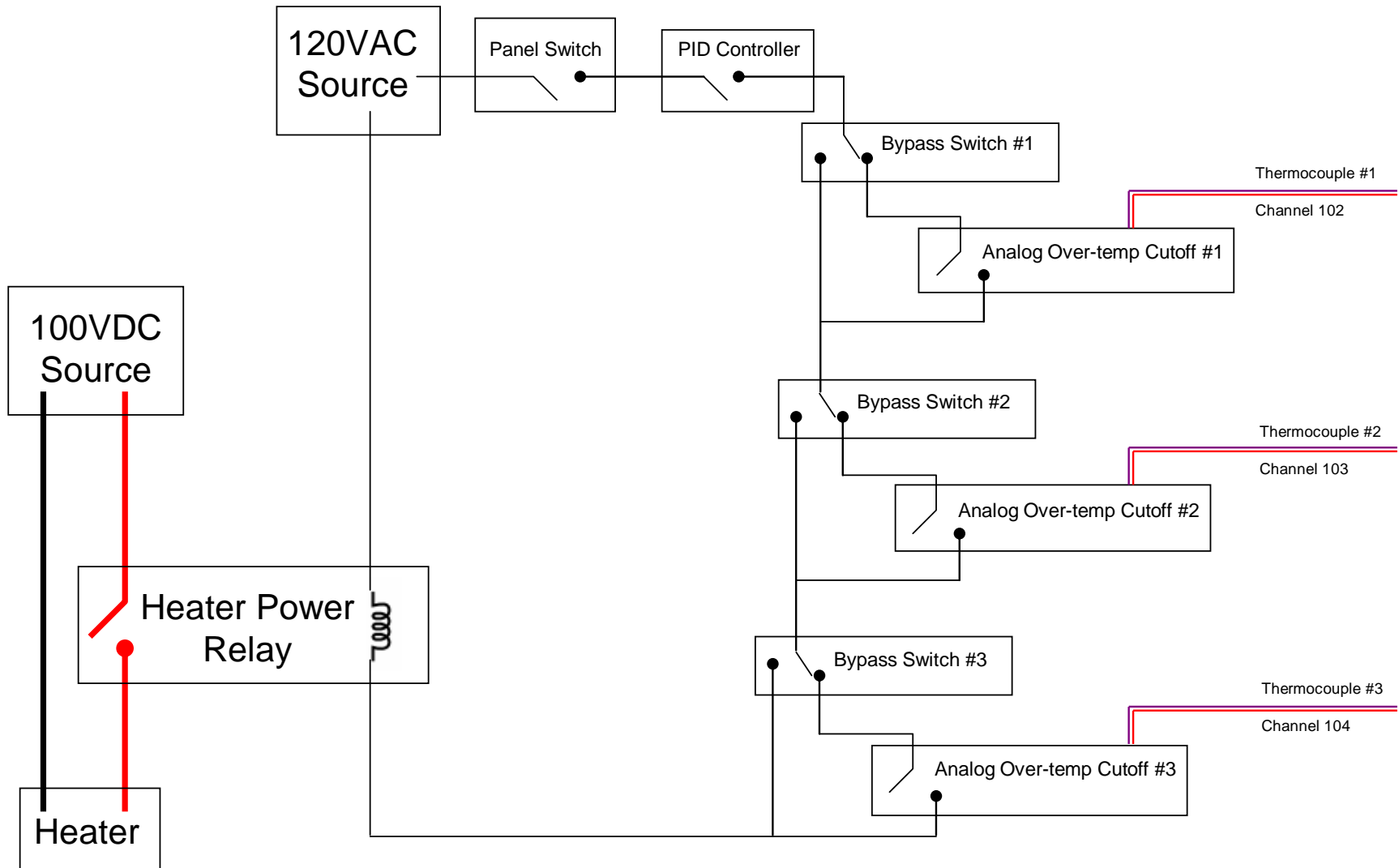
Control Panel



Power Panel



Array Triple Over-temp Cutoff Circuit



Appendix B: 2020 Joint Fastener Static Testing

The joint fastener strength values in the 80/20 literature were insufficient for the joint fasteners used on the frame. Static tests were conducted on a test structure. The first structure, shown in Figure BK and Figure BL, was assembled from 2020 extrusions and two 90° joining plates (P/N 4128) and two 90° corner brackets (P/N 4114). All screws were torqued to 90 in·lbs.

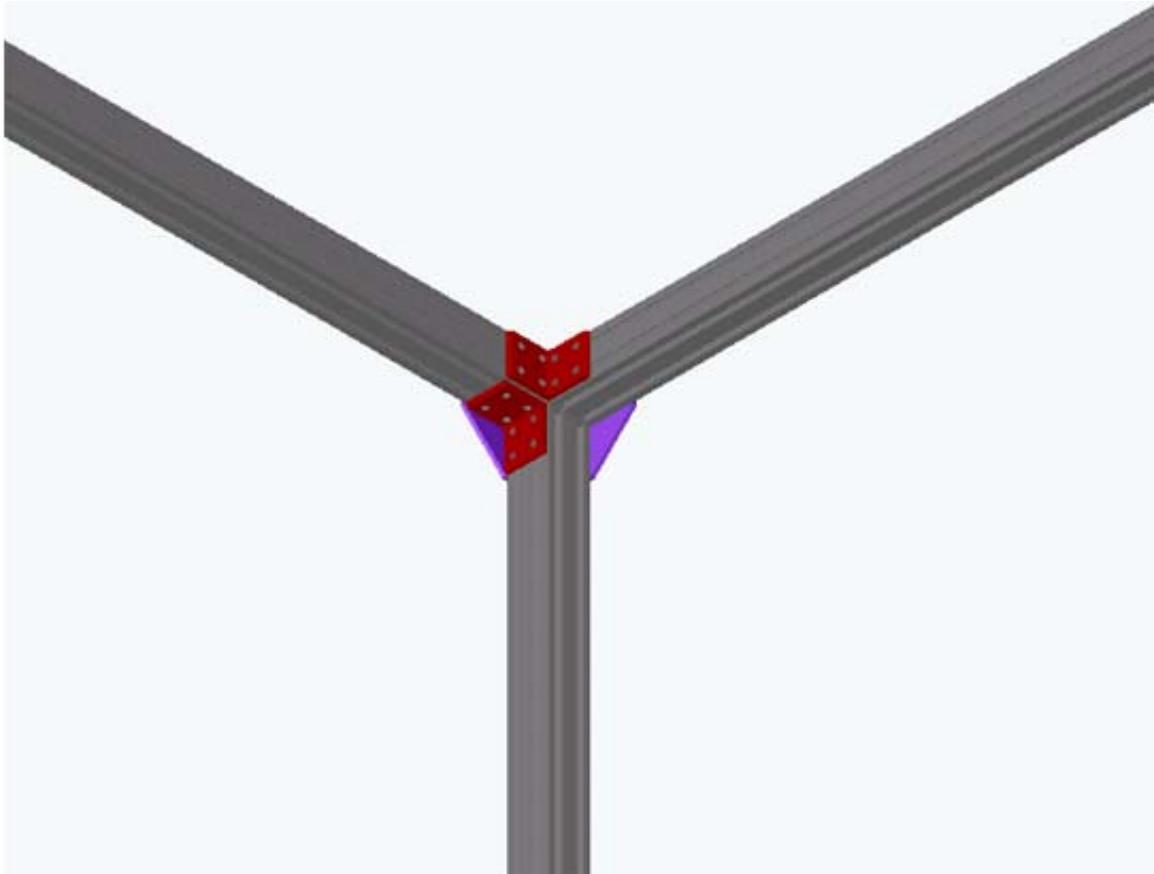


Figure BK: Corner Joint

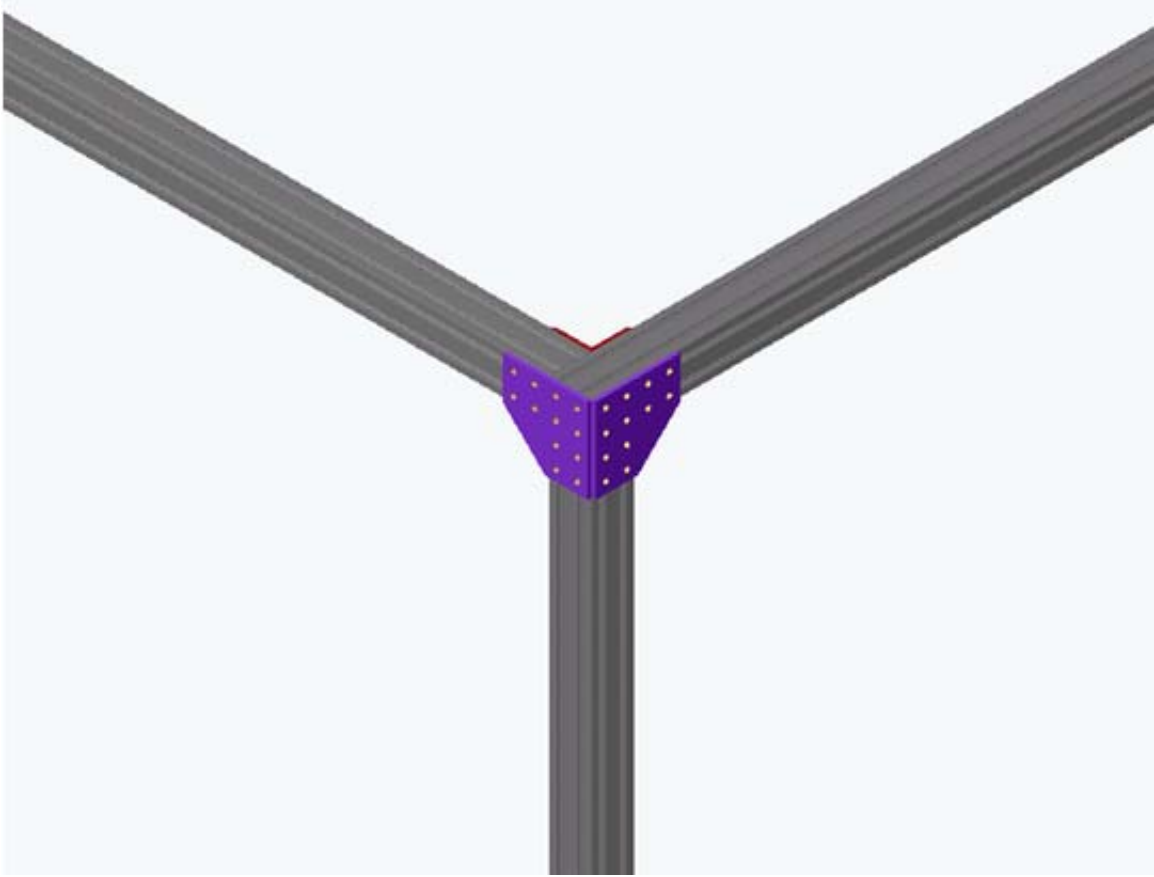


Figure BL: Corner Joint

A load, composed from three F-class weights—44.1 lbs, 55.1 lbs and 110.2 lbs, was placed 36 inches from the joint, as shown in Figure BM. The load was left in place for fifteen minutes. The results are tabulated in Table B1. After the last load was removed, the beam returned to a position of 2.2 inches compared to the starting position of 2.55 inches. Some of the deflection may be because of clamping arrangement. Disassembly did not show any visible deformation in the parts, i.e. plates and joints. The joint did not have ultimate failure.

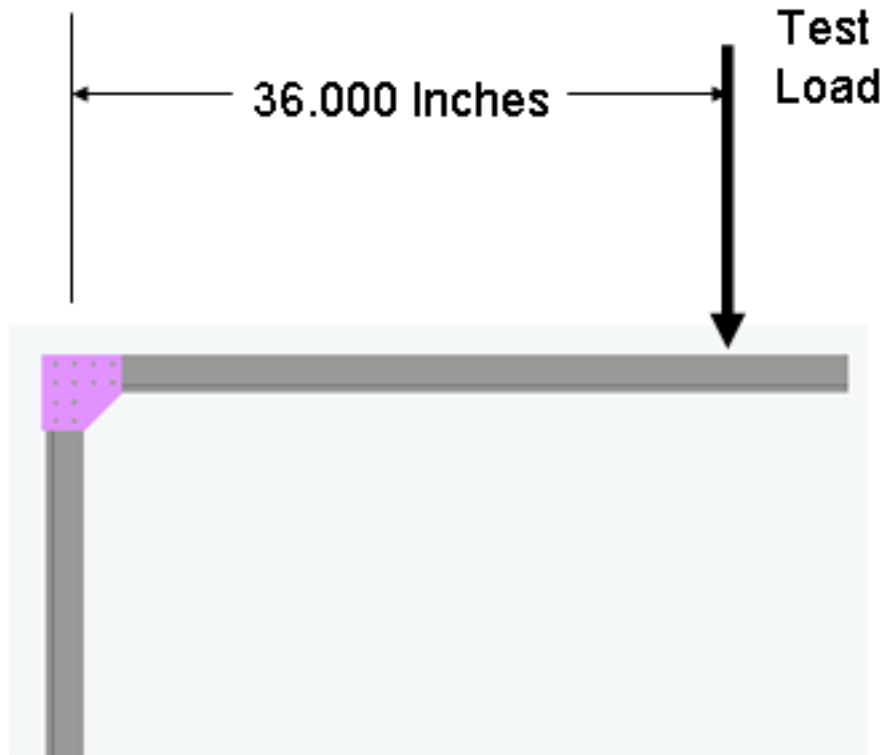


Figure BM: Corner Joint Load Point

Mass (lbs)	Moment (in·lbs)	Deflection (initial-final) inches
110.2	3967.2	(2.55-1.75) = 0.80
165.3	5950.8	(2.55-1.15) = 1.40
209.4	7538.4	(2.55-0.55) = 2.0

Table B1: Corner Bracket Loads

The second joint tested was the tee joint. It consists of a tee joint (P/N 4125) and two 90° corner brackets (P/N 4114). The joint is shown in Figure BN. This configuration was loaded in a similar manner to the corner joint, as shown in Figure BO. The results are in Table B2. After the last load was removed, the beam returned to 6.8 inches from a starting position of 7.55 inches. Some of the deflection may be because of clamping arrangement. Disassembly did not show any visible deformation in the parts, i.e. plates and joints. The joint did not have ultimate failure.

Mass (lbs)	Moment (in·lbs)	Deflection (initial-final) inches
110.2	3967.2	(7.55-6.8) = 0.75
165.3	5950.8	(7.55-6.0) = 1.55
209.4	7538.4	(7.55-5.25) = 2.30

Table B2: Tee Bracket Loads

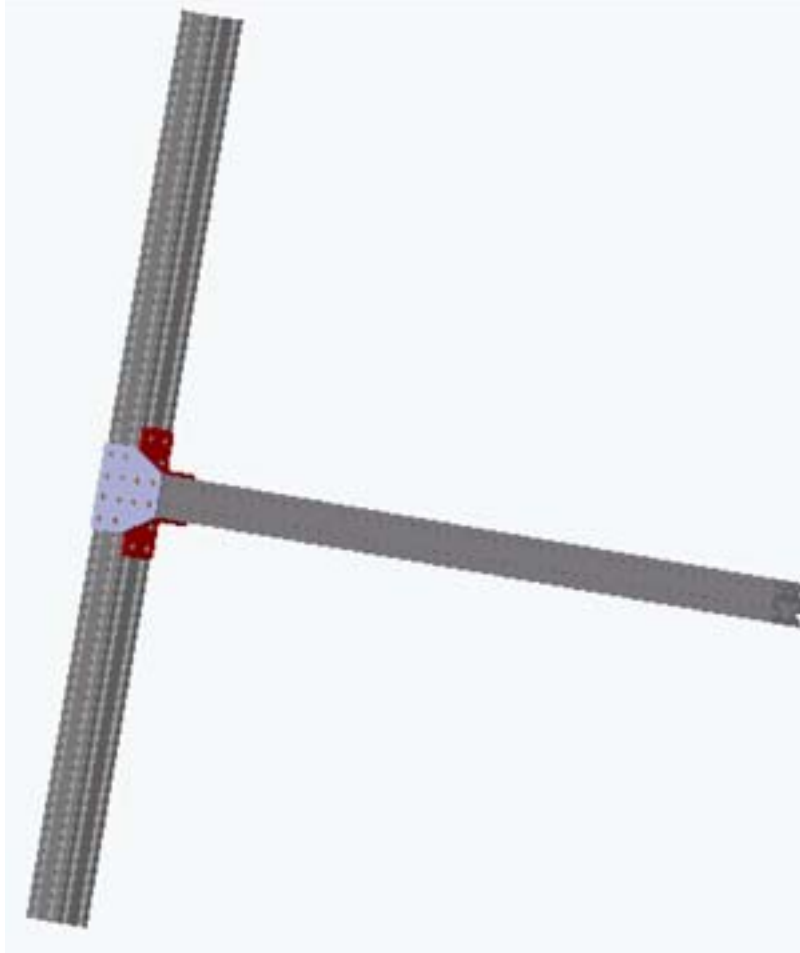


Figure BN: Tee Joint

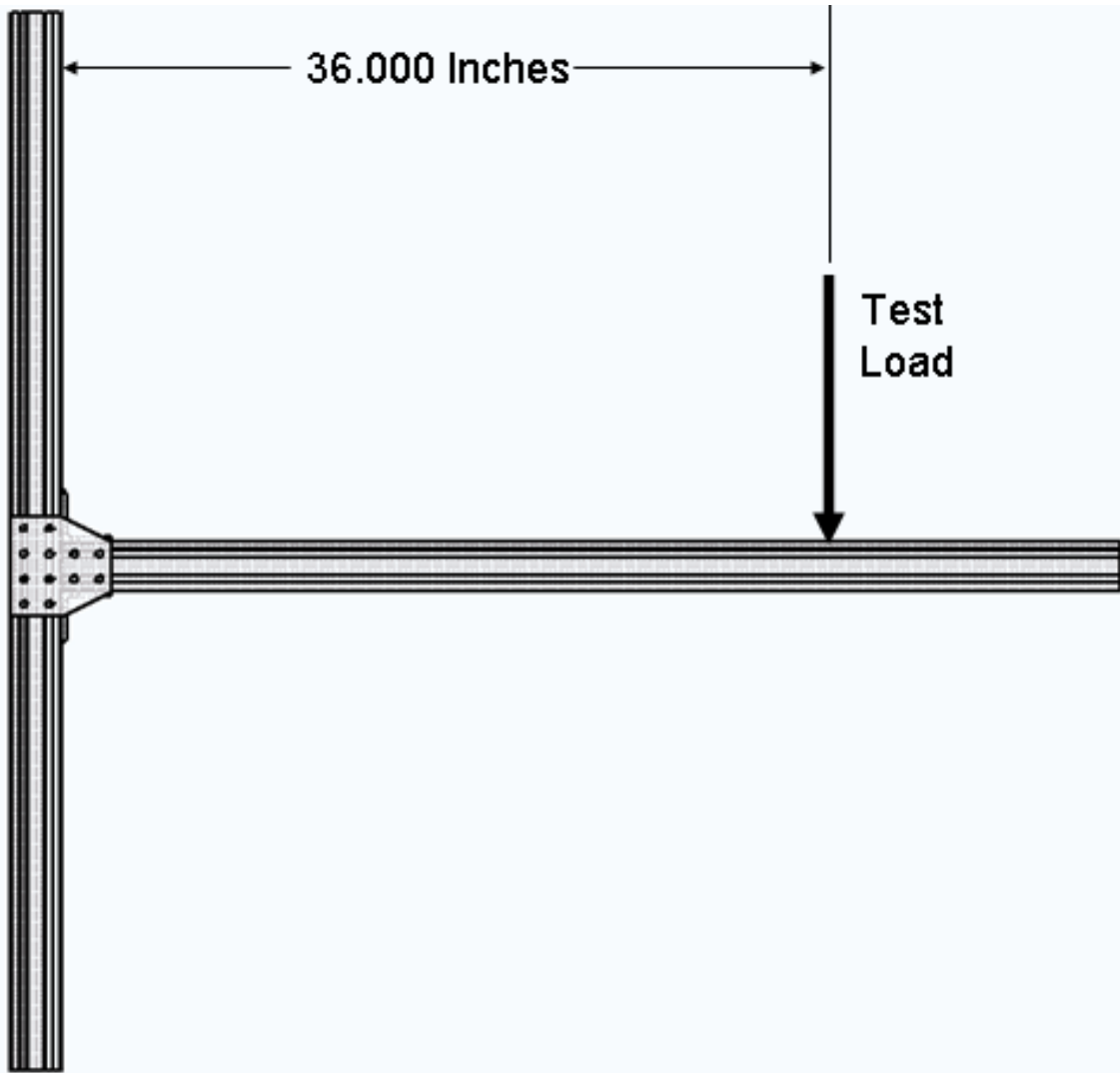


Figure BO: Tee Joint Point Load

A second structure, shown in Figure BP and Figure BQ, was assembled from 2020 extrusions and three 90° joining plates (P/N 4128) and three 90° corner brackets (P/N 4114). All screws were torqued to 90 in·lbs.



Figure BP: Corner Joint



Figure BQ: Corner Joint

A load, composed from five F-class weights—11.02, 22.05, 44.1 lbs, 55.1 lbs and 110.2 lbs, was placed 40 inches from the joint, as shown in Figure BR. The load was left in place for fifteen minutes. The results are tabulated in Table B3. Some of the deflection may be because of clamping arrangement. Disassembly did not show any visible deformation in the parts, i.e. plates and joints. The joint did not have ultimate failure.

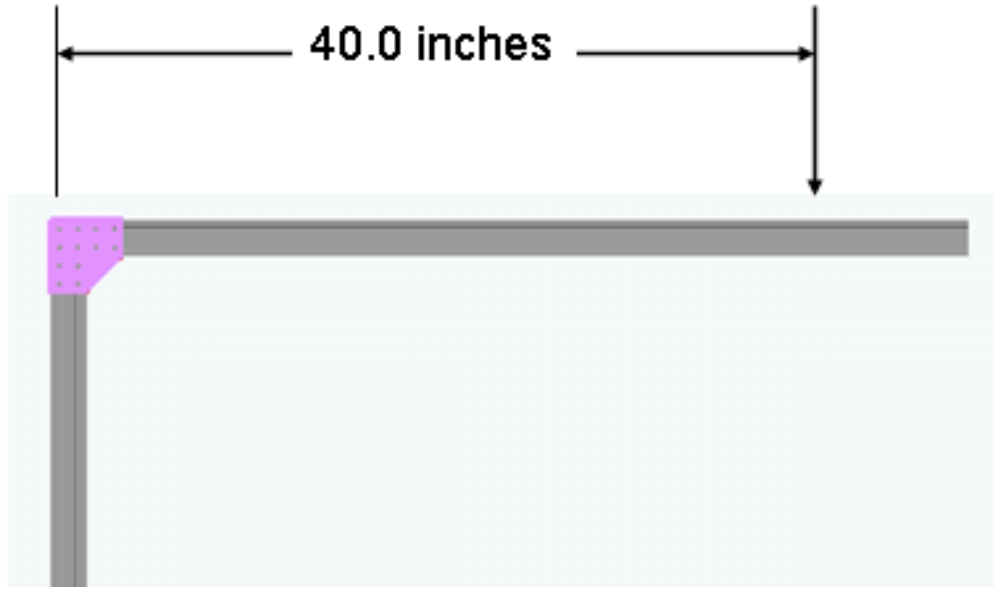


Figure BR: Corner Joint Load Point

Mass (lbs)	Moment (in·lbs)	Deflection (initial-final) inches
110.43	4417.2	(45-44) = 1.0
209.43	8377.2	(45-42.5) = 2.50
242.5	9700.0	(45-42) = 3.0

Table B3: Corner Bracket Loads

The second joint tested was the tee joint. It consists of a tee joint (P/N 4125) and two 90° corner brackets (P/N 4114). The joint is shown in Figure BS. This configuration was loaded in a similar manner to the corner joint, as shown in Figure BT. The results are in Table B4. Some of the deflection may be because of clamping arrangement. Disassembly did not show any visible deformation in the parts, i.e. plates and joints. The joint did not have ultimate failure.

Mass (lbs)	Moment (in·lbs)	Deflection (initial-final) inches
110.43	4417.2	(48.5-48.0) = 0.5
209.43	8377.2	(48.5-45.25) = 3.25
242.5	9700.0	(48.5-44.25) = 4.25

Table B4: Tee Bracket Loads

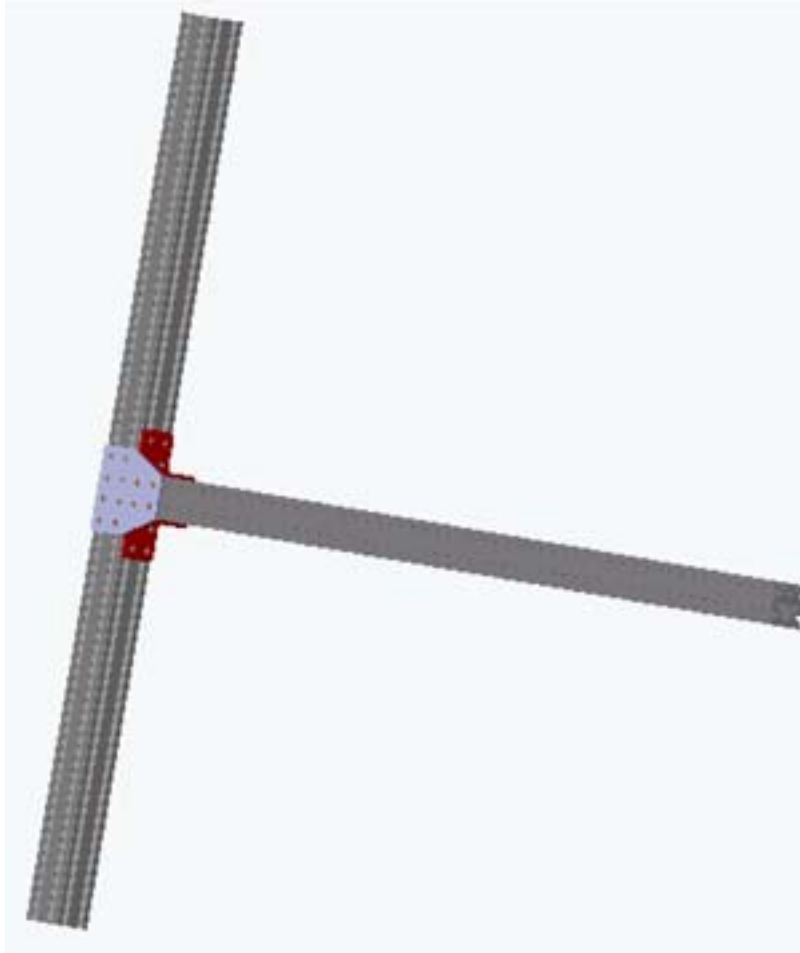


Figure BS: Tee Joint



Figure BT: Tee Joint Point Load

Appendix C: Experiment Drawings and Flow Schematic

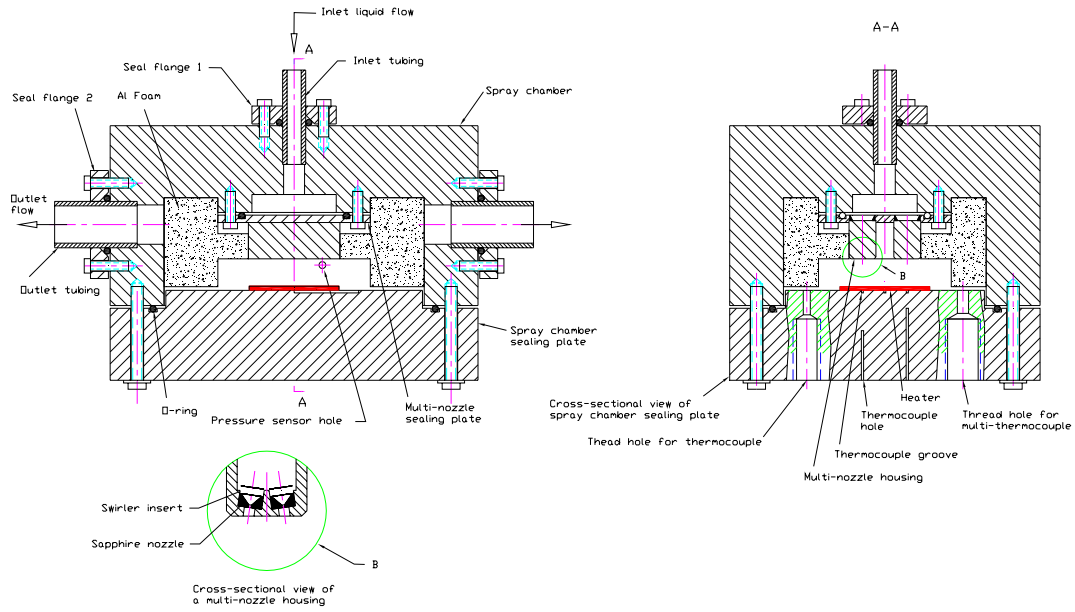


Figure CU: Section View of Spray Test Chamber

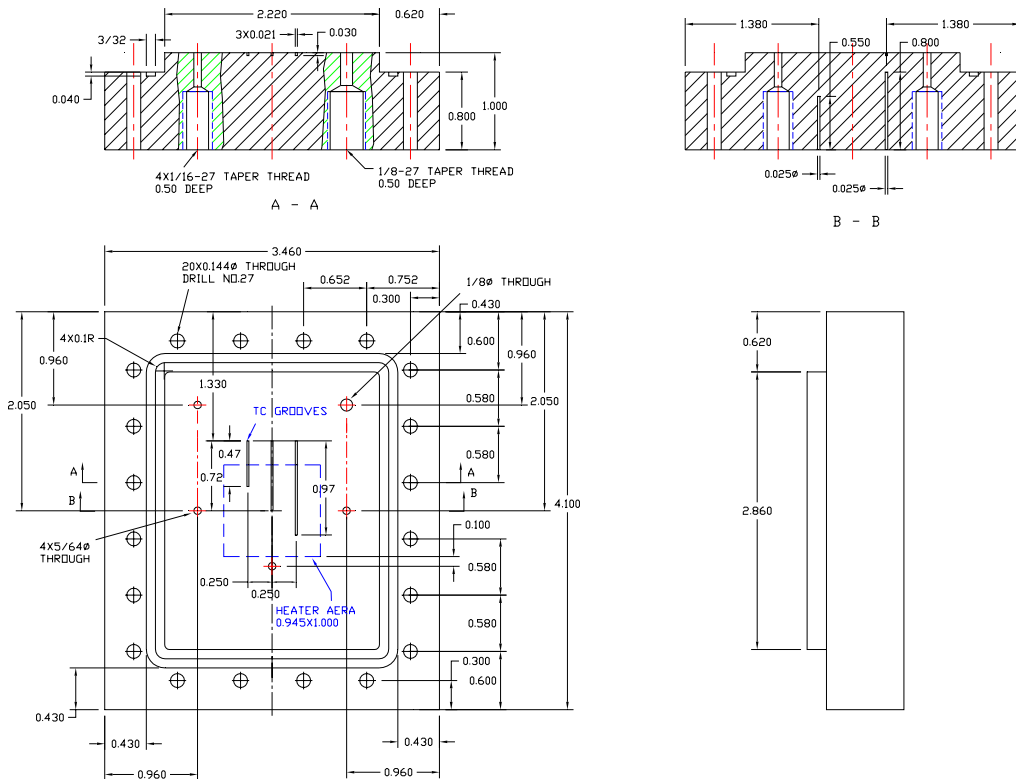


Figure CV: Hole Dimensional View of Spray Test Chamber

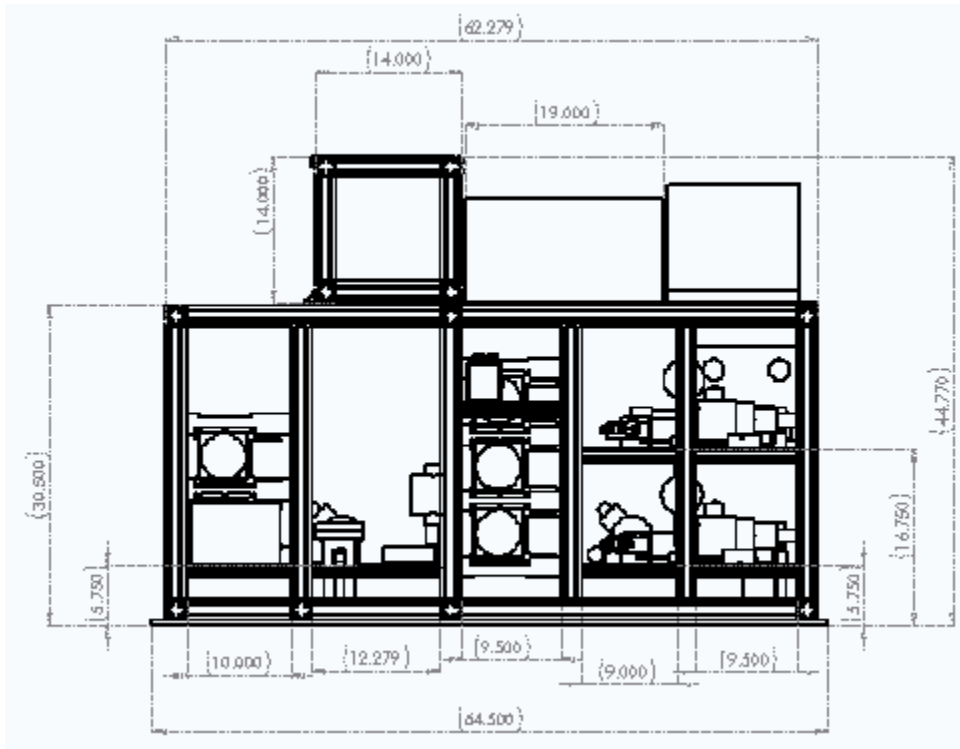


Figure CW: Side View of Rig

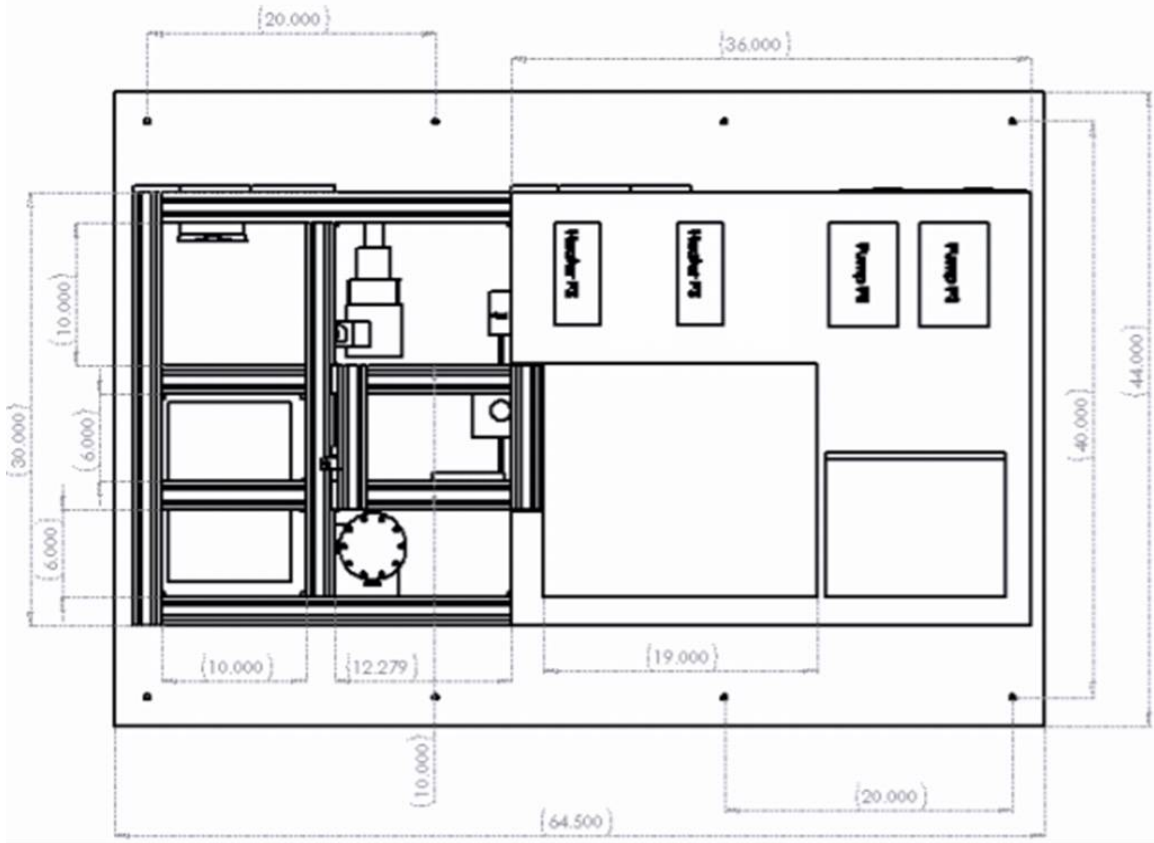


Figure CX: Top View of Rig

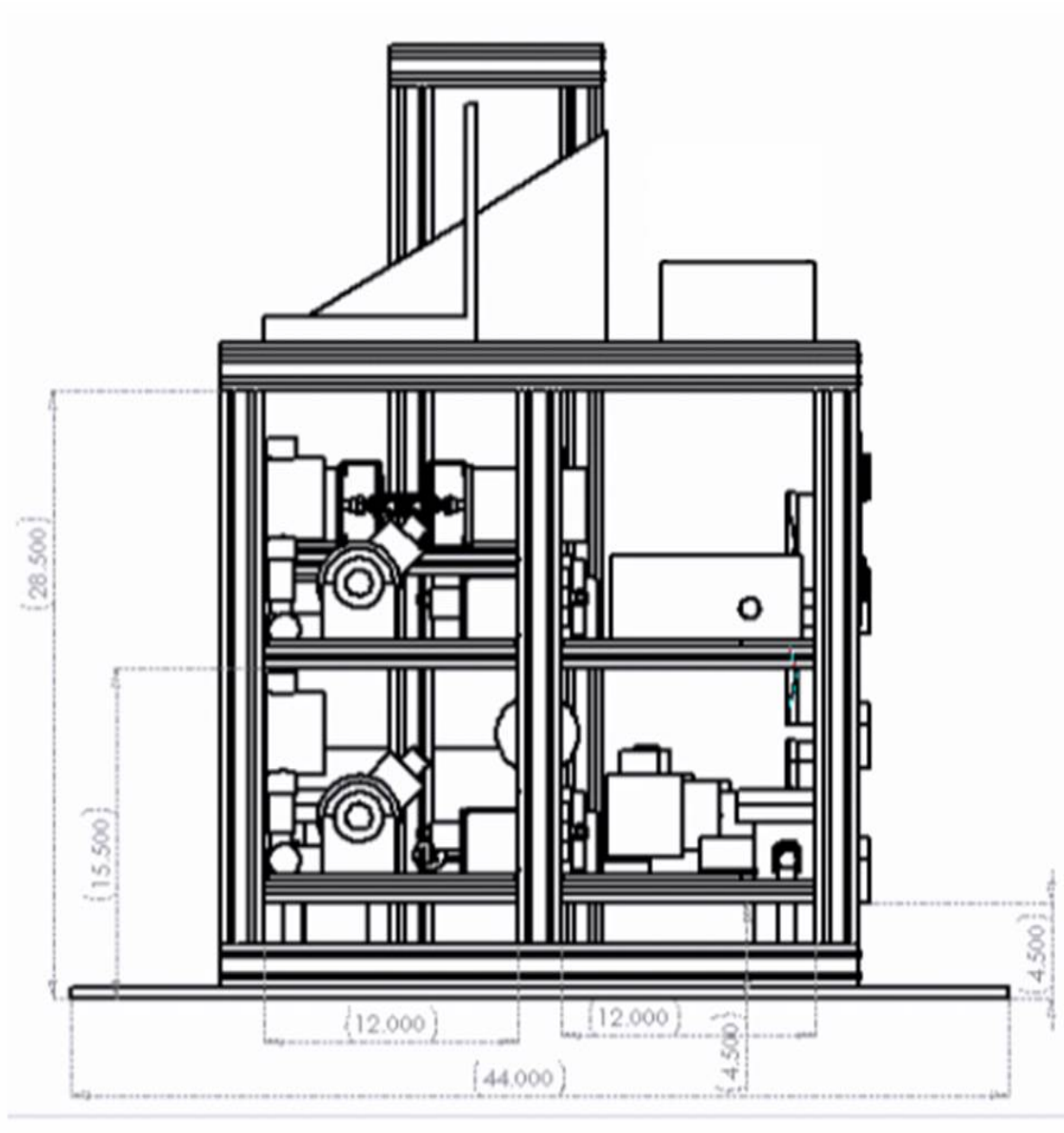


Figure CY: Rear View of Rig

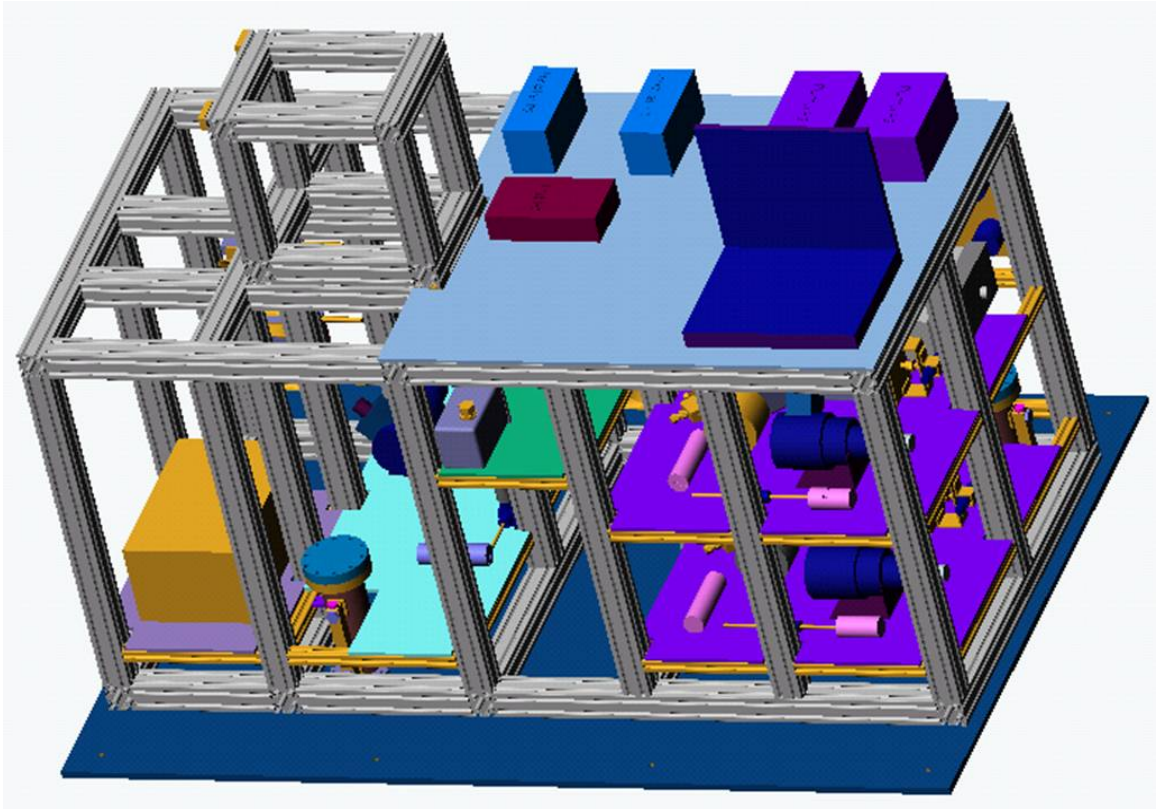


Figure CZ: Three-dimensional View of Rig

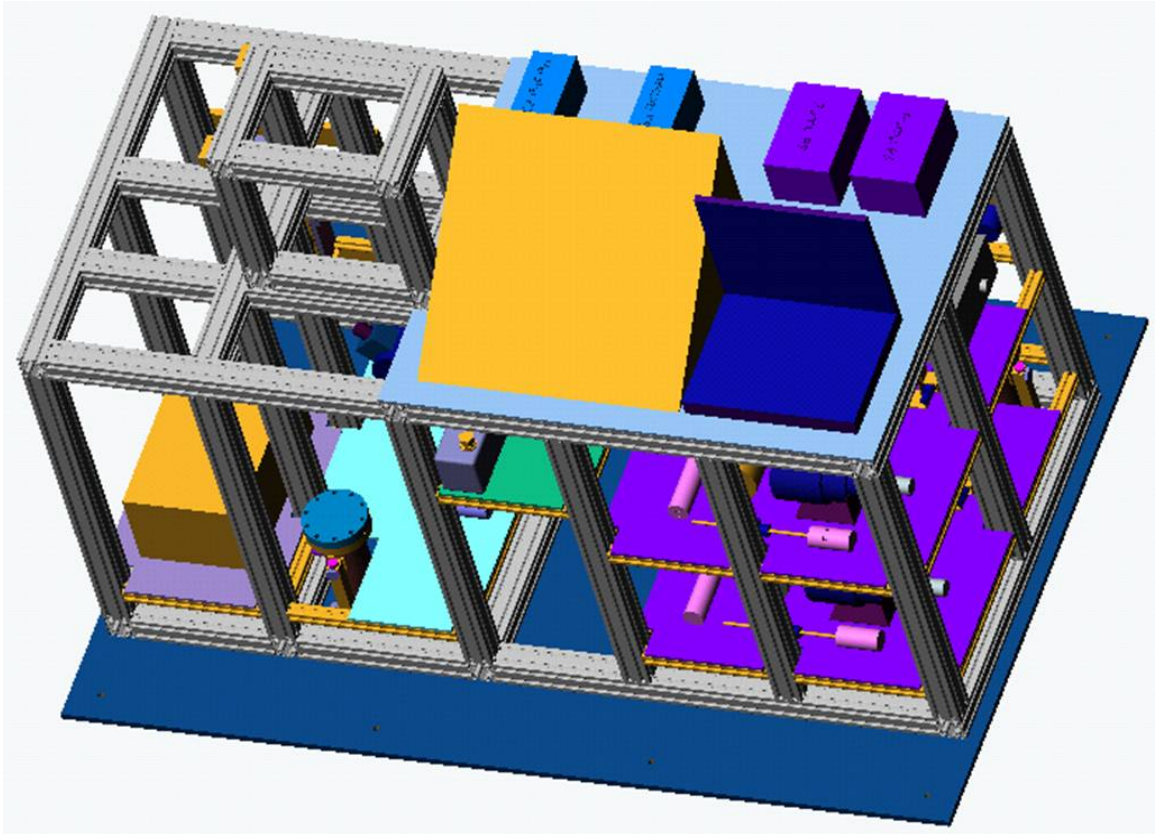


Figure CAA: Three-dimensional View of Rig

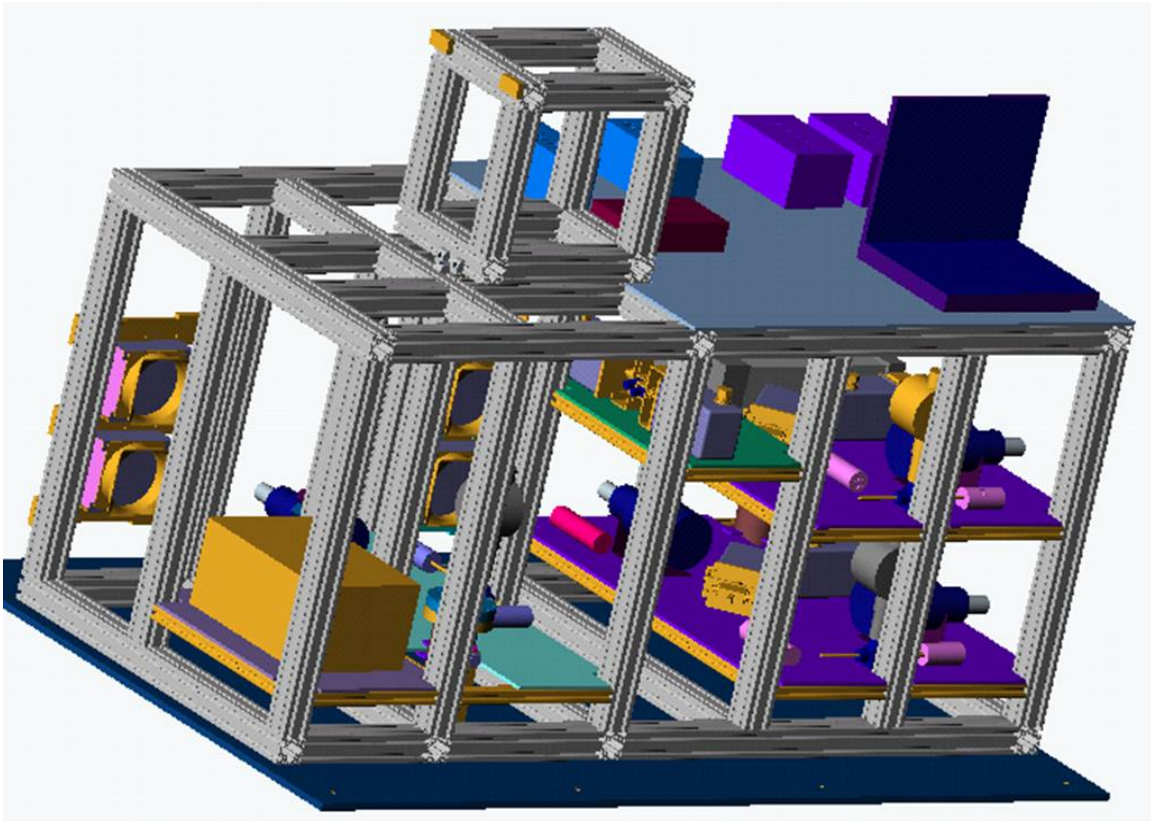


Figure CBB: Three-dimensional View of Rig



Figure CCC: Three-dimensional View of Rig

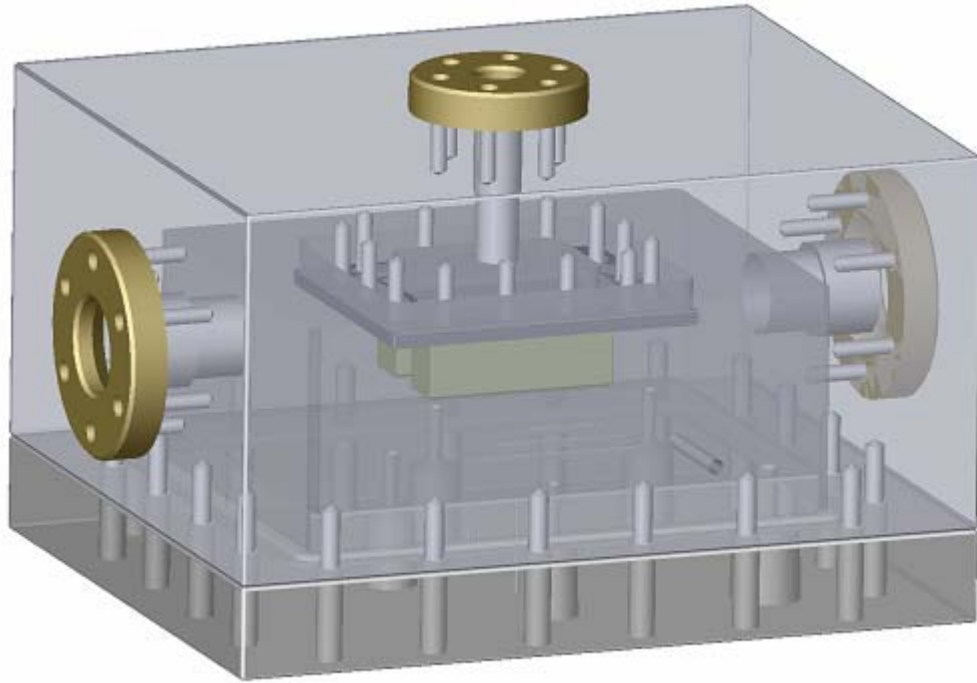


Figure CDD: Three-dimensional View of Chamber

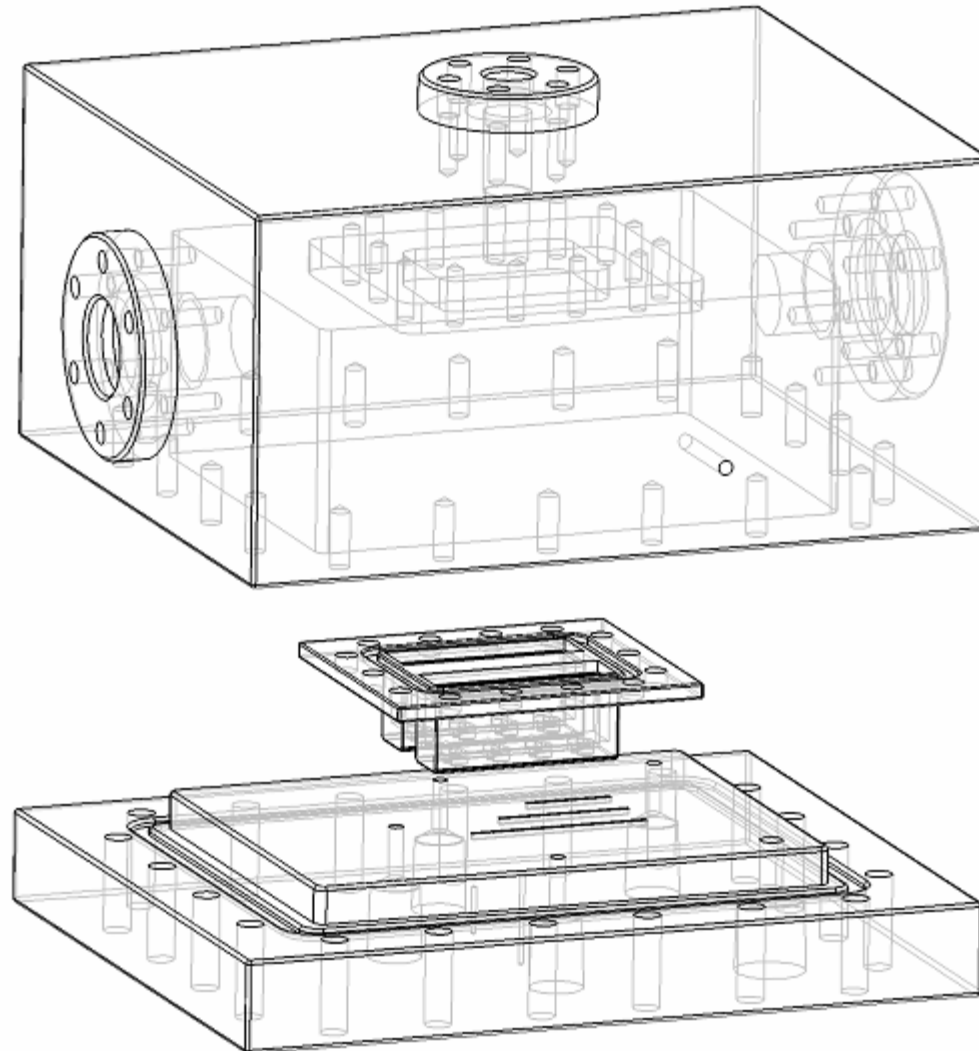


Figure CEE: Wire Frame View of Exploded Test Chamber

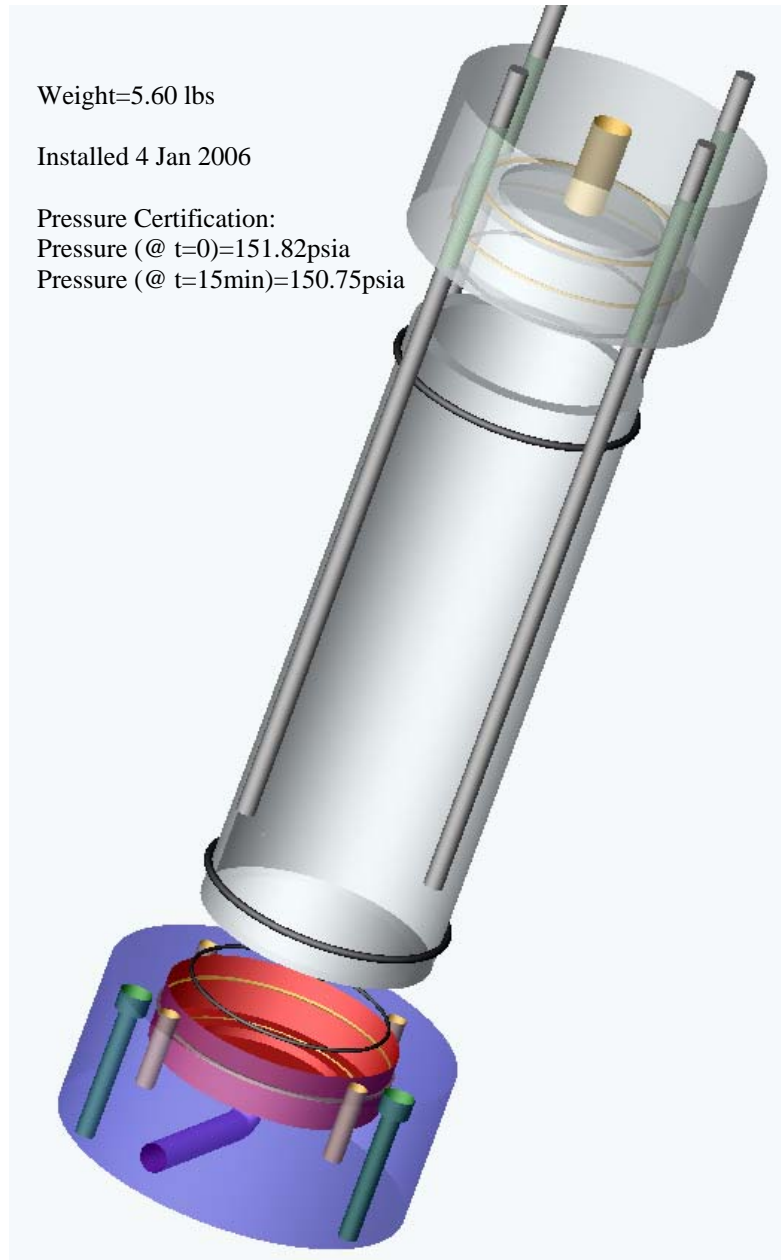
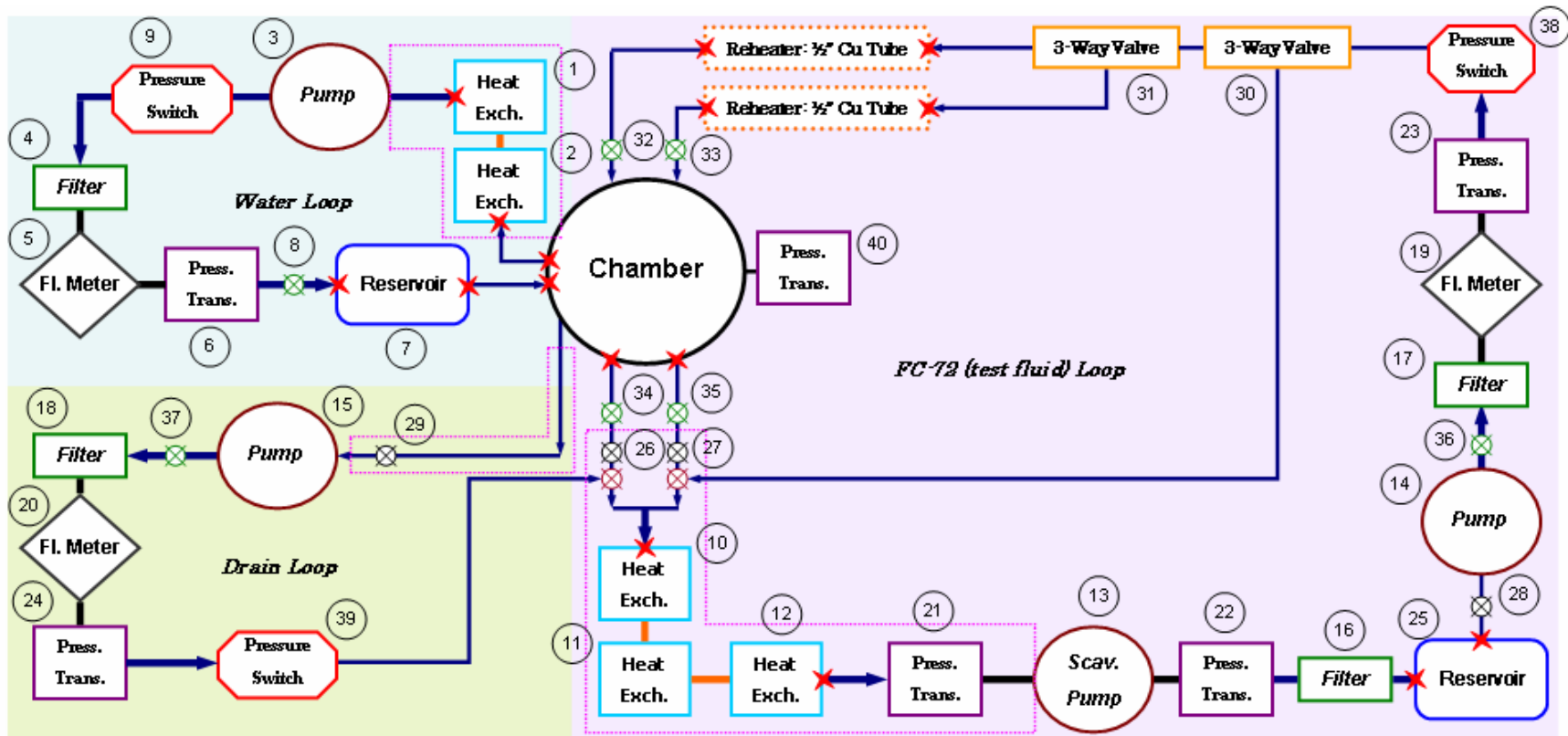


Figure CFF: Expanded view of FC-72 Reservoir



- | | | | |
|--|---|--|---|
| | 3/8" Polyflow; 350psi@ 21C, 240psi@ 43C | | Electric 2-way valve |
| | 1/4" Polyflow; 400psi@ 21C, 260psi@ 43C | | Drain/Fill Valve |
| | 3/8" St Steel; 4100 psi | | Throttling Valve |
| | 1/4" St Steel; 4400 psi | | Optional check valve (not in this loop) |
| | 3/8" Copper; 1840 psi | | Thermocouple location |
| | | | Areas of low pressure. All other regions are "high" pressure regions. |
- *Connections consist of standard, brass or steel compression fittings with metal ferrules (rated to that of the tubing).
- *Metal tube pressures are maximum suggested working pressures, as noted in the Parker catalog.
- *Copper tubing pressure includes a temperature derating factor, as noted in the Parker catalog.
- *Maximum expected pressure: 80 psi

Figure CGG: Flow Schematic

Appendix D: Pressure Certification

**Piping System Pneumatic Test Checklist
NASA Glenn Research Center**

	<u>Description</u>	<u>Initial</u>	<u>Date</u>
1.	System Index Number <u>(N/A)</u>	<u>RLP</u>	<u>30 Mar 07</u>
2.	Line Identification <u>(N/A)</u>	<u>RLP</u>	<u>30 Mar 07</u>
3.	Pneumatic Test Pressure, psig. <u>~135 (150 psia)</u>	<u>RLP</u>	<u>30 Mar 07</u>
4.	Operating Pressure, psig. <u>~85 (100 psia)</u>	<u>RLP</u>	<u>30 Mar 07</u>
5.	Pneumatic Test Fluid <u>N₂ gas</u>	<u>RLP</u>	<u>30 Mar 07</u>
6.	Test Fluid Temperature, °F <u>70 (ambient)</u>	<u>RLP</u>	<u>30 Mar 07</u>
7.	System Metal Temperature, °F <u>70 (ambient)</u>	<u>RLP</u>	<u>30 Mar 07</u>
8.	Verified Calibrated Gauges <u>Heine HAS-2, HAS-26010 Drexler Inst. 4-23-04</u>	<u>RLP</u>	<u>30 Mar 07</u>
9.	Pneumatic Pressure Source Verified	<u>RLP</u>	<u>30 Mar 07</u>
10.	Pneumatic Test Start, Date/Time <u>30 Mar 07 / 0940</u>	<u>RLP</u>	<u>30 Mar 07</u>
11.	Pneumatic Test Completion, Date/Time <u>30 Mar 07 / 1055</u>	<u>RLP</u>	<u>30 Mar 07</u>
12.	Visual Exam at Operating Pressure	<u>RLP</u>	<u>30 Mar 07</u>
13.	Pneumatic Test Performed by		
	Organization: <u>AFRL/PRPS</u>		

Remarks:
FC-72 loop system includes plumbing, valves, pumps, pressure gauges, reservoir, etc.

Inspector Rebekah Peterbaugh 30 Mar 07
 Signature Date

Witness [Signature] 30 Mar 07
 Signature Date

**Piping System Pneumatic Test Report
NASA Glenn Research Center**

System Description

1. Pipe Size 3/8", 1/4"
2. Wall Thickness —
3. Material st. steel, copper, poly-flu
4. Operating Pressure, psig. ~85 (100 psia)

Other Requirements

1. Restricted Distance, ft. (N/A)
2. Cold Shock (cryo only) Y/N, Date (N/A)
3. Leak Test (required), Date 30 Mar 07

Pneumatic Test Parameters

1. Pneumatic Test Date 30 Mar 07
2. Maximum Test Pressure, psig. ~135 (150 psia)
3. Test Fluid N₂ gas
4. Test Fluid Temperature, °F 70 (ambient)
5. System Metal Temperature, °F 70 (ambient)
6. Verified Gauge Calibration, Date 30 Mar 07
7. P_{atm} = 14.60 psia

Specific Check Points, % of Test Pressure

- | | | |
|-------|------------------|---------------|
| (75) | 1. 50% = | <u>77.18</u> |
| (90) | 2. 60% = | <u>91.10</u> |
| (105) | 3. 70% = | <u>105.70</u> |
| (120) | 4. 80% = | <u>120.80</u> |
| (135) | 5. 90% = | <u>135.78</u> |
| (150) | 6. 100% (max.) = | <u>150.50</u> |

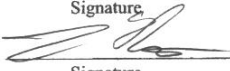
Time/Initials

- | | | |
|-----------|-------------------|--------------|
| Hold Time | <u>10 min</u> | <u>/ RLP</u> |
| Hold Time | <u>10 min</u> | <u>/ RLP</u> |
| Hold Time | <u>10 min</u> | <u>/ RLP</u> |
| Hold Time | <u>10 min</u> | <u>/ RLP</u> |
| Hold Time | <u>10 min</u> | <u>/ RLP</u> |
| Hold Time | <u>15 minutes</u> | <u>/ RLP</u> |

REMARKS:

FC-72 loop system includes plumbing, valves, pumps, pressure gauges, reservoir, etc.

Pneumatic Pressure Test Performed by

Organization	<u>AFRL/PRDS</u>	
Technicians	<u>Rebekah L. Puterbaugh</u>	<u>30 Mar 07</u>
	Signature	Date
		<u>30 Mar 07</u>
	Signature	Date
AFRL NASA Witness		<u>30 Mar 07</u>
	Signature	Date
Other	_____	_____
	Signature	Date

Form Dated 10/99

**Pressure Vessel Pneumatic Test Checklist
NASA Glenn Research Center**

	<u>Description</u>	<u>Initial</u>	<u>Date</u>
1.	Vessel Manufacturer <u>(N/A)</u>	<u>RLP</u>	<u>30 Mar 07</u>
2.	Vessel Serial Number <u>(N/A)</u>	<u>RLP</u>	<u>30 Mar 07</u>
3.	Pneumatic Test Pressure, psig. <u>~ 135 (150 psia)</u>	<u>RLP</u>	<u>30 Mar 07</u>
4.	Operating Pressure, psig. <u>~ 85 (100 psia)</u>	<u>RLP</u>	<u>30 Mar 07</u>
5.	Pneumatic Test Fluid <u>N₂ gas</u>	<u>RLP</u>	<u>30 Mar 07</u>
6.	Test Fluid Temperature, °F <u>70 (ambient)</u>	<u>RLP</u>	<u>30 Mar 07</u>
7.	Vessel Metal Temperature, °F <u>70 (ambient)</u>	<u>RLP</u>	<u>30 Mar 07</u>
8.	Verified Calibrated Gauges <u>Heik HAS-2, HAS-26010 Dwyer Inst. 4-23-04</u>	<u>RLP</u>	<u>30 Mar 07</u>
9.	Pneumatic Pressure Source Verified	<u>RLP</u>	<u>30 Mar 07</u>
10.	Pneumatic Test Start, Date/Time <u>30 Mar 07 / 0940</u>	<u>RLP</u>	<u>30 Mar 07</u>
11.	Pneumatic Test Completion, Date/Time <u>30 Mar 07 / 1055</u>	<u>RLP</u>	<u>30 Mar 07</u>
12.	Visual Exam at Operating Pressure	<u>RLP</u>	<u>30 Mar 07</u>
13.	Pneumatic Test Performed by		
	Organization: <u>AFRL/DRPS</u>		

Remarks:

Spray Chamber

Inspector Rebekah L. Piterbaugh 30 Mar 07
 Signature Date

Witness [Signature] 30 Mar 07
 Signature Date

**Pressure Vessel Pneumatic Test Report
NASA Glenn Research Center**

Vessel Description

- 1. Manufacturer (N/A)
- 2. Model Number (N/A)
- 3. Operating Pressure, psig. ~85(100psia)

Other Requirements

- 1. Restricted Distance, ft. (N/A)
- 2. Cold Shock (cryo only) Y/N, Date (N/A)
- 3. Leak Test (required), Date 30 Mar 07

Pneumatic Test Parameters

- 1. Pneumatic Test Date 30 Mar 07
- 2. Maximum Test Pressure, psig. ~135(150psia)
- 3. Test Fluid N₂ gas
- 4. Test Fluid Temperature, °F 70 (ambient)
- 5. Vessel Metal Temperature, °F 70 (ambient)
- 6. Verified Gauge Calibration, Date 30 Mar 07
- 7. Patm = 14.60 psia

Specific Check Points, % of Test Pressure

- (PSIA)
- (75) 1. 50% = 77.18
 - (90) 2. 60% = 91.10
 - (105) 3. 70% = 105.70
 - (120) 4. 80% = 120.80
 - (135) 5. 90% = 135.78
 - (150) 6. 100% (max.) = 150.50

Time/Initials

- Hold Time 10 min / RLP
- Hold Time 10 min / RLP
- Hold Time 10 min / RLP
- Hold Time 10 min / RLP
- Hold Time 10 min / RLP
- Hold Time 15 minutes / RLP

REMARKS:

Spray Chamber

Pneumatic Pressure Test Performed by

- Organization AFRL PRPS
- Technicians Rebekah L. Paterbaugh 30 Mar 07
Signature Date
- [Signature] 30 Mar 07
Signature Date
- AFRL [Signature] 30 Mar 07
NASA Witness Signature Date
- Other _____
Signature Date

Appendix E: Material Safety Data Sheet



Material Safety Data Sheet

Copyright, 2002, 3M Company. All rights reserved. Copying and/or downloading of this information for the purpose of properly utilizing 3M products is allowed provided that: (1) the information is copied in full with no changes unless prior written agreement is obtained from 3M, and (2) neither the copy nor the original is resold or otherwise distributed with the intention of earning a profit thereon.

SECTION 1: PRODUCT AND COMPANY IDENTIFICATION

PRODUCT NAME: FC-72 FLUORINERT Brand Electronic Liquid

MANUFACTURER: 3M

DIVISION: 3M Specialty Materials

ADDRESS: 3M Center
St. Paul, MN 55144-1000

EMERGENCY PHONE: 1-800-364-3577 or (651) 737-6501 (24 hours)

Issue Date: 09/05/2002

Supersedes Date: 01/24/2001

Document Group: 10-3789-4

Product Use:

Intended Use: For industrial use only. Not intended for use as a medical device or drug.
Specific Use: Testing Fluid or Heat Transfer Fluid for Electronics.

SECTION 2: INGREDIENTS

<u>Ingredient</u>	<u>C.A.S. No.</u>	<u>% by Wt</u>
PERFLUORO COMPOUNDS, (PRIMARILY COMPOUNDS WITH 6 CARBONS)	86508-42-1	100

SECTION 3: HAZARDS IDENTIFICATION

3.1 EMERGENCY OVERVIEW

Specific Physical Form: Liquid

Odor, Color, Grade: Colorless, odorless liquid.

General Physical Form: Liquid

Immediate health, physical, and environmental hazards: None known.

3.2 POTENTIAL HEALTH EFFECTS

Eye Contact:

Contact with the eyes during product use is not expected to result in significant irritation.

Skin Contact:

Contact with the skin during product use is not expected to result in significant irritation.

Inhalation:

No health effects are expected.

Ingestion:

No health effects are expected.

3.3 POTENTIAL ENVIRONMENTAL EFFECTS

This compound is completely fluorinated (perfluorinated), or it contains perfluorinated portions. Perfluoroalkyl groups resist degradation in most natural environments. This low-solubility substance has insignificant toxicity to aquatic organisms (Lowest LL50 or EL50 is >1000 mg/L). LL50 (Lethal Level) and EL50 are similar to LC50 and EC50, but tests the water phase from incompletely-miscible mixtures. Take precautions to prevent direct release of this substance to the environment.

ATMOSPHERIC FATE:

Perfluoro compounds (PFCs) are photochemically stable and expected to persist in the atmosphere for more than 1000 years. PFCs have high global warming potentials (GWP), exceeding 5000 (100-yr-ITH). The Ozone Depletion Potential (ODP) is Zero.

SECTION 4: FIRST AID MEASURES**4.1 FIRST AID PROCEDURES**

The following first aid recommendations are based on an assumption that appropriate personal and industrial hygiene practices are followed.

Eye Contact: Flush eyes with large amounts of water. If signs/symptoms persist, get medical attention.

Skin Contact: Wash affected area with soap and water. If signs/symptoms develop, get medical attention.

Inhalation: If signs/symptoms develop, remove person to fresh air. If signs/symptoms develop, get medical attention.

If Swallowed: No need for first aid is anticipated.

SECTION 5: FIRE FIGHTING MEASURES**5.1 FLAMMABLE PROPERTIES**

Autoignition temperature	<i>Not Applicable</i>
Flash Point	<i>Not Applicable</i>
Flammable Limits - LEL	Nonflammable
Flammable Limits - UEL	Nonflammable

5.2 EXTINGUISHING MEDIA

Material will not burn.

5.3 PROTECTION OF FIRE FIGHTERS

Special Fire Fighting Procedures: Wear full protective clothing, including helmet, self-contained, positive pressure or pressure demand breathing apparatus, bunker coat and pants, bands around arms, waist and legs, face mask, and protective covering for exposed areas of the head. Water may be used to blanket the fire. Exposure to extreme heat can give rise to thermal decomposition.

Unusual Fire and Explosion Hazards: No unusual fire or explosion hazards are anticipated. No unusual effects are anticipated during fire extinguishing operations. Avoid breathing the products and substances that may result from the thermal decomposition of the product or the other substances in the fire zone. Keep containers cool with water spray when exposed to fire to avoid rupture.

Note: See STABILITY AND REACTIVITY (SECTION 10) for hazardous combustion and thermal decomposition information.

SECTION 6: ACCIDENTAL RELEASE MEASURES

Accidental Release Measures: Observe precautions from other sections. Call 3M- HELPS line (1-800-364-3577) for more information on handling and managing the spill. Evacuate unprotected and untrained personnel from hazard area. The spill should be cleaned up by qualified personnel. Ventilate the area with fresh air. Contain spill. Working from around the edges of the spill inward, cover with bentonite, vermiculite, or commercially available inorganic absorbent material. Mix in sufficient absorbent until it appears dry. Collect as much of the spilled material as possible. Clean up residue with an appropriate organic solvent. Read and follow safety precautions on the solvent label and MSDS. Place in a metal container approved for transportation by appropriate authorities. Seal the container. Dispose of collected material as soon as possible.

In the event of a release of this material, the user should determine if the release qualifies as reportable according to local, state, and federal regulations.

SECTION 7: HANDLING AND STORAGE

7.1 HANDLING

Avoid skin contact with hot material. For industrial or professional use only. No smoking: Smoking while using this product can result in contamination of the tobacco and/or smoke and lead to the formation of the hazardous decomposition products mentioned in the Reactivity Data section of this MSDS. Store work clothes separately from other clothing, food and tobacco products. Use general dilution ventilation and/or local exhaust ventilation to control airborne exposures to below Occupational Exposure Limits. If ventilation is not adequate, use respiratory protection equipment.

7.2 STORAGE

Store away from heat. Keep container tightly closed. Keep container in well-ventilated area.

SECTION 8: EXPOSURE CONTROLS/PERSONAL PROTECTION

8.1 ENGINEERING CONTROLS

Provide appropriate local exhaust when product is heated. Provide appropriate local exhaust ventilation on open containers. For those situations where the fluid might be exposed to extreme overheating due to misuse or equipment failure, use with appropriate local exhaust ventilation sufficient to maintain levels of thermal decomposition products below their exposure guidelines.

8.2 PERSONAL PROTECTIVE EQUIPMENT (PPE)

8.2.1 Eye/Face Protection

Avoid eye contact.

The following eye protection(s) are recommended: Safety Glasses with side shields.

8.2.2 Skin Protection

Avoid skin contact with hot material. Wear appropriate gloves, such as Nomex, when handling this material to prevent thermal burns. Avoid skin contact.

Select and use gloves and/or protective clothing to prevent skin contact based on the results of an exposure assessment. Consult with your glove and/or protective clothing manufacturer for selection of appropriate compatible materials.

Gloves made from the following material(s) are recommended: Nitrile Rubber.

8.2.3 Respiratory Protection

Under normal use conditions, airborne exposures are not expected to be significant enough to require respiratory protection. Avoid breathing of vapors, mists or spray.

Select one of the following NIOSH approved respirators based on airborne concentration of contaminants and in accordance with OSHA regulations: Half facepiece or fullface air-purifying respirator with organic vapor cartridges. Consult the current 3M Respiratory Selection Guide for additional information or call 1-800-243-4630 for 3M technical assistance. If thermal degradation products are expected, use fullface supplied air respirator.

8.2.4 Prevention of Swallowing

Do not eat, drink or smoke when using this product. Wash exposed areas thoroughly with soap and water.

8.3 EXPOSURE GUIDELINES

None Established

SECTION 9: PHYSICAL AND CHEMICAL PROPERTIES

Specific Physical Form:	Liquid
Odor, Color, Grade:	Colorless, odorless liquid.
General Physical Form:	Liquid
Autoignition temperature	<i>Not Applicable</i>
Flash Point	<i>Not Applicable</i>
Flammable Limits - LEL	Nonflammable
Flammable Limits - UEL	Nonflammable
Boiling point	50 - 60 °C
Density	1.7 g/ml
Vapor Density	Approximately 11.7 [@ 20 °C] [Ref Std: AIR=1]
Vapor Pressure	Approximately 232 mmHg [@ 20 °C]
Specific Gravity	Approximately 1.7 [Ref Std: WATER=1]
pH	<i>Not Applicable</i>
Melting point	<i>Not Applicable</i>
Solubility in Water	Nil
Evaporation rate	> 1 [Ref Std: BUOAC=1]
Volatile Organic Compounds	Exempt
Percent volatile	Approximately 100 %
VOC Less H2O & Exempt Solvents	Exempt
Viscosity	Approximately 0.42 centistoke [@ 20 °C]

SECTION 10: STABILITY AND REACTIVITY

Stability: Stable.

Materials and Conditions to Avoid: Finely divided active metals; Alkali and alkaline earth metals; Heat(greater than 200 °C)

Hazardous Polymerization: Hazardous polymerization will not occur.

Hazardous Decomposition or By-Products**Substance**

Hydrogen Fluoride
Perfluoroisobutylene (PFIB)

Condition

At Elevated Temperatures - greater than 200 °C
At Elevated Temperatures - greater than 200 °C

Hazardous Decomposition: If the product is exposed to extreme condition of heat from misuse or equipment failure, toxic decomposition products that include hydrogen fluoride and perfluoroisobutylene can occur.

Hydrogen fluoride (CAS No. 7664-39-3) has an ACGIH Threshold Limit Value - Ceiling of 3 ppm (as fluoride), an OSHA Permissible Exposure Limit - Time Weighted Average of 3 ppm (as fluoride) and a revoked OSHA Permissible Exposure Limit - Short Term Exposure Limit (which is enforced by some State Right-To-Know programs) of 6 ppm (as fluoride). Hydrogen fluoride may cause respiratory tract irritation, dental or skeletal fluorosis and irritation or burns to the eyes or skin, particularly when dissolved in water (hydrofluoric acid). The odor threshold for HF is 0.04 ppm, providing good warning properties for exposure.

Perfluoroisobutylene(CAS No. 382-21-8) has an ACGIH Threshold Limit Value - Ceiling of 0.01 ppm. Perfluoroisobutylene may cause respiratory tract irritation, pulmonary edema, cyanosis, and effect on the hematopoietic system.

SECTION 11: TOXICOLOGICAL INFORMATION**Product-Based Toxicology Information:**

A Material Toxicity Summary Sheet (MTSS) has been developed for this product. Please contact the address listed on the first page of this MSDS to obtain a copy of the MTSS for this product.

Please contact the address listed on the first page of the MSDS for Toxicological Information on this material and/or its components.

SECTION 12: ECOLOGICAL INFORMATION**ECOTOXICOLOGICAL INFORMATION****Test Organism**

Fathead Minnow, Pimephales promelas
Water flea, Daphnia magna

Test Type

96 hours Lethal Concentration 50%
48 hours Effect Concentration 50%

Result

>1000 mg/l
>1500 mg/l

CHEMICAL FATE INFORMATION

<u>Test Type</u>	<u>Result</u>	<u>Protocol</u>
20 days Biological Oxygen Demand	Nil	
Chemical Oxygen Demand	Nil	

SECTION 13: DISPOSAL CONSIDERATIONS

Waste Disposal Method: Reclaim if feasible. As a disposal alternative, incinerate in an industrial or commercial facility in the presence of a combustible material. Combustion products will include HF. Facility must be capable of handling halogenated materials. To reclaim or return, check product label for contact.

EPA Hazardous Waste Number (RCRA): Not regulated

Since regulations vary, consult applicable regulations or authorities before disposal.

SECTION 14: TRANSPORT INFORMATION

ID Number(s):

98-0211-0216-9, 98-0211-0217-7, 98-0211-0267-2, 98-0211-1795-1, 98-0211-8068-6, 98-0212-2992-1, ZF-0002-0305-7, ZF-0002-0321-4, ZF-0002-0354-5, ZF-0002-0802-3, ZF-0002-1162-1

Please contact the emergency numbers listed on the first page of the MSDS for Transportation Information for this material.

SECTION 15: REGULATORY INFORMATION

US FEDERAL REGULATIONS

Contact 3M for more information.

311/312 Hazard Categories:

Fire Hazard - No Pressure Hazard - No Reactivity Hazard - No Immediate Hazard - No Delayed Hazard - No

STATE REGULATIONS

Contact 3M for more information.

CHEMICAL INVENTORIES

The components of this product are in compliance with the chemical notification requirements of TSCA.

All applicable chemical ingredients in this material are listed ~~237~~ in the European Inventory of Existing Chemical Substances (EINECS),

or are exempt polymers whose monomers are listed on EINECS.

The components of this product are listed on the Canadian Domestic Substances List.

The components of this product are listed on the Australian Inventory of Chemical Substances.

The components of this product are listed on Japan's Chemical Substance Control Law List (also known as the Existing and New Chemical Substances List.)

Contact 3M for more information.

INTERNATIONAL REGULATIONS

Contact 3M for more information.

This MSDS has been prepared to meet the U.S. OSHA Hazard Communication Standard, 29 CFR 1910.1200.

SECTION 16: OTHER INFORMATION

NFPA Hazard Classification

Health: 3 **Flammability:** 0 **Reactivity:** 0 **Special Hazards:** None

National Fire Protection Association Hazard Codes are designed for use by firefighters, sheriffs, or other emergency response teams who are concerned with the hazards of materials under emergency conditions. These NFPA codes are intended to include the hazards of the products of decomposition or combustion in a fire situation.

HMIS Hazard Classification

Health: 0 **Flammability:** 0 **Reactivity:** 0 **Protection:** X - See PPE section.

Hazardous Material Identification System (HMIS(r)) hazard ratings are designed to inform employees of chemical hazards in the workplace. These ratings are based on the inherent properties of the material under expected conditions of normal use and are not intended for use in emergency situations. HMIS(r) ratings are to be used with a fully implemented HMIS(r) program. HMIS(r) is a registered mark of the National Paint and Coatings Association (NPCA).

No revision information is available.

DISCLAIMER: The information in this Material Safety Data Sheet (MSDS) is believed to be correct as of the date issued. 3M MAKES NO WARRANTIES, EXPRESSED OR IMPLIED, INCLUDING, BUT NOT LIMITED TO, ANY IMPLIED WARRANTY OF MERCHANTABILITY OR FITNESS FOR A PARTICULAR PURPOSE OR COURSE OF PERFORMANCE OR USAGE OF TRADE. User is responsible for determining whether the 3M product is fit for a particular purpose and suitable for user's method of use or application. Given the variety of factors that can affect the use and application of a 3M product, some of which are uniquely within the user's knowledge and control, it is essential that the user evaluate the 3M product to determine whether it is fit for a particular purpose and suitable for user's method of use or application.

3M provides information in electronic form as a service to its customers. Due to the remote possibility that electronic transfer may have resulted in errors, omissions or alterations in this information, 3M makes no representations as to its completeness or accuracy. In addition, information obtained from a database may not be as current as the information in the MSDS available directly from 3M.

3M MSDSs are available at www.3M.com

Appendix F: Calibration Work Instruction

CALIBRATION WORK INSTRUCTION:

System Name: Variable Gravity Spray Cooling System
Identifying #: J18573
PI: Kirk L. Yerkes (937)255-6186
Organization: AFRL/PRPS
Owning Work Center (OWC): J9341
Location: Power Division, Thermal Laboratory; Bldg 18G, Room 041B
Date [MMDDYYYY]: 09212006

DESCRIPTION OF USE:

Conduct research concerning spray cooling in terrestrial and variable gravity conditions.

CALIBRATION DESCRIPTION:

CATEGORY I TMDE (GAGES, ETC.) IN SYSTEM					CATEGORY II TMDE USED TO CALIBRATE CAT I SYSTEM				CATEGORY III PMEL TMDE USED TO CAL. CAT II TMDE			
Cont. No.	Item Description	Operation Range or Value	Operation Tolerance	Interval	Item Description	Specified Range or Value	Specific Uncert.	I/II TUR	Item Description	Specified Range or Value	Uncert.	II/III TUR
VGSCS Temperature Measurement (5.1)												
	Test Cell Thermocouples	20-220 °C	±1.0 °C	12 months	Hart Sci. 1502A w/ 5628 RTD	20-280°C	±0.011°C Max @ 419°C	90.9:1				
	Ice Point (Hart Sci. 9101)	0°C	±0.05 °C Max @ 18-25°C ambient	12 months	Hart Sci. 1504 w/ 5642 Thermistor	0-60°C	±0.002°C @ 0°C	25:1				
VGSCS Pressure Measurement (5.2)												
	Pressure Transducer (Omega PX303-100A5V)	5.0-14.7 psia	±0.25 % Full Scale (Full Scale 15 psia)	12 months	Heise PTE-1 w/ Module HQS-2582	0-15 psia	±0.05 % reading	5:1				
VGSCS Flow Rate Measurement (5.3)												
	Turbine Flowmeter (Sponsler MF90CBPHA4X-V)	0.020-.501 GPM	±0.5% reading	12 months	Mettler Balance PC4400	500-4000g	±0.3 g (±0.06% @ 500g)	>=8.3:1				

1.0 Scope/Responsibility:

- 1.1 This document contains detailed directions on accomplishing calibrations for 3 measurement systems used within the Variable Gravity Spray Cooling System, Electrochemistry and Thermal Sciences Branch, Power Division, Propulsion Directorate, Air Force Research Lab.
- 1.2 The calibrations are accomplished on an end-end basis which includes the effects of the system-internal devices, as well as the end devices.
- 1.3 The accelerometer will be calibrated by the WPAFB PMEL organization.
- 1.4 The thermocouples, ice point, pressure transducers, and flow meters will be calibrated by AFRL/PRPS using the instructions provided within this Calibration Work Instruction (CWI).

2.0 Preliminary Operations:

- 2.1 Ensure the power cords for the test rig are plugged into both the rig and power outlets.
- 2.2 Place the breaker switches on all four power circuits into the “on” position.
- 2.3 Ensure that the kill switch on the control panel is not activated.
- 2.4 Push the start button on the control panel.
- 2.5 Turn the laptop on and log in.
- 2.6 Open the Agilent Benchlink software along with the desired scan setup.
- 2.7 Begin a data scan.
- 2.8 Allow the rig equipment to warm up for approximately 30 minutes, until the ready light on the ice point is activated.
- 2.9 VGSCS Temperature Measurement System
 - 2.9.1 Assemble equipment as follows:
 - 2.9.1.1 Thermistor probe and readout
 - 2.9.1.2 RTD temperature probe and readout
 - 2.9.1.3 Constant temperature bath
- 2.10 VGSCS Pressure Measurement System
 - 2.10.1 Ensure the FC-72 loop is drained of working fluid and properly purged.
 - 2.10.2 Assemble equipment as follows:
 - 2.10.2.1 Heise pressure calibrator
 - 2.10.2.2 Roughing pump
 - 2.10.2.3 Pressure calibration tubing assembly
 - 2.10.2.4 Stop watch
- 2.11 VGSCS Flow Rate Measurement System
 - 2.11.1 Assemble equipment as follows:
 - 2.11.1.1 4 liter flask
 - 2.11.1.2 2 length of flexible transfer tubing
 - 2.11.1.3 stop watch
 - 2.11.1.4 scale
 - 2.11.1.5 thermometer
 - 2.11.1.6 large, shallow secondary containment unit with absorbent blankets

3.0 Environmental Requirements:

- 3.1 Temperature: 50-90 °F

3.2 Humidity: N/A

4.0 Environmental Compensation:

4.1 Not required when operating within limits specified in section 3.0.

5.0 Calibration Process:

5.1 Ensure the CAT II TMDE is adequate for the calibration process, i.e.:

- 5.1.1 Calibrated by PMEL and has a current calibration certificate (label) attached.
- 5.1.2 Has sufficient range and accuracy to meet the requirements listed in the Calibration Description Table (previous page).
- 5.1.3 Visually inspect CAT II TMDE for damage.

5.2 VGSCS Temperature Measurement System:

- 5.2.1 Carefully remove thermocouple wires from the wells on the front of the ice point.
- 5.2.2 Place thermistor probe into one of the wells on the front of the ice point.
- 5.2.3 Record the ice point temperature.
- 5.2.4 Repeat steps 5.2.1 and 5.2.2, taking one reading every two minutes for a ten minute period, for each well on the ice point.
- 5.2.5 Average the readings taken for each well.
- 5.2.6 Verify that the readings fall between -0.05°C and 0.05°C .
- 5.2.7 Carefully return thermocouple wires to the respective wells on the front of the ice point.
- 5.2.8 Place RTD probe and test cell thermocouples in the bath, following manufacturer's instructions regarding depth and location.
- 5.2.9 Set the bath temperature to the low end of the range of interest.
- 5.2.10 Allow the bath to come to equilibrium.
- 5.2.11 Record the RTD temperature.
- 5.2.12 Run the data acquisition system and record the thermocouple readings for at least 2 minutes.
- 5.2.13 Save the data file under an appropriate file name.
- 5.2.14 Repeat steps 5.1.4 through 5.1.7 at 5 or more temperatures in the range of interest, including one at the high end of the range.
- 5.2.15 Enter the data into an Excel spread sheet.
- 5.2.16 Fit the data using the linear regression analysis add-in in Excel to obtain the slope and intercept of the thermocouple reading vs. RTD reading curves.
 - 5.2.16.1.1 Estimate the error using NIST standard error analysis.

Note: The above procedure may be automated through computer control.

5.3 VGSCS Pressure Measurement System:

- 5.3.1 Attach the tubing assembly to the roughing pump, the pressure calibrator, and the test rig, as specified on the tubing assembly.

- 5.3.2 Turn the pressure calibrator on.
- 5.3.3 Ensure the valve located on the tubing assembly is closed.
- 5.3.4 Plug the roughing pump into a power source, and slowly open the valve on the tubing assembly.
- 5.3.5 When the pressure calibrator reads approximately 5 psi, close the valve on the tubing assembly.
- 5.3.6 Systematically exercise all the valve controls located on the control panel, ensuring equal pressure distribution throughout the system.
- 5.3.7 If the pressure has increased as a result of the previous step, reopen the valve on the tubing assembly.
- 5.3.8 When the pressure calibrator reads approximately 5 psi, close the valve on the tubing assembly.
- 5.3.9 After allowing the pressure to equilibrate, note the starting pressure, start the stop watch, and ensure that the pressure does not drift more than 0.2 psi in one minute.
- 5.3.9.1 If the pressure drifts greater than the prescribed amount, detect and repair the source of the system leak, and repeat steps 5.2.4 through 5.2.10.
- 5.3.10 Open pressure transducer calibration program on the DAQ computer.
- 5.3.11 In 2 psi increments from 5 psia to 100 psia, press the pressure record button in the program and open the valve on the tubing assembly to the next pressure. This program will record 5 pressure readings and average the values.
- 5.3.12 Open the data file into Excel and fit the data using the linear regression analysis add-in in Excel to obtain the slope and intercept of the pressure transducer reading vs. pressure calibrator reading curves.
- 5.3.13 Estimate the error using NIST standard error analysis.

5.4 VGSCS Flow Rate Measurement System:

- 5.4.1 Place the secondary containment unit near the test rig. Into the unit, place the flask, scale and graduated cylinder.
- 5.4.2 Close the electric ball valve located on the test rig between the reservoir and the pump in the FC-72 loop.
- 5.4.3 Break the line between the valve and the pump, and attach extension tubing to the inlet of the pump.
- 5.4.4 Place the extension tubing into the 4L flask, ensuring it is long enough to reach the bottom. Such tubing will serve as the return line for the flow meter calibration.
- 5.4.5 Break the line between the flow meter and the pressure transducer in the FC-72 loop, and attach extension tubing to the exit of the flow meter.
- 5.4.6 Cap off the entrance to the pressure transducer and place the extension tubing into the 4L flask, ensuring it is long enough to reach into the top of both the flask and graduated cylinder. Such tubing will serve as the spray line for the flow meter calibration.
- 5.4.7 Pour approximately 3.5 liters of FC-72 into the flask.
- 5.4.8 Have the data acquisition system set to read and record the appropriate voltage channel.
- 5.4.9 Start the data acquisition system.

- 5.4.10 On the rig control panel, flip the switch for the nozzle pump (pump 1) into the on, or up, position.
- 5.4.11 Select a desired flow rate and, using the potentiometer for pump 1, adjust the flow rate until the computer attached to the data acquisition system reads the desired rate.
- 5.4.12 Allow the flow rate to stabilize, then stop and restart the data acquisition scan.
- 5.4.13 Transfer the spray line from the flask to the graduated cylinder and start the stop watch simultaneously.
- 5.4.14 Allow the flow to continue for a predetermined length of time (dependent upon the magnitude of the desired flow rate).
- 5.4.15 When the time has finished, quickly return the spray line back to the flask and stop the stop watch.
- 5.4.16 Record the volume, mass and temperature of the fluid in the graduated cylinder, along with the exact time from the stopwatch, and desired flow rate.
- 5.4.17 Stop the data acquisition system and save the output file, recording the file name.
- 5.4.18 Return the fluid to the flask and dry the graduated cylinder.
- 5.4.19 Repeat steps 5.3.12 through 5.3.19 a minimum of 5 times for each flow rate.
- 5.4.20 Enter the data into an Excel spread sheet as follows:
 - 5.4.20.1 Time in column A
 - 5.4.20.2 Mass in column B
 - 5.4.20.3 Temperature in column C
 - 5.4.20.4 Density (from literature) in column D
 - 5.4.20.5 Volume calculated from the mass and density in column E
 - 5.4.20.6 Measured volume in column F, as a check
 - 5.4.20.7 Calculated volume flow rate (column E/column A) in column G
 - 5.4.20.8 Average voltage from the saved data file in column H
- 5.4.21 Plot the Average Voltage (Column H) vs. the Volumetric Flow Rate (Column G) as a scatter plot (points only)
- 5.4.22 Fit a linear trend line through the points, and record the slope and intercept of this voltage vs. flow rate curve. This slope and intercept give the desired characterization curve.
- 5.4.23 Estimate the error using NIST standard error analysis.

SYSTEM EQUIPMENT:

<u>NOUN:</u>	<u>MANUFACTURER:</u>	<u>MODEL:</u>	<u>ID NUMBER:</u>	<u>Reference:</u>
Pressure Calibrator	Heise	PTE-1 w/ HQS-2582	J18507	CAT II TMDE
Thermocouple Calibrator	Hart Scientific	5628	J11556	CAT II TMDE
Scale	Mettler	PC4400	J2325	CAT II TMDE
Ice Point Calibrator	Hart Scientific	5642	Still Needed	CAT II TMDE
Pressure Transducer	Omega	PX303-100A5V	Not applicable	Transducer
Turbine Flowmeter	Sponsler	MF90CBPHA4X-V	Not applicable	Flow meter
Test Cell Thermocouples	Omega	Not applicable	Not applicable	Thermocouples
Zero Point Dry Well	Hart Scientific	9101	J11542	Ice Point
Accelerometer	Columbia	SA-307HPTX	Still Needed	Not applicable